KATHOLIEKE UNIVERSITEIT LEUVEN
FACULTEIT TOEGEPASTE WETENSCHAPPEN
DEPARTEMENT BURGERLIJKE BOUWKUNDE
LABORATORIUM voor HYDRAULICA
de Croylaan 2, B-3001 Leuven (Heverlee)

WIND WAVE MODELLING IN SHALLOW WATER

WITH APPLICATION TO THE SOUTHERN NORTH SEA

Promotor :
Prof. dr. ir. J. Berlamont

Proefschrift voorgedragen tot
het behalen van het doctoraat
in de toegepaste wetenschappen

door

Weimin LUO

Oktober 1995

Published by Katholieke Universiteit Leuven
Faculteit Toegepaste Wetenschappen
de Croylaan 2, 3001 Heverlee, Belgium

First published 1995

ISBN 90-5682-003-6

KATHOLIEKE UNIVERSITEIT LEUVEN
FACULTEIT TOEGEPASTE WETENSCHAPPEN
DEPARTEMENT BURGERLIJKE BOUWKUNDE
LABORATORIUM voor HYDRAULICA
de Croylaan 2, B-3001 Leuven (Heverlee)

WIND WAVE MODELLING IN SHALLOW WATER

WITH APPLICATION TO THE SOUTHERN NORTH SEA

Jury :
Prof. E. Aernoudt, voorzitter
Prof. J. Berlamont, promotor
Prof. E. Smets
Prof. G. De Roeck
Prof. J. Monbaliu
Prof. L.H. Holthuijsen
(Delft Univ. of Technology)

Proefschrift voorgedragen tot
het behalen van het doctoraat
in de toegepaste wetenschappen

door

Weimin LUO

U.D.C.551.311.3(261.26)

Oktober 1995

Preface

Ocean is so beautiful, complex and dangerous. I am fascinated with its feature and its mood - from the pacific tranquillity of long low swell to the angry, cruel North Sea in winter. However, I never imagined that I could write a Ph.D. thesis in ocean wave modelling. Only when I came to the Hydraulic Lab. of K.U. Leuven, did I become a oceanographer. I am sure that I would not have managed alone. Many people helped and supported me during these years.

First of all, I would like to express my deepest gratitude and thanks to my promoter Prof. J. Berlamont, for his continuous guidance, encouragements, constructive criticisms and financial support.

I am grateful to my reading committee members - Prof. E. Smets and Prof. G. De Roeck for their valuable comments and suggestions.

I want to thank Prof. J. Monbaliu. He guided me into the area of ocean wave modelling and introduced me to the international WISE (Waves in Shallow Environment) group. I really appreciate his continuous supervision, advice and valuable criticisms, his good ideas and his high spirits. With his help, many disappointments turned into interesting scientific results. His contribution has been essential to complete this work. I will never forget that he spent so much time to correct my English.

My appreciation is also extended to Prof. L.H. Holthuijsen, from Delft University of Technology, and to Dr. R.A. Flather, from Proudman Oceanographic Laboratory, for their advice, important remarks and interest in this study.

The implementation of the WAM model along the Belgian coast was

carried out in the framework of the European Space Agency Pilot Project PP2-B9. This work has directly benefited from this project. The use of the CONVEX C230 at the Management Unit of the North Sea Mathematical Models (MUMM) for running the WAM model is gratefully acknowledged. I wish to thank F. Ovidio, Dr. J.-R. Bidlot and D. Van den Eynde of MUMM for obtaining the altimeter data from ESA and the buoy measurements from the Rijksinsituut voor Kust en Zee (RIKZ, the Netherlands) and the Afdeling Waterwegen Kust (AWK, Belgium), for their help with the computer facilities and plotting software, and for the numerous and constructive discussions and suggestions.

I am indebted to Dr. S.L. Weber, from Koninklijk Nederlands Meteorologisch Instituut (KNMI), for providing the code for the eddy viscosity source term and for her valuable suggestions and comments on this work. I thank S. Hasselmann, from Max-Planck Institut fur Meteorologie in Hamburg, for authorising the use of the WAM code. I am also grateful to Dr. G.Ph. van Vledder, from Delft University of Technology, for providing the code for the depth-induced wave breaking source term.

I would like to emphasize the nice working atmosphere in the Hydraulic Lab. of K.U. Leuven. Many thanks go to all of the colleagues there. I am specially grateful to Dr. C.S. Yu, Dr. Z. Song, Dr. E. Toorman, E. Bresnan, I. Uyttebroeck, D. Uten, M. Elzeir and A. Bestawy for their encouragement and support. Thanks are also going to all my international friends "de buitenlanders", with whom I have shared sad and happy moments.

Finally, my great appreciation is to my husband Ye and my little daughter Sophie for their endless love, support, understanding.

October, 1995 in Leuven
Weimin LUO

Abstract

Increased marine activities, particularly in areas of off-shore exploitation and coastal development, have created an urgent need for improved knowledge of wave conditions in the shallow near-shore regions. In this work, objectives have been made to investigate the effects of bottom friction, depth-induced wave breaking, and tidal motions on the wave evolution in shallow water, and to apply the wave model (WAM Cycle 4) to the Belgian coastal waters.

Firstly, the effects of different bottom friction formulations on the energy balance equation were quantitatively investigated for fetch-limited shallow water conditions. It was found that the formulation of the bottom friction dissipation has a quite significant effect on the energy balance at shallower water depths. Among the five original formulations for the bottom friction dissipation investigated (i.e., an empirical expression based on the JONSWAP experiment (Hasselmann *et al.*, 1973), three expressions based on the drag law turbulent friction model (Hasselmann and Collins, 1968; Collins, 1972; Madsen *et al.*, 1988a) and one based on the eddy viscosity friction model (Weber, 1991a)), a difference as big as 70% for the total energy was reported for a water depth of 15 m and a wind friction velocity of 0.71 ms^{-1}. It is revealed that the whitecapping dissipation is dominant in shallow water. The contribution of bottom friction varies clearly with depth, and also from formulation to formulation. The role of bottom friction dissipation becomes more significant as the water becomes shallower.

Secondly, it has been proven mathematically and numerically that in shallow water cases, the scaling ability of the energy growth curves with the air friction velocity is model-dependent. The growth curves from the drag law models with a fixed dissipation coefficient C_f, scale with the air friction velocity u_{a*}. The drag law model with a dynamically changing friction factor, the empirical formulation and eddy viscosity model do not scale with the wind friction velocity u_{a*}. It is concluded that the shallow

water data which are presented in dimensionless form (scaled with the air friction velocity) cannot be used to evaluate different model results.

Thirdly, the equivalent bottom friction dissipation coefficients are developed so that all five bottom friction dissipation formulations give almost the same growth curves for the total energy and the peak frequency. The equivalent coefficients for the empirical formulation and the three drag law models were obtained and referred to the bottom roughness height in the eddy viscosity model for three different wind velocities and a nondimensional water depth of 300. The introduced error for other water depths is estimated to be of the order of 5%. The validity of using equivalent coefficients in real circumstances was tested in the southern North Sea. It is concluded that the use of the empirical JONSWAP formulation with the proper equivalent coefficients is, for many practical operational applications, not only computationally efficient, but should also produce results with the same order of accuracy as the more sophisticated models for the bottom friction dissipation.

Finally, wave conditions along the Belgian coast are hindcasted by using the Cycle 4 version of the WAM model for the period from October 1992 to March 1993. The hindcast results have been validated by ERS-1 satellite data and buoy data and by the cross comparison with the muWAVE model hindcasts. The Cycle 4 version of the WAM model has been extended with inclusion of the depth-limited wave breaking source term and with a choice for the bottom friction dissipation source term, i.e., the empirical JONSWAP formulation, the drag law expression or the eddy viscosity model. The effects of bottom friction, depth-induced wave breaking and tidal surge motion on the wave evolution in the Belgian coastal waters have been assessed quantitatively.

Contents

List of Figures

List of Tables

List of Symbols

Roman symbols

a : amplitude [m]

a_b : near-bottom excursion amplitude [m]

a_n : amplitude of nth wave component [m]

A : linear term in wind input

B : exponential term in wind input

c : phase velocity $[ms^{-1}]$

c : coefficient in JONSWAP bottom dissipation expression $[m^2s^{-3}]$

C : coefficient in bottom dissipation term (general) $[ms^{-1}]$

C_{ds} : dissipation coefficient in whitecapping dissipation

C_D : drag coefficient for air-sea interaction

C_{DC} : coefficient in Collins' bottom dissipation model $[ms^{-1}]$

C_{DHC} : coefficient in Hasselmann's and Collins' model $[ms^{-1}]$

C_{DM} : coefficient in bottom dissipation model of Madsen *et al.* $[ms^{-1}]$

C_E : coefficient in eddy viscosity model of Weber $[ms^{-1}]$

C_J : coefficient in empirical JONSWAP formulation $[ms^{-1}]$

C_f : drag coefficient for sea-bottom interaction

c_g : group velocity $[ms^{-1}]$

$\mathbf{c_g}$: group velocity vector $\mathbf{c_g} = (c_g \sin\theta, c_g \cos\theta)$ $[ms^{-1}]$

c_{ga} : absolute group velocity $[ms^{-1}]$

c_x : absolute group velocity in x direction $[ms^{-1}]$

c_y : absolute group velocity in y direction $[ms^{-1}]$

c_ω : rate of change of (intrinsic) frequency $[ms^{-1}]$

c_Ω : rate of change of (apparent) frequency $[ms^{-1}]$

c_θ : rate of change of wave direction $[ms^{-1}]$

$c_{\theta c}$: rate of change of wave direction due to current refraction $[ms^{-1}]$

$c_{\theta d}$: rate of change of wave direction due to depth refraction $[ms^{-1}]$

E_{tot} : total wave energy $[m^2]$

E^*_{tot} : nondimensional total energy in terms of air friction velocity

f : frequency $[Hz]$

f_{hf} : high frequency limit$[Hz]$

f_m : mean frequency $[Hz]$

f_{max} : the highest frequency in frequency grid $[Hz]$

f_p : peak frequency $[Hz]$

f_w : friction factor

f_{PM} : peak frequency of a Pierson-Moskowitz spectrum $[Hz]$

f_1 : the lowest frequency in frequency grid $[Hz]$

f^* : nondimensional frequency in terms of air friction velocity

f^*_p : nondimensional peak frequency in terms of air friction velocity

$F(f)$: frequency spectrum $[m^2s]$

$F_J(f)$: JONSWAP frequency spectrum $[m^2s]$

$F_{PM}(f)$: Pierson-Moskowitz frequency spectrum $[m^2s]$

$F(\mathrm{k})$: wave number spectrum $[m^3]$

$F(f,\theta)$: frequency directional spectrum $[m^2s]$

$F(\omega,\theta)$: angular frequency directional spectrum $[m^2s]$

$F^*()$: nondimensional spectrum in terms of air friction velocity

g : acceleration of gravity = 9.81 $[ms^{-2}]$

$G(\theta)$: spreading function

h : averaged water depth of sea [m]

h^* : nondimensional water depth in terms of air friction velocity

H : wave height [m]

H_m : maximum wave height [m]

H_{rms} : root mean square wave height [m]

H_s : significant wave height [m]

k : wave number $[m^{-1}]$

$\mathbf{k}$	: wave number vector (k, θ) $[m^{-1}]$
k_m	: mean wave number $[m^{-1}]$
$\mathbf{k}_n$	: wave number vector of nth mode $[m^{-1}]$
k_N	: bottom roughness height [m]
k_p	: wave number at the peak of the spectrum $[m^{-1}]$
k^*	: nondimensional wave number in terms of air friction velocity
k_N^*	: nondimensional K_N in terms of air friction velocity
$\hat{k}$	: mean inverse wave number $[m^{-\frac{1}{2}}]$
L	: wave length [m]
m	: fitting parameters in whitecapping dissipation
n	: fitting parameters in whitecapping dissipation
n	: number of wave components
N	: wave action density $[m^2 s^2]$
p	: pressure $[N m^{-2}]$
$\mathbf{r}$	: surface displacement vector [m]
R	: scaling factor in discrete interaction approximation
R	: radius of the earth [m]
S_{bf}	: bottom friction dissipation source term $[m^2]$
S_{br}	: depth-limited wave breaking dissipation source term $[m^2]$
S_{ds}	: whitecapping dissipation source term $[m^2]$
S_{in}	: wind input source term $[m^2]$
S_{nl}	: nonlinear interactions source term $[m^2]$
S_{tot}	: sum of all source terms $[m^2]$
S_{nl}^h	: nonlinear interactions source term for a finite depth $[m^2]$
t	: time [s]
t_1	: time lag [s]
T	: period [s]
$\mathbf{u}$	: wave motion horizontal particle velocity vector (u, v) $[ms^{-1}]$
u, v	: x, y component of mean current velocity $[ms^{-1}]$
u, v, w	: mean velocity field in wave boundary layer $[ms^{-1}]$
u_{a*}	: wind (air) friction velocity $[ms^{-1}]$
$\mathbf{U}$	: mean current vector (u, v) $[ms^{-1}]$

U_z : wind speed at a height of z meter $[ms^{-1}]$
U_5 : wind speed at a height of 5 meter $[ms^{-1}]$
U_{10} : wind speed at a height of 10 meter $[ms^{-1}]$
$U_{19.5}$: wind speed at a height of 19.5 meter $[ms^{-1}]$
$\mathbf{U}_b$: free stream orbital velocity vector $[ms^{-1}]$
u^* : wave boundary layer friction velocity $[ms^{-1}]$
u', v', w' : fluctuating velocity field in wave bottom boundary layer $[ms^{-1}]$
x : fetch [m]
x : space in direction from west to east [m]
$\mathbf{x}$: space coordinate vector $\mathbf{x} = (x, y)$ [m]
x^* : nondimensional fetch in terms of air friction velocity
y : space in direction from south to north [m]
z : vertical coordinate upwards from bottom [m]
z_c : critical height where wind speed equals to phase velocity [m]
z_0 : roughness length in atmospheric boundary layer [m]

Greek symbols

α : Phillips constant (=0.0081)
α_{br} : constant in depth-induced wave breaking
α_{ch} : Charnock constant
α_1, α_2 : wave breaking dissipation coefficients
$\bar{\alpha}$: integral wave steepness
$\bar{\alpha}_{PM}$: integral wave steepness for a Pierson-Moskowitz spectrum
β : empirical factor in the Komen *et al* wind input
β_m : empirical factor in the Janssen wind input
γ : peak enhancement factor
γ_1, γ_2 : wave breaking coefficients
δ : wave boundary layer thichness [m]
ϵ : eddy viscosity coefficient $[m^2 s^{-1}]$
η : sea surface elevation $[m]$
η_{br} : ratio of root mean square wave height to maximum wave height

η_d : whitecapping dissipation factor
θ : wave direction relative to the North
κ : von Karman constant
ρ_a : density of air $[kgm^{-3}]$
ρ_w : density of water $[kgm^{-3}]$
σ : peak width
σ_a : left peak width
σ_b : right peak width
τ : surface stress $[Nm^{-2}]$
τ : horizontal shear stress (τ_1, τ_2) in wave boundary layer$[Nm^{-2}]$
τ_b : horizontal bottom shear stress (τ_1, τ_2) $[Nm^{-2}]$
τ_w : wave induced stress (τ_{wx}, τ_{wy}) $[Nm^{-2}]$
τ_{hf} : high frequency contribution to wave induced stress $[Nm^{-2}]$
ϕ : phase [°]
ϕ_n : phase of nth wave component [°]
ψ : wind direction [°]
ω : angular (intrinsic) frequency $[rad/s]$
ω_n : angular (intrinsic) frequencies $[rad/s]$
$\bar{\omega}$: mean angular (intrinsic) frequency $[rad/s]$
$\hat{\omega}$: mean inverse angular (intrinsic) frequency $[s/rad]$
Ω : apparent frequency $[rad/s]$

Subscripts

a : air
b : bottom
i : position in direction from west to east
int : source terms integration
j : position in direction from south to north
k : position in angular direction
m : position in frequency space
$prop$: propagation contribution

s : source terms contribution

w : wave or water

Supscripts

n : propagation time level

$*$: nondimensional form in terms of air friction velocity

Chapter 1

Introduction

1.1 Background

Wave forecasting is of great importance not only for marine safety in coastal navigation, fishery activities, ferries and freak events (flooding, cyclones), but it also has considerable economic relevance for shipping routes, coastal structures, beach erosion and for avoiding storm damage in coastal zones. An objective forecast of ocean wave conditions requires a reliable numerical wave prediction model.

Since the first operational wave prediction empirical scheme developed by Sverdrup and Munk (1947), significant advances have been made in numerical wave prediction modelling. It was the introduction of the concept of a wave spectrum by Pierson *et al.* (1955) and of the spectral transport equation by Gelci *et al.* (1956, 1957) that marked the beginning of a new era in wave modelling. The important milestones were formed by the theoretical work of Phillips (1957) and Miles (1957) on wave generation and by Hasselmann's (1962) theory of four wave-wave interactions. For the first time it was possible to write down the general expression for the source functions (Hasselmann, 1962), in which the wind input, the nonlinear interaction and the whitecapping dissipation were included. The importance of nonlinear transfer in governing the shape and evolution of a wave spectrum was established by the Joint North Sea Wave Project (JONSWAP) (Has-

selmann *et al.*, 1973), leading to the development of the parametric wave models. The Sea Wave Modelling Project (SWAMP, 1985) study revealed a number of basic shortcomings in all ocean wave models of that time. Neither the **first generation** models, in which nonlinear interactions are neglected, nor the **second generation** models which incorporate them, but in a simplified parametrized form, could describe the wind-sea-swell transition well. Although both first and second generation models can be tuned to provide useful results for certain classes of wind fields, they are not reliable in extreme situations. In rapidly changing wind fields the deficiencies of these models were associated with inadequate parameterization of the nonlinear transfer processes. Wave forecasts for extreme conditions are, however, urgently needed. This has prompted a large international group of scientists, including G.J. Komen, L. Cavaleri, M. Donelan, K. Hasselmann, S. Hasselmann and P.A.E.M. Janssen, to work on a better kind of model. The breakthrough came from Hasselmann and Hasselmann (1985b) who proposed an efficient method to approximate the nonlinear interactions. This opened the way to the development of the **third generation** WAve Models, WAM type models, in which no restriction is imposed on the shape of the wave spectrum. Nowadays, the WAM code has been well tested and it is used to perform operational wave prediction globally at the European Centre for Medium-Range Weather Forecasts (ECMWF) in Reading and regionally in many other centres. The advances in remote sensing of ocean waves and the global measurements of wave spectra with the First European Remote Sensing Satellite ERS-1 have had a strong impact on the development of wave models and have stimulated and are still stimulating important new work in the area of wave data assimilation.

The wind is always blowing somewhere over the ocean. Once generated from the air-sea interaction, wind waves can dissipate, interact with each other and propagate over a long distance toward a coast. When waves propagate into a shallow water continental shelf sea, they start to feel the bottom and their energy is redistributed and dissipated more irregularly due to refraction, shoaling, bottom friction, percolation, depth limitation and

currents, etc. Prediction of wave conditions in shallow water has received in recent years increased emphasis in both the scientific and engineering communities. The early work can be found in Longuet-Higgins (1966), Collins (1972), Hasselmann *et al.* (1973), Shemdin *et al.* (1978), Cavaleri and Rizzoli (1981), etc. An extension work of SWAMP, which recommended the development of the WAM model, to shallow water (SWIM, 1985) was made by Bouws *et al.* (SWIM group, 1985). The SWIM study had revealed distinct differences between three second generation models (GONO, BMO and HYPA) in their treatment of shallow water effects. Therefore the WAM model, which is today's most advanced wave forecasting model, has been extended to shallow water continental shelf sea conditions. The first WAM model (WAMDI Group, 1988) included all wave physics in deep water. The source functions consist of the wind input, nonlinear interactions and whitecapping dissipation. The shallow water version of the model includes depth refraction (steady case) and a simple empirical bottom dissipation term of Hasselmann *et al.* (1973). The effect of relatively strong (steady) current was added into WAM by Hubbert and Wolf (1991). The depth-dependent breaking, which is very important in extreme shallow zones, is not yet included in the current version of the WAM model. The time-dependent water-level changes and currents variations are not taken into account. Now, the WISE (Waves in Shallow Environments) group, an international group of scientists, is investigating the capabilities and the limitations of third generation modelling in shallow water, and working on a state-of-the-art model (or a set of state-of-the-art models) for waves in shallow water that can be applied into the surfzone.

1.2 Aim and scope of the study

1.2.1 Effect of bottom friction dissipation models

Bottom friction dissipation is a dominant dissipation mechanism in the North Sea and the northwest European continental shelf. A number of different models can be found in the literature. They are: an empirical expres-

sion based on the JONSWAP experiment (Hasselmann *et al.*, 1973), three expressions based on the drag law turbulent friction model (Hasselmann and Collins, 1968; Collins, 1972; Madsen *et al.*, 1988a) and one based on the eddy viscosity friction model (Weber, 1991a). These five models have been widely used in many wave models, and the dissipation coefficients used in different cases were quite different. The question is, how these five formulations can affect results for the energy and peak frequency growth curves. The **first objective** of this study is to get a better understanding of bottom friction dissipation in shallow water, and to quantitatively investigate the effects of different bottom friction formulations and different coefficients on the energy balance for gravity waves in shallow water. In this respect, the energy transport equation will be solved in fetch-limited shallow water conditions with different bottom friction dissipation models.

In general, the growth curves in deep water are assumed to scale in terms of the air friction velocity. In the case of shallow water, the growth curves were also presented by many scientists (see, WAMDIG, 1988; Weber, 1989; Tolman, 1991; Komen *et al.*, 1994; Verhagen and Young, 1995, etc.) in the nondimensional form scaled by the air friction. These curves were used to evaluate different model results or to compare the numerical results with measurements. This way of presenting or comparing results, be it from numerical experiments or from field measurements, should be questioned. In this study the scaling ability of the growth curves in shallow water will be numerically investigated. A detailed mathematical analysis will be made to study the scaling behaviour of the growth curves from different bottom friction dissipation models.

1.2.2 Wave prediction along the Belgian coast

A wave prediction model is a very useful tool for the navigation of large sea vessels through the shallow entrance channels towards the Belgian harbours such as Antwerp and Zeebrugge. The Belgian coastal waters are quite shallow with long parallel sand banks. The wave model system - mu-WAVE - currently in operational use for the Belgian coast, is a model of the second

generation. Since the second generation model parametrizes the shape of the surface displacement spectrum with a limited number of parameters, it remains difficult to predict wave conditions, especially under rapidly changing wind fields. The **second objective** of this work is to implement the third generation WAM system (most recent version Cycle 4) for application to the Belgian coastal waters. To evaluate the quality of the WAM model results, appropriate validation should be made against observed data. This will be done using the ERS-1 satellite data, wave buoy data and by a cross comparison of wave prediction between mu-WAVE and WAM. The limitation and problems of the WAM Cycle 4, when it is applied to the Belgian shallow waters, should also be identified.

1.2.3 Development and test of equivalent bottom friction dissipation coefficients

The work of Luo and Monbaliu (1994) reported that the five original bottom friction dissipation models have significant effects on the fetch-limited growth curves. For a water depth of 15 m and a wind velocity of 0.71 ms^{-1} a difference as big as 70% for the energy growth curve was found. Our **third objective** is to examine the possibility of finding equivalent bottom friction dissipation coefficients so that the different formulations can produce the same or nearly the same levels for growth curves for the total energy and peak frequency.

In the standard WAM code, the computation of bottom friction dissipation is performed using the empirical formulation (Hasselmann *et al.*, 1973), with a mean value of 0.038 m^2s^{-3} for the dissipation coefficient. In this study, the eddy viscosity model and one of the drag law models will be implemented in the Cycle 4 version of the WAM model. The application of the developed equivalent coefficients in real circumstances will be tested for the southern North Sea region.

1.2.4 Effects of depth-limited wave breaking and currents

The bathymetry of the Belgian coast is very complicated. The water depth is quite limited. The water-level changes and current variations due to the tides and the wave breaking due to limited depth may be very important. The current version of the WAM model does not account for these factors, neither does the mu-WAVE model used for the prediction of waves at the Belgian coast. A numerical study of extreme waves in the North Sea, using Tolman's (1991b) model, has also shown that the inclusion of depth-induced wave breaking is necessary (Holthuijsen *et al.*, 1994). The inclusion of effects of non-stationary depth and currents was made in Tolman's (1991a) model WAVEWATCH. The work of Tolman (1991b) showed that the non-stationarity of the tidal currents (which is usually neglected) was found to affect mean parameters such as significant height and mean period up to 10%; spectral density values were affected up to 100%. Therefore, the **final objective** of the study is to investigate the effects of wave breaking due to depth-limitation on the wave evolution for the Belgian coastal zone. The possibility of coupling the WAM Cycle 4 with a tide surge model will be discussed.

1.3 Methodology

This thesis consists of seven chapters. The general background of ocean and shallow water wave modelling, along with the scope and aim of the study, is given in **chapter 1**.

In **chapter 2**, one will see a brief overview of wave physics and numerical techniques in shallow water wave modelling. A summary of important studies on wave generation, propagation, refraction, dissipation due to whitecapping, nonlinear interactions, bottom friction dissipation and depth-induced wave breaking will be provided. This chapter is intended to provide a ready reference material and a suitable basis for those who may start research work in wave modelling.

The detailed description of bottom friction dissipation modelling is

given in **chapter 3**. The energy transfer equation will be solved numerically for fetch-limited conditions in waters of limited depth in the first part of the chapter. The resulting growth curves for the total energy and peak frequency are obtained for five original bottom friction formulations. The effects of different formulations on the energy balance are inter-compared and evaluated. The results are also compared with the Coastal Engineering Research Centre growth curves. The second part of this chapter looks at the scaling ability of the growth curves of total energy and peak frequency in terms of wind friction velocity in the shallow water case. This is done by mathematical analysis and through numerical experiments.

Chapter 4 will be devoted to the wave prediction along the Belgian coast by using the Cycle 4 version of WAM. In this chapter, a short description of the WAM model system is given. The reader is referred to the WAM book by Komen *et al.* (1994) for the detailed description of this model and its physics and applications. In order to intercept the swell generated far away in the North Sea and to account for the complex bathymetry of the Belgian coast, the WAM code has been implemented in both a coarse grid with spatial resolution of 50 km (stereographical projection) and a fine grid with resolution of 10 km for the period from October 1992 to March 1993. Model parameters and the model area information about grid, bathymetry and wind field can be found in this chapter. The validation of the WAM results will be made by use of ERS-1 satellite data and buoy data to judge the quality of the model prediction. A comparison of the significant wave height and mean period prediction between mu-WAVE and WAM will be presented. The limitation and problems of the WAM system when it is applied to the Belgian shallow waters will be detected also.

Chapter 5 explores how, by proper adjustment of their dissipation coefficients, different formulations of the bottom friction dissipation can lead to the same effect on the energy balance for the fully developed stage. Equivalent coefficients referred to the bottom roughness height in the eddy viscosity model are developed for the empirical formulation and three drag law models in fetch-limited shallow water for three different wind velocities.

The validity of using equivalent coefficients is tested under real circumstances. Two other bottom friction dissipation models: a drag law model (Collins, 1972) and the eddy viscosity model [Weber, 1991a] have also been implemented for the application of the third generation WAM model in the Belgian coastal waters. The hindcasts are made for the period running from 1st to 28th February 1993 for the area of the southern North Sea. The results are compared with the measurements at different stations.

Chapter 6 presents effects of depth-limited wave breaking on the wave evolution in the Belgian shallow zone. The Cycle 4 version of the WAM model has been extended with a formulation for depth-limited wave breaking. The assessment of its performance against shallow water wave data is examined. The formulation for the wave breaking dissipation due to depth-limitation in shallow water is based on the expression of Battjes and Janssen (1978), which was modified to predict the energy loss per spectral component by Van Vledder (1995). In this chapter the possibility of coupling the WAM model with a tide surge model is investigated.

In **chapter 7**, summary and conclusions are presented. Recommendations are given for further research.

1.4 Main contributions

The main **contributions** of this work are:

1) The effects of different bottom friction formulations on the energy balance equation were quantitatively investigated for fetch-limited shallow water. It is found that the formulation of the bottom friction dissipation has a quite significant effect on the energy balance at shallower water depths. Among the five original formulations for the bottom friction dissipation (i.e., an empirical expression based on the JONSWAP experiment (Hasselmann *et al.*, 1973), three expressions based on the drag law turbulent friction model (Hasselmann and Collins, 1968; Collins, 1972; Madsen *et al.*, 1988a) and one based on the eddy viscosity friction model (Weber, 1991a)), a difference as big as 70% for the total energy was reported for a water depth

of 15 m and a wind friction velocity of 0.71 ms^{-1}. It is revealed that the whitecapping dissipation is dominant in shallow water. The contribution of bottom friction varies clearly with depth, and also from formulation to formulation. The role of bottom friction dissipation becomes more significant when the water becomes shallower.

2) It has been proven mathematically and numerically that in shallow water cases the scaling ability of energy growth curves with the air friction velocity is model-dependent. The growth curves from the drag law models with a fixed dissipation coefficient C_f, scale with the air friction velocity u_{a*}. The drag law model with a dynamically changing friction factor, the empirical formulation and eddy viscosity model do not scale with the wind friction velocity u_{a*}. It is proposed that the shallow water data which are presented in dimensionless form (scaled with the air friction velocity) cannot be used to evaluate different model results.

3) The equivalent bottom friction dissipation coefficients are developed so that all five bottom friction dissipation formulations give almost the same growth curves for the total energy and the peak frequency. The validity of using equivalent coefficients in real circumstance are tested in the southern North Sea. It is concluded that the use of the empirical JONSWAP formulation with the proper equivalent coefficients is, for many practical operational applications, not only computationally efficient, but should also produce results with the same order of accuracy as the more sophisticated models for the bottom friction dissipation.

4) Wave conditions along the Belgian coast are predicted by using the Cycle 4 version of the WAM model for the period from October 1992 to March 1993. The prediction results have been validated by ERS-1 satellite data and buoy data and by the cross comparison with the mu-WAVE model prediction.

5) The Cycle 4 version of the WAM model has been extended with the inclusion of the eddy viscosity and the drag law bottom friction dissipation model, of the depth-limited wave breaking dissipation. The effects of bottom friction, depth-induced wave breaking and tidal surge motion

on the wave evolution in the Belgian coastal waters have been assessed numerically.

Chapter 2

Wave Physics and Numerical Modelling

2.1 Introduction

When you face the great sea, in your eye you see, not the deep abyss where no light penetrates, not the great leviathans engulfing tiny creatures, but the innumerable waves are its form, its texture.

Several kinds of waves can and do occur in the ocean. They can be catalogued according to the nature of the restoring force as Coriolis waves, gravity waves, or surface tension waves. The surface gravity waves (including wind waves, tsunamis and tides) are most commonly seen along a sea shore. Wind waves are generated by the wind blowing over the water surface, tides are driven by the gravitational attraction of celestial bodies and tsunamis are caused by earthquakes. This last wave falls out of the scope of this work and is not discussed here. The wind waves typically have periods of 1 to 10 s, and wave lengths of a few to a few hundred meters. Tides usually have periods in the order of 10 h and wave lengths in the order of 1000 km. In general, wind waves are short waves and tides long waves. The main subject of the present study is short waves. The effects of tides on the wave action balance are also included in this chapter. The possible influences of changing water level and currents on wind wave evolution in

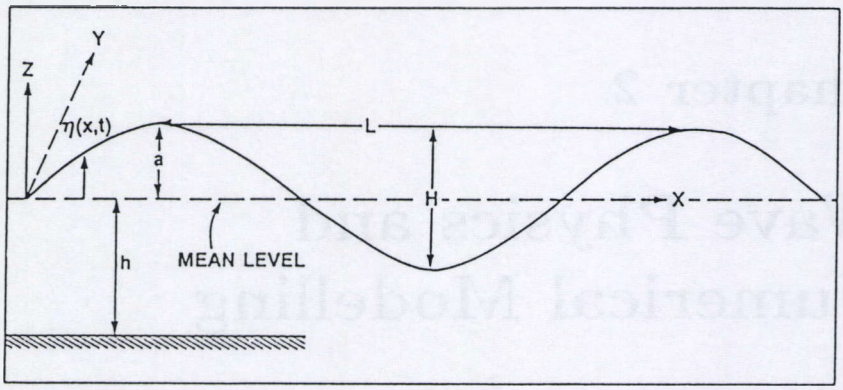

Figure 2.1: A monochromatic gravity wave

the Belgian shallow water zone will be discussed in chapter 6.

Short waves can propagate over a long distance. When the wind ceases in the generating area, or waves travel out of the wind force field, they become swell. When they approach the coastline, their energy is (partly) reflected or dissipated by breaking, bottom friction and the interaction with strong currents. This chapter presents the basics of wind wave dynamics, physics and numerical modelling in shallow water, where waves are with wave lengths which are long compared to the water depth.

2.2 Description of wind waves

2.2.1 Description of monochromatic waves

A monochromatic gravity wave can be represented by the vertical displacement of the water surface relative to the average water surface shown in figure 2.1. The sea bottom depth is denoted as h. Considering a simple plane sinusoidal wave in situations without currents, moving in the hori-

zontal x direction, the displacement $\eta(x,t)$ at time t can be represented as follows:

$$\eta(x,t) = a\cos(kx - \omega t + \phi) \tag{2.1}$$

where

t	: time $[s]$
x	: horizontal coordinate $[m]$
a	: amplitude $[m]$
k	: wave number $[m^{-1}]$
ω	: angular frequency $[Hz]$
ϕ	: phase [°]

Waves are characterized by the wave height H defined as the difference in surface elevation between the wave trough and the wave crest; the wave length L stated as the horizontal distance between two crests or troughs; the wave period T, described as the time needed for two successive wave crests to pass a fixed point (or the wave frequency, the inverse of the period); the wave direction defined as the direction from which the waves are coming with respect to the North direction; the wave steepness (H/L) specified as the ratio of wave height to wave length; and the wave age (c/U) defined as the ratio of phase velocity to wind speed. The following basic relations exist:

$$\begin{aligned} \omega &= 2\pi f \\ f &= \frac{1}{T} \\ k &= \frac{2\pi}{L} \end{aligned}$$

If an irrotational (potential) flow and incompressibility of water are assumed, with a small displacement compared to the water depth h, the dispersion relation for wind waves can be derived from the basic hydrodynamic equations (mass and momentum conservation equations) (see, Kinsman, 1965).

$$\omega^2 = gk\tanh(kh) \tag{2.2}$$

where

g	: acceleration of gravity = 9.81 $[ms^{-2}]$
h	: averaged water depth of sea $[m]$

Two different concepts of velocity are considered in wave propagation. The phase velocity c is the velocity at which the wave profile travels:

$$c = \frac{\omega}{k} \tag{2.3}$$

The group velocity is the velocity of a wave group at which the wave energy travels. Its absolute value is:

$$c_g = \frac{\partial \omega}{\partial k} \tag{2.4}$$

i.e.,

$$c_g = \frac{\omega}{k}(\frac{1}{2} + \frac{kh}{\sinh 2kh}) \tag{2.5}$$

The group velocity has the direction θ perpendicular to the wave crest.

If waves propagate in a medium that itself is moving with velocity U (such as a current), the frequency of waves passing a fixed point is called the apparent frequency Ω, expressed by the following Doppler type equation as

$$\Omega = \omega + \mathrm{k} \cdot \mathrm{U} \tag{2.6}$$

where

Ω	: apparent frequency
ω	: (intrinsic) frequency
k	: wave number vector (k, θ)
U	: mean current vector $[ms^{-1}]$

The group velocity observed at a fixed point is the absolute group velocity and equals

$$c_{ga} = \frac{\partial \omega}{\partial k} + \mathrm{U} \tag{2.7}$$

It is very important to distinguish between three main characteristic curves: streamline, wave orthogonal and wave ray (see also e.g., Christoffersen, 1985). The streamline travels in the direction of the moving medium velocity **U**. The orthogonal is normal to the wave front. It gives the direction of wave travel and has the wave number vector as a tangent. Finally, a wave ray goes in the direction of the absolute group velocity.

2.2.2 Spectral description of wind waves

The sea surface does not contain a single monochromatic wave but is a superposition of many different wave components:

$$\eta(\mathbf{x},t) = \sum_{n=1}^{\infty} a_n \cos(\mathbf{k}_n \cdot \mathbf{x} - \omega_n t + \phi_n) \tag{2.8}$$

where

$\mathbf{x}$	: space coordinate vector $[m]$
a_n	: amplitudes $[m]$
$\mathbf{k}_n$	: wave number vector $[m^{-1}]$
ω_n	: angular frequencies $[Hz]$
ϕ_n	: phases $[°]$
n	: number of wave components

Assuming that all phases ϕ_n, are stochastically independent and randomly distributed over the interval $(0,\ 2\pi)$, the central limit theorem states that the sea surface elevation at a fixed point has a Gaussian distribution. Its covariance function reads

$$< \eta(\mathbf{x},t)\eta(\mathbf{x}+\mathbf{r},t+t_1) > \tag{2.9}$$

where $\mathbf{r}$ is the displacement vector, t_1 is the time lag, and $<>$ denotes ensemble average. The Fourier transformation of the covariance (2.9) is the so-called wave spectrum, which is often used in wave dynamics.

The wave spectrum can be found in the literature in the forms $F(\mathrm{k})$, $F(\omega,\theta)$ and $F(f,\theta)$. The relationships between them are:

$$F(\omega,\theta) = k\frac{\partial k}{\partial \omega}F(\mathrm{k}) \tag{2.10}$$

$$F(f,\theta) = 2\pi F(\omega,\theta) \tag{2.11}$$

In this work the frequency and direction form $F(f,\theta)$ will be used for the wave spectrum.

From the wave spectrum, some fundamental parameters are defined, such as total energy (per unit area), significant wave height, peak frequency, etc.

The total energy E_{tot} is the integral of the wave spectrum over all the wave components, and given by

$$E_{tot} = \int F(f,\theta)df d\theta \tag{2.12}$$

The significant wave height H_s is the arithmetic mean height of the $\frac{1}{3}$ highest waves. It is approximately expressed as

$$H_s = 4\sqrt{E_{tot}} \tag{2.13}$$

The peak frequency f_p is the frequency which has the highest energy density (F integrated over direction).

2.2.3 Frequency spectrum formulation

The frequency spectrum is obtained from the two-dimensional spectrum $F(f,\theta)$ by integration with respect to direction:

$$F(f) = \int_0^{2\pi} F(f,\theta)d\theta \tag{2.14}$$

Several complicated formulations can be found for the frequency spectrum, like the spectrum formulations from Pierson and Moskowitz (1964), from the JONSWAP experiments (Hasselmann *et al.*, 1973), etc.

Based on 420 selected wave measurements recorded with a ship-borne wave recorder and using a similarity theory of Kitaigorodskii (1962), Pierson and Moskowitz found that the following expression fitted observations at the weather ships for wind speeds between 10 and 20 ms^{-1} for a well developed sea:

$$F_{PM}(f) = \alpha g^2 (2\pi)^{-4} f^{-5} \exp^{-\frac{5}{4}(\frac{f}{f_{PM}})^{-4}} \tag{2.15}$$

where

α : so-called Phillips constant (= 0.0081)
f_{PM} : peak frequency of the spectrum

$$f_{PM} = 0.13\frac{g}{U_{10}} = 0.14\frac{g}{U_{19.5}} \tag{2.16}$$

where U_{10} and $U_{19.5}$ are wind speed at the height of 10 m and 19.5 m, respectively.

Hasselmann *et al.* (1973) during the JONSWAP experiments found that the wind sea spectrum in the growing phase has a much sharper peak than the Pierson-Moskowitz spectrum. According to those experiments the so-called JONSWAP spectrum was proposed (see figure 2.2), which generalizes the Pierson-Moskowitz spectrum by including the fetch as an additional parameter:

$$F_J(f) = \alpha g^2 (2\pi)^{-4} f^{-5} \exp^{-\frac{5}{4}(\frac{f}{f_p})^{-4}} \gamma^{\exp^{\frac{-(f-f_p)^2}{2\sigma^2 f_p^2}}} \tag{2.17}$$

The shape parameters are:

γ : peak enhancement factor
σ : a factor determining the width of the peak enhancement

$$\sigma = \sigma_a \qquad f < f_p$$
$$\sigma = \sigma_b \qquad f \geq f_p$$

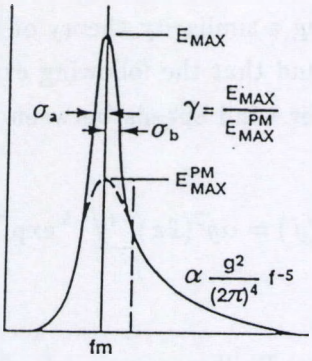

Figure 2.2: The JONSWAP spectrum (from Hasselmann *et al.*, 1973)

The mean values for γ, σ_a and σ_b are respectively 3.3, 0.07 and 0.09.

The scale parameters are:

α	: Phillips constant
f_p	: peak frequency of the spectrum

The scale parameters are dependent on the growth stage through the nondimensional fetch $\tilde{x}$

$$\begin{aligned} \alpha &= 0.076(\tilde{x})^{-0.22} \\ \tilde{f}_p &= 3.5(\tilde{x})^{-0.33} \end{aligned}$$

the nondimensional fetch $\tilde{x}$ and the nondimensional peak frequency $\tilde{f}_p$ are defined as

$$\tilde{x} = \frac{xg}{U_{10}^2}$$

$$\tilde{f}_p = \frac{f_p U_{10}}{g}$$

where x is the fetch and U_{10} is the wind speed at 10 meter height.

2.2.4 Wind in wave modelling

Wave models are driven by the surface wind fields. Accurate knowledge of the wind data is very important for the prediction of wind generated waves. There are two common ways to represent the wind speed, i.e., the wind friction velocity u_{a*} and the wind speed U_z at height z meter above the mean water level.

The air friction velocity is defined as the square root of the ratio of the surface stress τ caused by the wind and the air density ρ_a, i.e.,

$$u_{a*} = \sqrt{\frac{\tau}{\rho_a}} \tag{2.18}$$

The general method to calculate the wind speed U_z at height z meter is based on the logarithmic profile in the surface layer, given by (Panofsky and Dutton, 1984)

$$U_z = \frac{u_{a*}}{\kappa} \ln \frac{z}{z_0} \tag{2.19}$$

where κ is the von Karman constant (equal to about 0.4); z_0 is a roughness length, the simplest expression of which is given by Charnock (1955)

$$z_0 = \alpha_{ch} \frac{u_{a*}^2}{g} \tag{2.20}$$

with α_{ch} the Charnock constant.

In practice, the drag coefficient C_D is frequently used to relate the friction velocity (or surface stress) to the wind speed at a given height, which is defined as

$$C_D(z) = (\frac{u_{a*}}{U_z})^2 \tag{2.21}$$

For a logarithmic profile (eq(2.19)) it follows that

$$C_D(z) = \frac{\kappa^2}{\ln^2(z/z_0)} \tag{2.22}$$

The value of C_D depends on the choice of roughness length and on the height of observation. For a height of 10 m, Wu (1982) proposed an approximate formula for $C_D(10)$, which is often used in wave modelling,

$$C_D(10) = (0.8 + 0.065 U_{10}) 10^{-3} \tag{2.23}$$

where U_{10} is the wind speed at a height of 10 m.

Recent developments (Janssen, 1989; Janssen, 1991; Maat *et al.*, 1991; Smith *et al.*, 1992; Monbaliu, 1994) indicate a sea-state-dependence of the roughness length. The drag coefficient, therefore, depends not only on the roughness length and the height of observation but on the wave state as well. This dependence is taken into account in the Cycle 4 version of the WAM model (also see 2.3.2).

2.3 The energy and/or action balance equation

In the conventional approach of all models in deep water, the evolution of the wave spectrum $F(f, \theta, \mathbf{x}, \mathbf{t})$ is described by the spectral energy balance equation (SWAMP, 1985):

$$\frac{\partial F}{\partial t} + \mathbf{c_g} \frac{\partial F}{\partial \mathbf{x}} = S_{tot} \tag{2.24}$$

where

F	: wave energy spectrum $= F(f, \theta, \mathbf{x}, \mathbf{t})$
t	: time
$\mathbf{c_g}$	: group velocity vector $\mathbf{c_g} = (c_g \sin\theta, c_g \cos\theta)$
$\mathbf{x}$	: space coordinate $\mathbf{x} = (x, y)$
S_{tot}	: total source term

The first term on the left hand side indicates the temporal change rate of wave energy. The second term represents the propagation of energy. The right hand side is the total source term in deep water, which should include the wind input, the whitecapping dissipation and nonlinear wave interactions.

In the shallow water situation, the effect of depth, currents and bottom friction, etc., should be taken into account for wave evolution. In situations with nonuniform currents, the wave energy is not conserved due to an exchange of energy between waves and mean current. Wave action instead

of energy is conserved during propagation (Phillips, 1977). In this study, the generalized action balance equation governing the wave evolution in Cartesian coordinates is given by (Komen *et al.*, 1994)

$$\frac{\partial N}{\partial t} + \frac{\partial}{\partial x}(c_x N) + \frac{\partial}{\partial y}(c_y N) + \frac{\partial}{\partial \Omega}(c_\Omega N) + \frac{\partial}{\partial \theta}(c_\theta N) = \frac{S_{tot}}{\omega} \qquad (2.25)$$

The notations are

N	: wave action density $N(\Omega, \theta; \mathbf{x}, t) = F(\Omega, \theta; \mathbf{x}, t)/\omega$
t	: time
x	: space in direction from west to east
y	: space in direction from south to north
c_x	: absolute group velocity in x direction
c_y	: absolute group velocity in y direction
c_Ω	: rate of change of apparent frequency
c_θ	: rate of change of wave direction
S_{tot}	: total source term
Ω	: apparent frequency (eq(2.6))
θ	: wave direction relative to the North
ω	: (intrinsic) frequency

The first term on the left hand side represents the local rate of change of the wave action density. The second and third terms are the propagation of action density in the (x, y) space including bottom- and current- induced straining. The bottom-induced straining is commonly called shoaling. The last two terms account for depth and current refraction, and describe the redistribution of action density over the spectrum. The source terms should include all physical processes that contribute to the wave action density evolution.

The code in the Cycle 4 version of the WAM model solves the following energy balance equation in the moving coordinate system, in which only the ω coordinate is moving with the mean current velocity **U**:

$$\frac{\partial F}{\partial t} + \frac{\partial}{\partial x}(c_x F) + \frac{\partial}{\partial y}(c_y F) + \frac{\partial}{\partial \omega}(c_\omega F) + \frac{\partial}{\partial \theta}(c_\theta F) = S_{tot} \qquad (2.26)$$

with c_ω the rate of change of (intrinsic) frequency. Afterwards, the transformation of spectra from ω coordinate to Ω coordinate is made through equation (2.6).

The reason to do so is that in practical applications one usually deals with the wave energy spectra, since these are measured by buoys. This choice was made when the code of Cycle 4 version was written. The solution of the WAM Cycle 4 is equivalent to that from eq(2.25) for a steady state situation, e.g., a steady current field. Therefore, for the unsteady cases (e.g., tides where you have a time-dependent current field), the coupling between the tide surge model and the WAM wave model is essential (see Monbaliu and Luo, 1995). In chapter 6, the possibility of the coupling will be discussed.

In the following part of this section, the detailed formulation will be given for the wave action transport equation for action density since this is the most natural thing to do from a theoretical point of view. In the next section, the numerical scheme will be described according to the spectral energy balance equation from a practical application point of view.

2.3.1 Propagation

The conservation equation of the wave action density in case of finite depth and current reads

$$\frac{\partial N}{\partial t} + \frac{\partial}{\partial x}(c_x N) + \frac{\partial}{\partial y}(c_y N) + \frac{\partial}{\partial \Omega}(c_\Omega N) + \frac{\partial}{\partial \theta}(c_\theta N) = 0 \qquad (2.27)$$

The propagation velocities are expressed as

$$c_x = (\frac{\partial \Omega}{\partial k})_x \qquad (2.28)$$

$$c_y = (\frac{\partial \Omega}{\partial k})_y \qquad (2.29)$$

$$c_\Omega = \frac{d\Omega}{dt} \qquad (2.30)$$

$$c_\theta = \frac{d\theta}{dt} \qquad (2.31)$$

By using the dispersion relation of the Doppler type equation (2.6) and the following relation of the time derivative 'seen' by an observer moving with the absolute group velocity

$$\frac{d}{dt} = \frac{\partial}{\partial t} + c_x \frac{\partial}{\partial x} + c_y \frac{\partial}{\partial y} \tag{2.32}$$

equations (2.28) to (2.31) read

$$c_x = c_g \sin\theta + u \tag{2.33}$$

$$c_y = c_g \cos\theta + v \tag{2.34}$$

$$c_\Omega = \frac{\partial \omega}{\partial t} + c_x \frac{\partial \Omega}{\partial x} + c_y \frac{\partial \Omega}{\partial y} \tag{2.35}$$

$$c_\theta = \frac{\partial \theta}{\partial t} + c_x \frac{\partial \theta}{\partial x} + c_y \frac{\partial \theta}{\partial y} \tag{2.36}$$

where

u : the x component of mean current velocity
v : the y component of mean current velocity

equation (2.35) can be derived as (see Appendix A)

$$c_\Omega = \frac{d\omega}{dt} + k \sin\theta \frac{\partial u}{\partial t} + k \cos\theta \frac{\partial v}{\partial t} \tag{2.37}$$

It is easily seen that for steady currents cases, $\partial u/\partial t$ and $\partial v/\partial t$ are equal to zero, therefore, equation (2.37) thus becomes

$$\frac{d\Omega}{dt} = \frac{d\omega}{dt} \tag{2.38}$$

$d\omega/dt$ and $d\theta/dt$ are formulated as (see Appendix A and Brink-Kjaer (1984)).

$$\begin{aligned} \frac{d\theta}{dt} = & \frac{\omega}{\sinh 2kh}(\sin\theta \frac{\partial h}{\partial y} - \cos\theta \frac{\partial h}{\partial x}) \\ & + \sin\theta(\sin\theta \frac{\partial u}{\partial y} - \cos\theta \frac{\partial u}{\partial x}) \\ & + \cos\theta(\sin\theta \frac{\partial v}{\partial y} - \cos\theta \frac{\partial v}{\partial x}) \end{aligned} \tag{2.39}$$

$$\frac{d\omega}{dt} = \frac{\omega k}{\sinh 2kh}\left(\frac{\partial h}{\partial t} + u\frac{\partial h}{\partial x} + v\frac{\partial h}{\partial y}\right)$$
$$-c_g k \sin\theta\left(\sin\theta\frac{\partial u}{\partial x} + \cos\theta\frac{\partial u}{\partial y}\right)$$
$$-c_g k \cos\theta\left(\sin\theta\frac{\partial v}{\partial x} + \cos\theta\frac{\partial v}{\partial y}\right) \qquad (2.40)$$

Three examples of shallow water effects are discussed below.

Shoaling

If waves are incident normal to a beach with straight and parallel bottom contours, changes in the wave profile are caused solely by the change in water depth. This transformation is called wave shoaling. Let us now discuss the conservation equation in the situation where there are no currents. Assume that the beach is along the x direction. In this case, $\sin\theta = 0$, $\partial h/\partial x = 0$. Depth refraction does not contribute to the rate of change of wave direction ($d\theta/dt = 0$). For time-independent topography the conservation equation (2.27) of action density thus becomes the following energy density conservation equation

$$\frac{\partial F}{\partial t} + \frac{\partial}{\partial y}(c_g F) = 0 \qquad (2.41)$$

For the steady wave field (hence $\frac{\partial F}{\partial t} = 0$) one easily finds the energy density flux in the y direction, or

$$c_g F = \text{constant} \qquad (2.42)$$

One sees from equation (2.42) that the energy density is inversely proportional to the group velocity c_g. Wave shoaling from deep sea to shallow water over a sloping bottom occurs in this way: the waves first decrease with decreasing water depth (thus increasing the group speed), then they gradually increase in height to produce an asymmetrical wave profile (the group speed decreases), and finally the waves break with further decrease in water depth.

Depth refraction

Depth refraction of waves is the phenomenon of changes in the wave propagation velocity along the wave crest (which is the line of equal phase, this implies a constant wave period) due to variations in the water depth. The part of the wave in deeper water moves faster than the part in shallower water. Waves approaching shallow water tend to obtain a direction normal to the depth contours, while waves approaching deeper water tend to obtain a direction parallel to the depth contours. The wave energy is redistributed as a result of changes in the wave direction.

Consider a steady wave field without current and depth variation in time, the action density conservation equation (2.27) thus becomes the following energy density conservation equation

$$\frac{\partial}{\partial x}(c_g \sin\theta F) + \frac{\partial}{\partial y}(c_g \cos\theta F) + \frac{\partial}{\partial \theta}(c_{\theta d} F) = 0 \tag{2.43}$$

where $c_{\theta d}$ is the rate of change of wave direction due to depth variation in space. From equation (2.39) it is formulated as

$$c_{\theta d} = \frac{\omega}{\sinh 2kh}(\sin\theta \frac{\partial h}{\partial y} - \cos\theta \frac{\partial h}{\partial x}) \tag{2.44}$$

Now assume that the waves propagate along the x direction ($\cos\theta = 0$, $\sin\theta = 1$) parallel to the coast. Suppose that the depth decreases only towards the shore ($\partial h/\partial y > 0$) and $\partial h/\partial x = 0$. The energy spectrum F along a wave ray can be determined by

$$\frac{\partial}{\partial x}[(c_g + c_{\theta d})F] = 0 \tag{2.45}$$

The rate of change of wave direction is:

$$c_{\theta d} = \frac{\omega}{\sinh 2kh} \frac{\partial h}{\partial y} \tag{2.46}$$

Since $\partial h/\partial y > 0$, $c_{\theta d} > 0$. The wave rays will bend towards shallower water.

Current refraction

The current refraction results in a change of the wave direction, the wave propagation velocity and wave length will be modified. The rate of change of wave direction due to current (variation in space), $c_{\theta c}$, is expressed as

$$c_{\theta c} = \sin\theta(\sin\theta\frac{\partial u}{\partial y} - \cos\theta\frac{\partial u}{\partial x}) + \cos\theta(\sin\theta\frac{\partial v}{\partial y} - \cos\theta\frac{\partial v}{\partial x}) \tag{2.47}$$

For the waves propagating along the x direction ($\cos\theta = 0$) parallel to the coast, and assuming that the depth decreases only towards the coast, the rate of change of wave direction can be simplified as

$$c_{\theta c} = \frac{\partial u}{\partial y} \tag{2.48}$$

$c_{\theta c}$ is greater than zero in case of u decreasing towards the coast, implying that waves will bend towards the coast. The rate of change of frequency for the steady current case is described in equation (2.40).

2.3.2 Source terms

Wind input

Ocean waves are generated due to the instability of basic shear flow in the coupled air-water system when the wind is blowing over the sea. A lot of theoretical research work attempting the explanation of wave generation and growth by wind has been done. Two of the elaborate works are the linear growth theory (Phillips, 1957) and the exponential growth theory (Miles, 1957). The wind input source function is generally represented as a sum of linear growth and exponential gain:

$$S_{in} = A + BF \tag{2.49}$$

where S_{in} is the wind input source term, the linear term A represents external turbulent pressure forcing and is relevant for the first stage of the wave growth on an initially calm sea. It was first described by Phillips (1957) and is therefore called the Phillips' term. The exponential term

B is the so-called Miles' feedback mechanism. In wave models the linear term in the wind input is usually neglected since it is quickly overridden by the exponential term. The energy transfer from wind to waves has been measured by Snyder *et al.* (1981). Their results are comparable with the theoretical prediction of Miles (1957). The exponential growth rate is found to be

$$B = \max\{0, 0.25\frac{\rho_a}{\rho_w}(\frac{U_5}{c}\cos(\theta - \psi) - 1)\}\omega \tag{2.50}$$

where ρ_a and ρ_w are the density of air and water respectively, θ is the wave direction, ψ is the wind direction, U_5 is the wind speed at a height 5 m, and c is the phase speed ($= \frac{\omega}{k}$).

Komen *et al.* (1984) argued that the friction velocity u_{a*} is a more suitable scaling parameter than the wind speed at a certain height (e.g., U_5), and proposed the form

$$B = \max\{0, 0.25\frac{\rho_a}{\rho_w}(28\beta\frac{u_{a*}}{c}\cos(\theta - \psi) - 1)\}\omega \tag{2.51}$$

where β is an empirical factor introduced by Komen *et al.* (1984), its value is approximately equal to 1.

Actually, in the wind input expression of Snyder *et al.* (1981) or Komen *et al.* (1984) only the energy transfer from air to water is taken into account. Recent research work by Janssen (1989, 1991) showed that the effect of waves on the wind profile may be important to the wave evolution, and that the wind input term depends not only on the wind speed but on the sea state as well. Based on Janssen's quasi-linear theory of wind-wave generation (Janssen 1989, 1991). B is expressed as

$$B = \max\{0, \varepsilon\frac{\beta_m}{\kappa^2}x^2\mu\ln^4\mu\}\omega \qquad \mu < 1 \tag{2.52}$$

where ε is the ratio of air to water density (i.e., $\frac{\rho_a}{\rho_w}$), β_m is a constant (equal to 1.2), κ is the "von Karman" constant, equal to 0.41, x and μ are formulated by

$$x = \cos(\theta - \psi)\frac{u_{a*}}{c} \tag{2.53}$$

$$\mu = kz_c \tag{2.54}$$

where z_c is the critical height where the wind speed U is equal to the phase velocity of the wave, and

$$u_{a*} = U_{10}\sqrt{C_D(U_{10}, \tau_w)} \tag{2.55}$$

where U_{10} is the wind speed at 10 meter, C_D is the drag coefficient, which is a function of the wind speed at 10 meter and the wave-induced stress (τ_w).

μ can be formulated as

$$\mu = \frac{g z_0}{(\kappa c)^2} e^{\frac{\kappa}{x}} \tag{2.56}$$

where z_0 is the roughness length dependent on the wave state through the wave-induced stress τ_w, it is formulated as

$$z_0 = \frac{\alpha \tau}{g\sqrt{1 - \frac{\tau_w}{\tau}}} \tag{2.57}$$

with $\alpha = 0.01$ a constant, g the acceleration of gravity, $\tau = \rho_a u_{a*}^2$ the kinematic surface stress, and $\vec{\tau_w} = (\tau_{w_x}, \tau_{w_y})$ the wave-induced stress, i.e. the stress exerted by the waves on the wind, given by

$$\tau_{w_x} = \left(\int_0^{f_{hf}} \int_0^{2\pi} 2\pi f S_{in} \sin\theta df d\theta\right) + \sin\psi \tau_{hf} \tag{2.58}$$

$$\tau_{w_y} = \left(\int_0^{f_{hf}} \int_0^{2\pi} 2\pi f S_{in} \cos\theta df d\theta\right) + \cos\psi \tau_{hf} \tag{2.59}$$

where f_{hf} is the high frequency limit (also see eq(2.111) for definition), τ_{hf} is the high frequency contribution to the wave-induced stress. A detailed description can be found in Janssen (1991). From (2.58) and (2.59) it can be seen that the wave stress τ_w is a function of the wind input S_{in}. In turn, S_{in} is an implicit function of the spectra F.

The quasi-linear theory of wind input is in fair agreement with observations both in laboratory and in the field (see Komen *et al.* (1994), II.8 and IV.5), although there is considerable scatter in these observations. Therefore this theory has been implemented in the Cycle 4 version of the WAM model (Komen *et al*, 1994).

Dissipation due to whitecapping

Dissipation of ocean wind waves is thought to occur when waves break during the wave generation in a storm and later when the waves break as they approach a shoreline. Wave breaking is generally visible in the form of whitetopped waves called "whitecaps". Waves breaking depends strongly on the wave steepness. It occurs when the wave height is more than one tenth of the wave length. It represents a localized, strongly nonlinear interaction process which cannot be treated by standard mathematical techniques. The energy dissipations involved in wave breaking are not well understood.

Hasselmann (1974) investigated the effects of the whitecapping on the spectral balance by expressing the whitecapping dissipation in terms of an equivalent ensemble of random pressure pulses. It was shown that under very general conditions, the dissipation for all interaction processes which are weak-in-the-mean, even if they are strongly nonlinear locally, is quasi-linear with respect to the wave spectrum. He further derived a damping coefficient for whitecapping dissipation which is proportional to the square of the angular frequency. The dissipation coefficient and the associated dissipation function were found to be consistent with the structure of the energy balance derived from the JONSWAP data. Hasselmann 's expression is (Hasselmann, 1974)

$$S_{ds}(\mathrm{k}) = -\eta_d \omega^2 F(\mathrm{k}) \tag{2.60}$$

where $S_{ds}(\mathrm{k})$ is the whitecapping dissipation in wave number space, η_d is a proportionality factor dependent on the integral spectral parameters such as the average wave steepness.

Komen *et al.* (1984) proposed a dissipation function that allowed the existence of an equilibrium solution of the energy balance equation when waves are fully developed. The general dissipation function was suggested

$$S_{ds}(f,\theta) = -C_{ds}(\frac{\omega}{\bar{\omega}})^n(\frac{\bar{\alpha}}{\bar{\alpha}_{PM}})^m \bar{\omega} F(f,\theta) \tag{2.61}$$

where $S_{ds}(f,\theta)$ is the dissipation term due to whitecapping in (f,θ) space,

the C_{ds}, m and n are dissipation coefficients, $\bar{\omega}$ is the mean angular frequency defined as

$$\bar{\omega} = \frac{1}{E_{tot}} \int_0^{\infty} \int_0^{2\pi} F(f,\theta)\omega df d\theta \tag{2.62}$$

$\bar{\alpha}$ is the integral wave steepness parameter, expressed by

$$\bar{\alpha} = \frac{E_{tot}\bar{\omega}^4}{g^2} \tag{2.63}$$

and $\bar{\alpha}_{PM}$ is the theoretical value of $\bar{\alpha}$ for a Pierson-Moskowitz spectrum. It has a value of 4.5710^{-3}.

The dissipation coefficients C_{ds}, m and n are fitting parameters. The expression (2.61) corresponds to the result of Hasselmann (1974) when $n = 2$. Suggested values from Komen *et al.* (1984) are 3.3310^{-5} for C_{ds}, 2 for m and 2 for n. Monbaliu (1992) proposed an optimization approach to reproduce the fetch evolution of the total energy by tuning two selected parameters in the wind input and/or whitecapping dissipation source terms.

When the most recent theories on the wind input (Janssen, 1989, 1991) were applied, the dissipation source expression (2.62), which had been extensively used in operational wave models, had to be reconsidered in accordance with the new wind input term. In Cycle 4 version of the WAM model, the atmospheric boundary layer has been coupled with the water surface by using Janssen's theories. Therefore, in order to obtain a proper energy balance at the high-frequency end of the spectrum, the dissipation by whitecapping was extended by adding a k^2 term (Günther *et al.*, 1992),

$$S_{ds}(f,\theta) = -C_{ds}\hat{\omega}(\hat{k}^2 E_{tot})^2[(1-c_{dx})\frac{k}{\hat{k}} + c_{dx}(\frac{k}{\hat{k}})^2]F(f,\theta) \tag{2.64}$$

where $C_{ds} = 4.5$ and $c_{dx} = 0.5$ are constants, E_{tot} is the total wave variance, $\hat{\omega}$ and $\hat{k}$ are mean inverse angular frequency and mean inverse wave number. They are formulated by

$$\hat{\omega} = \frac{1}{E_{tot}} \int_0^{\infty} \int_0^{2\pi} F(f,\theta)\omega^{-1} df d\theta \tag{2.65}$$

$$\hat{k} = \frac{1}{E_{tot}} \int_0^{\infty} \int_0^{2\pi} F(f,\theta)k^{-\frac{1}{2}} df d\theta \tag{2.66}$$

Nonlinear interactions

As stated in section 2.2, the sea surface is a superposition of many different wave components. In a linear theory, those wave components do not interact with each other due to linear approximation, therefore all higher order terms are neglected. In reality, the nonlinear effects of resonant wave-wave interactions accumulate in time, affecting the evolution of the shape of the wave spectrum. The main result of these interactions is that the energy is redistributed from frequencies with high energy to frequencies with low energy.

The basic mechanism of nonlinear interaction was studied by Hasselmann (1962, 1963a,b). He found that a set of four waves could exchange energy when they fulfil the following resonance conditions:

$$\mathrm{k}_1 + \mathrm{k}_2 - \mathrm{k}_3 - \mathrm{k}_4 = 0 \tag{2.67}$$

$$\omega_1 + \omega_2 - \omega_3 - \omega_4 = 0 \tag{2.68}$$

A group of four interacting waves is referred to as a wave number quadruplet. The rate of energy change of the wave spectrum at wave number k is described by the Boltzman integral:

$$S_{nl}(\mathrm{k}) = \omega \int \sigma \delta(\mathrm{k}_1 + \mathrm{k}_2 - \mathrm{k}_3 - \mathrm{k}) \delta(\omega_1 + \omega_2 - \omega_3 - \omega) \times [N_1 N_2 (N_3 + N) - N_3 N (N_1 + N_2)] d\mathrm{k}_1 d\mathrm{k}_2 d\mathrm{k}_3 \tag{2.69}$$

where $S_{nl}(\mathrm{k})$ is the nonlinear interaction source term in wave number space, $N_i = \frac{F(\mathrm{k}_i)}{\omega_i}$ is the action density, σ is the four-wave interactions coefficient, δ stands for the Dirac delta function.

The explicit numerical evaluation of (2.69) for a given spectrum can be found in a lot of papers (Sell and Hasselmann, 1972; Webb, 1978; Masuda, 1981), however, the exact computations are extremely time consuming. An efficient method for a sufficiently accurate computation of the nonlinear interactions was introduced by Hasselmann and Hasselmann (1981), based on the symmetry characteristics of the nonlinear transfer. In this method a discretized eight-dimensional wavenumber space is constructed and a very

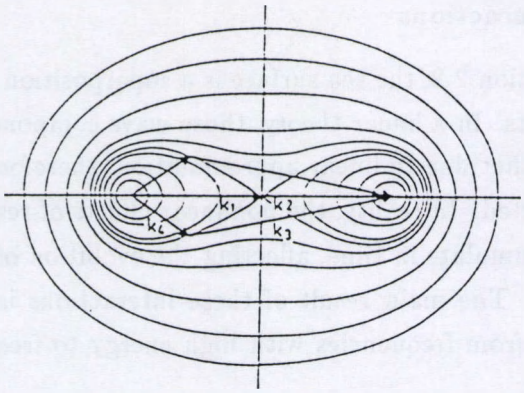

Figure 2.3: The two interaction configurations used in the discrete interaction approximation (from Hasselmann and Hasselmann, 1985)

large set of wavenumber quadruplets with many different configurations was used. Later, Hasselmann and Hasselmann (1985a) incorporated the symmetric method in a numerical wave prediction model, so-called EXACT-NL, and saved computing time by precomputing the integration grid and the interaction coefficient. However, EXACT-NL is still too slow for an operational global wave model. Further simplifications, namely the discrete interaction approximation, were made by Hasselmann *et al.* (1985). They found that the exact nonlinear transfer could be simulated well by just one mirror-image pair of intermediate range interactions configurations. In each interaction configuration, two wave numbers are taken as identical $k_1 = k_2 = k$. The wave numbers k_3 and k_4 of the first configuration are of different magnitudes and of different angles, as required by the resonance conditions. The second configuration is then a mirror image of the first by reflecting the wave numbers k_3 and k_4 with respect to the k axis (see figure 2.3). The angles θ_3, θ_4 of wave numbers k_3 (k_+) and k_4 (k_-) are found (from the resonance conditions) to be 11.5° and -33.6°, respectively. The four frequencies are

$$\omega_1 = \omega_2 = \omega$$

$$\omega_3 = \omega(1+\lambda_{nl}) = \omega_+ \qquad (2.70)$$
$$\omega_4 = \omega(1-\lambda_{nl}) = \omega_-$$

where a value of 0.25 for λ_{nl} gives good agreement with the exact computations (Hasselmann *et al.*, 1985).

The nonlinear interactions for one wave number quadruplet are given by:

$$\begin{pmatrix} \Delta S_{nl} \\ \Delta S_{nl}^{+} \\ \Delta S_{nl}^{-} \end{pmatrix} = \begin{pmatrix} -2 \\ 1 \\ 1 \end{pmatrix} Cg^{-4} f^{11} [F^2 (\frac{F^+}{(1+\lambda_{nl})^4} + \frac{F^-}{(1-\lambda_{nl})^4}) - 2\frac{FF^+F^-}{(1-\lambda_{nl}^2)^4}] \qquad (2.71)$$

where C is a constant equal to 3 10^7. F^+ and F^- are the energy densities (in (f,θ) space) at the interacting wave numbers $\mathbf{k_3}$ and $\mathbf{k_4}$, which are calculated by bilinear interpolation within the discrete spectrum in (f,θ) space (for detailed calculation, see Luo (1990)). The net source function S_{nl} should sum equation (2.71) over all wavenumbers, directions and interactions configurations.

This discrete interaction approximation has been applied in the WAM model for the deep sea nonlinear interaction calculation. The nonlinear interactions for shallow water S_{nl}^h can be related to the deep water S_{nl} through a straightforward scale transformation with a single scale parameter R (Hasselmann and Hasselmann, 1981),

$$S_{nl}^h = R(k_m h) S_{nl} \qquad (2.72)$$

where k_m is the mean wave number. The scaling factor R depends only on the nondimensional depth $k_m h$.

When the value of $k_m h$ is greater than 1, scaling factor R is well reproduced by the following relation

$$R(x) = 1 + \frac{5.5}{x}(1 - \frac{5x}{6}) \exp^{-\frac{5x}{4}} \qquad (2.73)$$

where $x = k_m h$. This approximation is used in the WAM model, the value for $k_m h$ is greater than 0.5 in the WAM code.

Bottom dissipation

Dissipation of wave energy due to wave-bottom interactions can occur due to various linear or nonlinear bottom dissipation mechanisms determined by the bottom topography and sediment properties. An overview of the different wave bottom dissipation mechanisms is given by Shemdin *et al.* (1978), who consider percolation, bottom friction, bottom motion (soft muddy bottom) and scattering on bottom irregularities. The relative strength of these mechanism is dependent on the bottom conditions. For fine sandy bottoms as found in the North Sea, the bottom friction is dominant (Shemdin *et al.*, 1978).

One knows that in the case of short period free surface waves in deep water, the wave motion does not extend to the bottom and hence rotation cannot be generated. In shallow water the wave motion reaches the bottom and the wave boundary layer with rotational flow is generated. Rotation generated at boundaries penetrates from there into the fluid and dissipates the wave energy in the form of turbulent friction. Although the wave boundary is generally thin, the generated shear stress and the turbulent intensity are rather large and of essential importance to wave evolution in shallow water.

The energy dissipation of the wave motion due to bottom friction can be derived from the wave boundary equation. For a 3-D wave boundary layer, consider a (x, y, z) coordinate system, the mean velocity field is defined as (u, v, w), and the fluctuating velocity (u', v', w'). It is assumed that the wave boundary layer thickness is very thin (in the order of a few centimetres for short waves with period 10s, Van Rijn, 1991) as the flow will reverse before a significant boundary layer thickness has developed and the eddies generated before flow reversal will die out rapidly. The moment equation for boundary layer flow is expressed as

$$\frac{\partial \mathbf{u}}{\partial t} + (\mathbf{u} \cdot \nabla)\mathbf{u} + w\frac{\partial \mathbf{u}}{\partial z} + \frac{1}{\rho_w}\nabla p = \frac{\partial}{\partial z}(\frac{\tau}{\rho_w}) \qquad (2.74)$$

where $\mathbf{u}$ is the horizontal particle velocity (u, v) of the wave motion, t is the time, z is the vertical coordinate measured upwards from the bed, ρ_w is

the density of water, $\nabla = (\partial/\partial x, \partial/\partial y)$ is the horizontal gradient operator, p is the pressure, and τ is the horizontal shear stress (τ_1, τ_2). They are defined as

$$\frac{\tau_1}{\rho_w} = -\overline{u'w'} \tag{2.75}$$

$$\frac{\tau_2}{\rho_w} = -\overline{v'w'} \tag{2.76}$$

The exact solution of equation (2.74) is impossible to obtain due to the existence of the nonlinear term and small wave steepness ($kA_b << 1$, with k the wave number and A_b the excursion amplitude of flow motion just outside the boundary layer). Therefore, the wave boundary layer solution is approached by using the straightforward asymptotic method (Trowbridge and Madsen, 1984; Nayfeh, 1973). Correct to first order in wave steepness, equation (2.74) becomes

$$\frac{\partial \mathbf{u}}{\partial t} + \frac{1}{\rho_w}\nabla p = \frac{\partial}{\partial z}\left(\frac{\tau}{\rho_w}\right) \tag{2.77}$$

For the detailed derivation of equation (2.77) from equation (2.74) one is referred to the work done by Luo (1992).

The boundary conditions are:

- outside the boundary layer

$$\tau = 0 \tag{2.78}$$

- at the top of the boundary layer

$$\mathbf{u} = \mathbf{U}_b \tag{2.79}$$

$$\nabla p = -\rho_w \frac{\partial \mathbf{U}_b}{\partial t} \tag{2.80}$$

  where $\mathbf{U}_b$ is the free stream orbital velocity.

- at the bottom

$$\tau = \tau_b \tag{2.81}$$

$$\mathbf{u} = 0 \tag{2.82}$$

The energy dissipation per unit area of the bed is determined by

$$\begin{aligned} S_{bf} &= -<\int_0^{h+\eta} \tau \cdot \frac{\partial \mathbf{u}}{\partial z} dz> \\ &= -<[\tau \cdot \mathbf{u}]_0^{h+\eta}> + <\int_0^{h+\eta} \mathbf{u} \cdot \frac{\partial \tau}{\partial z} dz> \end{aligned} \tag{2.83}$$

where $<>$ denotes the ensemble mean, η is the oscillating water surface elevation. The first term in the right hand side of equation (2.83) disappears by using the boundary conditions (2.78) and (2.82), and

$$\begin{aligned} S_{bf} &= <\int_0^{h+\eta} \mathbf{u} \cdot \frac{\partial \tau}{\partial z} dz> \\ &= <\int_0^{h+\eta} (\mathbf{U}_b + \mathbf{u} - \mathbf{U}_b) \cdot \frac{\partial \tau}{\partial z} dz> \\ &= <[\mathbf{U}_b \cdot \tau]_0^{h+\eta}> - <\int_0^{h+\eta} \tau \cdot \frac{\partial \mathbf{U}_b}{\partial z} dz> \\ &\quad + <\int_0^{h+\eta} (\mathbf{u} - \mathbf{U}_b) \cdot \frac{\partial \tau}{\partial z} dz> \end{aligned} \tag{2.84}$$

The first term in the right hand side of equation (2.84) becomes

$$-<\mathbf{U}_b \cdot \tau_b> \tag{2.85}$$

The second term vanishes because τ is zero outside the wave boundary layer and $\frac{\partial \mathbf{U}_b}{\partial z}$ equals zero in the boundary layer. By use of the boundary layer equation (2.77), the third term in equation (2.84) becomes

$$<\int_0^{\delta} (\mathbf{u} - \mathbf{U}_b) \cdot (\rho_w \frac{\partial \mathbf{u}}{\partial t} + \nabla p) dz> + <\int_{\delta}^{h+\eta} (\mathbf{u} - \mathbf{U}_b) \cdot \frac{\partial \tau}{\partial z} dz> \tag{2.86}$$

where δ is the thickness of the wave boundary layer. Since the pressure gradient is independent of the height in the wave boundary layer, it equals its value at the top of the layer. Using the boundary conditions (2.80) ($\nabla p = -\rho \frac{\partial \mathbf{U}_b}{\partial t}$) at the top of the boundary layer and (2.78) ($\tau = 0$) outside the boundary layer, equation (2.86) becomes

$$<\int_0^{\delta} \frac{1}{2} \rho_w \frac{\partial}{\partial t} (\mathbf{u} - \mathbf{U}_b)^2 dz> \tag{2.87}$$

Because the wave motion is periodic in time, the value of equation (2.87) becomes zero. Therefore, the energy dissipation (2.83) of the wave motion due to friction is

$$S_{bf} = - < \mathbf{U}_b \cdot \tau_b > \tag{2.88}$$

It implies that the wave energy dissipation due to the bottom friction equals the work done by the (basically unknown) bottom stress on the (known) free stream orbital bottom velocity.

There are different models to parametrize the turbulent bottom shear stress in (2.88), such as the eddy viscosity model and the drag law model. The eddy viscosity model relates the bottom shear stress to the vertical gradient of the velocity through an eddy viscosity coefficient ϵ

$$\frac{\tau}{\rho_w} = \epsilon \frac{\partial \mathbf{u}}{\partial z} \tag{2.89}$$

The drag law model relates the bottom shear stress to the velocity at the top of the wave boundary layer through a drag coefficient C_f.

$$\frac{\tau}{\rho_w} = C_f \mid \mathbf{U}_b \mid \mathbf{U}_b \tag{2.90}$$

Depending on the parametrization of the turbulent bottom shear stress, a number of different expressions for the bottom friction dissipation can be found in ocean wave modelling. The ones used for this study are: an empirical expression based on the JONSWAP experiment (Hasselmann *et al.*, 1973), three expressions based on the drag law turbulent friction model (Hasselmann and Collins, 1968; Collins, 1972; Madsen *et al.*, 1988a) and one based on the eddy viscosity friction model (Weber, 1991a). The detailed description of these five models will be presented in chapter 3.

Depth-induced wave breaking

Waves break when their height reaches a certain limiting value relative to their length or to the water depth. In deep sea, waves break when their steepness exceeds a certain value. However, the type of wave breaking discussed here is taking place as a result of decreasing water depth in shallow

water. Breaking waves exhibit different forms, principally depending on the incident wave height, and on the beach slope. The forms of breaking waves have been classified into three categories, i.e., spilling breaker, plunging breaker and surging breaker .

In the very shallow water area (surfzone), the dissipation of wave energy in the breaking process is a very important source term. A successful model for computing the local mean rate of energy dissipation in random breaking waves was derived by Battjes and Janssen (1978). A further calibration and verification of Battjes' and Janssen's model was carried out by Battjes and Stive (1985). The average dissipation rate per unit area in random waves (mean frequency f_m, rms-waveheight H_{rms}) breaking with random height in shallow water (depth h), is expressed as (Battjes and Janssen, 1978)

$$D = \frac{1}{4}\alpha_{br} Q_b f_m \rho_w g H_m^2 \tag{2.91}$$

where α_{br} is a constant of order one, f_m is mean frequency, ρ_w is the density of water, H_m is the maximum wave height, Q_b is the local fraction of breaking waves, it can be obtained by implicitly solving the following equation (Battjes and Janssen, 1978)

$$Q_b = 1 + \eta_{br}^2 \ln Q_b \tag{2.92}$$

where η_{br} is defined as

$$\eta_{br} = \frac{H_{rms}}{H_m} \tag{2.93}$$

where H_{rms} is the root-mean-square wave height and H_m is the maximum wave height, which can be computed according to a combined steepness and depth-limited breaking criterion (Battjes and Stive, 1985):

$$H_m = \frac{\gamma_1}{k_m} \tanh(\frac{\gamma_2}{\gamma_1} k_m h) \tag{2.94}$$

where γ_1 and γ_2 are the wave breaking coefficients, k_m is the mean wave number.

The above breaking-wave model only predicts the total dissipation rate, but not its spectral distribution, which is required in spectral energy balance models. One approach is to distribute the total rate in proportion

to the local spectral density, on the assumption that the breaking does not alter the spectral shape. Laboratory observations by Beji and Battjes (1993) of wave breaking on, and passing over a bar lend support to such assumption. By using this approach, Holthuijsen *et al.* (1993) included the depth-limited breaking term in a recently developed spectral wave model for the coastal zone. Van Vledder (1995) investigated the performance of a full third generation model in shallow water with formulation for surf breaking. In chapter 6 of this work, the effect of depth-limited wave breaking on wave evolution in the Belgian waters will be examined by the implementation of the Van Vledder's model into the Cycle 4 version of the WAM model.

2.4 Numerical scheme

In order to model the wave evolution, the energy balance equation is solved using a finite difference method. The five-dimensional wave spectrum is discretized in five arguments, x, y, t, f and θ. The x-y Space will be represented by the gridpoints. The spectrum is evaluated every propagation time step. A propagation time step may be divided into several source integration time steps. The wind fields are kept constant during a wind time step. The ratio of all time steps should be an integer. The (f, θ) frequency-direction grid normally has a resolution of 25 frequencies and 12 directions. The frequency bands are set on a logarithmic scale, with $\Delta f/f = 0.1$. The starting frequency may be chosen arbitrarily. Normally, it is selected to be 0.042 Hz.

2.4.1 The discrete energy balance equation

In the WAM numerical model, the energy transport equation (2.26) is replaced by a finite difference equation. Time is discretized in propagation time steps. The discrete version of (2.26) expresses the spectrum F^{n+1} at time t^{n+1} $(= t^n + \Delta t_{prop})$ in terms of F^n. The contributions from the advection term and from the source terms are calculated separately. Firstly, the energy transport equation (2.26) without the source terms is integrated.

The increment due to the advection is defined as

$$\Delta_{prop}(F^n) = (F^{n+1} - F^n)_{prop} \tag{2.95}$$

and $\frac{\Delta_{prop}(F^n)}{\Delta t}$ corresponds to $-[\frac{\partial}{\partial x}(c_x F) + \frac{\partial}{\partial y}(c_y F) + \frac{\partial}{\partial \theta}(c_\theta F) + \frac{\partial}{\partial \omega}(c_\omega F)]$, which is determined by using the first order upwinding scheme (see section 2.4.2.). Then, the changes of spectrum due to the source terms are calculated. The propagation time step can be split into several source term integration time steps. For example, the propagation time step is split into two source term integration time steps of $\Delta t_{int} = 0.5\Delta t_{prop}$, the source term increment reads:

$$\Delta_{int} F^n = (F^{n+\frac{1}{2}} - F^n)_s \tag{2.96}$$

$$\Delta_{int} F^{n+\frac{1}{2}} = (F^{n+1} - F^{n+\frac{1}{2}})_s \tag{2.97}$$

To solve $\Delta_{int} F / \Delta t_{int}$, an implicit scheme is used for the source term integration (see section 2.4.3).

After two source term time steps (i.e., one propagation time step), the source term increment then becomes

$$\Delta_s F = (F^{n+1} - F^n)_s = \Delta_{int} F^n + \Delta_{int}(F^n + \Delta_{int} F^n) \tag{2.98}$$

Finally, the spectrum at time t^{n+1} can be expressed as

$$\begin{aligned} F^{n+1} &= F^n + \Delta_{prop}(F^n) + \Delta_s(F^n) \\ &= F^n + \Delta_{prop}(F^n) + \Delta_{int}(F^n) + \Delta_{int}(F^n + \Delta_{int}(F^n)) \end{aligned} \tag{2.99}$$

We need an initial wave spectrum F_0 to run the model. For the WAM model, the source term F vanishes for $F = 0$, no matter how hard the wind is blowing. In nature, waves would be generated even if $F_0 = 0$. Therefore the model always takes a non-zero spectrum F_0. In the WAM model, there are two ways to deal with F_0: initialize F_0 by a previous model run for time t_0 (restart spectrum), or take a young windsea JONSWAP spectrum (JONSWAP, 1973) according to the wind field at time t_0. For coast lines the zero energy influx is assumed. For a nested grid run, the open boundary condition is determined by a coarser grid run.

2.4.2 The propagation scheme

The energy transport equation without source terms is given by

$$(\frac{\partial F}{\partial t})_{prop} = -\frac{\partial}{\partial x}(c_x F) - \frac{\partial}{\partial y}(c_y F) - \frac{\partial}{\partial \omega}(c_\omega F) - \frac{\partial}{\partial \theta}(c_\theta F) \qquad (2.100)$$

To discretize equation (2.100), the propagation step of the WAM model uses a first order upwinding scheme since this scheme is the simplest to implement, requires less computer time and memory, and gives reasonable results. The finite difference, control volume form of equation (2.100) (note that the one-dimensional form can be found in the WAM book (Komen *et al.*, 1994)) can be expressed as

$$\begin{aligned}\frac{F^{n+1}_{i,j,k,m} - F^{n}_{i,j,k,m}}{\Delta t_{prop}} = & -\frac{(c_x F)^n_{i+1/2,j,k,m} - (c_x F)^n_{i-1/2,j,k,m}}{\Delta x} \\ & -\frac{(c_y F)^n_{i,j+1/2,k,m} - (c_y F)^n_{i,j-1/2,k,m}}{\Delta y} \\ & -\frac{(c_\theta F)^n_{i,j,k+1/2,m} - (c_\theta F)^n_{i,j,k-1/2,m}}{\Delta \theta} \\ & -\frac{(c_\omega F)^n_{i,j,k,m+1/2} - (c_\omega F)^n_{i,j,k,m-1/2}}{\Delta \omega} \qquad (2.101)\end{aligned}$$

where i denotes the position in direction from west to east (x), j indicates the position in direction from south to north (y), k represents the position in the angular direction (θ), m denotes the position in the frequency space (f), and n is the propagation timestep (t). The $i+1/2$, $i-1/2$, etc., indices refer to the fluxes on the control volume faces, which are given by,

$$\begin{aligned}(c_x F)^n_{i+1/2,j,k,m} = & \frac{1}{2}\{[(c_x)_{i+1/2} - \mid (c_x)_{i+1/2} \mid] F^n_{i+1,j,k,m} \\ & + [(c_x)_{i+1/2} + \mid (c_x)_{i+1/2} \mid] F^n_{i,j,k,m}\} \\ (c_x F)^n_{i-1/2,j,k,m} = & \frac{1}{2}\{[(c_x)_{i-1/2} - \mid (c_x)_{i-1/2} \mid] F^n_{i,j,k,m} \\ & + [(c_x)_{i-1/2} + \mid (c_x)_{i-1/2} \mid] F^n_{i-1,j,k,m}\} \\ (c_y F)^n_{i,j+1/2,k,m} = & \frac{1}{2}\{[(c_y)_{j+1/2} - \mid (c_y)_{j+1/2} \mid] F^n_{i,j+1,k,m} \\ & + [(c_y)_{j+1/2} + \mid (c_y)_{j+1/2} \mid] F^n_{i,j,k,m}\}\end{aligned}$$

$$
\begin{aligned}
(c_y F)^n_{i,j-1/2,k,m} &= \frac{1}{2}\{[(c_y)_{j-1/2} - \mid (c_y)_{j-1/2} \mid] F^n_{i,j,k,m} \\
&\quad + [(c_y)_{j-1/2} + \mid (c_y)_{j-1/2} \mid] F^n_{i,j-1,k,m}\} \qquad (2.102)\\
(c_\theta F)^n_{i,j,k+1/2,m} &= \frac{1}{2}\{[(c_\theta)_{k+1/2} - \mid (c_\theta)_{k+1/2} \mid] F^n_{i,j,k+1,m} \\
&\quad + [(c_\theta)_{k+1/2} + \mid (c_\theta)_{k+1/2} \mid] F^n_{i,j,k,m}\} \\
(c_\theta F)^n_{i,j,k-1/2,m} &= \frac{1}{2}\{[(c_\theta)_{k-1/2} - \mid (c_\theta)_{k-1/2} \mid] F^n_{i,j,k,m} \\
&\quad + [(c_\theta)_{k-1/2} + \mid (c_\theta)_{k-1/2} \mid] F^n_{i,j,k-1,m}\} \\
(c_\omega F)^n_{i,j,k,m+1/2} &= \frac{1}{2}\{[(c_\omega)_{m+1/2} - \mid (c_\omega)_{m+1/2} \mid] F^n_{i,j,k,m+1} \\
&\quad + [(c_\omega)_{m+1/2} + \mid (c_\omega)_{m+1/2} \mid] F^n_{i,j,k,m}\} \\
(c_\omega F)^n_{i,j,k,m-1/2} &= \frac{1}{2}\{[(c_\omega)_{m-1/2} - \mid (c_\omega)_{m-1/2} \mid] F^n_{i,j,k,m} \\
&\quad + [(c_\omega)_{m-1/2} + \mid (c_\omega)_{m-1/2} \mid] F^n_{i,j,k,m-1}\}
\end{aligned}
$$

and the control volume face velocities are given by

$$
\begin{aligned}
(c_x)_{i+1/2} &= \frac{1}{2}[(c_x)^n_{i+1,j,k,m} + (c_x)^n_{i,j,k,m}] \\
(c_x)_{i-1/2} &= \frac{1}{2}[(c_x)^n_{i,j,k,m} + (c_x)^n_{i-1,j,k,m}] \\
(c_y)_{j+1/2} &= \frac{1}{2}[(c_y)^n_{i,j+1,k,m} + (c_y)^n_{i,j,k,m}] \\
(c_y)_{j-1/2} &= \frac{1}{2}[(c_y)^n_{i,j,k,m} + (c_y)^n_{i,j-1,k,m}] \qquad (2.103)\\
(c_\theta)_{k+1/2} &= \frac{1}{2}[(c_\theta)^n_{i,j,k+1,m} + (c_\theta)^n_{i,j,k,m}] \\
(c_\theta)_{k-1/2} &= \frac{1}{2}[(c_\theta)^n_{i,j,k,m} + (c_\theta)^n_{i,j,k-1,m}] \\
(c_\omega)_{m+1/2} &= \frac{1}{2}[(c_\omega)^n_{i,j,k,m+1} + (c_\omega)^n_{i,j,k,m}] \\
(c_\omega)_{m-1/2} &= \frac{1}{2}[(c_\omega)^n_{i,j,k,m} + (c_\omega)^n_{i,j,k,m-1}]
\end{aligned}
$$

Substitute (2.102) and (2.103) into (2.101), the propagation increment is presented as

$$
\begin{aligned}
&\Delta_{prop}(F^n_{i,j,k,m}) = F^{n+1}_{i,j,k,m} - F^n_{i,j,k,m} \\
= \; & -\frac{\Delta t_{prop}}{4\Delta x}\{(c_x)^n_{i+1,j,k,m} - (c_x)^n_{i-1,j,k,m} \\
+ \; & \mid (c_x)^n_{i+1,j,k,m} + (c_x)^n_{i,j,k,m} \mid + \mid (c_x)^n_{i,j,k,m} + (c_x)^n_{i-1,j,k,m} \mid\} F^n_{i,j,k,m}
\end{aligned}
$$

$$
\begin{aligned}
&- \frac{\Delta t_{prop}}{4\Delta x}\{(c_x)^n_{i+1,j,k,m} + (c_x)^n_{i,j,k,m} - |\,(c_x)^n_{i+1,j,k,m} + (c_x)_{i,j,k,m}\,|\}F^n_{i+1,j,k,m}\\
&+ \frac{\Delta t_{prop}}{4\Delta x}\{(c_x)^n_{i,j,k,m} + (c_x)_{i-1,j,k,m} + |\,(c_x)^n_{i,j,k,m} + (c_x)^n_{i-1,j,k,m}\,|\}F^n_{i-1,j,k,m}\\
&- \frac{\Delta t_{prop}}{4\Delta y}\{(c_y)^n_{i,j+1,k,m} - (c_y)^n_{i,j-1,k,m}\\
&+ |\,(c_y)^n_{i,j+1,k,m} + (c_y)^n_{i,j,k,m}\,| + |\,(c_y)^n_{i,j,k,m} + (c_y)^n_{i,j-1,k,m}\,|\}F^n_{i,j,k,m}\\
&- \frac{\Delta t_{prop}}{4\Delta y}\{(c_y)^n_{i,j+1,k,m} + (c_y)^n_{i,j,k,m} - |\,(c_y)^n_{i,j+1,k,m} + (c_y)^n_{i,j,k,m}\,|\}F^n_{i,j+1,k,m}\\
&+ \frac{\Delta t_{prop}}{4\Delta y}\{(c_y)^n_{i,j,k,m} + (c_y)^n_{i,j-1,k,m} + |\,(c_y)^n_{i,j,k,m} + (c_y)^n_{i,j-1,k,m}\,|\}F^n_{i,j-1,k,m}\\
&- \frac{\Delta t_{prop}}{4\Delta \theta}\{(c_\theta)^n_{i,j,k+1,m} - (c_\theta)^n_{i,j,k-1,m}\\
&+ |\,(c_\theta)^n_{i,j,k+1,m} + (c_\theta)^n_{i,j,k,m}\,| + |\,(c_\theta)^n_{i,j,k,m} + (c_\theta)^n_{i,j,k-1,m}\,|\}F^n_{i,j,k,m}\\
&- \frac{\Delta t_{prop}}{4\Delta \theta}\{(c_\theta)^n_{i,j,k+1,m} + (c_\theta)^n_{i,j,k,m} - |\,(c_\theta)^n_{i,j,k+1,m} + (c_\theta)^n_{i,j,k,m}\,|\}F^n_{i,j,k+1,m}\\
&+ \frac{\Delta t_{prop}}{4\Delta \theta}\{(c_\theta)^n_{i,j,k,m} + (c_\theta)^n_{i,j,k-1,m} + |\,(c_\theta)^n_{i,j,k,m} + (c_\theta)^n_{i,j,k-1,m}\,|\}F^n_{i,j,k-1,m}\\
&- \frac{\Delta t_{prop}}{4\Delta \omega}\{(c_\omega)^n_{i,j,k,m+1} - (c_\omega)^n_{i,j,k,m-1}\\
&+ |\,(c_\omega)^n_{i,j,k,m+1} + (c_\omega)^n_{i,j,k,m}\,| + |\,(c_\omega)^n_{i,j,k,m} + (c_\omega)^n_{i,j,k,m-1}\,|\}F^n_{i,j,k,m}\\
&- \frac{\Delta t_{prop}}{4\Delta \omega}\{(c_\omega)^n_{i,j,k,m+1} + (c_\omega)^n_{i,j,k,m} - |\,(c_\omega)^n_{i,j,k,m+1} + (c_\omega)^n_{i,j,k,m}\,|\}F^n_{i,j,k,m+1}\\
&+ \frac{\Delta t_{prop}}{4\Delta \omega}\{(c_\omega)^n_{i,j,k,m} + (c_\omega)^n_{i,j,k,m-1} + |\,(c_\omega)^n_{i,j,k,m} + (c_\omega)^n_{i,j,k,m-1}\,|\}F^n_{i,j,k,m-1}
\end{aligned}
\tag{2.104}
$$

One should note that the disadvantage of the first order upwinding scheme conventionally used in the WAM model, is the numerical instabilities due to the large time step such that the Courant-Friedrichs-Lewy (CFL) criterion is violated. The CFL criterion in the WAM code states that the following inequalities must be satisfied.

$$\Delta t < \Delta x / c_{g1} \tag{2.105}$$

$$\Delta t < \Delta y / c_{g1} \tag{2.106}$$

where c_{g1} $(= g/4\pi f_1)$ is the group velocity at the lowest frequency $f_1 = 0.04177hz$ in deep sea. According to the CFL criterion, a short propagation time step is required for very high resolution. In most applications, the

propagation time is larger than or equal to the source term time step, which is usually 20 min.

2.4.3 Source term integration scheme

The source part of the energy balance equation (2.26), is given by

$$(\frac{\partial F}{\partial t})_s = S_{tot} \tag{2.107}$$

An implicit scheme was developed in the WAM model for the source function integration to enable the use of an integration time step that was greater than the dynamic adjustment time of the highest frequencies still treated prognostically in the model. The implicit second order, centred difference form of equation (2.107) is given by

$$\frac{F^{n+r}_{i,j,k,m} - F^{n}_{i,j,k,m}}{\Delta t_{int}} = \frac{1}{2}(S^{n+r}_{i,j,k,m} + S^{n}_{i,j,k,m}) \tag{2.108}$$

where r indicates the ratio of the source term time step to the propagation time step, say, 1/2. Thus, the change of source function in one source time step or 1/2 propagation time step is:

$$\Delta_{int} F_{i,j,k,m} = \frac{\Delta t_{int}}{2}(S^{n+1/2}_{i,j,k,m} + S^{n}_{i,j,k,m}) \tag{2.109}$$

Since none of the source terms are linear, Taylor expansions are introduced. By disregarding the neglegible (Komen *et al.*, 1994) off diagonal contributions of the function derivatives in the expansions, the increment of spectrum due to the source terms for one integration time step is expressed as

$$\Delta_{int} F_{i,j,k,m} = \frac{\Delta t_{int}}{2}[1 - \frac{1}{2}\Lambda_n(u^{n+1/2}_{a*})]^{-1}(S^{n}_{i,j,k,m}(u^{n+1/2}_{a*}) + S^{n}_{i,j,k,m}(u^{n}_{a*})) \tag{2.110}$$

where Λ_n is the diagonal matrix of the derivative $(\partial S^{n}_{i,j,k,m}/\partial F^{n}_{i,j,k,m})$ of source functions, u_{a*} is the air friction velocity. Remark that the source terms may also depend on the friction velocity at time level $n + r$. For the detailed description of the source term integration scheme one is referred to

WAMDIG (1988) and the WAM book by Komen *et al.* (1994). Note that equations (2.104) and (2.110) are only used up to a high-frequency limit. In the WAM model, this limit is set to be

$$f_{hf} = \min\{f_{max}, \max(2.5f_m, 4f_{PM})\} \tag{2.111}$$

where f_{max} is the highest frequency of the discrete frequency grid, f_m is the mean frequency, and f_{PM} is the Pierson-Moskowitz frequency.

For frequencies below the high-frequency limit, the spectrum is called a prognostic part of the spectrum. Beyond this limit f_{hf}, the spectrum is supposed to have a diagnostic tail. An f^{-5} tail is added in the WAM model, and the diagnostic part of the spectrum is given by

$$F(f,\theta) = F(f_{hf},\theta)(\frac{f}{f_{hf}})^{-5} \tag{2.112}$$

2.5 Summary and conclusions

In this chapter a detailed mathematical and physical basis of the wave dynamics and wave modelling has been described. Starting from the description of the wave, wave parameters such as wave height, length, period, frequency, wave number, etc., were presented. Following the spectral concept of waves, several wave spectrum formulations were given. The wave evolution is represented by the spectral energy and/or action density transport equation. The emphasis was on the application of wind generated waves travelling in shallow water. Different processes like shoaling, depth refraction, current refraction are involved in wave propagation. The source terms include wind input, whitecapping dissipation, nonlinear interactions, bottom friction dissipation and depth-limited wave breaking. Finally, some numerical techniques to solve the spectral energy balance equation were discussed.

A distinction was made between the spectral action density balance equation and the energy balance equation. The energy balance equation is generally applied in cases where currents are absent or where the currents

field is steady in time. In the case of an unsteady current field, the action density balance equation should be considered due to the non-conserved total energy. The generalized action density balance equation is given by Komen *et al.*. The shallow water effects like shoaling, depth and current refraction, etc. were described. The detailed formulations for the stationary depth refraction rate and for the steady currents refraction rate were clearly presented.

Since the theoretical studies of Miles and Phillips in the late fifties, several suitable expressions for modelling the wind input term were given in the literature. Two expressions were kept for further use in this work. One is the expression proposed by Snyder *et al.* and modified by Komen *et al.*. The other one is the expression based on the quasi-linear theory of Janssen, which has been implemented in the Cycle 4 of the WAM model. For shallow water, the phase velocity in the wind input expressions is depth-dependent.

Based on the study of Hasselmann relating the effect of whitecapping on the spectral energy balance, the whitecapping dissipation has been described to be quasi-linear, i.e. linear but with proportionality constants depending on the integral spectral properties. The dissipation expression from Komen *et al.*, which allows for the existence of an equilibrium solution of the energy balance equation at the fully developed sea, is chosen in this study. This dissipation function has been adjusted in order to obtain a proper balance at the high frequency end of the spectrum by adding a k^2 term in the Cycle 4 of the WAM model. Our knowledge of the whitecapping dissipation is still very limited. The challenge remains to work out the constants from first principles.

The nonlinear interaction source term is the best known among various source terms. It is based on first principles and is therefore considered to be known exactly. Although there exists a model called EXACT-NL, which computes the nonlinear interactions S_{nl} exactly, it is still too slow for an operational wave model. The discrete interaction approximation to S_{nl} is employed for further study. The extension of the deep sea nonlinear

interactions into shallow water has been made by introducing the single scale parameter R of Hasselmann and Hasselmann.

The bottom friction dissipation in shallow water has been derived from the wave boundary layer equation. It is expressed as the work done by the (basically unknown) bottom stress on the (known) free stream orbital bottom velocity. According to different models to parametrize the turbulent bottom shear stress, such as the eddy viscosity model and the drag law model, different bottom dissipation formulations are found in wave modelling. This study will further investigate the effects of different bottom friction dissipation models on the wave evolution. The detailed description of different friction dissipation formulations will be given in chapter 3.

The depth-induced wave breaking was also included in this work. The total dissipation rate of wave breaking is based on Battjes and Janssen, and extended to predict the energy loss per spectral component following Van Vledder. This approach is supported by the experimental observations by Beji and Battjes that wave breaking on and passing over a bar does not change the spectral shape of wave evolution. This source term will be implemented in the Cycle 4 of the WAM model for further study (chapter 6). However, the limited range of these experimental conditions does not allow wide-ranging conclusions. Further research work is needed in this topic.

In order to solve the energy balance equation in the steady current case, the mixed numerical scheme, used in the Cycle 4 of the WAM model, was completely presented in a five-dimensional (x, y, t, f, θ) coordinate system. For the wave propagation a first order upwinding scheme is used. For the source term integration, an implicit second order, centred difference scheme was applied. Some other higher order schemes may be used for the propagation computation.

Chapter 3

Effects of the Bottom Friction Formulation on Energy Balance

3.1 Introduction

The evolution of wind waves is described by the spectral energy balance equation. It is generally assumed that in the deep sea when the wind sea is fully-developed, the total energy and the peak frequency reach asymptotic values, and there is a balance between wind input, dissipation due to whitecapping and resonant wave-wave interactions (Komen *et al.*, 1984). As waves propagate from deep into shallow water, they begin to encounter the sea bed and dissipate the energy by various linear or nonlinear bottom dissipation mechanisms determined by the bottom topography and sediment properties. An overview of the different wave bottom dissipation mechanisms is given by Shemdin *et al.* (1978). They contain percolation that causes viscous damping of energy by water seeping through the pores of the sandy bottom, friction created by the orbital motion of water particles under wave conditions, motion of a soft muddy bottom and scattering on bottom irregularities. The relative strength of these mechanisms is dependent on the bottom conditions. For fine sandy bottoms (0.1 mm

< mean grain diameter < 0.4 mm) or where wave-generated sand ripples occur, as found in many continental shelves (Dingler and Inman, 1976), the bottom friction is dominant (Shemdin *et al.*, 1978). Since our main area of interest is the North Sea and the North West European continental shelf, our discussion is restricted to the bottom friction dissipation as the dominant dissipation mechanism. For the dissipation due to bottom friction, a few different formulations can be found in the literature. For this study five formulations were retained: an empirical expression based on the JONSWAP experiment (Hasselmann *et al.*, 1973), three expressions based on the drag law turbulent friction model (Hasselmann and Collins, 1968; Collins, 1972; Madsen *et al.*, 1988a) and one based on the eddy viscosity friction model (Weber, 1991a). These five models have widely been used in many wave models, and dissipation coefficients used in different cases were quite different.

To obtain a better understanding of the friction dissipation process, it is instructive to investigate quantitatively the effects of different bottom friction formulations and different coefficients on the energy balance. The five formulations for the bottom friction dissipation in shallow water have been implemented in a one-dimensional third generation wave model for the fetch-limited case. We want to examine how different the original contributions are in terms of the resulting total energy and peak frequency. To do this the source terms for the bottom dissipation are formulated in section 3.2 in a form proposed by Weber (1991a,b) which facilitates comparison. The results of the corresponding wave model runs can be found in section 3.3.

In general, the growth curves in deep water are assumed to scale in terms of the air friction velocity. For the shallow water case, they are also presented in the nondimensional form scaled to the wind velocity by a lot of scientists (see, WAMDGI, 1988; Weber, 1989; Tolman, 1991; Komen *et al.*, 1994; Verhagen and Young, 1995, etc.). These curves were used to evaluate different model results or to compare the numerical results with measurements. In section 3.4, the general assumption that the growth

curves for the total energy and the peak frequency scale in terms of the air friction velocity is questioned in the shallow water case. The effect of the wind friction velocity on the energy growth curves for the fetch-limited shallow water case is investigated in numerical experiments and by mathematical analysis.

3.2 Models for bottom friction dissipation

The general form for the bottom friction dissipation can be written as (Weber, 1991a,b):

$$S_{bf} = -C \frac{k}{\sinh 2kh} E(f,\theta) \tag{3.1}$$

with k the wave number of the spectral component, h the water depth, f the frequency, θ the direction of a wave component, and $E(f,\theta)$ the two-dimensional frequency spectrum. C is a model-dependent dissipation coefficient with the dimension of a velocity $[ms^{-1}]$. The dissipation coefficient formulations for the five different models retained in this study can be found in Table 3.1. The detailed description follows below.

Table 3.1: Five dissipation coefficient formulations.

Formulations	References	Coefficients
$C_J = \frac{2c}{g}$	Hasselmann *et al.*, 1973	$c = 0.038\ m^2 s^{-3}$
$C_{DHC} = 2C_f\{\delta_{ij}\langle U\rangle + \langle\frac{U_i U_j}{U}\rangle\}$	Hasselmann and Collins, 1968	$C_f = 0.015$
$C_{DC} = 2C_f\langle U^2\rangle^{\frac{1}{2}}$	Collins, 1972	$C_f = 0.015$
$C_{DM} = \frac{8}{3\pi} f_w \sqrt{2}\langle U^2\rangle^{\frac{1}{2}}$	Madsen *et al.*, 1988a	f_w or K_N
$C_E = u^*(T_{\underline{k}}(\zeta_0) + T_k^*(\zeta_0))$	Weber, 1991a	$K_N = 4$ cm

3.2.1 An empirical expression

The simplest form for the bottom friction dissipation was proposed by Hasselmann *et al.* (1973) who applied the Hasselmann and Collins (1968) theory to measure the decay of swell in the JONSWAP experiment (Has-

selmann *et al.*,1973). C_J is assumed to be constant:

$$C_J = \frac{2c}{g} \tag{3.2}$$

In the JONSWAP experiment, the empirical coefficient c was found to vary over two orders of magnitude, with a mean value for c of 0.038 $m^2 s^{-3}$. No correlation was found with the tidal phase or velocity. Hasselmann and Collins (1968) assumed that the bottom stress can be modeled by a drag law where the characteristic velocity is the current immediately outside the thin wave boundary (i.e. the superposition of the mean current velocity and the wave orbital velocity). A two-layer eddy viscosity model as, e.g., proposed by Christoffersen and Jonsson (1985) may be a better representation of the combined wave-current flow than a one-layer drag law model. This empirical dissipation formulation with the mean value ($0.038 m^2 s^{-3}$) has been used in wave models by WAMDI (1988) and Cavaleri *et al.* (1988, 1989, 1991), and performed well. The energy balance in finite water depth for fetch-limited conditions was investigated with the use of this empirical expression ($c = 0.038\ m^2 s^{-3}$) by Weber (1988). She found that the energy levels for the fully developed stage and for the lower water depths are much higher than the empirical CERC growth curves. Also, Bouws and Komen (1983) found that the empirical formulation with a mean value for c of 0.038 $m^2 s^{-3}$ yielded too low dissipation rates for a depth-limited wind sea case in the Southern North Sea. They selected a value of 0.067 $m^2 s^{-3}$ for c in order to obtain a 'correct' equilibrium solution for a steady sea state ($U_{10} = 25\ ms^{-1}$, $h = 35$ m).

3.2.2 Three expressions based on the drag law model

Hasselmann and Collins (1968) derived a formulation for the bottom friction dissipation. They related the turbulent bottom stress to the external flow by means of a quadratic drag friction law. The dissipation coefficient is expressed by:

$$C_{DHC} = 2C_f\{\delta_{ij}\langle U\rangle + \langle\frac{U_i U_j}{U}\rangle\} \tag{3.3}$$

where δ_{ij} is the Kronecker delta function; $\langle \cdot\cdot \rangle$ denotes the ensemble average; U is equal to $(U_1^2+U_2^2)^{\frac{1}{2}}$, U_1 and U_2 are the bottom velocity components. C_f is a drag coefficient determined experimentally as a function of the scaled bottom roughness (e.g., scaled with the excursion amplitude). Hasselmann and Collins (1968) proposed a value of 0.015 for C_f. Weber (1991a) rewrote (3.3) as:

$$C_{DHC} = 2C_f\langle U_1^2\rangle^{\frac{1}{2}}\{F_1(A)\cos^2(\theta-\phi) + F_2(A)\sin^2(\theta-\phi)\} \qquad (3.4)$$

with

$$A = 1 - \frac{< U_2^2 >}{< U_1^2 >}$$

The angle $(\theta - \phi)$ is the direction of a wave component relative to the main axis of the bottom velocity spectrum, F_1 and F_2 are functions of the hypergeometric function (Abramowitz and Stegun, 1965). The details of the calculation for (3.4) is described in Weber (1989) and in the internal report by Luo (1992).

Collins (1972) simplified the above dissipation coefficient (equation (3.3)) by leaving out the dependence on the direction of the wave component and by using the total wave induced bottom velocity only.

$$C_{DC} = 2C_f\langle U^2\rangle^{\frac{1}{2}} \qquad (3.5)$$

where

$$\langle U^2\rangle^{\frac{1}{2}} = \sqrt{\int\int \frac{2gk}{\sinh 2kh} E(f,\theta)df d\theta} \qquad (3.6)$$

He applied a fixed drag coefficient C_f (= 0.015) also. This simplified drag law dissipation form has been used in various wave models, see e.g. SWIM (1985), Cavaleri and Rizzoli (1981), and Abdalla and Özhan(1993). Both the simplified drag law form (Collins, 1972, $C_f = 0.015$) and the empirical dissipation form ($c = 0.038\ m^2s^{-3}$) have been used in a wave model by Li and Mao (1991), and they reported that in an idealized test case where a uniform wind speed of 20 ms^{-1} blows over an infinite region of finite water depth, the empirical dissipation form produced, in comparison to the

simplified drag law dissipation formulation, growth curves which were in better agreement with the CERC and KNMI growth curves (Li and Mao, 1991).

Madsen *et al.* (1988a) derived a formulation similar to the one proposed by Hasselmann and Collins (1968) based on the drag friction law:

$$C_{DM} = \frac{8}{3\pi} f_w \sqrt{2} \langle U^2 \rangle^{\frac{1}{2}} \tag{3.7}$$

where the constant $\frac{8}{3\pi}$ can be replaced by the constant 1 (Madsen *et al.*, 1988b), the factor $\sqrt{2}$ appears due to the replacement of the amplitude of the near-bottom orbital velocity used in the original formulation (Madsen *et al.*, 1988a) by the rms-value of the near bottom instantaneous velocity. The friction factor f_w in the Madsen *et al.* model is a function of the bottom roughness height (K_N) and parameters characterized by the wave conditions. It can be estimated using the formulation of Jonsson (1966):

$$\frac{1}{4\sqrt{f_w}} + \log_{10} \frac{1}{4\sqrt{f_w}} = m_f + \log_{10} \frac{a_b}{K_N} \tag{3.8}$$

where m_f is a constant. A value of -0.08 for m_f was determined experimentally by Jonsson and Carlsen (1976). The bottom roughness height K_N depends on the flow field and the sediment properties. The near-bottom excursion amplitude a_b is formulated as:

$$a_b = \sqrt{2 \int \int \frac{1}{\sinh^2 kh} E(f,\theta) df d\theta} \tag{3.9}$$

This dissipation form was implemented in a parametric windsea model for finite water depths by Graber and Madsen (1988), and in a third-generation model for wind waves in combined wave-current flow by Tolman (1991). Graber and Madsen (1988) incorporated the bottom dissipation using a tuned constant friction factor f_w. Tolman (1991) reported that a constant bottom roughness height K_N ranging between 2 cm and 5 cm produced a good agreement between numerical results and measurements for the nondimensional wave height and period. Here a value of 4 cm for K_N will be used, the same as used in the eddy viscosity model (Weber, 1991b).

Recently Tolman (1994), discussed a movable-bed bottom friction model, which combines the Madsen *et al.* (1988) drag law model with the Grant and Madsen (1982) bottom roughness model for a movable-bed. He found that the effects of movable-beds on the bottom friction are important for swell propagation in conditions of initial ripple-formation. For a depth-limited wind sea, movable-bed effects are probably insignificant because the wave conditions generally lead to washed-out ripples where the roughness is insensitive to sediment or wave parameters. According to Tolman (1994) a single and pre-defined bottom roughness height will make models, which do not incorporate movable-bed effects, to be potentially successful. This movable-bed bottom friction model will not be considered here.

3.2.3 An expression based on the eddy viscosity model

With a one-layer eddy viscosity model, based on the random turbulent wave boundary layer and using perturbation theory, the following dissipation coefficient was derived (Weber, 1991a):

$$C_E = u^*(T_{\underline{k}}(\zeta_0) + T^*_{\underline{k}}(\zeta_0)) \tag{3.10}$$

u^* is the wave boundary layer friction velocity and can be determined as a function of wave number, wave spectrum, bottom boundary layer thickness and bottom roughness height. $T_{\underline{k}}$ is a dimensionless function and $T^*_{\underline{k}}$ is the complex conjugate of $T_{\underline{k}}$. When the roughness height is given, the values for u^* and $T_{\underline{k}}$ can be worked out iteratively with an initial u^*. Details of the calculation procedure can be found in Weber (1989).

This formulation was implemented in a regional third generation WAM model for the Texel storm hindcast case, and a value of 4 cm for the bottom roughness height K_N was selected according to the flow conditions in the Southern North Sea (Weber, 1991b). Because of the better prediction of the significant wave height it was suggested that the eddy viscosity formulation (K_N = 4 cm) is to be preferred upon the empirical JONSWAP expression ($c = 0.038\ m^2 s^{-3}$). It might however be unfair to assume that

the mean value of the coefficient c in the empirical JONSWAP bottom friction dissipation formulation is the most suitable and most representative value for the whole North Sea, and especially for the Southern North Sea (cf. Bouws and Komen, 1983).

To save computing time Weber (1991b) defined an approximate linear eddy viscosity dissipation coefficient which implies that the spectral peak frequency is assumed to be representative for the entire spectrum. The approximate linear eddy viscosity model still costs three times as much CPU time as the empirical JONSWAP formulation. She then proposed a simplified version for this approximate model by using a numerically determined characteristic velocity at the top of bottom boundary layer in terms of spectral parameters obtained from the empirical CERC curves. However, the approximate and the simplified linear eddy viscosity models will not be considered here.

3.3 Evaluation of the original formulations

3.3.1 The governing equation

The evolution of ocean wave spectra can be described by the energy transfer equation. For flat bottom shallow water conditions and in the absence of currents the equation takes the form:

$$\frac{\partial E}{\partial t} + \mathbf{C_g} \cdot \frac{\partial E}{\partial \mathbf{x}} = S_{tot} \tag{3.11}$$

with E $(= E(f, \theta, \mathbf{x}, t))$ the two-dimensional frequency spectrum, f the frequency, θ the direction of a wave component, $\mathbf{x}$ the space coordinates, t time and $\mathbf{C_g}$ the group velocity. S_{tot} $(= S_{tot}(f, \theta, \mathbf{x}, t))$ is the total source term, which is the sum of wind input S_{in}, whitecapping dissipation S_{ds}, bottom dissipation S_{bot} and nonlinear interactions S_{nl}. The bottom dissipation term S_{bot} may in principle take the form of any bottom dissipation mechanism. This study is limited to the friction form S_{bf} in areas of fine sand or with sand ripples (see section 3.2).

In the one-dimensional case (one space coordinate x) and in the asymptotic stationary limit, the dependence of the wave field on distance will produce the idealized fetch-limited growth of waves, and the above equation becomes:

$$C_g \frac{\partial E}{\partial x} = S_{tot} \tag{3.12}$$

This equation is solved numerically by an implicit scheme (WAMDI, 1988). In finite depth the relations between the group velocity C_g, wave number k, angular frequency ω and water depth h are given by:

$$\begin{aligned} C_g &= \frac{1}{2}\sqrt{\frac{g}{k}\tanh(kh)}[1 + \frac{2kh}{\sinh(2kh)}] \\ \omega &= \sqrt{gk\tanh(kh)} \end{aligned}$$

The source terms are briefly formulated here for completeness. A more extensive discussion can be found in WAMDI (1988).

According to the parameterization proposed by Snyder *et al.* (1981) on the basis of direct measurements of the work done by the atmospheric pressure fluctuations on the waves, the wind input S_{in} is taken as:

$$S_{in}(f,\theta) = max\{0, 0.25\frac{\rho_a}{\rho_w}(28\beta\frac{u_{a*}}{C}\cos\theta_w - 1)\}\omega E(f,\theta) \tag{3.13}$$

ρ_a and ρ_w are densities of air and water respectively, C $(= \omega/k)$ the phase velocity of the wave, and θ_w the wave direction with respect to the wind direction. The empirical factor β is taken as 1, and the friction velocity of air u_{a*} is used rather than the mean wind speed U_5 or U_{10} (Komen *et al.*, 1984).

The dissipation due to whitecapping is based on the Hasselmann (1974) whitecapping theory and the Komen *et al.* (1984) whitecapping parameterization in deep water. In order to represent the dependence of the dissipation on the wave steepness for finite water depth, the dissipation is expressed in terms of the wavenumber. To enhance the stability of the implicit scheme, the inverses of the mean wave number and the mean angular frequency during the mean period are used (WAMDI, 1988). The dissipation S_{ds} due

to whitecapping for shallow water is given by:

$$S_{ds} = -2.59\hat{\omega}\frac{k}{\hat{k}}(E_{tot}\hat{k}^2)^2 E(f,\theta) \tag{3.14}$$

where

$$\begin{aligned}
\hat{\omega} &= [E_{tot}^{-1}\int E(f,\theta)\omega^{-1}dfd\theta]^{-1} \\
\hat{k} &= [E_{tot}^{-1}\int E(f,\theta)k^{-\frac{1}{2}}dfd\theta]^{-2} \\
E_{tot} &= \int\int E(f,\theta)dfd\theta
\end{aligned}$$

According to the parameterization of the nonlinear energy transfer by Hasselmann and Hasselmann (1981), the nonlinear interactions for finite water depth can be related to the deep water S_{nl}^d through a straightforward scale transformation with a single scale parameter R.

$$S_{nl}^h = R(k_p h)S_{nl}^d \tag{3.15}$$

The scaling factor is given by

$$R(k_p h) = 1 + \frac{5.5}{k_p h}(1 - \frac{5}{6}k_p h)\exp^{-\frac{5}{4}k_p h} \tag{3.16}$$

and is valid for $k_p h > 1$ (WAMDI, 1988; in fact the actual $k_p h$ cut-off in the WAM source code is greater than 0.5). In this chapter all values for $k_p h$ are greater than 1.

The discrete interaction approximation (Hasselmann *et al.*, 1985) is used for the calculation of the nonlinear interactions in deep water S_{nl}^d.

For the bottom friction dissipation S_{bf}, only the empirical formulation is used in WAM. For the present study the other four expressions described in section 3.2 are also implemented in the one-dimensional model for the fetch-limited case.

3.3.2 Initial conditions

A JONSWAP spectrum was taken as the initial spectrum:

$$E_J(f) = \frac{\alpha g^2}{(2\pi)^4 f^5}\exp^{-\frac{5}{4}(\frac{f}{f_p})^{-4}}\gamma^{\exp^{\frac{-(f-f_p)^2}{2\sigma^2 f_p^2}}}$$

with α, f_p, γ and σ the usual JONSWAP parameters (Hasselmann *et al.*, 1973). α and γ had values of 0.02 and 3.3 respectively. The initial condition for all water depths was kept the same so that the growth curves start from the same point. The initial peak frequency was equal to 0.17 Hz, which corresponds to a spectrum in water of 15 m depth where the waves just start to interact with the bottom according to the $k_p h$ criterion ($k_p h = 1.83$) (Weber, 1989), which says that replacing the shallow water expression by the deep water expression for the dispersion relation gives an error of at most 5%.

The spreading function took the empirical form (Arthur, 1949):

$$G(\theta) = \begin{cases} \frac{2}{\pi} \cos^2 \theta & \text{if } \mid \theta \mid \leq \frac{\pi}{2} \\ 0 & \text{otherwise} \end{cases}$$

42 frequencies and 12 directions were used, the angular resolution was 30°, the range of frequencies was from 0.04177 Hz to 2.08 Hz with a geometric (or logarithmic) frequency spacing $\Delta f/f$ of 0.1. The wind friction velocity u_{a*} was taken to be 0.71 ms^{-1}. The corresponding wind speed U_{10} is about 15.6 ms^{-1} (using the relation of Wu, 1982).

Although a JONSWAP spectrum with an f^{-5}-tail was taken as an initial spectrum, in the calculation an f^{-4}-tail was attached beyond 2.5 f_p for deep sea conditions. In finite water depth, it was replaced by a $k^{-2.5}$-tail according to the dimensional arguments of Kitaigorodskii *et al.* (1975). The runs are annotated by J1 for the empirical JONSWAP expression, DHC1 for the drag law expression of Hasselmann and Collins (1968), DC1 for the simplified drag law formulation of Collins (1972), DM1 for the drag law model with the dynamically changing friction factor of Madsen *et al.* (1988) and E1 for the eddy viscosity formulation of Weber (1991,a). For all combinations simulation runs were made for four different water depths: 15 m, 30 m, 60 m and 120 m. The 120 m run is essentially a deep water run.

3.3.3 Results

Growth curves

The growth curves for the total energy and the peak frequency are shown in Figure 3.1 and 3.2 respectively for water depths of 120 m, 60 m, 30 m and 15 m. The difference between the growth curves for the five original formulations is very small for water depths of 60 m and 120 m. However, the difference between the asymptotic values for the five formulations is quite significant at shallower water depths. The maximum difference is between DM1 and J1, 70% for the total energy and 30% for the peak frequency for a water depth of 15 m. The empirical JONSWAP bottom formulation J1 has the highest asymptotic energy and lowest asymptotic peak frequency level amongst the five formulations; the simplified drag law expression DC1 produces a higher energy and a lower peak frequency level than the eddy viscosity formulation E1 and drag law formulation DHC1 (E1 and DHC1 are very close). The Madsen *et al.* formulation DM1 creates the lowest asymptotic energy and the highest asymptotic peak frequency level. These findings are valid for the 30 m and 15 m runs, except that for the 30 m run the asymptotic energy and peak frequency level for the empirical formulation J1 and the simplified drag law formulation DC1 are nearly equal (3% difference for the total energy, 1% for the peak frequency). Comparison with the growth curves of CERC in figures 3.1 and 3.2 will be discussed later on.

Compared to deep water conditions, the total energy is reduced and the peak frequency increased in shallow water. The contribution of the bottom friction dissipation to the energy balance, i.e., the amount of the energy reduction and the shift of the peak frequency, is depending on the water depth and the bottom friction dissipation formulation used.

C values for fully developed stage

Figure 3.3 displays the original dissipation coefficient values for C_J, C_{DHC}, C_{DC}, C_{DM} and C_E for a water depth of 15 m at the fully developed stage. It

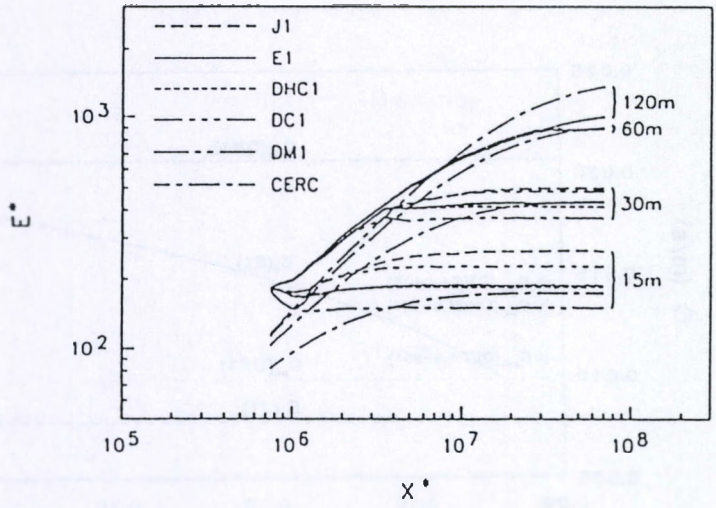

Figure 3.1: Growth curves of nondimensional total energy E^* (equal to Eg^2/u_{a*}^4) as a function of nondimensional fetch X^* (equal to xg/u_{a*}^2) for different bottom dissipation formulations (Here $u_{a*} = 0.71\ ms^{-1}$; for the Coastal Engineering Research Center (CERC) growth curves, $E = H_s^2/14.4$).

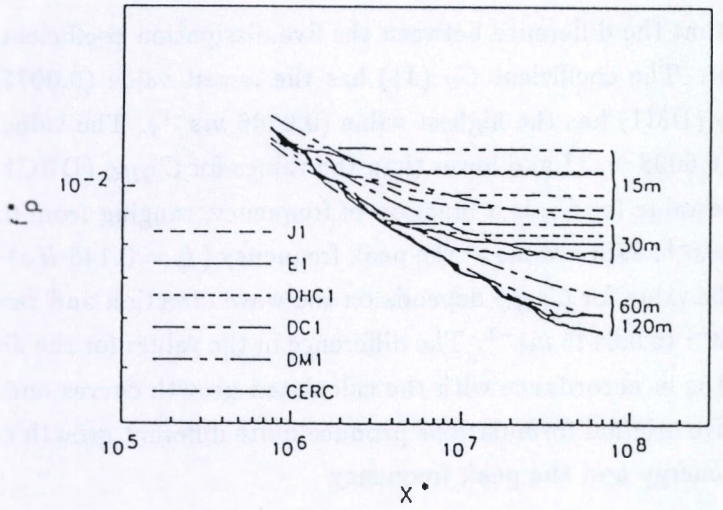

Figure 3.2: Growth curves of nondimensional peak frequency f_p^* (equal to $f_p u_{a*}/g$) as a function of nondimensional fetch X^* (equal to xg/u_{a*}^2) for different bottom dissipation formulations (Here $u_{a*} = 0.71\ ms^{-1}$; for the Coastal Engineering Research Center (CERC) growth curves, $f_p = 0.9/T_s$).

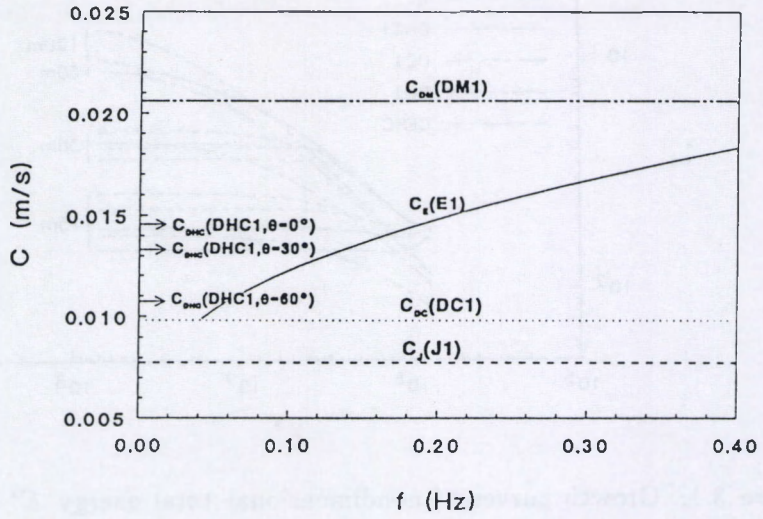

Figure 3.3: The values for the dissipation coefficient C (in (3.7)) from the five original formulations for a water depth of 15 m at the fully developed stage (Here $u_{a*} = 0.71 ms^{-1}$).

is found that the difference between the five dissipation coefficients is quite significant. The coefficient C_J (J1) has the lowest value ($0.00775\ ms^{-1}$), and C_{DM} (DM1) has the highest value ($0.0206\ ms^{-1}$). The value for C_{DC} (DC1) is $0.0098\ ms^{-1}$ and lower than the values for C_{DHC} (DHC1) and C_E (E1). The value for C_E is a function of frequency, ranging from $0.01\ ms^{-1}$ to $0.018\ ms^{-1}$, with a value at the peak frequency ($f_p = 0.145\ Hz$) of $0.0136\ ms^{-1}$. The value for C_{DHC} depends on the wave direction and ranges from $0.0108\ ms^{-1}$ to $0.0145\ ms^{-1}$. The difference in the values for the dissipation coefficient is in accordance with the calculated growth curves and explains why the five original formulations produce quite different growth curves for the total energy and the peak frequency.

Contribution of source terms

In order to investigate the relative overall contribution that bottom dissipation makes to the energy balance in the five formulations J1, E1, DHC1,

DC1 and DM1, the integral of wind input, dissipation through whitecapping and bottom dissipation in the range of $0 < f < 2.5 f_p$ is calculated:

$$\tilde{S}_i = \int_0^{2.5 f_p} S_i(f, \theta) df d\theta$$

where S_i represents S_{in}, S_{ds} or S_{bot}.

Figure 3.4 and 3.5, respectively, show the ratio between the bottom dissipation and the wind input and the ratio between the bottom dissipation and dissipation through whitecapping for J1, E1, DHC1, DC1 and DM1 at the fully developed stage. The ratios vary clearly with depth, and also from formulation to formulation although the variation is relatively small compared to that resulting from water depth, e.g., the ratio of the bottom dissipation to the wind input varies from 22 percent (DM1) to 26 percent (J1) for a water depth of 15m and from 15 percent (J1) to 18 percent (E1, DHC1) for a water depth of 30m. In Figure 3.5 we notice that the dissipation by whitecapping is dominant for shallow water. However, the role of bottom dissipation becomes more and more significant when the water becomes more and more shallow, e.g., for a water depth of 15m the bottom dissipation is nearly half of the dissipation due to whitecapping.

For all five formulations there exists a good balance between the various source terms. The relative contributions of the various source terms at the fully developed stage for J1, E1, DHC1, DC1 and DM1 are displayed in Figure 3.6a,b,c,d,e. The bottom dissipation is comparable to the dissipation by whitecapping on the forward face of the spectrum and around the peak frequency f_p, while on the backward face of the spectrum, the energy is mainly balanced by whitecapping dissipation and nonlinear interactions, and bottom dissipation is rather small. Comparing the other source terms from the J1, E1, DHC1, DC1 and DM1 runs, we noticed that the absolute peak values for the J1 run are the largest and those from the DM1 the smallest. For example the wind input source term for the J1 run has a peak value of about $0.002 m^2$ compared to $0.0015 m^2$ for the DM1 run. This is of course due to the fact that the source terms are proportional to the equilibrium spectral energy.

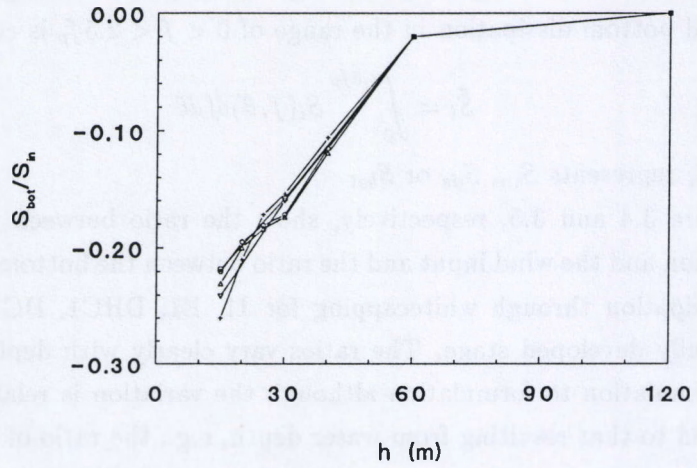

Figure 3.4: The ratio of the bottom friction dissipation to the wind input for the fully developed wind sea as a function of water depth for the five original formulations: J1 (pluses); E1 (triangles); DHC1 (circles); DC1 (inverted triangles); DM1 (squares) (Here $u_{a*} = 0.71ms^{-1}$).

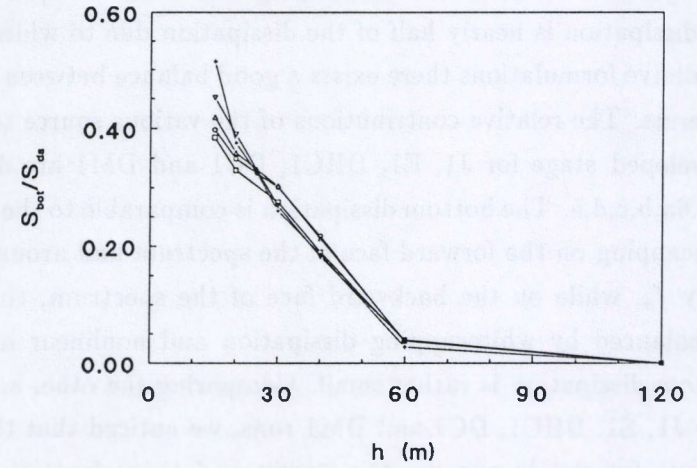

Figure 3.5: The ratio of the bottom friction dissipation to the whitecapping dissipation for the fully developed wind sea as a function of water depth for the five original formulations: J1 (pluses); E1 (triangles); DHC1 (circles); DC1 (inverted triangles); DM1 (squares) (Here $u_{a*} = 0.71ms^{-1}$).

(a)

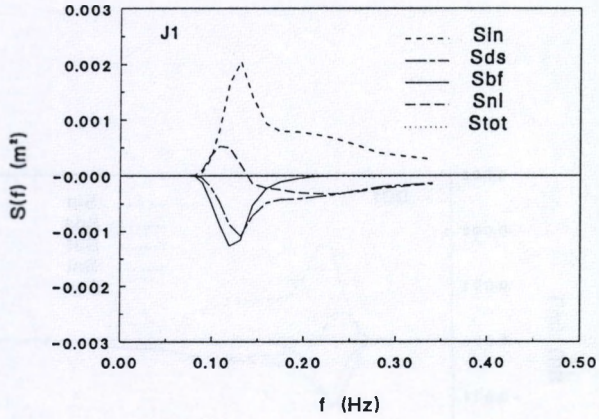
J1
Sin
Sds
Sbf
Snl
Stot
S(f) (m²)
f (Hz)

(b)

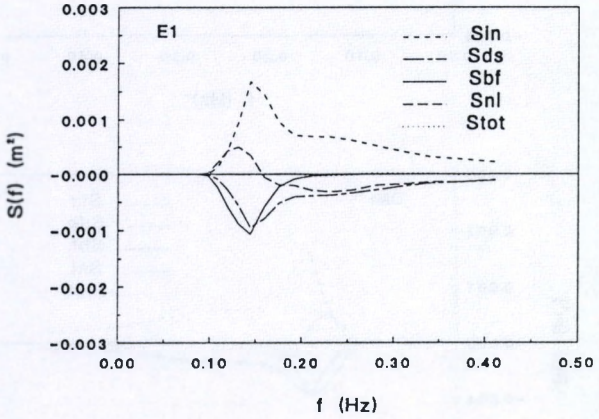
E1
Sin
Sds
Sbf
Snl
Stot
S(f) (m²)
f (Hz)

(c)

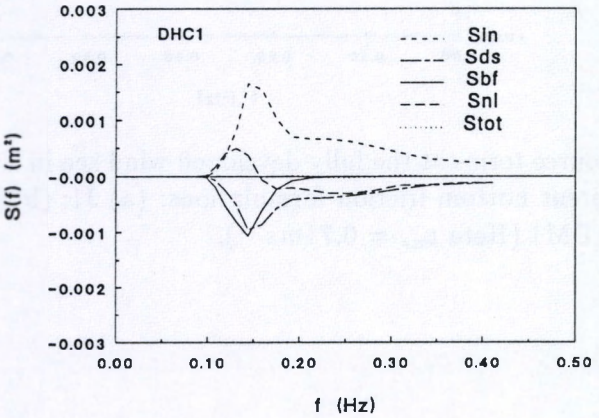
DHC1
Sin
Sds
Sbf
Snl
Stot
S(f) (m²)
f (Hz)

(d)

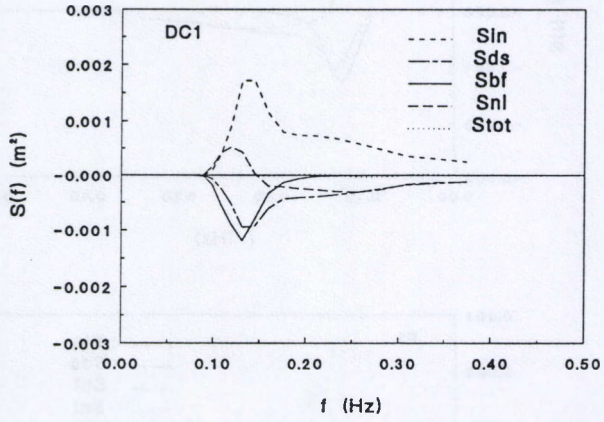

(e)

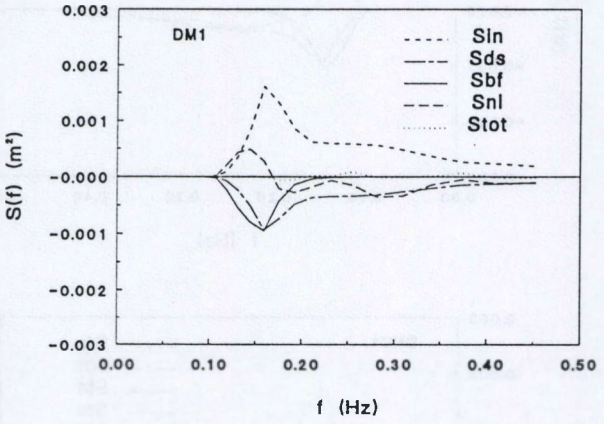

Figure 3.6: Source terms at the fully developed wind sea in a water depth of 15 m for different bottom friction formulations: (a) J1; (b) E1; (c) DHC1; (d) DC1; (e) DM1 (Here $u_{a*} = 0.71 ms^{-1}$).

Table 3.2: The relative CPU time used for five dissipation formulation.

Empirical JONSWAP (1973) (3.2)	J1	100
Collins (1972) (3.5)	DC1	250
Hasselmann and Collins (1968) (3.4)	DHC1	350
Madsen *et al.* (1988a) (3.7)	DM1	400
Weber (1991a) (3.10)	E1	500

Relative CPU time

Normally one knows that the empirical JONSWAP formulation is the simplest one and needs the least amount of computing time. The eddy viscosity model is the most complicated one, and costs the most computing time owing to the iterative determination of the bottom friction velocity. Although the determination of the required CPU time for different formulations depends on computer hardware and also on the efforts toward efficient coding, an indication of the relative CPU time used for these five original formulations referenced to the empirical formulation is still instructive (see Table 3.2). From Table 3.2 one finds that the eddy viscosity model and Madsen *et al.*'s model are much more expensive compared to the empirical expression. In order to produce the same or nearly the same growth curves and also save the computing time, I will seek to examine in how far it is possible to find equivalent dissipation coefficients in Chapter 5.

3.3.4 Comparison with the CERC growth curves

To judge the performance of the various formulations properly, a comparison between field measurement and the results in this study should be made. Unfortunately there are no detailed measurements of wave growth in shallow water for fetch-limited conditions up to now. To have a first impression of the performance the empirical Bretschneider's growth curves (CERC, 1977) could be used. From Figure 3.1 and 3.2 one could already see that for shallower water depths the energy growth curves from J1, DHC1,

DC1 and E1 give higher values than the CERC curves, but DM1 produces lower asymptotic energy values than the CERC curves. The difference of the total energy between J1 and CERC is the largest (40% for the asymptotic energy value at a water depth of 15 m). The DHC1 and E1 growth curves are very close to the CERC values (5% and 8% difference respectively for the asymptotic energy value at a water depth of 15 m). Compared to the CERC growth curves, E1 and DHC1 overestimate the peak frequency at the fully developed state. The comparison with the CERC growth curves cannot be considered conclusive with respect to the correct formulation or even to the correct magnitude of the bottom friction dissipation process. Hopefully measurements in shallow water conditions as by Young *et al.* (1994) will clarify the picture.

3.4 Scaling in terms of wind friction velocity

Deep water growth curves for the total energy and the peak frequency scale with the air friction velocity u_{a*} and the acceleration of gravity g, see e.g. Hasselmann *et al.* (1973). For the shallow water case, the nondimensional total energy E^* ($= Eg^2/u_{a*}^4$) or nondimensional wave height H_s^* ($= H_s g/u_{a*}^2$) were usually presented as a function of the nondimensional water depth h^* ($= hg/u_{a*}^2$) (see WAMDI, 1988; Weber, 1989; Tolman, 1991; Komen *et al.*, 1994; Verhagen and Young, 1995). These curves were used to evaluate different model results (see e.g. Weber, 1989) or to compare the numerical results with measurements. This way of presenting or comparing results, be it from numerical experiments or from field measurements, should be questioned since there is no physical reason that the growth curves for shallow water cases should scale with the air friction velocity.

In this study numerical experiments were done by keeping the nondimensional water depth fixed. Three different wind friction velocities were used: 0.5 ms^{-1}, 0.71 ms^{-1} and 1.0 ms^{-1} (the corresponding wind speed U_{10}: 12.5 ms^{-1}, 16.5 ms^{-1}, 21.5 ms^{-1}). The initial values for the nondimensional peak frequency f_p^* ($= f_p u_{a*}/g$) and the nondimensional fetch x^*

Table 3.3: Initial values for different wind friction velocities.

h_*	$u_{a*}(ms^{-1})$	$h(m)$	$k_p(m^{-1})$	$f_p(Hz)$	$x(km)$
	0.5	7.5	0.245	0.24	18
300	0.71	15	0.122	0.17	37
	1.0	30	0.061	0.12	73

$(= xg/u_{a*}^2)$ were kept the same for all runs as in the run for a nondimensional water depth h^* of 300. For this nondimensional water depth the peak wave number k_p (the wave number corresponding to the peak frequency f_p) was chosen according to the $k_p h$ criterion ($k_p h = 1.83$). Other parameters were obtained from the JONSWAP deep water parametric relations (Hasselmann *et al.*, 1973), see Table 3.3 and section 3.3.2.

For the runs with larger nondimensional water depths (1200, 2400), the growth curves for the total energy are identical since the bottom dissipation only plays a minor role. For runs with nondimensional water depths less than 1200 the growth curves for the total energy from J1, DM1 and E1 are quite different (between 10% and 30%), while the growth curves from DC1 and DHC1 are identical for the same nondimensional water depth. The asymptotic total energy as a function of nondimensional water depth and wind friction velocity is displayed in Figure 3.7 for the bottom friction formulation E1 as an example. Figure 3.8 shows one sample of the energy growth curves for a nondimensional water depth of 300 for E1 with three different wind friction velocities. The results for J1 and DM1 are similar and not shown here.

One can also prove analytically that the bottom friction dissipation source term scales with the wind friction velocity u_{a*} for the drag law expressions with fixed drag coefficient only. For the empirical JONSWAP formulation, the eddy viscosity model and the drag law model with a dynamically changing friction factor, the bottom friction dissipation source

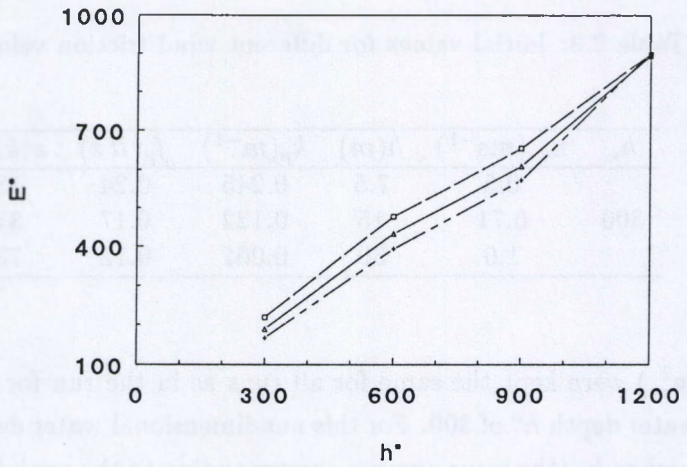

Figure 3.7: Growth curves of nondimensional total energy E^* (equal to Eg^2/u_{a*}^4) as a function of nondimensional water depth h^* (equal to hg/u_{a*}^2) for three different wind friction velocities u_{a*} for the eddy viscosity formulation E1: squares denote $u_{a*} = 0.5\ ms^{-1}$; triangles denote $u_{a*} = 0.71\ ms^{-1}$; pluses denote $u_{a*} = 1.0\ ms^{-1}$.

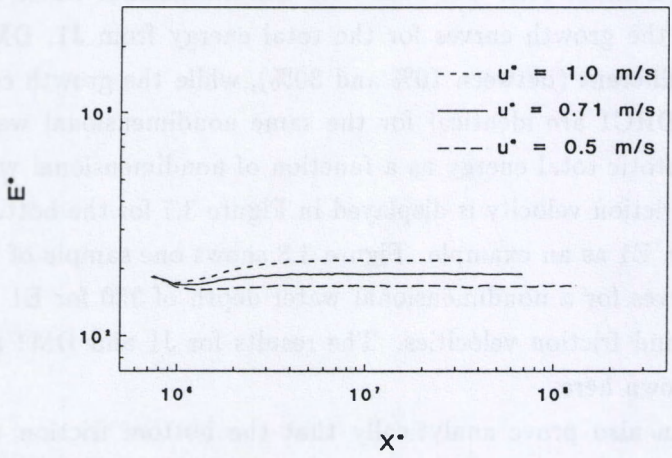

Figure 3.8: Growth curves of nondimensional total energy E^* (equal to Eg^2/u_{a*}^4) as a function of nondimensional fetch X^* (equal to xg/u_{a*}^2) in a nondimensional water depth h^* (equal to hg/u_{a*}^2) of 300 for three different wind friction velocities u_{a*} for the eddy viscosity formulation E1.

term does not scale with u_{a*}. The detailed induction analysis can be seen as follows. Firstly, the energy transport equation is presented in nondimensional form:

$$C_g^* \frac{\partial E^*}{\partial x^*} = S_{in}^* + S_{ds}^* + S_{bf}^* + S_{nl}^* \tag{3.17}$$

where all parameters are nondimensionalized with the wind friction velocity u_{a*} and the acceleration of gravity g, and are indicated by a superscript $*$. The nondimensional source terms and group velocity are then formulated as:

$$S_{in}^*(f^*,\theta) = max\{0, 0.25\frac{\rho_a}{\rho_w}(28\beta\frac{k^*}{\omega^*}\cos\theta_w - 1)\}\omega^* E^*(f^*,\theta) \tag{3.18}$$

$$S_{ds}^*(f^*,\theta) = -2.59\hat{\omega}^*\frac{k^*}{\hat{k}^*}(E_{tot}^*\hat{k}^{*2})^2 E^*(f^*,\theta) \tag{3.19}$$

$$S_{nl}^*(f^*,\theta) = R(k_p^* h^*) S_{nl}^{d*}(f^*,\theta) \tag{3.20}$$

$$S_{bf}^*(f^*,\theta) = -C^*\frac{k^*}{\sinh 2k^* h^*} E^*(f^*,\theta) \tag{3.21}$$

$$C_g^* = \frac{1}{2}\sqrt{\frac{1}{k^*}\tanh(k^* h^*)[1 + \frac{2k^* h^*}{\sinh(2k^* h^*)}]} \tag{3.22}$$

The definitions of all nondimensional forms are:

$$C_g^* = \frac{C_g}{u_{a*}}$$

$$f^* = \frac{f u_{a*}}{g}$$

$$\omega^* = \frac{\omega u_{a*}}{g}$$

$$k^* = \frac{k u_{a*}^2}{g}$$

$$h^* = \frac{hg}{u_{a*}^2}$$

$$E^*(f^*,\theta) = \frac{E(f,\theta)g^3}{u_{a*}^5}$$

$$E_{tot}^* = \frac{E_{tot} g^2}{u_{a*}^4}$$

$$S_i^*(f^*,\theta) = \frac{S_i(f,\theta)g^2}{u_{a*}^4}$$

where i represents as the wind input term, the whitecapping dissipation, nonlinear interactions or bottom friction dissipation.

Now take two or more different air friction velocities. For a specific f^*, the values for ω^* and k^* remain the same (keeping in mind that k^*h^* and kh are always identical).

Assume that the nondimensional energy $E^*(f^*, \theta)$ is the same for the same nondimensional initial fetch x_0^*. From equations (3.18), (3.19), (3.20) one can easily see that the nondimensional source terms for the wind input $S_{in}^*(f^*, \theta)$, for the whitecapping dissipation $S_{ds}^*(f^*, \theta)$, for the nonlinear interaction $S_{nl}^*(f^*, \theta)$ match for different wind friction velocities. Also the nondimensional group velocity or energy transport velocity C_g^* (3.22) is the same. If there is now also no difference for the nondimensional bottom friction dissipation source term S_{bf}^*, then the solution to the differential equation for the nondimensional energy transport (3.17) will be independent of the air friction velocity u_{a*}. And the conclusion would be that the energy growth curve scales in terms of wind friction velocity. However, if the nondimensional bottom friction dissipation is different for different wind friction velocity u_{a*}, the energy growth curve will not scale. The validity of scaling the wave energy with the wind friction velocity in limited water depth depends on the scaling ability of the used formulation for the bottom friction dissipation. For the empirical JONSWAP formulation the nondimensional dissipation coefficient C^* in (3.21) can be formulated as:

$$C_J^* = \frac{2c}{u_{a*}g} \tag{3.23}$$

One notices that the nondimensional value for C_J^* will change when the wind friction velocity changes if c is kept constant. Therefore, the nondimensional bottom friction dissipation S_{bf}^* will be different for the same nondimensional fetch x^* but different wind friction velocity. The energy growth curve will not scale with the wind friction velocity for the empirical JONSWAP bottom friction dissipation formulation.

For the drag law models with a fixed drag coefficient C_f, we restrict the explanation to the simplified drag law formulation (Collins, 1972). The

procedure for the drag law model (Hasselmann and Collins, 1968) is similar. For the simplified drag law model (Collins, 1972) the nondimensional coefficient C^* is formulated as follows:

$$C^*_{DC} = 2C_f \langle U^{*2} \rangle^{\frac{1}{2}} \tag{3.24}$$

where the nondimensional bottom velocity is:

$$\langle U^{*2} \rangle^{\frac{1}{2}} = \sqrt{\int\int \frac{2k^*}{\sinh 2k^* h^*} E(f^*, \theta) df^* d\theta} \tag{3.25}$$

The value for $\langle U^{*2} \rangle^{\frac{1}{2}}$ will stay the same for the same nondimensional fetch x^* but different wind friction velocity u_{a*}. Since the value for C_f is constant independent of the wind friction velocity, the nondimensional coefficient C^* and also bottom friction dissipation S^*_{bf} will not change with the friction velocity u_{a*}. Therefore the energy will scale with the wind friction velocity for the drag law models with a fixed drag coefficient.

For the drag law model with a dynamically changing friction factor f_w, the formulation for C^* is written as:

$$C^*_{DM} = \sqrt{2} \frac{8}{3\pi} f_w \langle U^{*2} \rangle^{\frac{1}{2}} \tag{3.26}$$

And equation (3.8) for the friction factor f_w is reformulated as:

$$\frac{1}{4\sqrt{f_w}} + \log_{10} \frac{1}{4\sqrt{f_w}} = m_f + \log_{10} \frac{a^*_b}{K^*_N} \tag{3.27}$$

where

$$a^*_b = \sqrt{2 \int\int \frac{1}{\sinh^2 k^* h^*} E^*(f^*, \theta) df^* d\theta}$$

$$K^*_N = \frac{K_N g}{u^2_{a*}}$$

The value for a^*_b and $\langle U^{*2} \rangle^{\frac{1}{2}}$ will stay the same for different wind friction velocities u_{a*}. But the value for K^*_N will be different for different wind friction velocities u_{a*} due to the constant roughness height selected. Thus the

value for f_w will be also different. Therefore the bottom friction dissipation and the energy do not scale in terms of the wind friction velocity for the drag law model of Madsen *et al.* (1988a).

For the eddy viscosity model the nondimensional coefficient $T^*_{\underline{k}}$ and the bottom friction velocity u^* change with different friction velocities because the nondimensional roughness height K^*_N ($= K_N g/u^2_{a*}$) differs depending on the wind friction velocity for a constant bottom roughness height. Similar to the above, it can be proven that the bottom friction dissipation and the energy do not scale with the wind friction velocity. Actually Weber's simplified linear eddy viscosity model (1991b) performs the same as the Madsen *et al.* (1988a) model in view of the scaling of the growth curves with the wind friction velocity. Like in the Madsen *et al.* model, the dissipation coefficient in Weber's simplified model is proportional to the characteristic velocity (at the top of the bottom boundary layer) determined by spectral parameters and a nondimensional factor, which is a function of the bottom roughness height and an exterior length scale.

3.5 Conclusion

The energy balance equation was solved numerically for fetch-limited shallow water with five different bottom friction dissipation models. It is found that the formulation of the bottom friction dissipation has a quite significant effect on the energy balance at shallower water depths. It has little effect on the energy balance at larger water depths. Among the five original formulations for the bottom friction dissipation, the empirical JONSWAP formulation with a mean coefficient of 0.038 $m^2 s^{-3}$ (Hasselmann *et al.*, 1973) predicts the highest asymptotic energy levels and the lowest asymptotic peak frequency levels; the simplified drag law expression ($C_f = 0.015$, Collins, 1972) yields higher asymptotic energy levels and lower asymptotic frequency levels than the eddy viscosity formulation ($K_N = 4$ cm, Weber, 1991a) and the drag law formulation ($C_f = 0.015$, Hasselmann and Collins, 1968); the Madsen *et al.* drag law model ($K_N = 4$ cm) results in the lowest

asymptotic energy levels and the highest asymptotic peak frequency levels. This finding is explained by the fact that the values for the dissipation coefficient C from the five original formulations are quite different and therefore have a different effect when the energy is integrated over the frequency and the angle space.

From the analysis of the source terms, it is revealed that the whitecapping dissipation is dominant in shallow water. The contribution of bottom friction varies clearly with depth, and also from formulation to formulation. The role of bottom friction dissipation becomes more and more significant when the water becomes more and more shallow, for example, for a water depth of 15 m the total bottom friction dissipation is nearly half of the total whitecapping dissipation. For all five formulation a good balance between the various source terms was found. The bottom friction dissipation is comparable to the whitecapping dissipation on the forward face of the spectrum and around the peak frequency. While on the backward face of the spectrum, the energy is mainly balanced by whitecapping dissipation and nonlinear interactions, and the bottom friction dissipation is rather small. The absolute peak values of the source terms are different for different bottom friction dissipation models. The empirical JONSWAP formulation results in the largest absolute peak value and those from the Madsen *et al.* ($K_N = 4\ cm$) the smallest.

It appears that among these five models the empirical JONSWAP formulation is the most economic model in terms of computation time. The eddy viscosity model is the most expensive one, costs four times more CPU time than the empirical one. The Madsen *et al.* drag law formulation is the second most expensive model. The simplified drag law expression of Collins is cheaper than the complete drag law formulation of Hasselmann and Collins. For research work regarding to dissipation modelling, especially when connected to morphological processes, a model with a better description of what happens inside the wave boundary layer is to be preferred. The eddy viscosity model and the drag law model with variable friction factor (with or without movable-bed effects) can provide more

detailed information about the bottom boundary layer, and are therefore believed to be physically more correct. However, there is no data evidence to prefer one or the other. Further study is essential to find the true story. Moreover the difficulty to predict the bottom roughness height remains. For operational wave forecasting models it does not always seem worthwhile to spend the extra calculation effort. The empirical formulation should suffice in most circumstances.

It has been proven mathematically that the drag law models with a fixed dissipation coefficient C_f scale with the air friction velocity u_{a*}. The drag law model with a dynamically changing friction factor, the empirical formulation and eddy viscosity model do not scale with the wind friction velocity u_{a*}. Also numerical experiments have shown that only the growth curves obtained from either one of the drag law formulations with the fixed drag coefficient scale with the wind friction velocity. When applying the other three formulations for the bottom friction dissipation source term, differences as big as 30% for the nondimensional asymptotic energy level are obtained at the same nondimensional water depth when the air friction velocity is increased from 0.5 ms^{-1} to 1.0 ms^{-1}. For larger nondimensional water depths, the growth curves for the total energy and the peak frequency at the same nondimensional water depth are nearly identical. This is to be expected since the bottom friction dissipation source term plays an insignificant role.

From the analysis of scaling ability of shallow water growth curves from different bottom friction dissipation models, it is concluded that the shallow water data which are presented in dimensionless form (scaled with the air friction velocity) cannot be used to evaluate different model results.

Chapter 4

Wave Prediction along the Belgian Coast

4.1 Introduction

In Belgium, wave prediction is very useful in the navigation control of large ships towards the harbours of Antwerp and Zeebrugge. To perform wave prediction, reliable and accurate numerical wave models are essential. Since the first operational wave prediction scheme developed by Sverdrup and Munk (1947), numerical wave prediction models have gone through three major stages – the first, second, third generation wave model of development respectively taking placing in the 1960's, 70's and 80's. Currently, spectral wave models based on the energy balance equation of a wave spectrum are used operationally for many of the world oceans. The wave forecasting system mu-WAVE currently in operation for the Belgian coast, uses the wave model HYPAS (Van den Eynde, 1991), which is a second generation wave model. As it is known, the second generation model parametrizes the shape of the surface displacement spectrum with a limited number of parameters, resulting in the difficulty to simulate the corresponding wave field to all kinds of wind fields specially rapidly changing wind fields. With increasing availability of computer power, the third generation wave model - WAM has been developed, which solves the full energy transport equation

and have no 'a priori' restriction on the evolution of the shape of the wave spectrum. The Cycle 4 version of the WAM model has been implemented in the framework of the research project – ESA ERS-1 Pilot Project PP2-B9. The model was applied to wave prediction for the southern North Sea area, where the Belgian coast is located, for a period from October 1992 to March 1993. The model will use the same grids (coarse grid and fine grid) and the same wind field as the mu-WAVE system. The validation of the WAM model results has been made by use of ERS-1 satellite data and buoy data. The cross-comparison between the WAM model and the mu-WAVE results was also made.

4.2 Description of the WAM model package

The WAM model code was developed over a period of about seven years, and is fairly general. Spectral resolution and spatial resolution are flexible and the model can be run globally and/or regionally with open and closed boundaries. Open boundaries are important in case one wishes to use results from a coarse resolution run as boundary conditions for a fine mesh, limited area model run. Options such as shallow water, depth refraction or current refraction may be chosen. For the detailed description of the WAM model software package, one is referred to Günther *et al.*(1992).

The WAM model system consists of three major program parts: pre-processing, processing and post-processing programs. It is designed to run as a module of a more general system or as a stand-alone program. It is set-up for a CRAY computer with a UNICOS operating system. The pre- processing programs generate the model grid, bathymetry-dependent dispersion relation, etc. Post- processing programs are provided for archiving and for further analysis of the model output. Note that a workstation version is now available as well and it has been installed on the SUN workstation at the Laboratory of Hydraulics of K. U. Leuven.

The pre-processing programs contain PREPROC and PRESET. The program PREPROC generates all time independent information for the

wave model. Based on a regional or global topographic data set provided by the user, the model grid is created in the form required for the model. The frequency and angular arrays are also generated. PREPROC expects a current data set if the current refraction option is activated. If the nested fine grids are generated, the information for the output, input and interpolation of boundary spectra are precomputed and stored in separate files for the coarse and fine (sub) grid models. The program PRESET generates an initial wave field for a wave cold start. For land points the zero energy influx is assumed. At all sea points either the initial JONSWAP spectrum is used or the initial spectra are computed from the local initial winds according to fetch law with a $\cos^2$ direction distribution.

The processing programs contain CHIEF and BOUINT. The program BOUINT is used for nested grids. It interpolates, in time and in space, the output spectra from the coarse grid model run onto the fine grid along the interface boundaries of the coarse and fine grids. The program CHIEF uses the output files of PREPROC as set-up files and the files generated by PRESET or a former model run as initial values. A wind input file has to be provided by the user. The energy transport equation is integrated with independently chosen propagation, source terms, wind input and wind output time steps (note that all time step ratios must be an integer or inverse integer). A number of model options and parameters may be selected by the user in the program input, such as, Cartesian or spherical coordinates, deep or shallow water, with or without depth refraction or with depth and current refraction, nested grids, time or no time interpolation, etc. All run time dependent files are fetched dynamically. These files are named by a fixed file name convention. The user has the control over directory names and paths through the model input. The model results are saved in four kinds of binary files: the gridded output files (MAP*) of significant wave height, mean wave direction, mean frequency, friction velocity, wave direction, peak frequency, drag coefficient and normalized wave-induced stress; swell gridded output files (SWE*) of parameters like wave height, swell direction, mean wind- wave direction and mean swell frequency; spectra

at selected grid points or stations (SPE*); swell spectra at selected grid points or stations (SWS*). The data can be printed out through the post-processing programs.

The post-processing programs consist of four programs: PGRID, PSWGRID, PSPEC and PSWSPEC. PGRID prints the gridded output files (MAP*) of mean sea state parameters. PSWGRID prints gridded output files (SWE*) of swell parameters. PSPEC and PSWSPEC print the output files of spectra (SPE*) and swell spectra (SWS*), respectively.

4.3 The installation on a CONVEX C230

Since 1988, the Management Unit of the Mathematical Model of the North Sea and the Scheldt Estuary (M.U.M.M.) has supported the CAMME (Computer Assisted Management of the Marine Environment) Computer Center. This computer center possesses a Convex C230 supercomputer, a vector computer with three parallel processors. Since M.U.M.M. and the Laboratory of Hydraulics of K. U. Leuven jointly work on the ESA ERS-1 Pilot Project PP2-B9, and since M.U.M.M. already had all necessary information (wind fields, buoy data, satellite data, etc.) on their computer, the WAM model was also installed on their Convex C230 system.

First, the running procedure commands had to be converted from the Cray UNICOS to UNIX. Some system-specific FORTRAN routines also had to be adapted in the program codes, e.g., the ISHELL subroutine had to be replaced by the SYSTEM function; BUFFER IN/OUT had to be changed to UNFORMATTED READ/WRITE and UNIT functions were deleted, etc. The detailed changes for each program can be found in Appendix A of the internal report by Luo (1995). All modules are now running on the CONVEX C230.

To verify the implementation of the WAM-model on Convex C230, a set of benchmark cases supplied with the model (test runs defined for the standard SWAMP case 2) were processed. The results were found to be identical to those produced by the standard version.We concluded that the

model transfer from Cray to Convex C230 was successful.

4.4 Model area

The wave model integrates the wave energy transport equation over a certain region and so a definition of the model area (coastlines geometry) is required. For the shallow water area, the energy propagation and the dissipation source terms all depend on the water depth, therefore, a definition of the model bathymetry is also required. As a first approach, the local application of the WAM model is restricted to the northwest European continental shelf and the southern North Sea near the Belgian coast.

4.4.1 The general description

In order to intercept swell generated far away that may travel to the Belgian coast, the WAM model was applied on a coarse grid covering the northwest European continental shelf. Since the bathymetry and the geometry are complicated by the presence of many sand banks and gullies in the southern North Sea, near the Belgian coast, a fine grid model is essential. Therefore, the WAM model was implemented on both coarse and fine grids (in stereographic projection). The fine grid is nested in the coarse grid. For the coarse grid model, a cold start is selected. The warm start is used for the fine grid, where the boundary information is provided by the previous coarse grid run. The grids are identical to the ones used by the mu-WAVE system, which was formed by the second generation wave model HYPAS (Van den Eynde, 1991).

4.4.2 The wave model grids

The stereographic projection

One way to map part of the surface of a sphere to part of a plane is to use a stereographic projection. One has to see the stereographic projection as the projection of the points of a sphere with radius R onto a plane Π with

coordinate system (x_p, y_p) (see figure in Appendix B). The projection of a point X on the sphere is the intersection between the ray going through the South pole and through the point X, and the projection plane Π. This projection plane Π is fixed at a certain latitude ϕ_o and is parallel to the plane tangent to the North pole (also parallel to the equator plane). The projection formulas allow to convert a point on the (i,j) grid to a point on the sphere (and vice versa). The i-direction runs more or less east-west, while the j-direction runs more or less north-south.

The coarse grid

The coarse grid covers the North Sea from 48°N to 70°N latitude and 7°W to 12°E longitude on a grid of 25 x 48 points, with a spatial resolution of 50 km x 50 km. Since a stereographic projection was used for the grid description, equation (2.26) is then solved using Cartesian coordinates. The definition of stereographic projection coordinates x_p and y_p is as follows in terms of latitudes ϕ (positive for the Northern hemisphere, negative for the Southern) and longitudes λ (positive for the Eastern hemisphere, negative for the Western):

$$x_p = R(1+\sin 56.787°)\tan\frac{90°-\phi}{2}\cos(\lambda-95°) \quad (4.1)$$

$$y_p = R(1+\sin 56.787°)\tan\frac{90°-\phi}{2}\sin(\lambda-95°) \quad (4.2)$$

where R is the radius of the earth, equal to 6,356,912 m. A point (i, j) on the coarse grid can be defined by

$$i = 15.0+\frac{x_p}{50,000} \quad (4.3)$$

$$j = -40.0-\frac{y_p}{50,000} \quad (4.4)$$

Figure 4.1 shows the coarse grid model domain with active points and the indication of the interface border of the nested grid. The exact locations and indexes of the coarse grid buoy stations are displayed in Table 4.1 (also see Ovidio *et al.*, 1994a). The bathymetry used for the coarse grid model runs is given in figure 4.2.

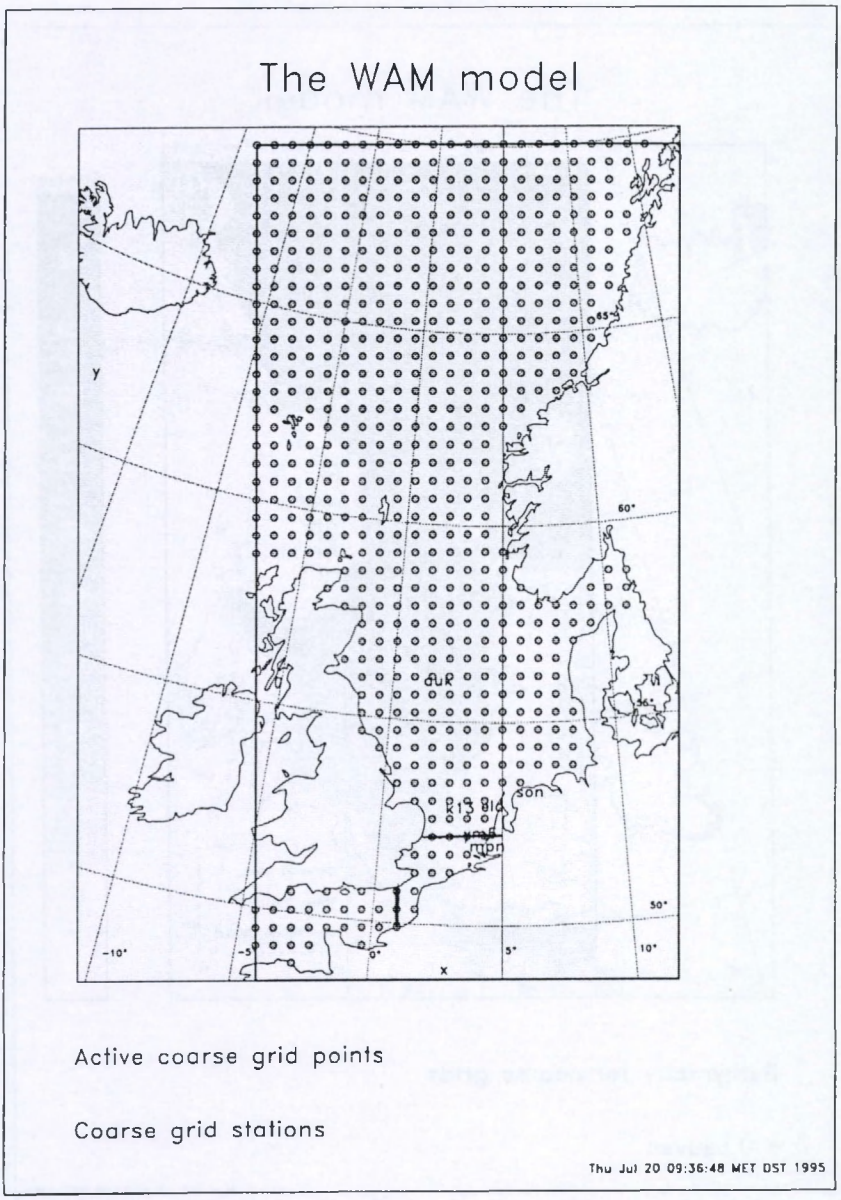

Figure 4.1: The coarse grid active points and the buoy location as indicated by the respective three letter symbols in Table 4.1.

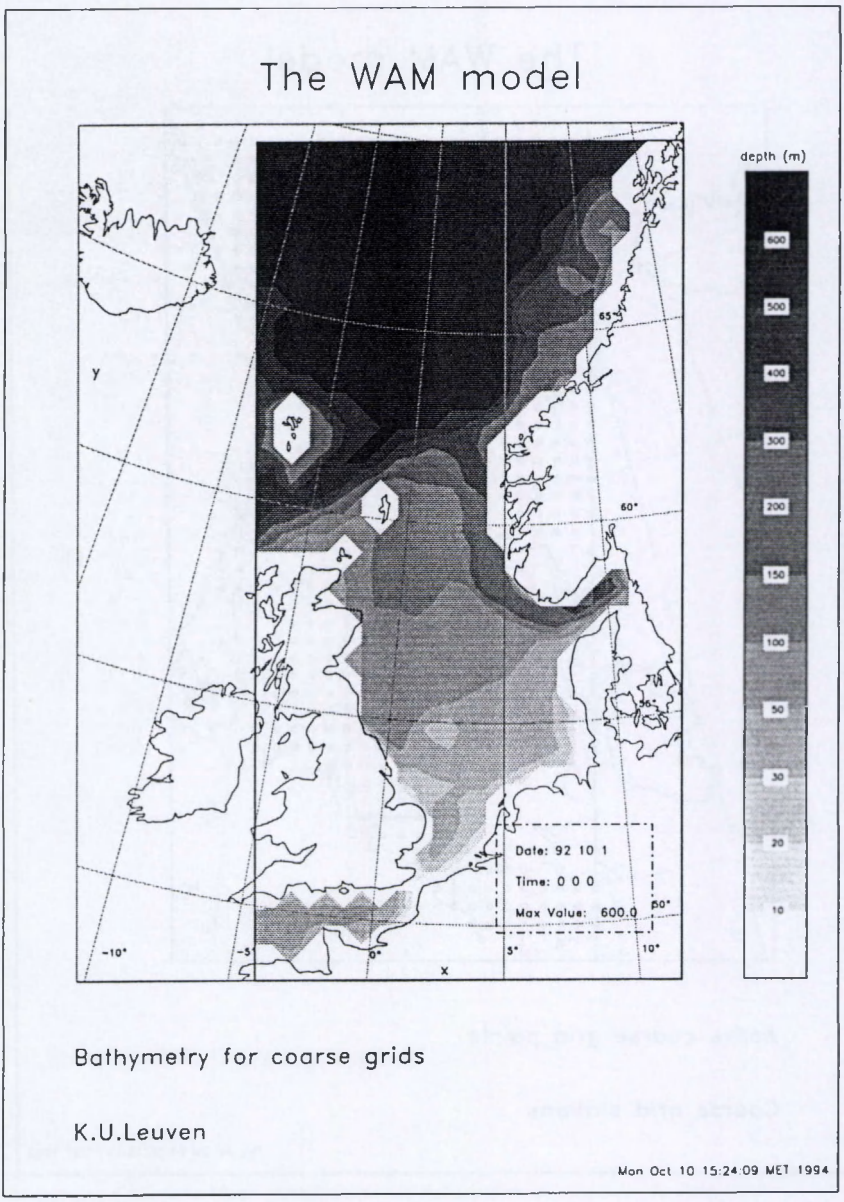

Figure 4.2: The coarse grid bathymetry.

Table 4.1: Coarse grid wave stations locations.

				index		model index	
Station	Code	Latitude	Longitude	i	j	i	j
Platform Auk	auk	56°23'59"N	2°03'56"E	11.39	30.41	11	30
Eierland	eld	53°12'03"N	4°35'18"E	14.44	37.67	14	38
Platform k13	k13	53°13'01"N	3°13'12"E	12.59	37.60	13	38
Meetpost Noordwijk	mpn	52°16'26"N	4°17'46"E	14.02	39.77	14	40
Munitiestort Ijmuiden	ym6	52°33'00"N	4°04'00"E	13.71	39.14	14	39

Table 4.2: Fine grid wave stations locations.

				exact index		output index	
Station	Code	Latitude	Longitude	i	j	i	j
Akkaert	akk	51°24'49"N	2°46'18"E	15.11	9.40	15	9
A2-buoy	a2b	51°21'58"N	3°07'47"E	17.64	10.04	18	10
Europlatform	eur	51°59'55"N	3°16'35"E	18.91	2.85	19	3
Lichteiland Goeree	leg	51°55'05"N	3°40'02"E	21.63	3.84	22	4
Westhinder	weh	51°55'05"N	2°26'30"E	12.74	9.65	13	10

The fine grid

To account for the bathymetric details in the Southern Bight, near the Belgian coast, it was decided to set up a fine grid for this region. The grid consists of 26 x 26 points and it has a spatial resolution of 10 km x 10 km. The definition of a point index (i, j) on the fine grid can be expressed by

$$i = 31.0 + \frac{x_p}{10,000} \tag{4.5}$$

$$j = -399.0 - \frac{y_p}{10,000} \tag{4.6}$$

Figure 4.3 shows the model domain geometry with fine grid active points. The exact locations and indexes of the fine grid wave stations can be found in Table 4.2 (also see Ovidio *et al.*, 1994a). The bathymetry used for all fine grid runs is displayed in figures 4.4.

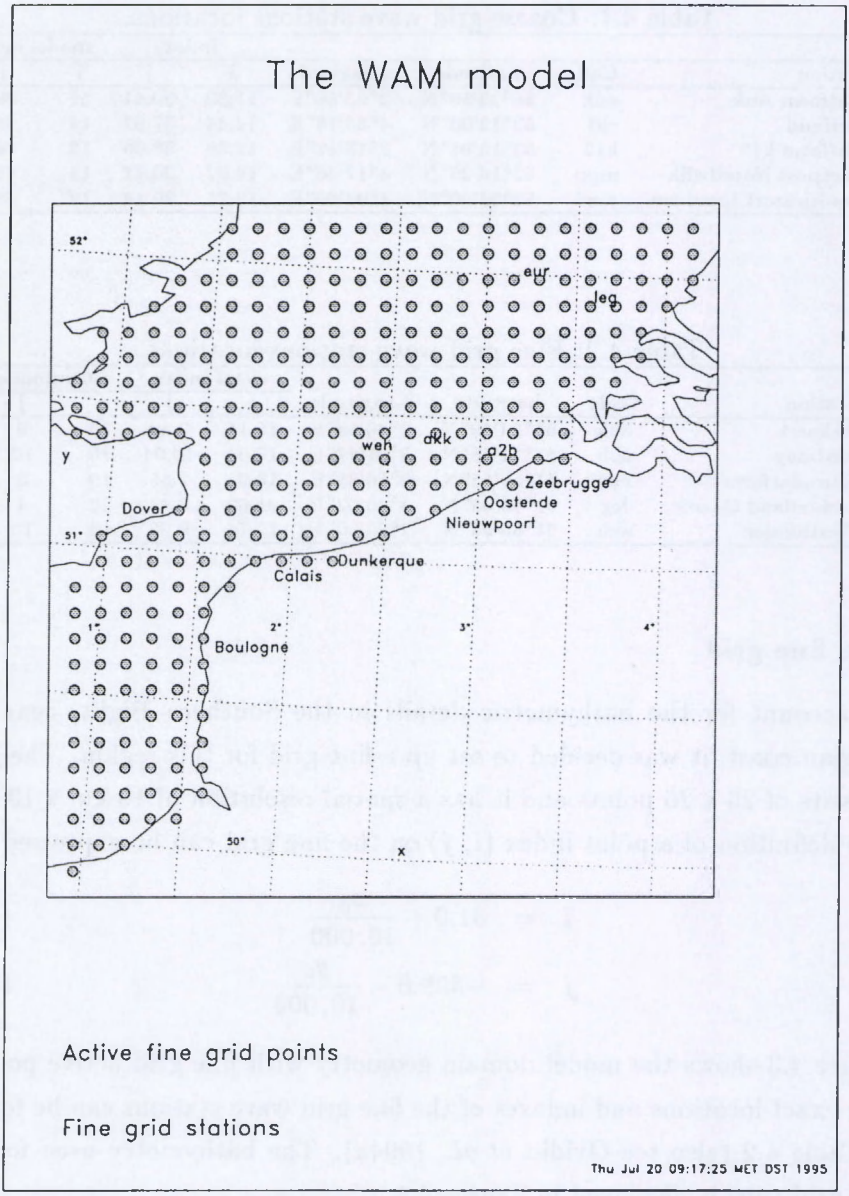

Figure 4.3: The fine grid active points and the buoy locations indicated by the respective three letter symbols in Table 4.2.

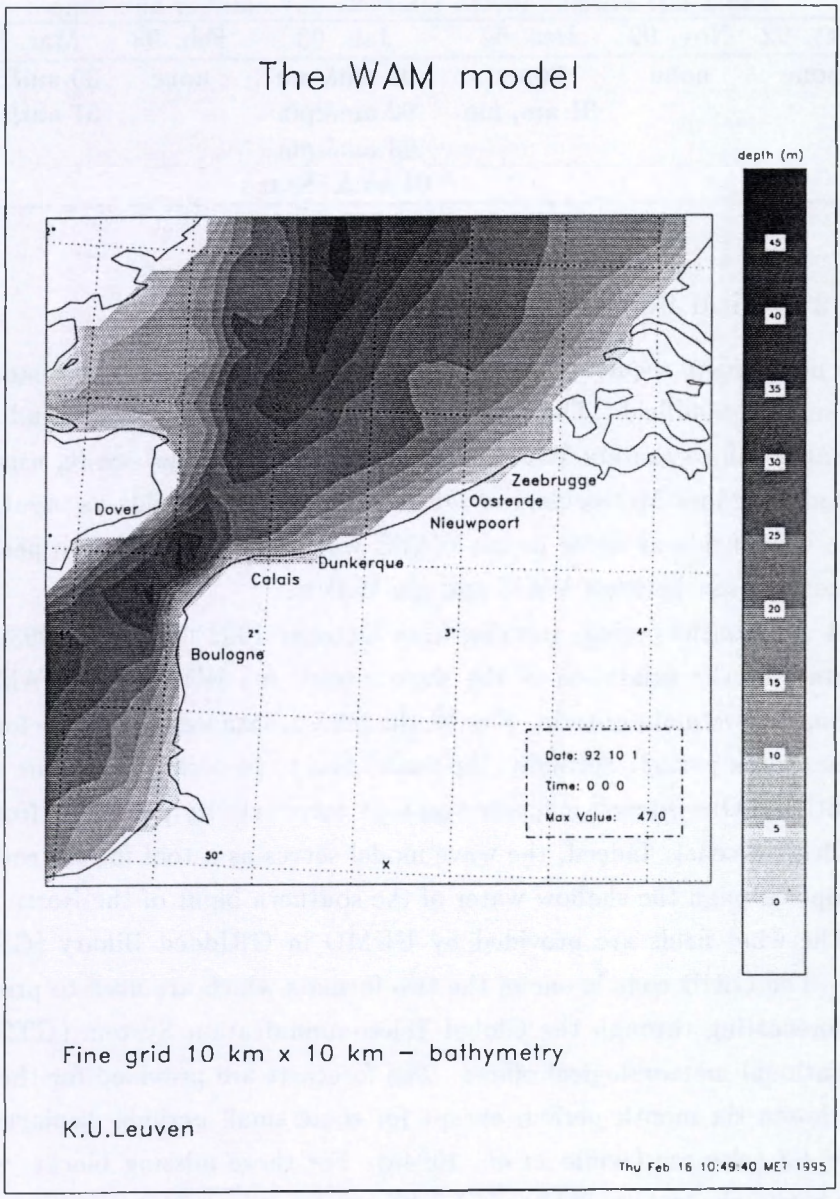

Figure 4.4: The fine grid bathymetry.

Table 4.3: Missing meteo forecast: day number and time.

Oct. 92	Nov. 92	Dec. 92	Jan. 93	Feb. 93	Mar. 93
none	none	30pm	01 am&pm	none	30 am&pm
		31 am, pm	02 am&pm		31 am&pm
			03 am&pm		
			04 am&18pm		

4.4.3 Wind fields

The main input required by the WAM wave model is the time history of the surface windfield. The wave model benefits from the best wind data available. Since the mu-WAVE system, in its operational mode, uses the United Kingdom Meteorological Office (UKMO) wind fields as input, the same wind fields as those in mu-WAVE will be used in order to perform the comparison between WAM and mu-WAVE.

A six months period, running from October 1992 to March 1993, was selected for the validation of the wave models mu-WAVE and WAM according to two main criteria. Firstly, the ERS-1 data were available for the entire chosen period. Secondly, the model had to be tested in various wave conditions. Our interest is focused on high wave activity periods in front of the Belgian coast. Indeed, the wave model serves as a tool for the routing of ships through the shallow water of the southern bight of the North Sea.

The wind fields are provided by UKMO in GRIdded Binary (GRIB) code. The GRIB code is one of the two formats which are used to provide the forecasting through the Global Telecommunication System (GTS) to the national meteorological offices. The forecasts are provided for the entire chosen six month period, except for some small periods displayed in Table 4.3 (also see Ovidio *et al.*, 1994a). For those missing blocks, wind fields set to the last available wind fields are used in order to get a continuous set of data for the whole period. At M.U.M.M., the wind forecast in GRIB code is first decoded, thereafter, the data are bilinearly interpolated

in space to arrive from the data on the geographical grids to the wind fields on the stereographical HYPAS coarse input grid. A small program was made to convert these HYPAS wind input data to the WAM model format (see Appendix B of the internal report by Luo (1995)).

4.5 Hindcast results

4.5.1 Model parameters

The wave activity for the selected six month period is hindcasted by the WAM model. There are two models, i.e., the coarse grid model and the fine grid model. They run separately. For different models, different model parameters are required. The parameters used for the coarse grid and the fine grid runs are displayed in Table 4.4 and 4.5. The model options such as Cartesian coordinates, shallow water, depth refraction, nested grids, etc. are selected. The empirical JONSWAP formulation was used for computation of the bottom dissipation. The detailed user inputs for the coarse grid and the fine grid runs can be found in Appendix C and D respectively of the internal report by Luo (1995).

4.5.2 Global grid results

The hindcast for the coarse grid domain was made month by month for the entire selected period. The predicted significant wave heights for the whole domain are printed every six hours for the whole period. The time series of the significant wave height, the mean period, the mean frequency and the mean wave direction are outputted for each month and at every buoy station (this part of results will be shown in section 4.7 together with the comparison between the model prediction and the buoy data).

Figure 4.5 shows the significant wave height mean difference between mu-WAVE and the WAM for the whole six months. Superimposed are the mean forcing wind vectors (only one out of two are plotted for clarity). One sees that a relatively good agreement exists in the North Sea, the difference

Table 4.4: Model parameters used for the coarse grid model.

Symbol	Value	Meaning
DEPTHA	5.	Minimum water depth for shallow water tables
NANG	12	Number of angles
NBINP	1	Number of boundary points from the previous run
NBLC	1	Equal to NBLO with current refraction, otherwise, take 1
NBLD	3	Equal to NBLO with depth refraction, otherwise take 1
NBLO	3	Number of blocks
NBMAX	142	Maximum number of boundary points (=2(NGX+NGY)*2-4)
NDEPTH	54	Length of shallow water tables
NFRE	25	Number of frequencies
NGX	25	Number of longitudes in grid
NGY	48	Number of latitudes in grid
NIBLC	1	Equal to NIBLO with current refraction, otherwise, take 1
NIBLO	512	Number of points in block
NIBL1	512	Equal to NIBLO for multiblock case, otherwise, take 1
NMAXC	60	Number of boundary points for coarse grid, otherwise, take 1
NMAXF	1	Number of boundary points for fine grid, otherwise, take 1
MOUTP	100	Maximum number of output places or stations
MOUTT	130	Maximum number of output times
NOVER	23	Maximum number points in first latitude of blocks

Table 4.5: Model parameters used for the fine grid run.

Symbol	Value	Meaning
DEPTHA	5.	Minimum water depth for shallow water tables
NANG	12	Number of angles
NBINP	7	Number of boundary points from the previous run
NBLC	1	Equal to NBLO with current refraction, otherwise, take 1
NBLD	2	Equal to NBLO with depth refraction, otherwise take 1
NBLO	2	Number of blocks
NBMAX	100	Maximum number of boundary points (=2(NGX+NGY)*2-4)
NDEPTH	54	Length of shallow water tables
NFRE	25	Number of frequencies
NGX	26	Number of longitudes in grid
NGY	26	Number of latitudes in grid
NIBLC	1	Equal to NIBLO with current refraction, otherwise, take 1
NIBLO	304	Number of points in block
NIBL1	304	Equal to NIBLO for multiblock case, otherwise, take 1
NMAXC	1	Number of boundary points for coarse grid, otherwise, take 1
NMAXF	35	Number of boundary points for fine grid, otherwise, take 1
MOUTP	20	Maximum number of output places or stations
MOUTT	160	Maximum number of output times
NOVER	21	Maximum number points in first latitude of blocks

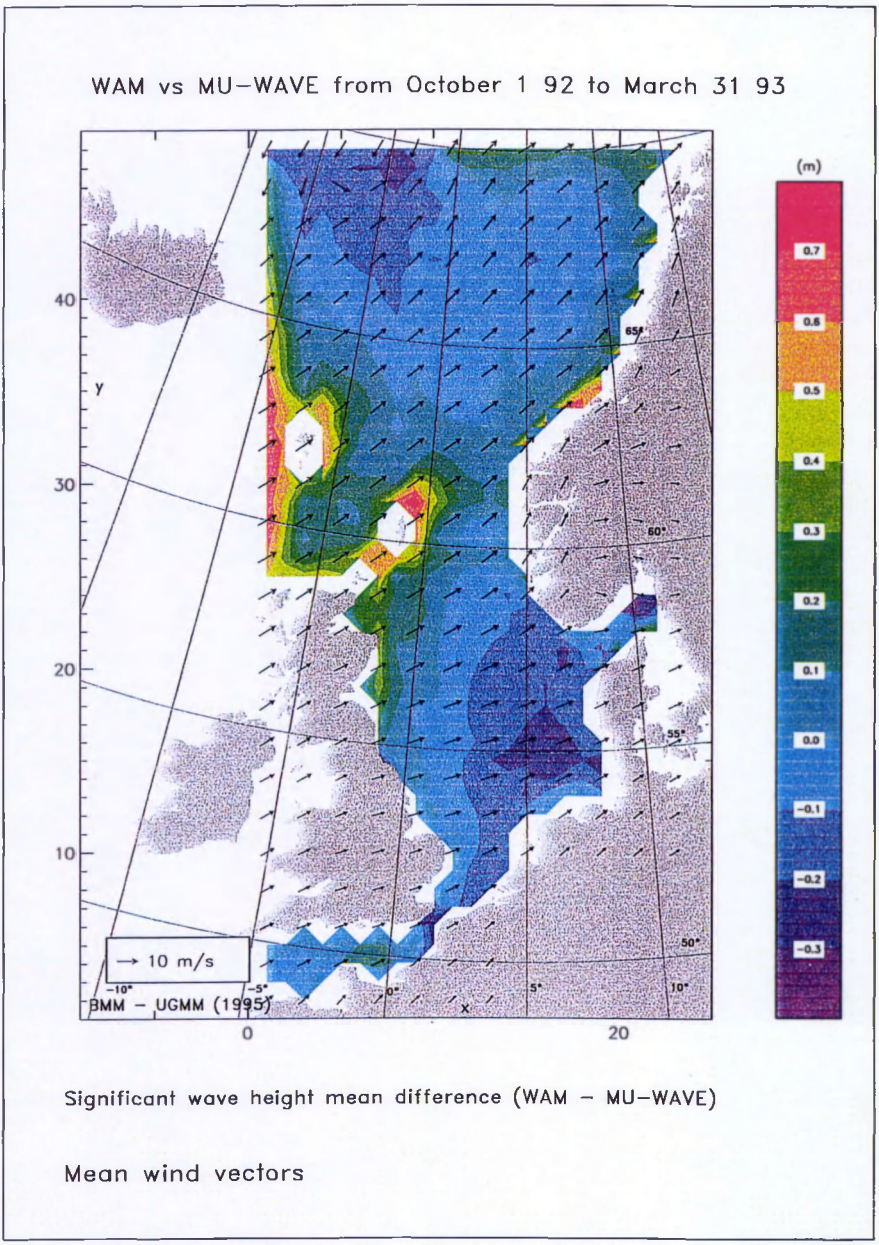

Figure 4.5: The significant wave height mean difference between WAM and mu-WAVE (WAM *minus* mu-WAVE) for the entire study period. The wind vectors averaged over the same time span is presented as well.

is less than 0.1 m for the prediction of the significant wave height. In the southern North Sea, mu-WAVE predicts a slightly larger (in the order of 0.2 m) significant wave height than WAM. However, there is a relatively large disparity at the open boundary of the model domain as well as at some physical boundaries. Although both models apply limited fetch laws at these open boundaries, the implementation of these conditions may result in a quite different local behaviour.

To show an example of a global grid hindcast result, a two-days window from October 6 at 6h GMT to October 8 at 0h GMT were selected. Figures 4.6 to 4.13 present the wind wave evolution and development for these two days. One can see that during this period a frequent strong north-easterly wind blew over the southern part of the North Sea. A very fast build-up of high wave activity (about 3.5 m for the significant wave height), which is bound to propagate into the model domain, can be found in front of the Belgian and Dutch coasts with an important fetch for more than one day from October 6 at 6h GMT to October 7 at 0h GMT (see figures 4.6-4.9). Afterwards, the wave activity gradually decreased from October 7 at 6h GMT to October 8 at 0h GMT when the wind calmed down (see figures 4.10-4.13). The northern part of the domain, for this period, had the prevailing westerly winds, and a very strong wave activity appeared along the Norwegian coast. Figures 4.7, 4.8, 4.9, 4.11, 4.12, 4.13 also show the satellite tracks (heavy solid line) crossing the model domain during this period. The comparison between the model and the satellite data for these tracks will be discussed in the next section.

4.6 Validation by use of satellite data

Even before satellite wave data became available on a quasi-operational basis, the recognized potential of these data had a strong influence on wave modelling. One of the principal motivations for developing the third generation wave model WAM was to provide a state-of-the-art model for the assimilation of global wind and wave data from satellites for improved

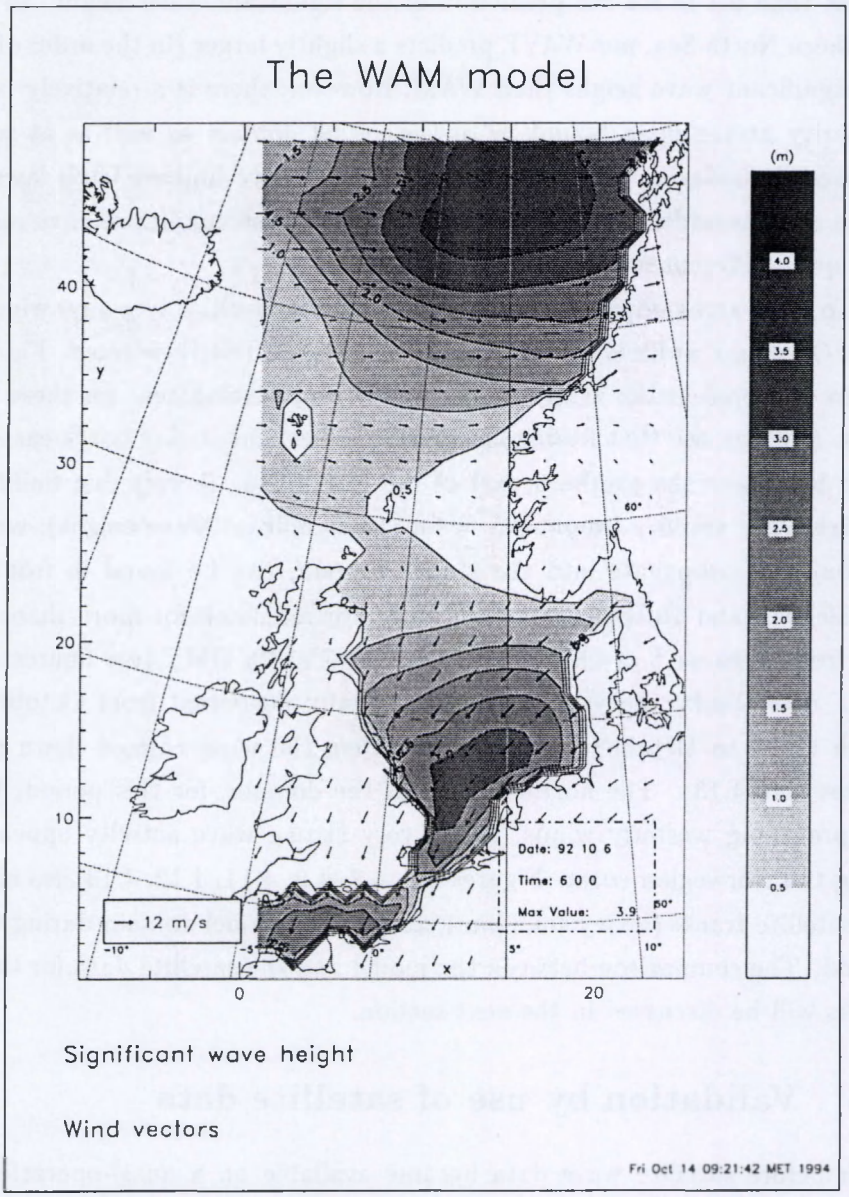

Figure 4.6: The predicted significant wave height for the coarse grid domain for October 6 at 6h GMT. The wind vectors used to force the wave model are presented as well. No satellite track crossed the model domain for that time.

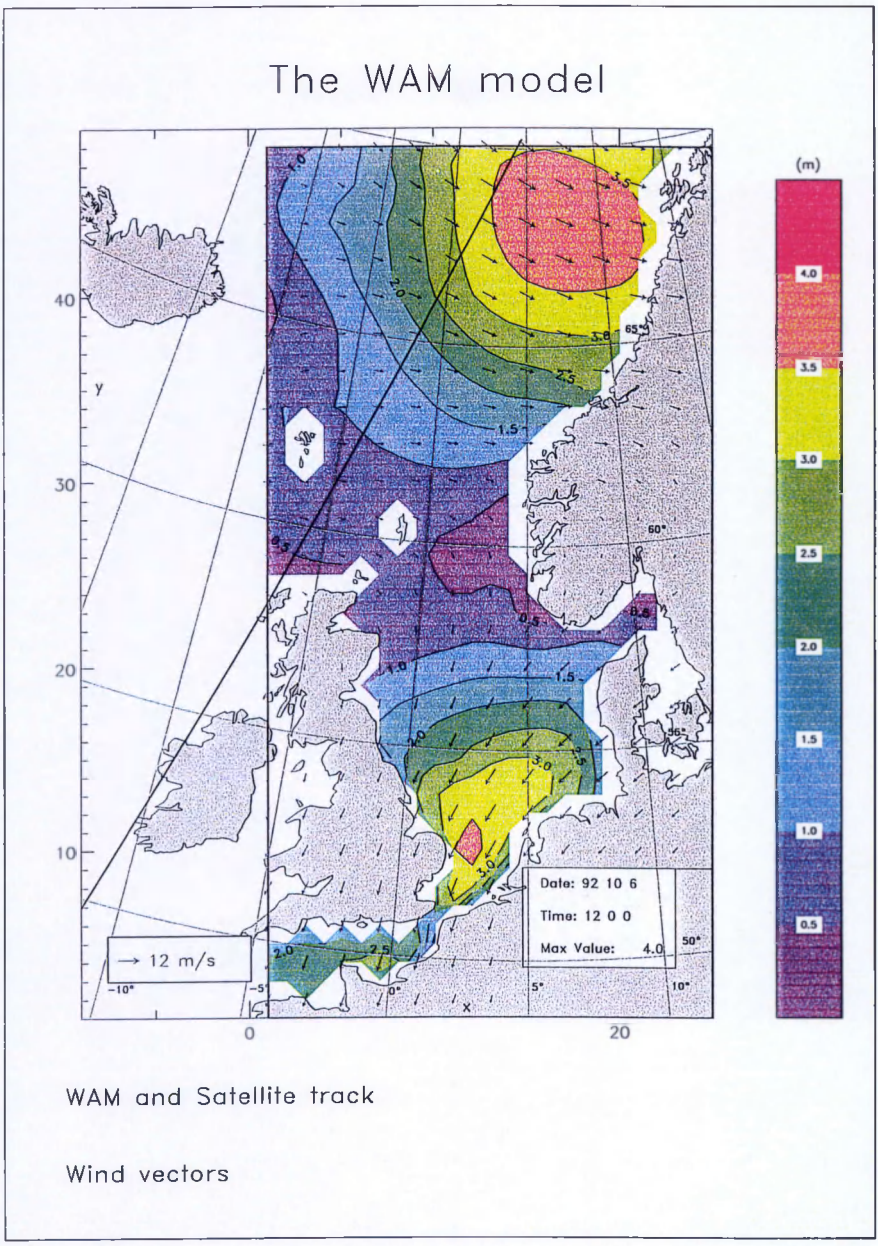

Figure 4.7: The predicted significant wave height for the coarse grid domain for October 6 at 12h GMT. The wind vectors used to force the wave model are presented as well. Also shown is the ERS-1 ground track that crossed the domain a few minutes before that time.

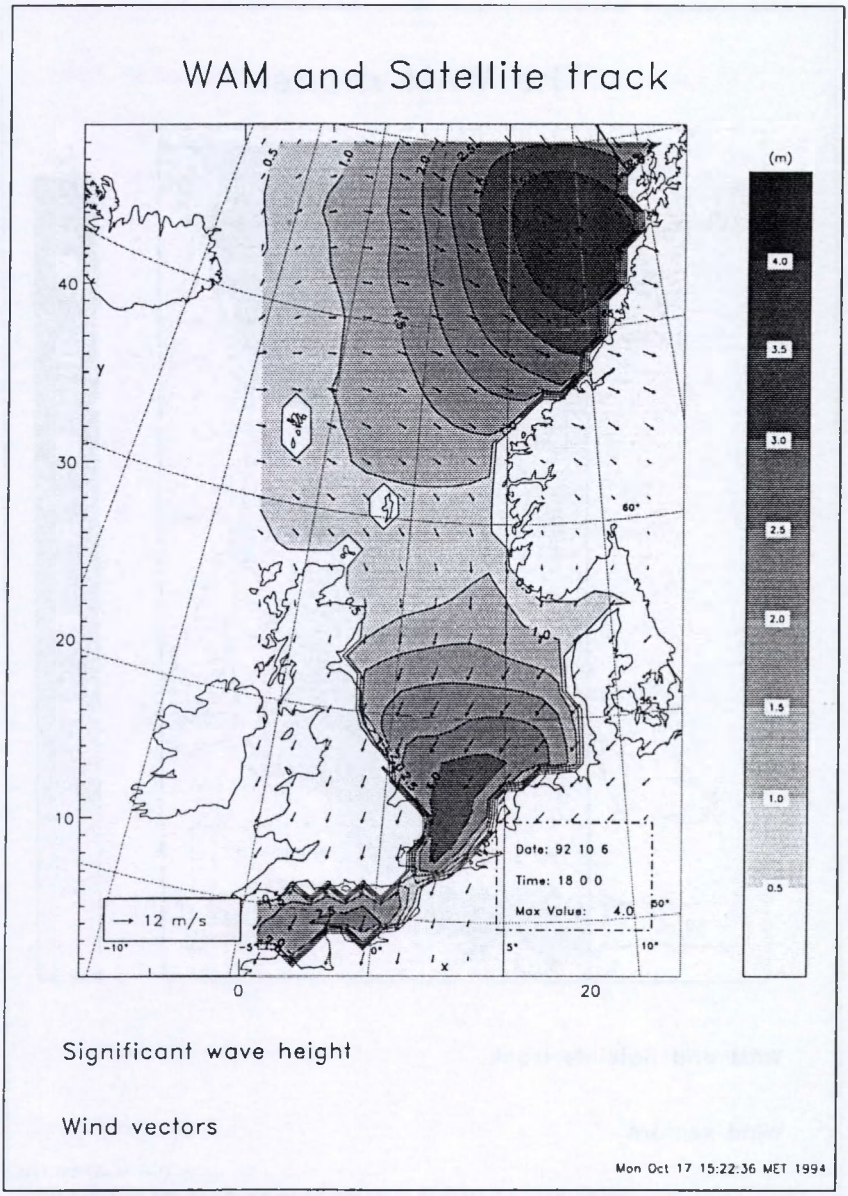

Figure 4.8: The predicted significant wave height for the coarse grid domain for October 6 at 18h GMT. The wind vectors used to force the wave model are presented as well. Also shown is the ERS-1 ground track that crossed the model domain 2 hours later than that time. This track is not analyzed.

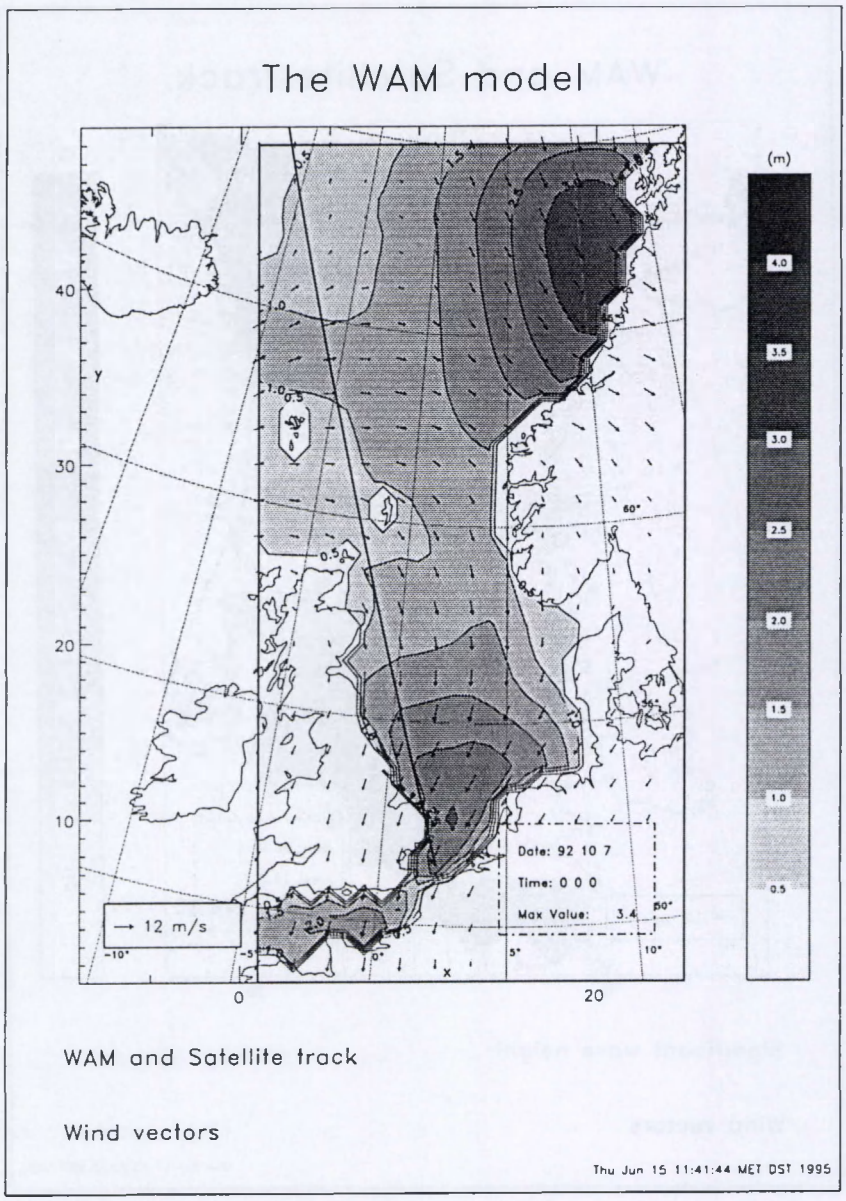

Figure 4.9: The predicted significant wave height for the coarse grid domain for October 7 at 0h GMT. The wind vectors used to force the wave model are also presented. Also shown is the ERS-1 ground track that crossed the domain 2 hours earlier than that time.

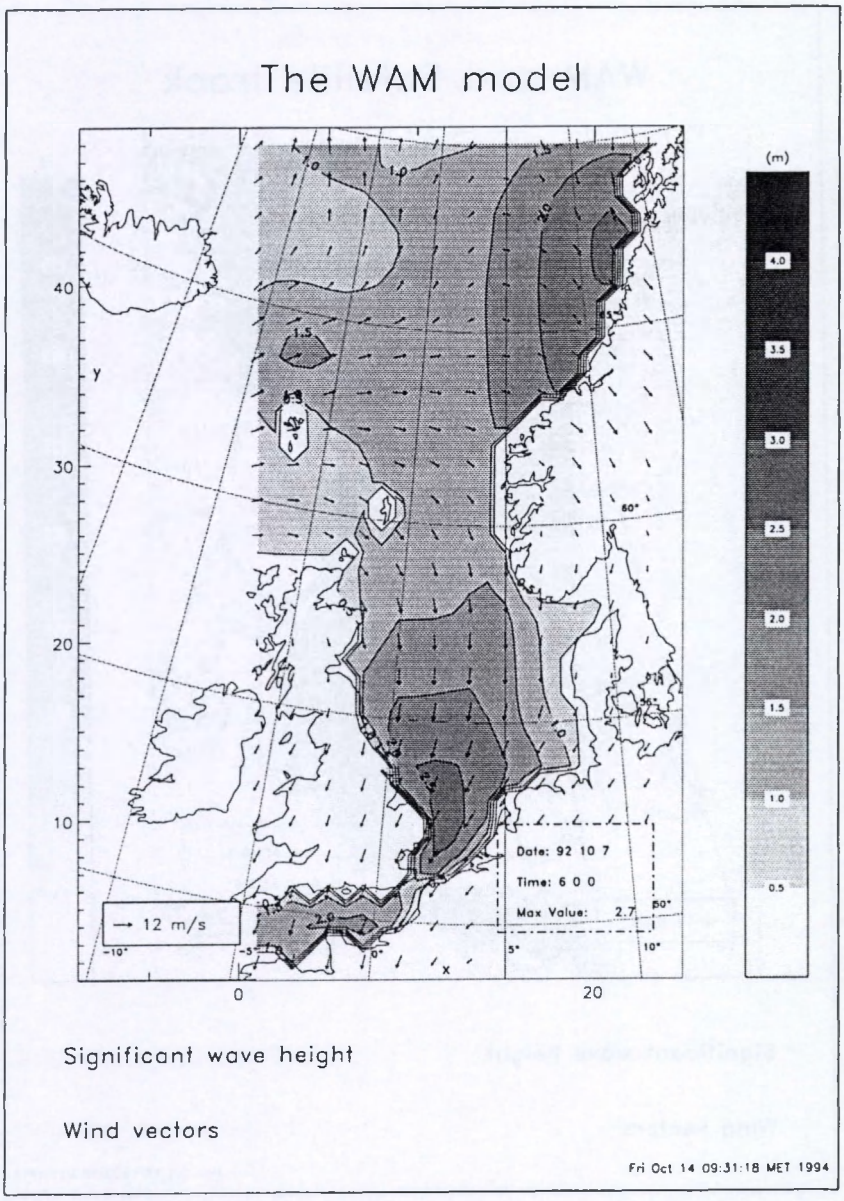

Figure 4.10: The predicted significant wave height for the coarse grid domain for October 7 at 6h GMT. The wind vectors used to force the wave model are presented as well. No satellite track crossed the domain during that time.

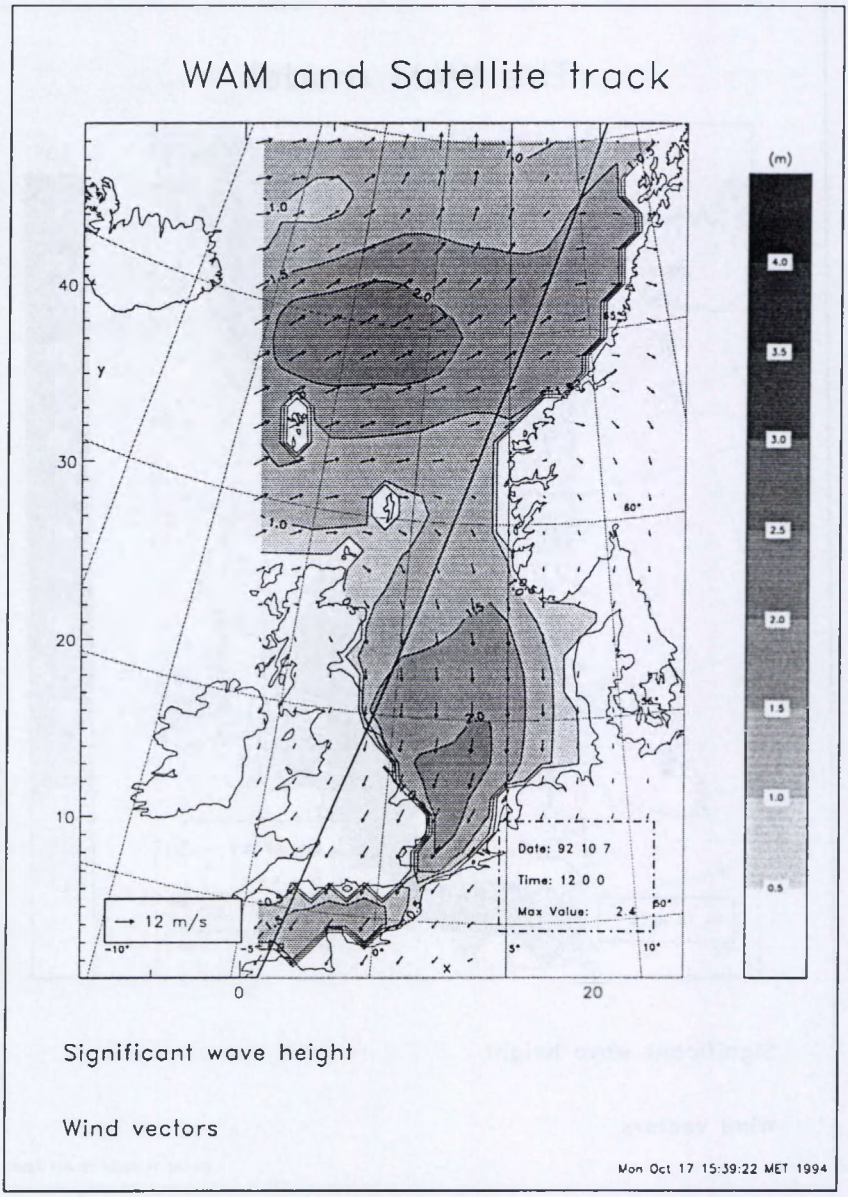

Figure 4.11: The predicted significant wave height for the coarse grid domain for October 7 at 12h GMT. The wind vectors used to force the wave model are also presented. Also shown is the ERS-1 ground track that crossed the domain half an hour earlier than that time.

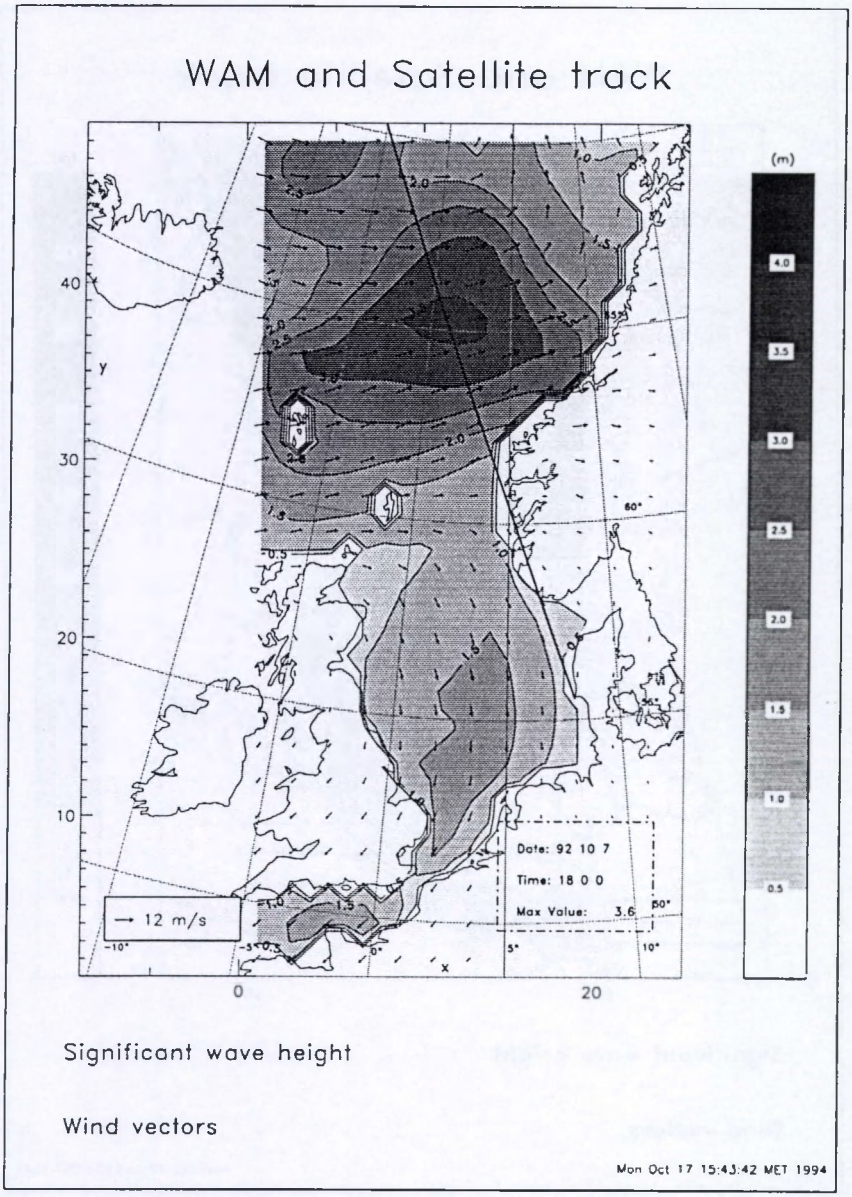

Figure 4.12: The predicted significant wave height for the coarse grid domain for October 7 at 18h GMT. The wind vectors used to force the wave model are also presented. Also shown is the ERS-1 ground track that crossed the domain 3 hours later than that time.

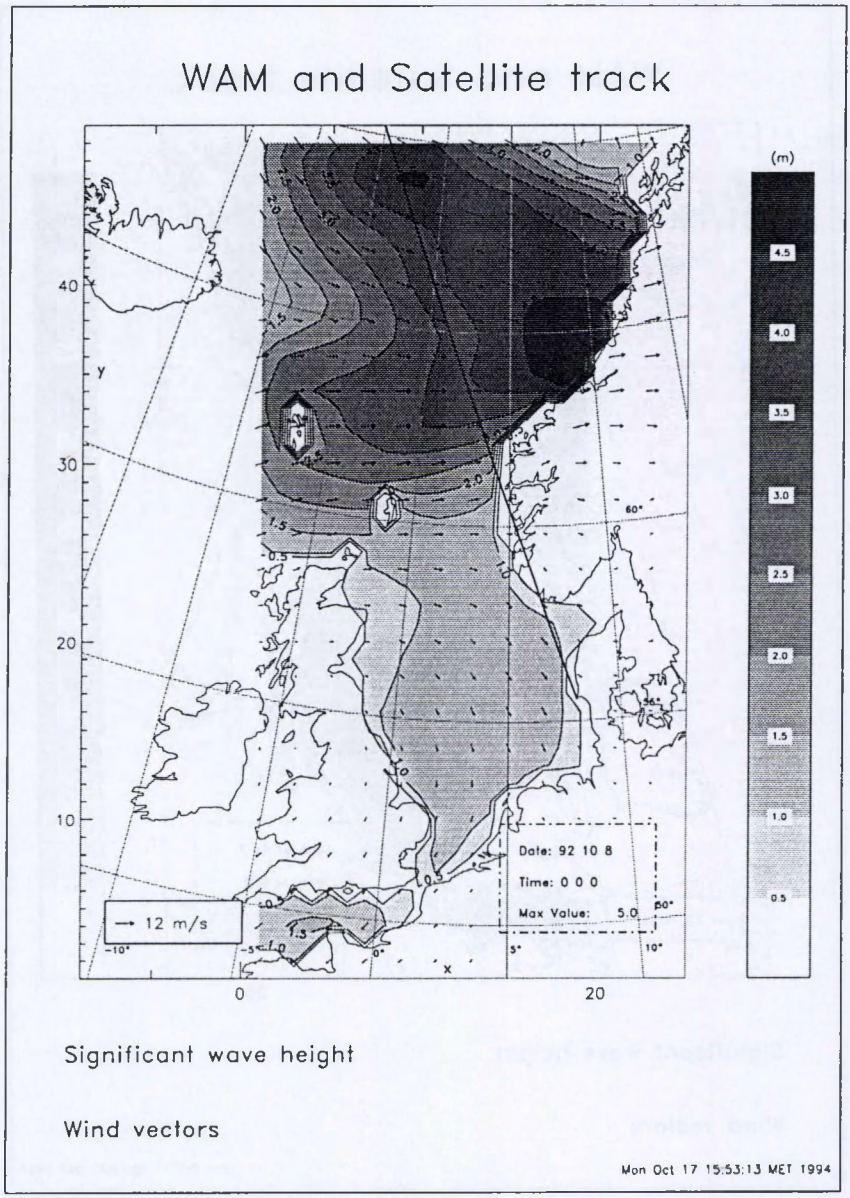

Figure 4.13: The predicted significant wave height for the coarse grid domain for October 8 at 0h GMT. The wind vectors used to force the wave model are also presented. Also shown is the ERS-1 ground track that crossed the domain 3 hours earlier than that time.

wind and wave field analysis and forecasting. Through the launch of ocean observing satellites, wave modellers are now for the first time receiving detailed wave data on a global, continuous basis. This can be expected to have a profound impact on wave modelling. Research work on the analysis and assimilation of satellite wave data was first stimulated by the availability of SEASAT and GEOSAT off-line altimeter data, and has received a major impetus since the provision of near-real-time ERS-1 data. In the following a short description of the ERS-1 will be given, the validation of the WAM model using the ERS-1 wave data and the cross comparison with mu-WAVE for the coarse grid model domain will be presented (also see Ovidio *et al.*, 1994b).

4.6.1 ERS-1 general description

The first European Remote Sensing Satellite (ERS-1) was launched by the European Space Agency (ESA) on July 17, 1991. It is the first of a series of satellites entirely devoted to remote sensing from a polar orbit. Its instruments allow for the determination of many relevant oceanic parameters (for a complete list see ERS-1 User Handbook, 1991). In our study we are only interested in those instruments whose sensors can provide information about the sea state and/or surface wind forcing. These are the radar altimeter, the wind scatterometer and the Synthetic Aperture Radar (SAR) functioning in wave mode. These data were requested from ESA, but only the altimeter and scatterometer data have been obtained in a type called *fast delivery product copy*, in which a minimal number of calibrations and corrections of the data are performed by the ESA ground stations. These data are extracted by M.U.M.M. in the framework of the ESA ERS-1 Pilot Project PP2-B9. Figure 4.14 shows the ERS-1 satellite ground track density for the 35-day cycle (also see Ovidio *et al.*, 1994a), as extracted from the global data set for a geographical box that extends from 15° to 19°E longitude and from 48°N to 75°N latitude. The WAM model domain lies in the rectangular box (heavy solid lines). Our current validation exercise will be performed with the radar altimeter. The validation of the UKMO

wind model by comparison with the scatterometer data has been carried out by M.U.M.M. in the above mentioned project, the results can be found in Ovidio *et al.* (1994a).

The radar altimeter provides a measure of the significant wave height through the distortion of the mean shape of the return pulse. The earlier return from the wave crests and the retarded return from the wave troughs leads to a broadening of the return pulse which can be directly related to the significant wave height. To determine the mean pulse shape, several hundreds pulses need to be averaged, yielding one significant wave height measurement about every 7 km along the satellite track. For a Gaussian sea surface, the relation between the pulse shape and the rms sea surface displacement can be computed theoretically. The typical accuracy of ERS-1 radar altimeter significant wave height measurements is of the order of 0.5m or 10% for wave heights between 1 and 20 m, whichever is greater. The radar altimeter also provides useful information on the wind speed, which can be determined from the power σ_o of the return pulse. For moderate winds (3 to 12 ms^{-1}) the wind speed can be measured from the radar altimeter with an accuracy of about ± 2 ms^{-1} (ERS-1 User Handbook, 1991).

4.6.2 Global grid comparison

The global wave height mean differences between the altimeter observations and the WAM outputs for the entire study period are displayed in figure 4.15. Also shown in the figure are the mean wind vectors for the whole period. From the figure it can be found that there exists a relatively good agreement in the North Sea region (within 0.5 m difference) and in particular in the southern North Sea region (within 0.25 m difference). However, at the northern open sea boundary, one sees a big underestimation from the model, the difference is of the order of 1 m. At the western open sea boundary in the northern part of the domain, a very strong discrepancy is visible, and the model underpredicts the significant wave height in the order of 1.25 m as compared to the satellite observations. This serious underpre-

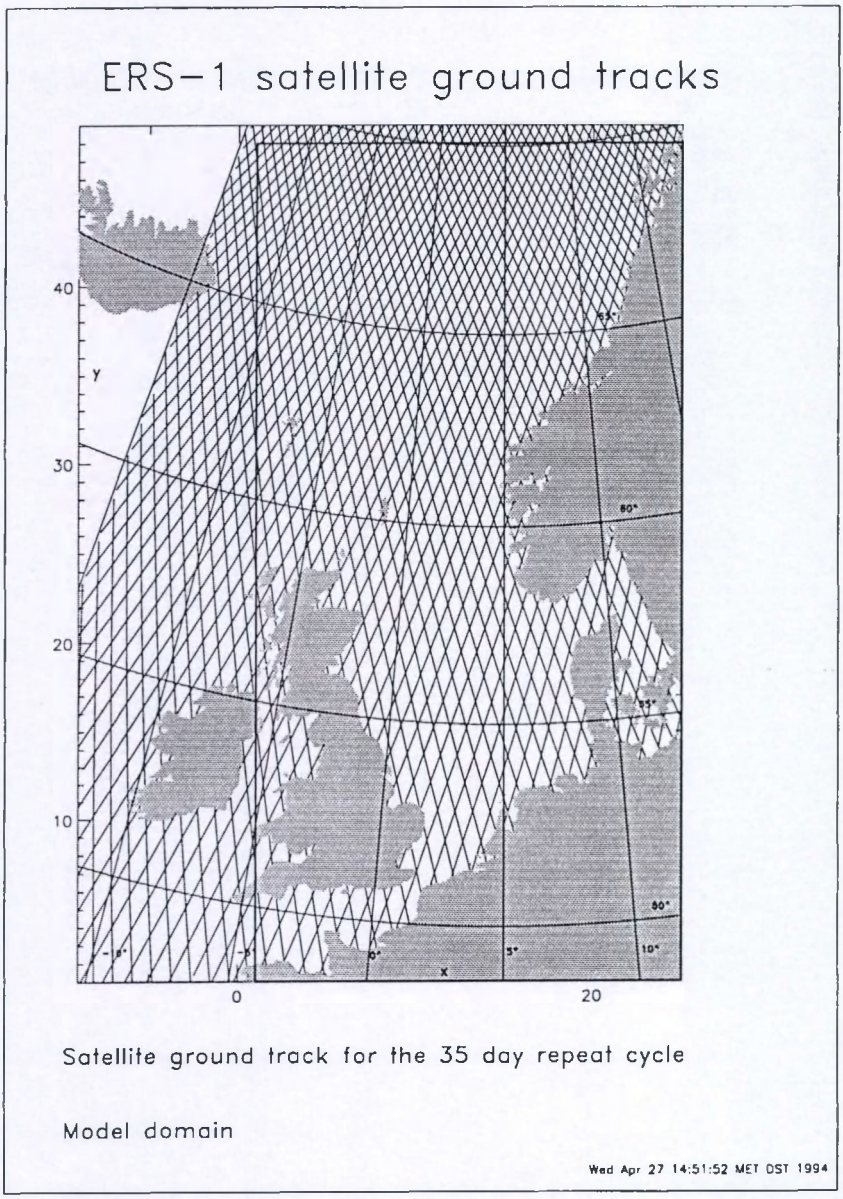

Figure 4.14: ERS-1 satellite ground track density for the 35-day repeat cycle.

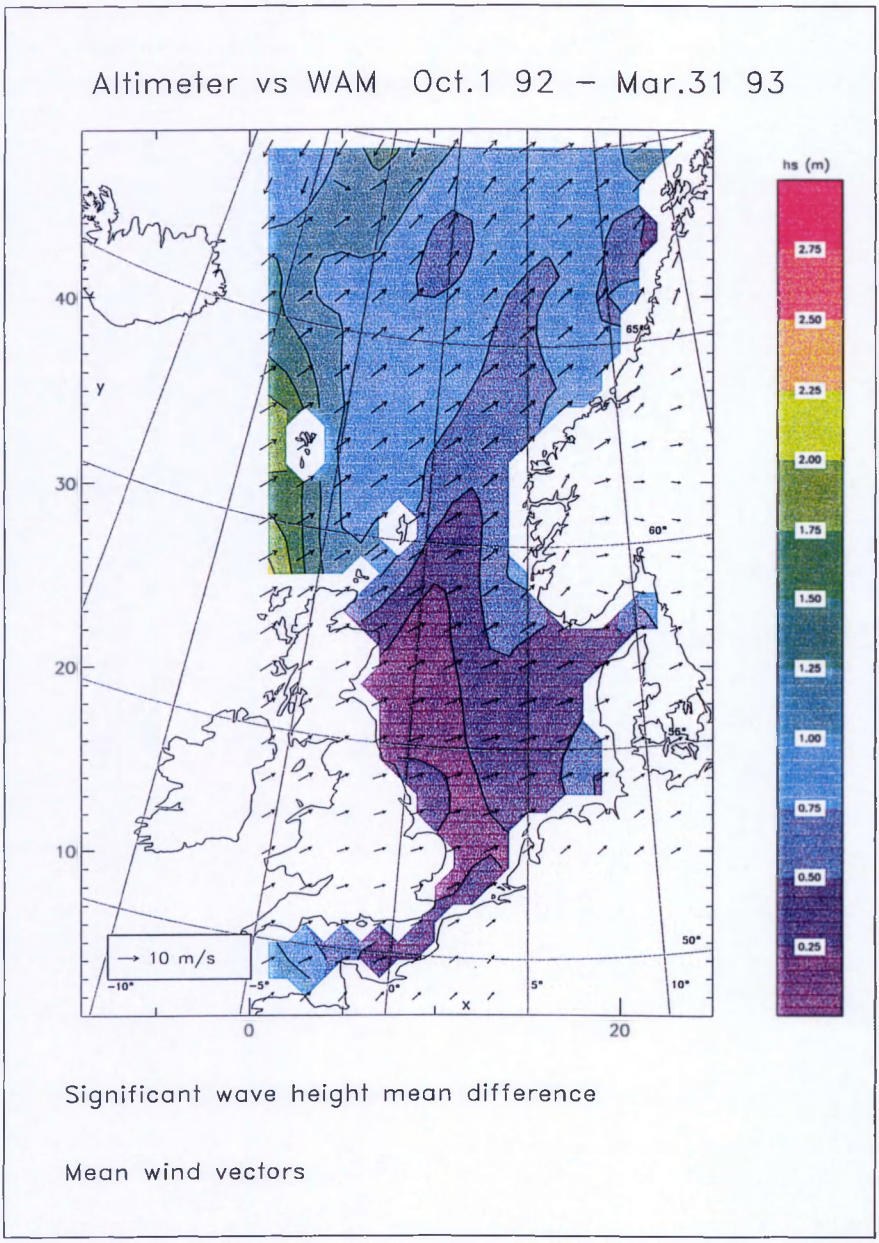

Figure 4.15: The significant wave height mean difference between the altimeter observations and the WAM results (altimeter *minus* WAM) for the entire study period. The wind vectors averaged over the same time span is presented as well.

diction decreases rapidly eastward. In the whole North Atlantic region, the model underestimates the significant wave height with about 0.75 m. This northern zone is often under the influence of large low pressure fields or storms, and swell energy packets created there may travel down to the southern Bight or to the Belgian coast. Therefore the underprediction in the northern zone may influence the predicted results along the Belgian coast. The reason for the underestimation at the open sea boundary is due to the fact that in the WAM model, open boundaries are treated as walls, where the fetch limited law is applied. Therefore, the energy generated outside the model domain cannot propagate inside the domain, is missed by the model. In fact, the use of the closed boundaries is unrealistic. An energy forcing scheme to simulate the propagation of the North Atlantic swells into the model may improve the model prediction results. Alternatively the implementation of the global wave model results forecasted in ECMWF into the coarse grid open boundaries may be an other solution to this problem (see Ovidio *et al.*, 1995a,b).

4.6.3 Statistical analysis

To verify the reliability of the predictions of the WAM model, a statistical analysis is essential. It provides the background information for judging the performance of the hindcast of the model.

Statistical parameters

The statistics formulations used for the present analysis are taken from Zambresky (1989) and Romeiser (1993). The parameters used and their definitions are described as follows. Note that the X_i represents the observed values, while the Y_i are values from the model. The number of observed and computed values is denoted by N.

- **Mean**

$$\overline{X} = \frac{1}{N}\Sigma X_i \tag{4.7}$$

- **Bias**: the difference between the mean of the observations and the mean of the model results.

$$\text{Bias} = \overline{X} - \overline{Y} \tag{4.8}$$

- **RMSE**: root-mean-square error, it is the root of the squared error between the observations and the model results.

$$RMSE = \sqrt{\frac{1}{N}\Sigma(Y_i - X_i)^2} \tag{4.9}$$

- **RMSE$_s$**: systematic root-mean-square error, it is the systematic part of the root-mean- square error, i.e., the root of the squared difference between the least squares regression line through the modelled results and the ideal regression line $\hat{Y}_i = X_i$.

$$RMSE_s = \sqrt{\frac{1}{N}\Sigma(\hat{Y}_i - X_i)^2} \tag{4.10}$$

where the $\hat{Y}_i$ is defined in terms of the slop and the intercept of the least squares regression line.

$$\hat{Y}_i = mX_i + b \tag{4.11}$$

$$m = \frac{N\Sigma X_i Y_i - \Sigma X_i \Sigma Y_i}{N\Sigma X_i^2 - (\Sigma X_i)^2} \tag{4.12}$$

$$b = \overline{Y} - m\overline{X} \tag{4.13}$$

- **RMSE$_u$**: unsystematic root-mean-square error, it is the unsystematic part of the RMSE or the scatter of the model results around the least squares regression line, i.e., the root of the squared difference between the actual model results and the least squares regression line.

$$RMSE_u = \sqrt{\frac{1}{N}\Sigma(Y_i - \hat{Y}_i)^2} \tag{4.14}$$

- **Correlation coefficient**

$$r = \frac{\Sigma(X_i - \overline{X})(Y_i - \overline{Y})}{\sqrt{\Sigma(X_i - \overline{X})^2 \Sigma(Y_i - \overline{Y})^2}} \tag{4.15}$$

Table 4.6: Regions limits

Region	y min	y max
Channel	1	6
North Sea	7	24
North Atlantic	25	48

- **S.I.**: scatter index, it is the ratio of the RMSE and the square root of the product of the mean of the model and the mean of the observation.

$$S.I. = \frac{RMSE}{\sqrt{\overline{XY}}} \tag{4.16}$$

Remark that from all the parameters listed above, the bias, the RMSE and the S.I. are the most frequently used.

Statistical results

From the previous section, it is clear that the performances of the model are rather different between the different parts of the domain. We have divided the coarse grid domain into three regions, denoted by CHANNEL, NORTH SEA and NORTH ATLANTIC regions according to the y coordinate of the model grid. The detailed definition of these regions can be found in Table 4.6. Note that the y coordinate at the most northern boundary is 48, and the y value at the most southern boundary is 1. The statistical analysis of the significant wave height and the wind speed between the altimeter and the model is presented in Table 4.7 for different regions. Also shown is the cross comparison between WAM and mu-WAVE. The positive bias between the altimeter observations and the model predictions indicates an underestimation of the H_s value by the model.

One easily sees that the WAM model produces better results than mu-WAVE for the whole domain, for the North Atlantic region and for the channel region. Both models underestimate the significant wave height for the whole domain, especially in the North Atlantic (open sea) region,

Table 4.7: Statistical analysis for the significant wave height H_s (m) and the wind speed U (ms^{-1}) between the altimeter and models.

		H_s(WAM)			H_s(mu- WAVE)			U		
		Bias	S.I.	RMSE	Bias	S.I.	RMSE	Bias	S.I.	RMSE
Whole	Oct.	0.81	0.49	0.98	0.69	0.47	0.97	0.40	0.23	1.83
	Nov.	0.74	0.39	1.03	0.72	0.40	1.04	0.81	0.23	2.16
	Dec.	0.93	0.41	1.29	0.98	0.44	1.38	1.14	0.25	2.47
	Jan.	0.59	0.30	1.17	0.89	0.38	1.44	1.10	0.20	2.52
	Feb.	0.73	0.32	1.00	0.78	0.38	1.17	0.72	0.20	2.16
	Mar.	0.74	0.37	1.00	0.65	0.40	1.10	0.57	0.21	2.05
	6 m	0.77	0.38	1.08	0.78	0.41	1.18	0.78	0.22	2.20
Channel	Oct.	0.70	0.56	0.87	0.72	0.53	0.81	0.65	0.20	1.70
	Nov.	0.77	0.51	1.00	1.00	0.66	1.20	0.33	0.16	1.63
	Dec.	0.87	0.72	0.94	0.83	0.67	0.90	1.36	0.30	2.21
	Jan.	0.60	0.33	0.70	0.84	0.47	0.93	-0.28	0.19	1.72
	Feb.	0.74	0.78	0.80	0.60	0.59	0.66	0.85	0.24	1.57
	Mar.	0.76	0.95	0.85	0.59	0.72	0.73	-0.16	0.18	1.01
	6 m	0.74	0.58	0.87	0.77	0.60	0.90	0.46	0.21	1.71
North Sea	Oct.	0.63	0.42	0.68	0.48	0.35	0.60	0.23	0.18	1.30
	Nov.	0.33	0.26	0.55	0.30	0.27	0.57	0.25	0.16	1.43
	Dec.	0.47	0.32	0.57	0.36	0.27	0.51	0.69	0.24	1.95
	Jan.	-0.32	0.22	0.75	-0.10	0.17	0.54	-0.14	0.13	1.76
	Feb.	0.31	0.26	0.57	0.32	0.30	0.66	0.19	0.20	1.80
	Mar.	0.28	0.25	0.49	0.10	0.23	0.48	-0.43	0.17	1.45
	6 m	0.31	0.28	0.61	0.27	0.26	0.57	0.15	0.18	1.62
North Atlantic	Oct.	0.86	0.50	1.04	0.74	0.48	1.04	0.44	0.24	1.95
	Nov.	0.85	0.41	1.12	0.82	0.41	1.13	0.97	0.25	2.33
	Dec.	1.04	0.41	1.41	1.13	0.44	1.52	1.24	0.24	2.58
	Jan.	0.82	0.30	1.26	1.14	0.40	1.60	1.47	0.21	2.70
	Feb.	0.83	0.32	1.08	0.90	0.38	1.26	0.85	0.20	2.25
	Mar.	0.84	0.37	1.09	0.77	0.40	1.20	0.80	0.21	2.17
	6 m	0.83	0.38	1.22	0.91	0.42	1.29	0.94	0.23	2.33

with biases of the order of 0.83m for WAM and 0.91 m for mu-WAVE. A very large scatter index (about 60%) can be found in the channel region. However, a much better agreement between the altimeter and models is obtained in the North Sea region, with a bias of the order of 0.31 m and a scatter index of the order of 28% for WAM, and with a bias of the order of 0.27 m and a scatter index of the order of 26% for mu-WAVE. For the North Sea region, mu-WAVE gives a bit better results than WAM. To give a more visual view of the agreement between the observation and the model, a scatter diagram is shown in figure 4.16 for WAM in the North Sea region. One sees that the worst predictions occur mostly at relatively low wave height (< 2 m).

It is also interesting to see that the wind speed is underestimated by the model (UKMO) as compared to the altimeter wind data, mainly in the North Atlantic region and particularly in the winter period. The predictions of the wind speed in the North Sea are quite good. The scatter index (about 20%) and the root-mean-square error (about 2 ms^{-1}) show that the UKMO winds are of good quality. However, the comparison of the scatterometer wind speed with the one from the UKMO model showed that the wind speed was overestimated by the UKMO model (see Ovidio *et al.*, 1994a), the confirmation of the reliability of the satellite data needs a cross validation of these remotely sensed measurements with buoy data (see section 4.7.3).

4.6.4 Track comparison

To give a clearer picture (than statistical analysis) of the comparison between the satellite data and the model predictions, the coarse grid model results are compared to the satellite observations for a selected set of satellite sub-tracks.

The first sub-track selected is shown in figure 4.7, the dark solid line stretching from the northern open boundary to the south-western part of Ireland. The cross-comparison of the significant wave height between WAM, mu-WAVE and the altimeter for this sub-track is displayed in figure

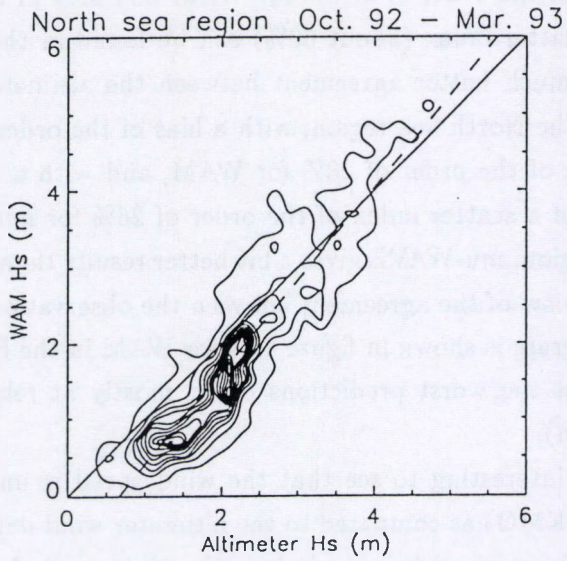

Figure 4.16: Scatter diagram for significant wave height.

4.17a. The comparison shows that there exists a relatively big difference for the significant wave height between the satellite observations and the models' predictions near the open boundaries. A better agreement is obtained in the interior of the domain. The wind observations (in figure 4.17b) from the altimeter contain much variability, and the model winds are much smoother than the observations.

The second ground track shown in figure 4.9 cuts through most of the domain. It is a representative track starting from the most northern open boundary and ending in the southern North Sea. Wave energy generated from the prevailing northern winds is bound to propagate into the model domain in the southern North Sea region. The predicted wave height displayed in figure 4.18a shows that a strong wave activity appears in the southern North Sea ($10 < y < 20$) region. Relatively good agreement is achieved between the satellite observations and model predictions. The mu-WAVE predictions even exceeds the satellite data in the southern North Sea region. This is not surprising if one notices that the mu-WAVE has been

(a)

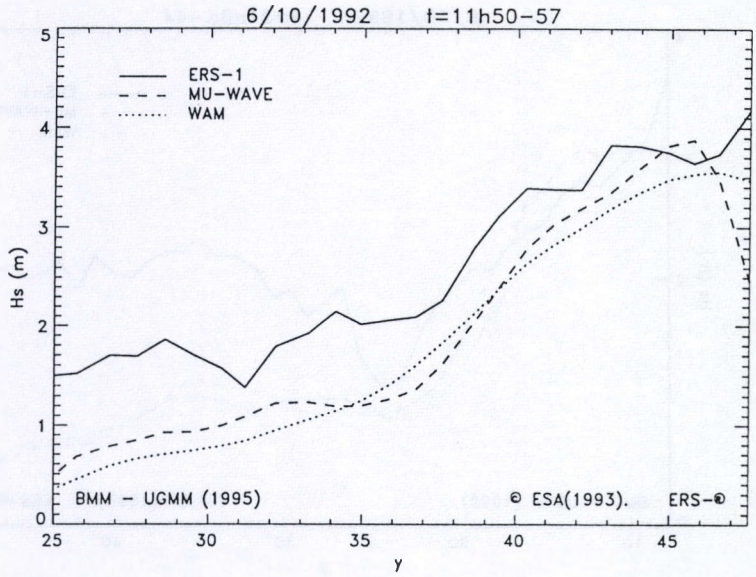

(b)

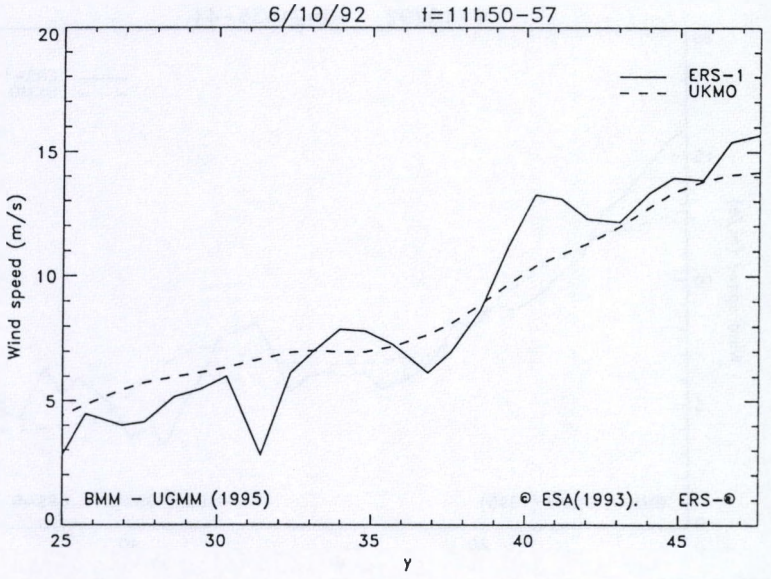

Figure 4.17: Comparison between the altimeter observations and models for October 6 1992 for the satellite ground track shown in figure 4.7: (a) for significant wave height; (b) for wind speed.

(a)

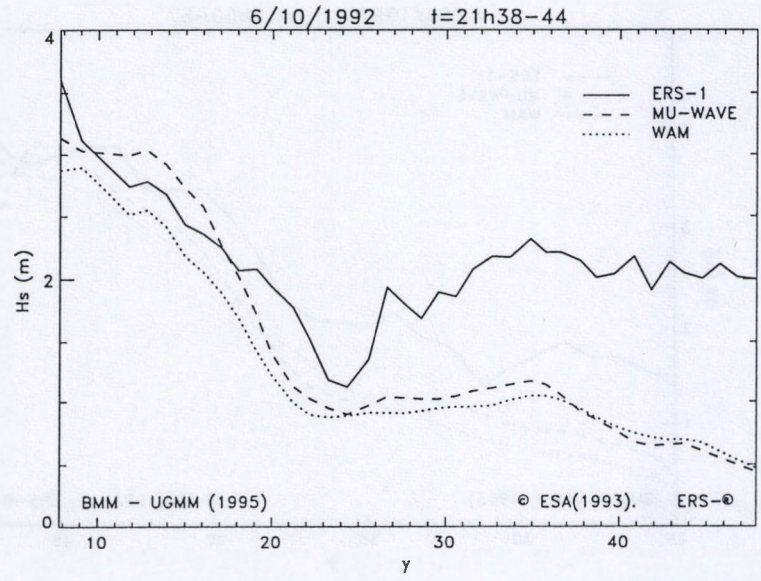

(b)

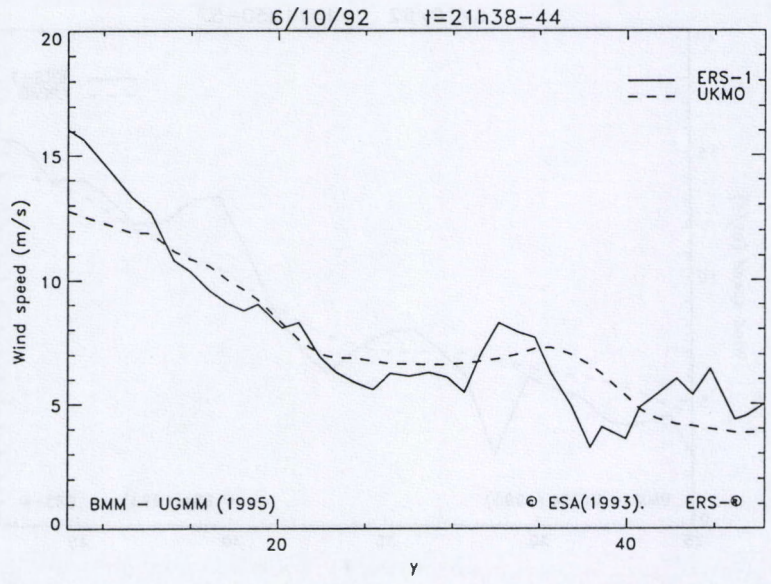

Figure 4.18: Comparison between the altimeter observations and models for October 6 1992 for the satellite ground track shown in figure 4.9: (a) for significant wave height; (b) for wind speed.

tuned in this main region of interest. In this section, the WAM model has not yet been tuned! In chapter 5, it will be shown that the use of tuned equivalent bottom friction coefficients will improve the shallow water forecasts. The winds used to force models are smoother than the observed ones (see figure 4.18b).

The following sub-track (see figure 4.11) covers the entire domain running along the Norwegian coast through England and including the narrow channel region. It is a very characteristic track that reflects the quality of the model hindcast. Figure 4.19a presents the significant wave height from models and from satellite data. Both models underestimate the wave height, specially in the northern part of the domain. However, the WAM improves the significant wave height prediction along the Norwegian coast with respect to the mu-WAVE results. It is a good verification that the WAM model contains today's knowledge of the physics for the wave evolution. It can respond to wind changes much better than the second generation model – mu-WAVE, since there is a changing wind field pattern over the Norwegian Sea a few hours preceding the satellite observation. For the wind, there is a good agreement between the UKMO wind model and the altimeter observation (figure 4.19b) except for the entry and exit regions. The last track cuts through the middle of the upper domain (figures 4.12 and 4.13), as well as through a short segment between Denmark and Norway. The significant wave height along this sub-track is displayed in figure 4.20a for the WAM hindcast and the altimeter observations. Figure 4.20b shows the wind speed from the UKMO model, which is used to force the WAM model, and from the satellite observations. Along this sub-track, both wave models are not always underpredicting the significant wave height. It is very important to note that this wave height overprediction from wave models is correlated to the wind speed overestimation of the UKMO wind model. As shown in figure 4.20a, the overprediction of the wave height from the WAM is less than that from the mu-WAVE. The wave field in this example was mainly wind sea generated by the fast moving storm (see figure 4.12 and 4.13), and shows that the WAM adjusts

(a)

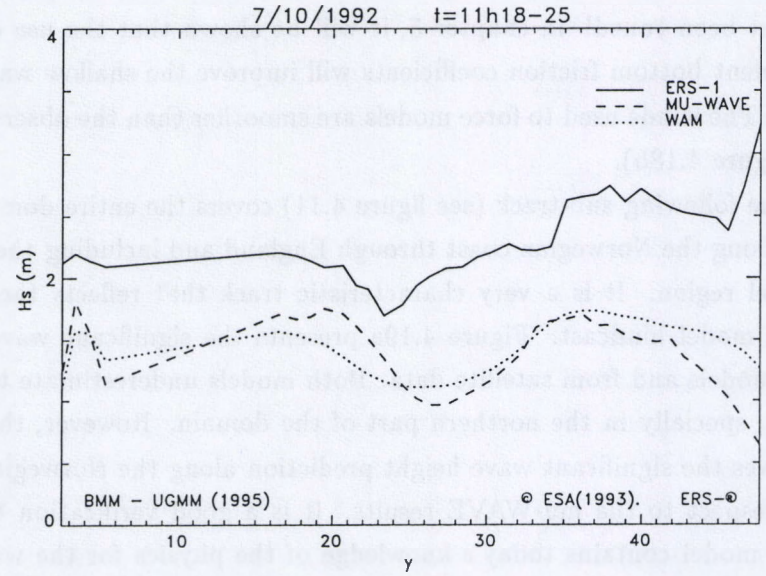

(b)

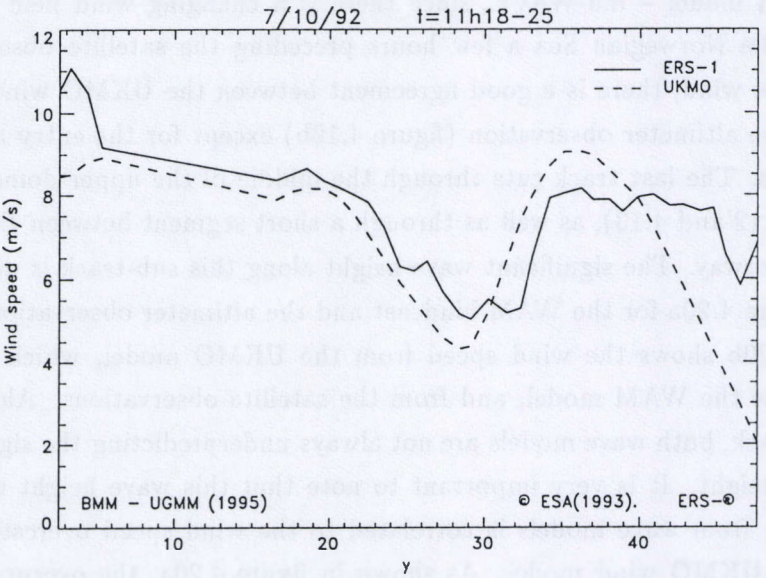

Figure 4.19: Comparison between the altimeter observations and models for October 7 1992 for the satellite ground track shown in figure 4.11: (a) for significant wave height; (b) for wind speed.

(a)

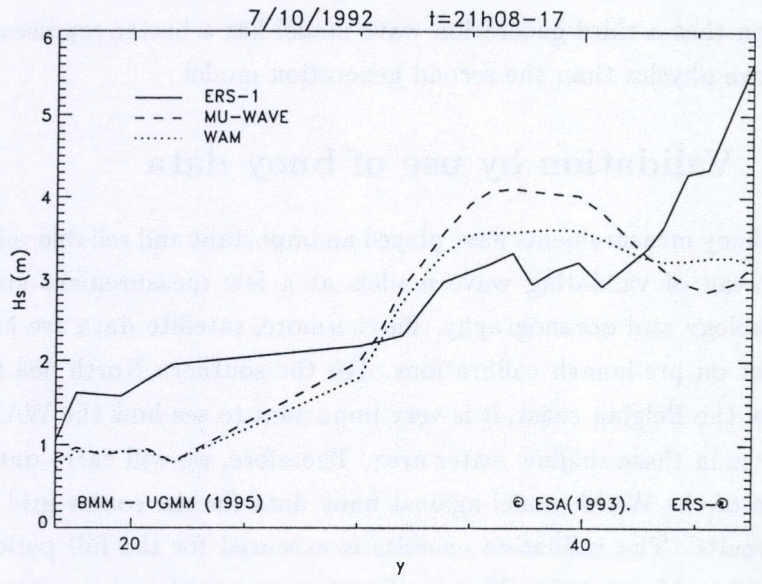

(b)

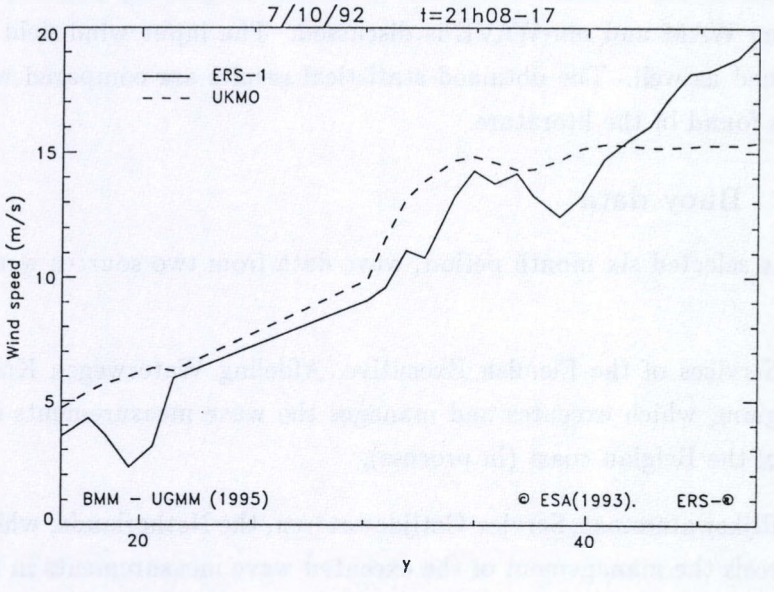

Figure 4.20: Comparison between the altimeter observations and models for October 7 1992 for the satellite ground track shown in figure 4.12: (a) for significant wave height; (b) for wind speed.

to the fast moving situation more easily than mu-WAVE. It is another indication that a third generation wave model has a better representation of the wave physics than the second generation model.

4.7 Validation by use of buoy data

Wave buoy measurements have played an important and reliable role mainly as a mean of validating wave models at a few measurement stations in meteorology and oceanography. Furthermore, satellite data are highly dependent on pre-launch calibrations. For the southern North Sea region in front of the Belgian coast, it is very important to see how the WAM model performs in these shallow water area. Therefore, we will carry out the validation of the WAM model against buoy data for the coarse grid and fine grid results. The validation exercise is executed for the full period October 1992 to March 1993. The significant wave height and the mean period are used for the validation exercise. Also the comparison of model results between WAM and mu-WAVE is discussed. The input wind field will be examined as well. The obtained statistical results are compared with the results found in the literature.

4.7.1 Buoy data

For the selected six month period, wave data from two sources were available:

- Services of the Flemish Executive, Afdeling Waterwegen Kust, Belgium, which executes and manages the wave measurements in front of the Belgian coast (in process).
- Rijkswaterstaat, Service Getijdewateren, the Netherlands, which controls the management of the executed wave measurements in front of the Dutch coast.

The buoy data were received by M.U.M.M.. In order to compare the buoy measurements with the model results, Ovidio *et al* (1994a, 1995a) from

M.U.M.M. made the extraction of data, including the necessary quality control procedures and the required temporal smoothing of high frequency variability not represented by the numerical model. The evaluation study on the WAM model has considered significant wave height (H_s), mean period (T_m) and wind speed as important parameters for evaluation against buoy data.

4.7.2 Wave model statistics found in literature

Since many different wave models were developed during the past years and were tested in many different situations, a larger number of statistical analyses can be found in literature. We will concentrate on the results from the third generation WAM model. Table 4.8 shows the statistics of the bias, scatter index and the root mean square error of the significant wave height, and the mean period where available (also see Table 3a in Ovidio and Van den Eynde (1993)). The definition of the bias, the RMSE and the S.I. is mentioned to section 4.6.3.

Table 4.8: Wave model statistics found in literature.

Significant wave height					
Model	Bias (m)	S.I. (%)	RMSE (m)	References	Remarks
Operational					
WAMS	0.82/1.48	20/38	0.96/1.63	Zam., 1986a	Storm
WAMS	0.36/1.37	23/34	1.13/1.69	Zam., 1986b	Storm
Analyzed					
WAMS	0.08/0.40	15/21	0.61/0.96	Zam., 1986a	Storm
WAMS	0.26	19	0.96	Zam., 1986b	Storm
WAM	-0.4/-0.22	22/37	0.47/0.82	Zam., 1989	Storm
NEDWAM	-0.18/0.13	10/21	.23/.88	Ric., 1986	
NEDWAM(REF)	-0.61/-0.13	16/20	0.32/0.74	Mas., 1993	911215-920225
Data assimilation					
NEDWAM(DA1)	-0.08/0.54	16/21	0.33/0.7	Mas., 1993	911215-920225
NEDWAM(DA2-3)	0.01/0.36	16/19	0.31/0.69	Mas., 1993	911215-920225
Mean period					
Model	Bias (s)	S.I. (%)	RMSE (s)	Ref.	Remarks
WAM	-0.71/-0.01	18/21	1.44/1.99	Zam.	Storm

When investigating this table, it can be found that the third generation operational model produces results with a bias in the order of 1.04 m,

a scatter index about 28.5%, and the root mean square error of 1.35 m for the significant wave height. The third generation wave model with analyzed wind force yields results with a bias in the order of 0.27 m, a scatter index of 20.5% and a root mean square error of 0.67 m. The results of the models clearly depend on the quality of the input wind fields. It is clear that the results obtained with analyzed wind fields, which can be assumed to be of better quality than the forecasted wind fields, are much better than the results of the operational runs. These conclusions were also found in Zambresky, 1986a. Since the mean significant wave height is higher during storm conditions than during continuous longer periods, the scatter indices during storm conditions can be expected to be slightly lower than the scatter indices of the longer period simulations. The results produced by the models including wave height assimilation show improved biases. Concerning the mean period, no conclusions can be drawn, due to the sparse information.

4.7.3 Significant wave height

Results

To give a more visual picture of the comparison between the WAM predictions and the observations, a sample verification at five locations is displayed in figures 4.21 a-e for the period January 1993. Also shown in the figures are the mu-WAVE results. The results of the statistical evaluations for the comparison between modelled and measured significant wave height are summarized in Table 4.9. The results are presented for each station, each month separately and for the entire period.

Discussion of the results

Examining figures 4.21 a-e, one sees that a good agreement between the model results and the buoy data is found for both models. At all of the locations, WAM tends to underestimate the wave height during the first three days. The mu-WAVE model, on the other hand, produces very nice

Table 4.9: Statistical analysis for the significant wave height H_s (m) and wind speed U (ms^{-1}) between the buoy data and models.

		H_s(WAM)			H_s(mu-WAVE)			wind speed U		
		Bias	S.I.	RMSE	Bias	S.I.	RMSE	Bias	S.I.	RMSE
auk	Oct.	0.52	0.38	0.67	0.36	0.35	0.64	-0.58	0.23	1.58
	Nov.	0.33	0.23	0.61	0.24	0.22	0.59	-0.79	0.17	1.81
	Dec.	0.32	0.22	0.48	0.18	0.19	0.44	-0.97	0.19	1.67
	Jan.	0.13	0.19	0.78	0.54	0.21	0.83	-1.75	0.19	2.53
	Feb.	0.21	0.22	0.51	0.18	0.29	0.69			
	Mar.	0.25	0.28	0.53	0.06	0.23	0.47			
	6 m	0.29	0.24	0.60	0.26	0.25	0.62			
k13	Oct.	0.46	0.34	0.54	0.16	0.21	0.38	-0.70	0.21	1.84
	Nov.	0.29	0.23	0.47	0.17	0.20	0.42	0.05	0.13	1.29
	Dec.	0.26	0.28	0.39	0.13	0.26	0.38	-0.16	0.17	1.29
	Jan.	0.04	0.17	0.41	0.23	0.20	0.45	-0.26	0.15	1.67
	Feb.	0.15	0.29	0.42	-0.07	0.23	0.35	-0.35	0.19	1.30
	Mar.	0.19	0.32	0.39	-0.02	0.25	0.34	0.62	0.19	1.39
	6 m	0.26	0.28	0.44	0.09	0.23	0.38	-0.11	0.17	1.46
mpn	Oct.	0.46	0.55	0.57	0.17	0.30	0.36	1.15	0.25	1.90
	Nov.	0.48	0.53	0.71	0.18	0.32	0.48	1.27	0.20	1.88
	Dec.	0.24	0.50	0.42	-0.02	0.33	0.32	0.70	0.20	1.45
	Jan.	0.34	0.43	0.67	0.21	0.33	0.55	0.64	0.15	1.52
	Feb.	0.37	0.69	0.60	-0.02	0.33	0.36	0.46	0.20	1.21
	Mar.	0.19	0.43	0.31	-0.08	0.30	0.26	0.83	0.23	1.49
	6 m	0.35	0.53	0.57	0.07	0.33	0.40	0.85	0.21	1.60
ym6	Oct.	0.67	0.53	0.80	0.56	0.53	0.83	0.18	0.25	1.83
	Nov.	0.41	0.30	0.57	0.23	0.25	0.50	0.53	0.20	2.00
	Dec.	0.21	0.34	0.34	-0.02	0.23	0.26	-0.02	0.25	1.78
	Jan.	-0.01	0.23	0.49	-0.05	0.19	0.41	-0.03	0.17	1.84
	Feb.	-0.14	0.42	0.41	-0.35	0.43	0.46	0.04	0.20	1.30
	Mar.	-0.03	0.23	0.21	-0.18	0.32	0.32	0.28	0.18	1.26
	6 m	0.17	0.36	0.50	0.02	0.34	0.50	0.07	0.28	1.70
cur	Oct.	0.55	0.43	0.61	0.29	0.25	0.40	1.66	0.22	2.07
	Nov.	0.49	0.38	0.65	0.25	0.28	0.51	1.26	0.20	2.07
	Dec.	0.38	0.41	0.48	0.16	0.22	0.29	0.98	0.22	1.65
	Jan.	0.24	0.25	0.52	0.03	0.24	0.51	0.65	0.15	1.52
	Feb.	0.29	0.34	0.37	0.05	0.26	0.32	0.25	0.18	1.13
	Mar.	0.22	0.34	0.31	0.02	0.26	0.27	1.04	0.22	1.43
	6 m	0.37	0.36	0.51	0.14	0.26	0.39	0.83	0.20	1.56
leg	Oct.	0.09	0.28	0.23	0.02	0.27	0.22	2.27	0.36	2.77
	Nov.							1.90	0.26	2.50
	Dec.	0.31	0.48	0.43	0.11	0.28	0.29	1.28	0.287	2.06
	Jan.	0.21	0.30	0.54	-0.03	0.28	0.53	1.15	0.19	1.91
	Feb.	0.35	0.46	0.46	0.06	0.27	0.32	0.80	0.25	1.54
	Mar.	0.22	0.42	0.33	0.02	0.39	0.36	1.57	0.30	1.98
	6 m	0.27	0.39	0.46	0.03	0.30	0.39	1.42	0.26	2.09
all	6 months	0.28	0.36	0.51	0.10	0.29	0.45	0.62	0.22	1.68

(a)

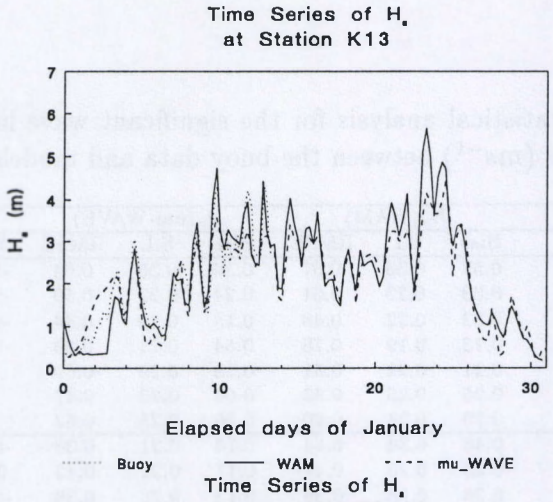
Time Series of H_s
at Station K13
H_s (m)
Elapsed days of January
Buoy
WAM
mu_WAVE

(b)

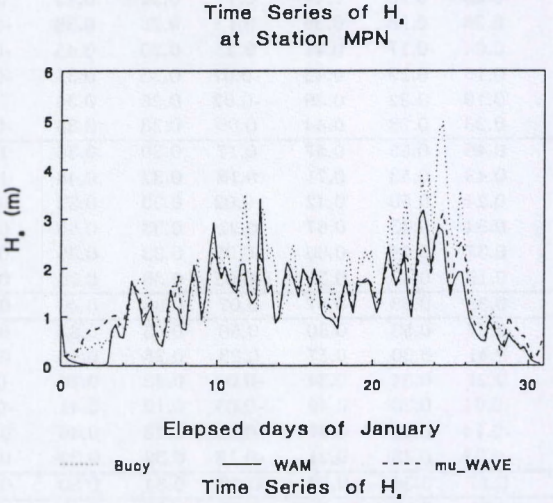
Time Series of H_s
at Station MPN
H_s (m)
Elapsed days of January
Buoy
WAM
mu_WAVE

(c)

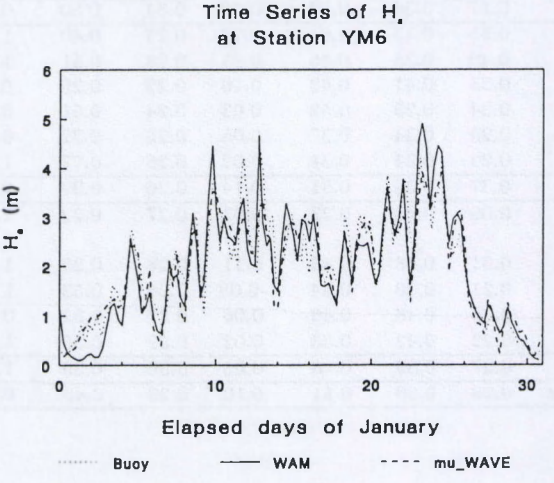
Time Series of H_s
at Station YM6
H_s (m)
Elapsed days of January
Buoy
WAM
mu_WAVE

(d)

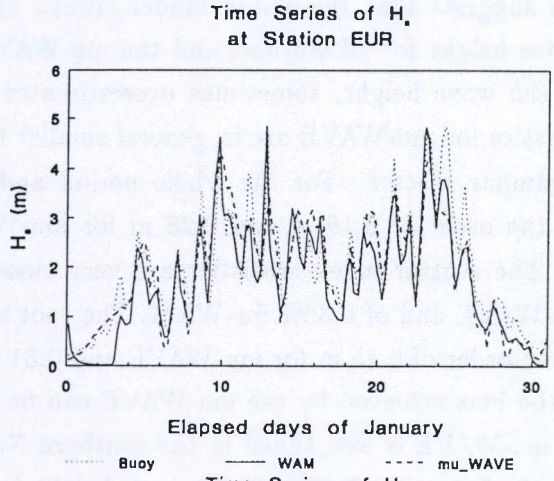

(e)

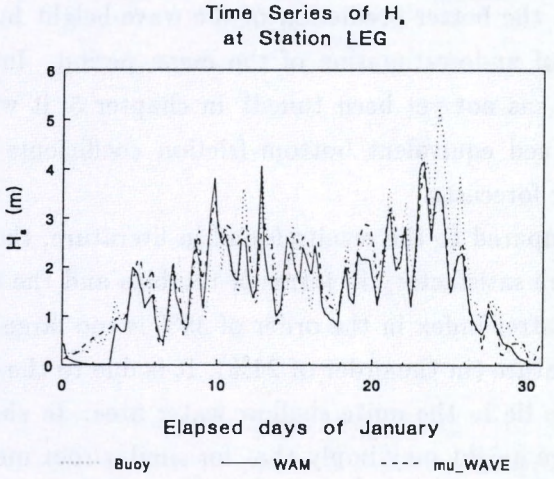

Figure 4.21: Comparison of time series of significant wave height between the WAM and mu- WAVE predictions and buoy data for January 1993 at different buoy stations: (a) k13; (b) mpn; (c) ym6; (d) eur; (e)leg.

results at the beginning. In general, the wave height maxima generated by WAM agree quite well with the measured values, and even better than the mu-WAVE hindcasts.

The table suggests that the WAM model always underestimates the significant wave height for all stations and the mu-WAVE sometimes underestimates the wave height, sometimes overestimates the wave height. The bias statistics for mu-WAVE are in general smaller than those for the WAM, with similar scatter. For the whole period and all stations, the biases are of the order of 0.10 m and 0.28 m for mu-WAVE and WAM, respectively. The scatter index statistics are very close, in the order of 0.29% for mu-WAVE and of 0.36% for WAM. The root mean square error levels are in the order of 0.45 m for mu-WAVE and 0.51 m for WAM. The reduction of the bias achieved by the mu-WAVE can be attributed to the fact that the mu-WAVE is well tuned in the southern North Sea. We will see later that the better prediction of the wave height by mu-WAVE is at the sacrifice of underestimation of the mean period. In this section, the WAM model has not yet been tuned! In chapter 5, it will be shown that the use of tuned equivalent bottom friction coefficients will improve the shallow water forecasts.

When compared to the results found in literature, the results obtained with WAM are satisfactory in terms of the bias and the root mean square error. The scatter index in the order of 39% is too large compared to one found in literature (in the order of 24%). It is due to the fact that stations discussed here lie in the quite shallow water area. In shallow water area, the lower wave height may imply that for similar root mean square errors, the scatter index may be higher than in deep water.

It is clear now that there is, in general, an underestimation of the wave characteristics in the WAM model results, even though the bias is small enough to make them acceptable for most practical purposes. However, it is instructive to see where these biases come from and how.

The first reason for the underprediction of the significant wave height lies partly in the underprediction of the wind speed by the UKMO wind

model. A good example of this can be found in figure 4.21b at station mpn and in figure 4.21e at station leg. For these two stations the underprediction of the model results is very serious for the storm on the 24th and the 25th of January. When checking the wind data, a severe underprediction (in the order of about 4 ms^{-1}) of the UKMO wind speed, which was used to force the model, was found for this storm. The underprediction of wind force gives rise to 'not enough' wind input, thus an underestimation of the wave height. Remember that the altimeter wind data (table 4.7) showed the underprediction of the wind by the UKMO model, especially in the North Atlantic region. Therefore, data assimilation of the altimeter wind data should improve the model result. This is, however, outside the scope of this study.

Another reason may be due to the 'incorrect' open boundary condition used for the coarse grid model, which results in the underestimation of the swell energy coming from the North Atlantic region. The assimilation of the global WAM wave forecast from ECMWF to correct our coarse grid boundary condition may therefore also improve the model prediction.

Additionally, one has to face the consequences from the representation of the buoy on a discrete grid. In general, the model results are available only at the active grid points. And the buoy locations cannot be expected to coincide with one of them. Therefore, certain approximations are made, either by choosing for the comparison the closest grid point (as done for this study), or by interpolating among the mesh points surrounding the buoy location. Both approximations are adequate if the field is locally smooth. However, if there are strong spatial gradients (like in front of the Belgian coast), the error may be significant. The smaller the grid size, the more limited will be the errors for these approximations.

In order to improve the WAM model prediction in this shallow zone, we may want to include more wave physics in the model. Since the spatial resolution used in this study is too coarse to account for the large depth variability, wave processes like bottom refraction and bottom dissipation will be poorly represented by the model. Moreover, wave-current interac-

tions, which may be important in front of the Belgian and Dutch coast, are poorly represented in the WAM model. The effects of currents on the wave evolution are not yet taken into account in this phase of the work. Wave breaking due to very limited water depth is also still missed in the model. Some further investigation will be discussed in chapter 6.

4.7.4 Mean period

Results

Similar to the results of the significant wave height, the results of WAM in modelling the mean wave period are shown in figures 4.22 a-e for five stations for the period January 1993. Also shown in the figures are the mu-WAVE results. The results of the statistical evaluation of the comparison between modelled and measured mean period are summarized in Table 4.10. The results are presented for each station, each month separately and for the entire period.

Discussion of the results

From figures 4.22 a-e, one finds that reasonable agreement between the model results and the buoy data is found for both models. At all of the locations, the WAM tends to overestimate the mean period compared to the buoy data for this month, while mu-WAVE produces underestimated results.

The table suggests that WAM most of time gives negative biases (overestimation) in the order of 0.56 s for the mean wave period at all stations during the whole period. The mu-WAVE model produces positive biases in the order of 0.24 s (underestimation). The scatter index statistics are close, in the order of 18% for WAM and 17% for mu-WAVE. The root mean square error levels are in the order of 0.93 s for WAM and 0.80 s for mu-WAVE.

When compared to the results found in literature (Zambresky,1986b, bias: -0.71s/-0.01s; S.I.: 18%/21%; RMSE: 1.44s/ 1.99s), the results ob-

Table 4.10: Statistical analysis for the mean period T_M (s) between the buoy data and models.

		T_m(WAM)			T_m(mu-WAVE)		
		Bias	S.I.	RMSE	Bias	S.I.	RMSE
auk	Oct.	-0.51	0.14	0.80	0.69	0.20	1.08
	Nov.	-0.91	0.17	1.10	0.17	0.13	0.77
	Dec.	-0.82	0.19	1.22	0.42	0.18	1.02
	Jan.	-1.47	0.21	1.62	0.07	0.09	0.64
	Feb.	-0.76	0.19	1.24	0.39	0.20	1.15
	Mar.	-0.73	0.18	1.03	0.19	0.16	0.87
	6 m	-0.87	0.19	1.20	0.32	0.16	0.94
k13	Oct.	-0.40	0.11	0.58	0.31	0.15	0.78
	Nov.	-0.70	0.15	0.83	0.07	0.12	0.64
	Dec.	-0.39	0.14	0.68	0.40	0.18	0.83
	Jan.	-0.88	0.17	1.01	0.09	0.12	0.65
	Feb.	-0.65	0.19	1.00	0.35	0.18	0.87
	Mar.	-0.48	0.16	0.78	0.44	0.19	0.86
	6 m	-0.54	0.15	0.79	0.30	0.16	0.79
mpn	Oct.	-0.07	0.12	0.57	0.47	0.17	0.75
	Nov.	-0.10	0.12	0.57	0.51	0.18	0.82
	Dec.	0.08	0.16	0.68	0.38	0.20	0.82
	Jan.	-0.29	0.15	0.80	0.72	0.22	1.01
	Feb.	-0.30	0.18	0.86	0.37	0.17	0.76
	Mar.	-0.07	0.16	0.69	0.47	0.21	0.82
	6 m	-0.12	0.15	0.70	0.49	0.19	0.83
ym6	Oct.	-0.40	0.12	0.61	0.57	0.20	0.94
	Nov.	-0.59	0.14	0.77	0.08	0.12	0.63
	Dec.	-0.29	0.14	0.65	0.18	0.15	0.65
	Jan.	-0.83	0.18	1.04	-0.18	0.13	0.71
	Feb.	-0.72	0.21	1.05	0.22	0.15	0.67
	Mar.	-0.43	0.18	0.87	0.49	0.20	0.87
	6 m	-0.55	0.17	0.86	0.23	0.16	0.76
eur	Oct.	-0.61	0.15	0.74	0.14	0.11	0.50
	Nov.	-0.78	0.19	0.94	-0.12	0.12	0.56
	Dec.	-0.43	0.16	0.69	0.19	0.15	0.61
	Jan.	-1.02	0.22	1.18	-0.45	0.18	0.93
	Feb.	-1.08	0.29	1.37	0.04	0.14	0.60
	Mar.	-0.66	0.21	0.94	0.22	0.17	0.66
	6 m	-0.76	0.21	1.00	0.05	0.15	0.65
leg	Oct.	-0.80	0.23	0.94	0.27	0.12	0.45
	Nov.						
	Dec.	-0.31	0.15	0.64	0.33	0.19	0.74
	Jan.	-0.87	0.20	1.05	-0.36	0.19	0.94
	Feb.	-1.04	0.29	1.34	0.08	0.15	0.66
	Mar.	-0.39	0.19	0.80	0.39	0.21	0.80
	6 m	-0.72	0.22	1.03	0.05	0.18	0.79
All stations	6 m	-0.56	0.18	0.93	0.24	0.17	0.80

(a)

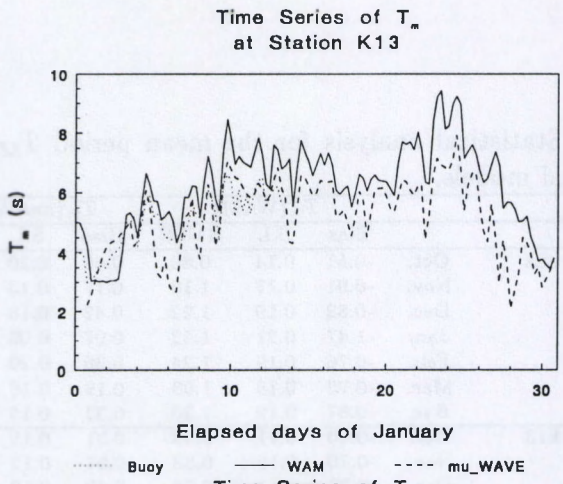
Time Series of T_m
at Station K13
T_m (s)
0
2
4
6
8
10
0
10
20
30
Elapsed days of January
Buoy
WAM
mu_WAVE

(b)

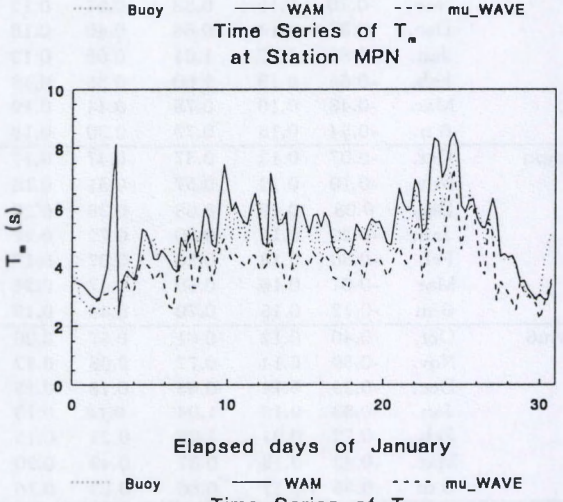
Time Series of T_m
at Station MPN
T_m (s)
0
2
4
6
8
10
0
10
20
30
Elapsed days of January
Buoy
WAM
mu_WAVE

(c)

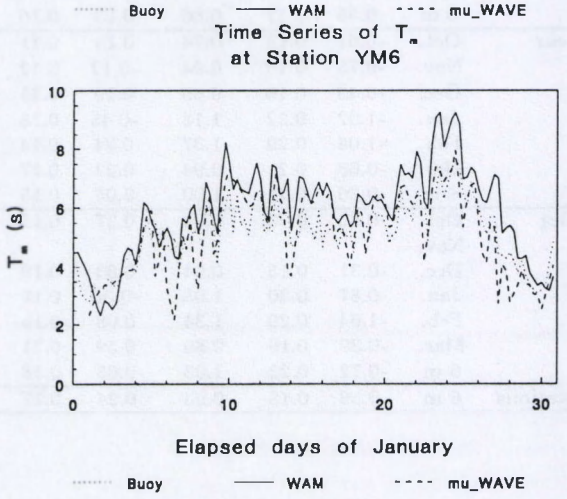
Time Series of T_m
at Station YM6
T_m (s)
0
2
4
6
8
10
0
10
20
30
Elapsed days of January
Buoy
WAM
mu_WAVE

(d)

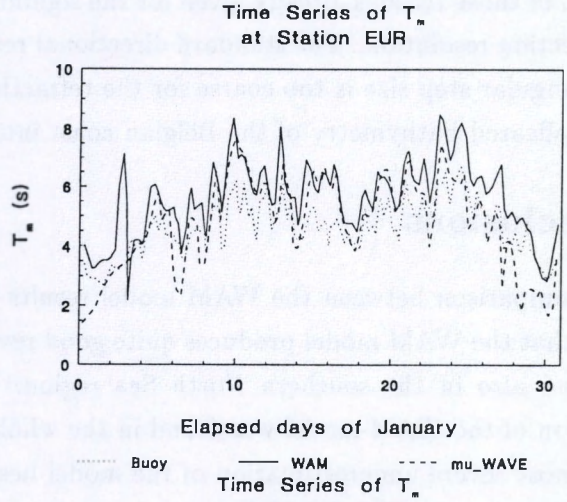

(e)

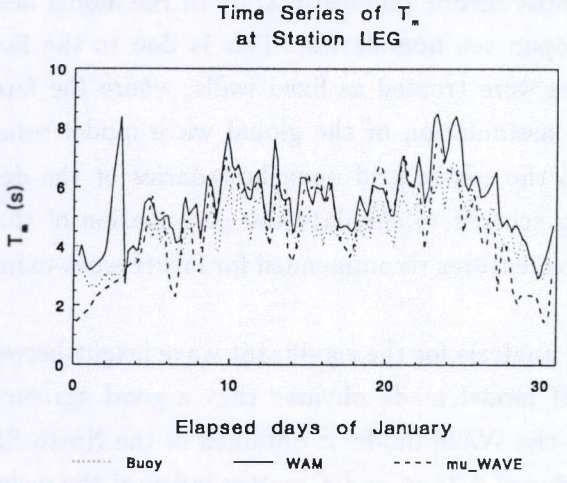

Figure 4.22: Comparison of time series of mean wave period between the WAM and mu-WAVE predictions and buoy data for January 1993 at different buoy stations: (a) k13; (b) mpn; (c) ym6; (d) eur; (e)leg.

tained with WAM are satisfactory in terms of the bias (-0.56 s), the scatter index (19%) and the root mean square error (0.89s).

An additional reason for the overestimated mean period of the WAM model, on top of those reasons already given for the significant wave height, is the low direction resolution. The standard directional resolution in WAM is 30°. This angular step size is too coarse for the refraction calculation to take the complicated bathymetry of the Belgian coast into account.

4.8 Conclusions

Global grid comparison between the WAM model results and the satellite data showed that the WAM model produces quite good results in the North Sea region and also in the southern North Sea region. However, a big underprediction of the WAM model was found in the whole North Atlantic region. The most severe underestimation of the model lies at the northern and western open sea boundaries. This is due to the fact that the open sea boundaries were treated as fixed walls, where the fetch limited law is applied. The assimilation of the global wave model results forecasted at ECMWF into the coarse grid open boundaries or the development of an energy forcing scheme to simulate the propagation of the North Atlantic swells, are two measures recommended for future work to improve the model results.

Statistical analysis for the significant wave height between the altimeter and the WAM model made obvious that a good agreement between the altimeter and the WAM model is obtained in the North Sea region, with a bias of the order of 0.31 m and a scatter index of the order of 28%. WAM underestimates the significant wave height for the whole domain, especially in the North Atlantic (open sea) region, with biases in the order of 0.83m. A very large scatter index (about 58%) was found in the channel region. It was found that the wind speed is underestimated by the UKMO model, mainly in the North Atlantic region and particularly in the winter period. However, the predictions of the wind speed in the North Sea are quite good.

The scatter index (about 20%) and the root-mean-square error (about 2 ms^{-1}) show that the UKMO winds are of good quality in the North Sea region.

From the global grid comparison between the WAM and the mu-WAVE results it was found that both models perform quite similarly in the North Sea. In the southern North Sea, mu-WAVE predicts a slightly larger (in the order of 0.2 m) the significant wave height than WAM. There is a relatively large disparity at the open boundary of the model domain as well as at some physical boundaries. Although both models apply limited fetch laws at these open boundaries, the implementation of these conditions may result in a big differential local behaviour.

The cross comparison between the satellite data, the WAM and the mu-WAVE models result along a selected set of subtracks showed that there exists a good agreement between observation and model predictions along the satellite subtrack except at the open sea boundary. It was found that the WAM model performs much better for a fast moving storms and responds much faster to wind changes than the mu-WAVE model.

The statistical analysis between the buoy data and the WAM model predictions showed that the WAM model underestimates the significant wave height and overestimates the mean wave period with biases in the order of 0.28 m and 0.56 s, respectively. The significant wave height predicted by WAM are satisfactory in terms of the bias and the root mean square error as compared to the results found in literature. The scatter index in the order of 36% is larger as compared to the one found in literature (in the order of 24%) since the buoy locations discussed in this study lie in the quite shallow water area, which results in a higher scatter index than in deep water for similar root mean square error. The mean period is well simulated by the WAM in terms of the bias, the scatter index and the root mean square error as compared to the statistics found in literature.

For the prediction of the significant wave height the mu-WAVE model has slightly smaller bias (between the buoy data and model results) as compared to WAM, with similar scatter index and root mean square error.

However, WAM, in general, gives better predictions for storm conditions. For the mean period, mu-WAVE underestimates the prediction and WAM overestimates it as compared to the buoy data. For both models, the scatter index and root mean square error are similar for the mean period prediction.

The main reason for the underprediction of the significant wave height and the overestimation of the mean wave period lies in the underprediction of the wind speed by the UKMO wind model; the 'incorrect' open boundary condition used for the coarse grid model; the consequences from the representation of the buoy station on a discrete grid; too coarse spatial resolution and too low directional resolution used in this work to account for the significant depth variability; and the poor representation of wave-currents interactions by the model. Further efforts are required in the area of data assimilation, high resolution in space and direction, more wave physics including (cf wave breaking) and the coupling between wave and tide models.

Chapter 5

Development and Test of Equivalent Dissipation Coefficients

5.1 Introduction

Shallow water wave forecasting models have to take the wave-bottom interactions into account. For sandy bottoms or where wave generated sand ripples occur, as found in many continental shelves, bottom friction dissipation is the major wave-bottom interaction dissipation mechanism. In the last decades several different bottom friction dissipation formulations have been developed, including an empirical expression based on the JONSWAP experiment (Hasselmann *et al.*, 1973), three drag law models (Hasselmann and Collins, 1968; Collins, 1972; Madsen *et al.*, 1988) and the eddy viscosity model (Weber, 1991a). These formulations have been used widely in many operational wave models. The effects of different bottom friction formulations on the energy balance were quantitatively investigated by Luo and Monbaliu (1994) (also see Chapter 3). They found that these formulations for the bottom friction source term result in quite different growth curves for the total energy and the peak frequency for depth-limited wind generated waves in the fetch-limited case. For a water depth of 15 m and a wind

friction velocity of 0.71 ms^{-1} (the corresponding U_{10} equals 15.6 ms^{-1}) a difference as big as 70% for the total energy was reported. Moreover, the CPU time used for prediction of the bottom dissipation is quite different for these five bottom friction dissipation formulations. Among these five formulations the empirical JONSWAP formulation is the simplest one, and needs the least amount of computing time. The eddy viscosity model and Madsen's drag law model are the most complicated ones, and cost the most computing time. These two models however contain more physical information because they model the bottom boundary layer more accurately and will therefore allow extension to modelling wave induced sediment motion. The main difficulty to use these two models is the prediction of the bottom roughness height (K_N). Generally the bottom roughness is determined by the flow field and the sediment properties. If sandy bottoms are considered, the shape of the ripples can change the value of the bottom roughness height. Although Grant and Madsen (1982) proposed to model the ripple roughness for the moveable-bed from the grain diameter and the wave condition, Tolman (1990) argued that the Grant and Madsen (1982) formulation showed a strong discontinuity in bottom roughness, and in numerical experiments small changes in the selected grain diameter could produce either no difference or a large difference in the calculated wave height. He proposed to select the bottom roughness K_N to be constant, and this constant could be calibrated for a model to fit available measurements.

In section 5.2 it will be investigated how, by proper adjustment of their dissipation coefficients, different formulations of the bottom friction dissipation can lead to the same effect on the energy balance for fetch-limited shallow water waves at the fully developed stage. Equivalent coefficients referred to the bottom roughness height in the eddy viscosity model are developed for the empirical formulation and three drag law models in fetch-limited shallow water for three different wind friction velocities (also see Luo *et al.*, 1994). In section 5.3, three different models for the bottom friction dissipation: the empirical expression (Hasselmann *et al.* , 1973),

a drag law model (Collins, 1972) and the eddy viscosity model (Weber, 1991a) have been implemented in the Cycle 4 version of the WAM model. The hindcasts are made for the period running from the 1st to the 28th February 1993 for the area of the southern North Sea. The results from different bottom friction formulations are compared with each other and with the measurements for different stations as well. The validity of using equivalent coefficients will be tested in real circumstances in section 5.4 (also see Luo *et al.*, 1995).

5.2 Development of equivalent coefficients in fetch-limited shallow water

5.2.1 The governing equation

The evolution of ocean wave spectra can be described by the energy transport equation. For the one- dimensional fetch-limited shallow water conditions and with a flat bottom the equation takes the form (also see equation(3.11)):

$$C_g \frac{\partial F}{\partial x} = S_{tot} \tag{5.1}$$

with C_g the group velocity in shallow water, F $(= F(f, \theta, x, t))$ the frequency spectrum, f the frequency, θ the direction of a wave component, x the fetch. S_{tot} $(= S_{tot}(f, \theta, x, t))$ is the total source term, which is the sum of wind input S_{in} (3.13), whitecapping dissipation S_{ds} (3.14), bottom friction dissipation S_{bf} and nonlinear interactions S_{nl} (3.15). For the bottom friction dissipation S_{bf}, the five expressions described in 3.2 were applied.

5.2.2 The initial conditions

In the present study numerical experiments were done for a nondimensional water depth h^* $(h^* = hg/u_{a*}^2)$ of 300. Three different wind friction velocities were used: 0.5 ms^{-1}, 0.71 ms^{-1}, 1.0 ms^{-1} (the corresponding wind speed U_{10}: $12.5ms^{-1}$, $15.6ms^{-1}$, $21.5ms^{-1}$; using the relation of Wu, 1982). The initial conditions can be found in Table 3.2.

5.2.3 Results

First of all the eddy viscosity model was implemented. For each wind friction velocity, 10 runs have been made with 10 different bottom roughness heights $K_N(W)$ (Weber, 1991a), resulting in 10 different asymptotic levels for the total energy. Secondly the other four models were also implemented, however in order to reproduce the same asymptotic energy level as the eddy viscosity model, the dissipation coefficients $c(J)$ (JONSWAP, 1973), $C_f(HC)$ (Hasselman and Collins, 1968), $C_f(C)$ (Collins, 1972) and $K_N(M)$ (Madsen *et al.*, 1988) were adequately chosen, and the energy transport equation (5.1) was solved with the new source term. Note these values were obtained by trial and error.

Figure 5.1 shows the resulting equivalent coefficient curves for the different models. For an arbitrary bottom roughness height $K_N(W)$ in the eddy viscosity model it is always possible to find equivalent dissipation coefficients for the other four models. Equivalent dissipation coefficients increase with increasing bottom roughness $K_N(W)$. For different wind friction velocities the equivalent coefficients are different. The equivalent roughness height $K_N(M)$ seems to be fairly unsensitive to the change of the air friction velocity when the $K_N(W)$ value is relatively small.

As an example one can take a bottom roughness height $K_N(W)$ of 4 cm as suggested by Weber (1991b). For a wind friction velocity of 0.71 ms^{-1} this choice results in an equivalent value 0.0667 m^2s^{-3} for $c(J)$, 0.025 for $C_f(C)$, 0.0142 for $C_f(HC)$ or 1.8 cm for $K_N(M)$ to produce (nearly) the same energy level. The run number definition corresponding to this set of equivalent coefficients can be found in Table 5.1. The c value of 0.0667 m^2s^{-3} agrees with the value proposed by Bouws and Komen (1983). For a wind friction velocity of 1.0 ms^{-1} the equivalent coefficients are 0.0726 m^2s^{-3} for $c(J)$, 0.017 for $C_f(C)$, 0.00978 for $C_f(HC)$ and 1.94 cm for $K_N(M)$. Using a wind friction velocity of 0.5 ms^{-1}, a value of 0.0612 m^2s^{-3} for $c(J)$, 0.038 for $C_f(C)$, 0.0235 for $C_f(HC)$ or 1.49 cm for $K_N(M)$ is found to be equivalent to the bottom roughness $K_N(W)$ of 4

(a)

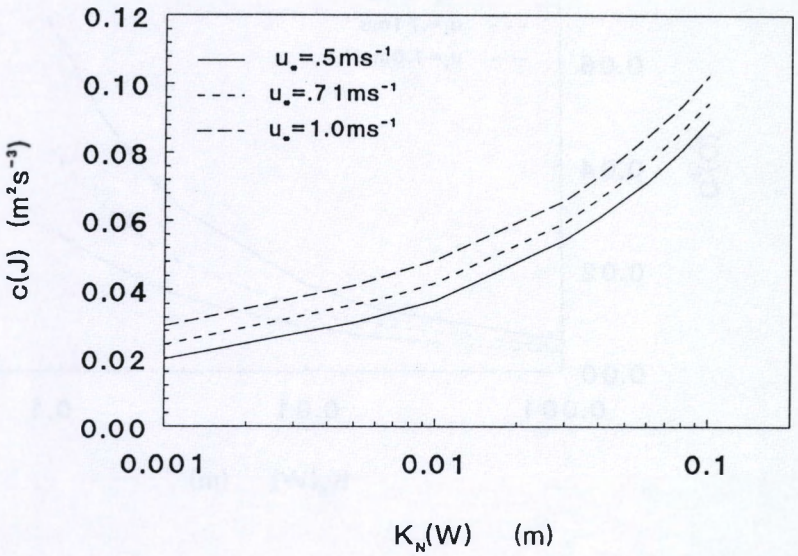
0.12
0.10
0.08
0.06
0.04
0.02
0.00
c(J) (m²s⁻³)
u*=.5ms⁻¹
u*=.71ms⁻¹
u*=1.0ms⁻¹
0.001
0.01
0.1
K_N(W) (m)

(b)

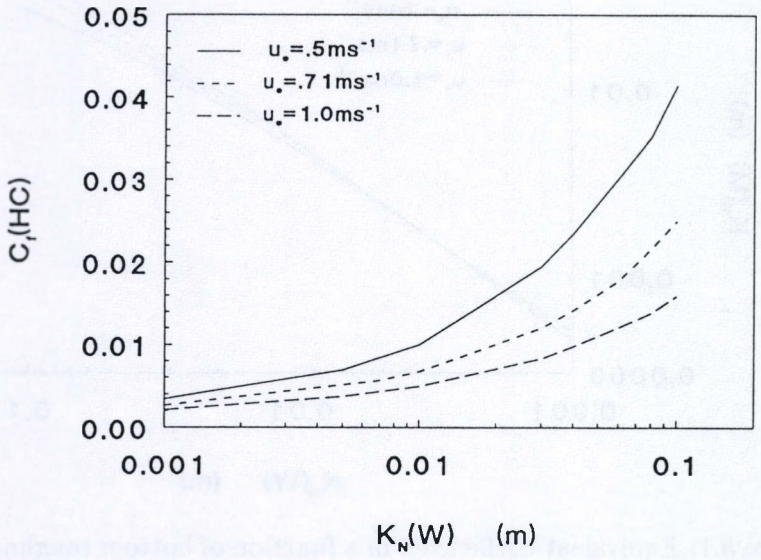
0.05
0.04
0.03
0.02
0.01
0.00
C_f(HC)
u*=.5ms⁻¹
u*=.71ms⁻¹
u*=1.0ms⁻¹
0.001
0.01
0.1
K_N(W) (m)

(c)

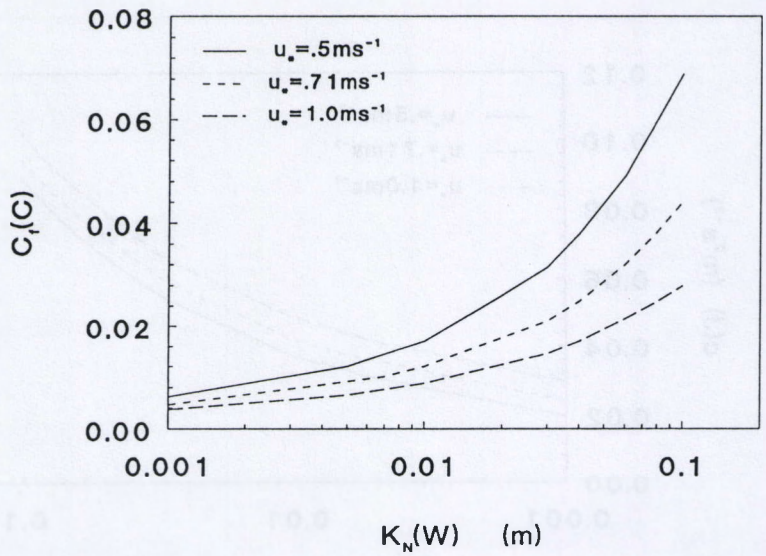

(d)

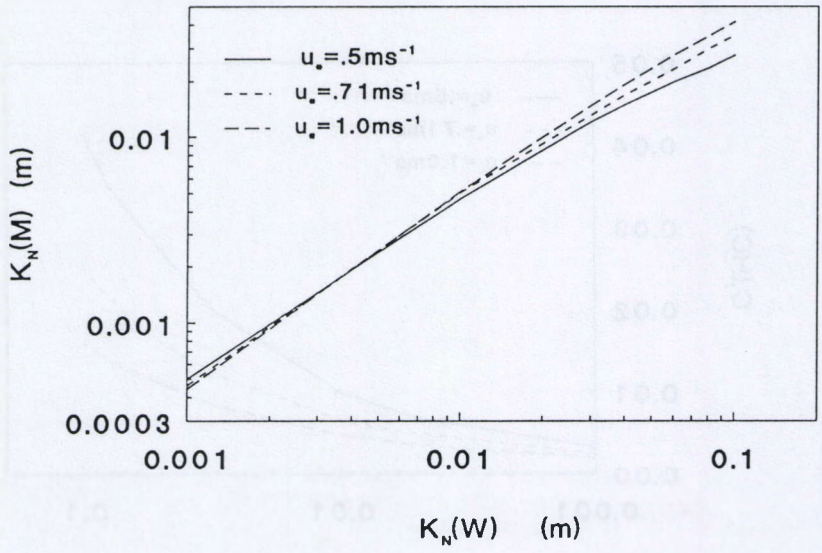

Figure 5.1: Equivalent coefficients in a function of bottom roughness height $K_N(W)$: (a) for $c(J)$; (b) for $C_f(HC)$; (c) for $C_f(C)$; (d) for $K_N(M)$.

cm. The equivalent roughness height $K_N(M)$ is nearly identical for different air friction velocities when the roughness height $K_N(W)$ is smaller than 1 cm. On the other hand, a value of 0.038 m^2s^{-3} for $C(J)$ as proposed in JONSWAP (Hasselmann *et al.*, 1973), corresponds to an equivalent bottom roughness height $K_N(W)$ of 0.69 cm for a wind friction velocity of 0.71 ms^{-1}, to 1.12 cm and 0.35 cm for wind friction velocities of 0.5 ms^{-1} and 1.0 ms^{-1} respectively. For a wind friction velocity of 0.71 ms^{-1}, an equivalent value 0.69 cm for the roughness height $K_N(W)$ in the eddy viscosity formulation, 0.0056 for $C_f(HC)$ in the drag law formulation or 0.01 for $C_f(C)$ in the simplified drag law expression or 0.345 cm for $K_N(M)$ in the Madsen *et al.* drag law model must be used. For this set of equivalent coefficients, run number can also be found in Table 5.1.

In the literature there have been some comparisons made of the behaviour of different bottom friction dissipation formulations (cf Li and Mao, 1991; Weber, 1991b). However, they did not use equivalent coefficients in their comparison. For example, a value of 0.015 for the coefficient C_f in the simplified drag law formulation, as used in Li's and Mao's study (Li and Mao, 1991), is not comparable to the mean value of 0.038 m^2s^{-3} for the coefficient c in the empirical formulation at the wind speed 20 ms^{-1} (this speed was selected in Li's and Mao's study).

5.2.4 Evaluation of equivalent growth curves

It has been shown that the bottom friction dissipation coefficients can be tuned to be equivalent so that all five formulations give almost the same growth curves for the total energy and the peak frequency. One typical set of these equivalent coefficients is referred to the eddy viscosity formulation E1 with roughness height 4 cm for a wind friction velocity of 0.71 ms^{-1} and for a water depth 15 m (i.e., a nondimensional water depth 300). One should use an equivalent value 0.0667 m^2s^{-3} for c in the empirical JONSWAP formulation, 0.025 for C_f in the simplified drag law expression (Collins, 1972) or 0.0142 for C_f in the drag law formulation (Hasselmann and Collins, 1968) and 1.8 cm for K_N in the drag law model of Madsen *et al.*. Equivalent

Table 5.1: Combinations of run number, bottom friction dissipation formulations and related coefficients.

models	run number	coefficients
Empirical formulation (3.2)	J1	$c(J) = 0.038 m^2 s^{-3}$
(Hasselmann *et al.*, 1973)	J2	$c(J) = 0.0667 m^2 s^{-3}$
Drag law formulation (3.4)	DHC1	$C_f(HC) = 0.015$
(Hasselmann and Collins, 1968)	DHC2	$C_f(HC) = 0.0056$
	DHC3	$C_f(HC) = 0.0142$
Simplified drag law form (3.5)	DC1	$C_f(C) = 0.015$
(Collins, 1972)	DC2	$C_f(C) = 0.025$
	DC3	$C_f(C) = 0.010$
Drag law formulation (3.7)	DM1	$K_N(M) = 4cm$
(Madsen *et al.*, 1988a)	DM2	$K_N(M) = 1.8cm$
	DM3	$K_N(M) = 0.345cm$
Eddy viscosity model (3.10)	E1	$K_N(W) = 4.0cm$
(Weber, 1991a)	E2	$K_N(W) = 0.69cm$

coefficients obtained in the previous section are for a nondimensional water depth of 300. Are these coefficients still valid for other nondimensional water depths? With this set of equivalent coefficients, five runs are carried out for a water depth of 30 m and a wind friction velocity of 0.71 ms^{-1} (i.e., a nondimensional water depth of 600).

Figures 5.2 and 5.3 respectively show the total energy and the peak frequency growth curves for the J2, DHC3, DC2, DM2 and E1 runs with water depths of 15 m and 30 m. For the shorter fetches these equivalent values create a bit of difference (1%-5% for the energy, 0.5%-2% for the peak frequency). For a water depth of 30 m the run J2 ($c = 0.0667\ m^2 s^{-3}$) creates a 7% lower and a 4% higher asymptotic level for the total energy and for the peak frequency respectively as compared to the run E1 ($K_N = 4\ cm$); the DHC3 ($C_f = 0.0142$) and DC2 ($C_f = 0.025$) runs both produce slightly lower (about 2.5%) values for the total energy and slightly higher (about 2%) values for the peak frequency than the run E1 ($K_N = 4\ cm$). For

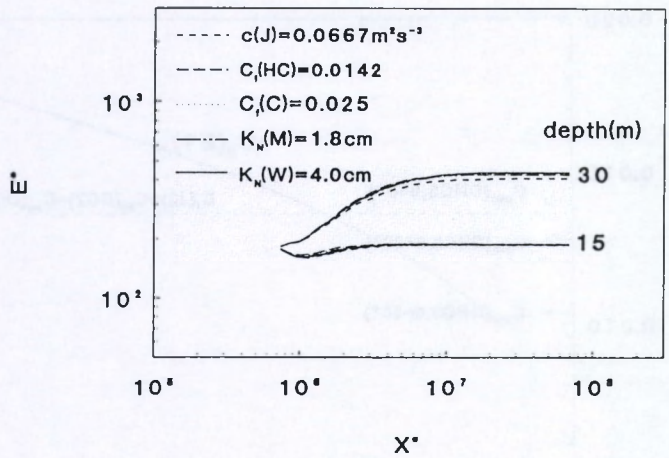

Figure 5.2: Growth curves of nondimensional total energy E^* (equal to Eg^2/u_{a*}^2) as a function of nondimensional fetch X^* (equal to xg/u_{a*}^2) in water of 15 m and 30 m depths for one set of equivalent dissipation coefficients (Here $u_{a*} = 0.71 ms^{-1}$).

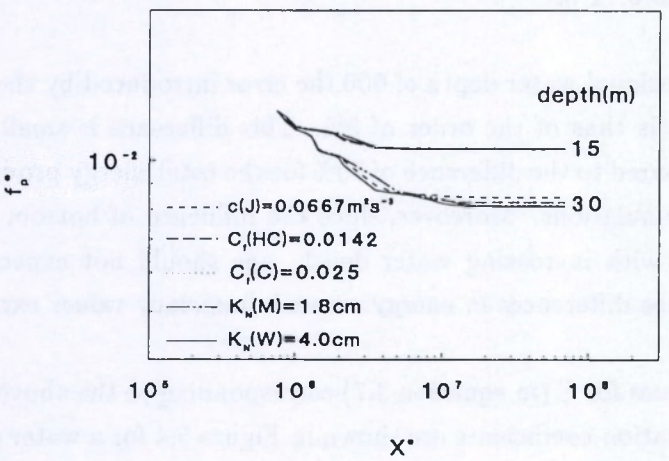

Figure 5.3: Growth curves of nondimensional peak frequency f_p^* (equal to $f_p u_{a*}/g$) as a function of nondimensional fetch X^* (equal to xg/u_{a*}^2) in water of 15 m and 30 m depths for one set of equivalent dissipation coefficients (Here $u_{a*} = 0.71\ ms^{-1}$).

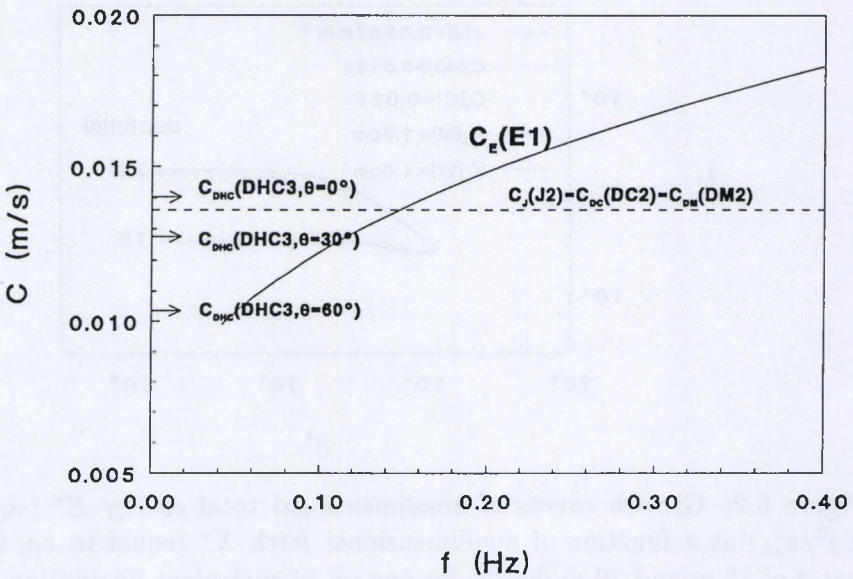

Figure 5.4: The values for C (in (3.7)) corresponding to the five equivalent dissipation coefficients for a water of 15 m at the fully developed stage sea (Here $u_{a*} = 0.71\ ms^{-1}$).

a nondimensional water depth of 600 the error introduced by the equivalent coefficients is thus of the order of 5%. This difference is small, especially when compared to the difference of 70% for the total energy produced by the original formulations. Moreover, since the influence of bottom dissipation diminishes with increasing water depth, one should not expect for other depths to see differences in energy or peak frequency values exceeding this error level.

The values for C (in equation 3.7) corresponding to the above five equivalent dissipation coefficients are shown in Figure 5.4 for a water depth of 15 m and a wind friction velocity of 0.71 ms^{-1} at the fully developed stage. One can see that the value for C_J from J2 exactly equals the value for C_{DC} from DC2 and for C_{DM} from DM2. Although the values for C_{DHC} (DHC3) and C_E (E1) are respectively dependent on the wave direction and

on the frequency, the values for C_J (J2), C_{DC} (DC2) and C_{DM} (DM2) lie in the range of C_{DHC} and C_E values; for example, the value for C_E (E1) around the peak frequency ($f_p = 0.145\ Hz$) is equal to the value for C_J and C_{DC}. This explains why the five tuned equivalent coefficients have a nearly identical effect on the total energy and the peak frequency.

Another typical set of equivalent coefficients is referred to the empirical JONSWAP formulation with the mean $c(J)$ value of 0.038 m^2s^{-3}. To produce the same asymptotic level for the total energy and the peak frequency for a wind friction velocity of 0.71 ms^{-1} and for a water depth of 15 m, an equivalent value 0.69 cm for the roughness height $K_N(W)$ in the eddy viscosity formulation, 0.01 for $C_f(C)$ in the simplified drag law expression or 0.0056 for $C_f(HC)$ in the drag law formulation and 0.345 cm for $K_N(M)$ in the drag law model of Madsen *et al.* must be used. For a water depth of 30 m the runs E2, DHC2, DC3 and DM3 (run number definition can be found in Table 5.1) predict at most 7% more for the total energy and 4% less for the peak frequency as compared to the run J1 (see figures 5.5 and 5.6).

Although the eddy viscosity model (Weber, 1991a) and the drag law model from Madsen *et al.* (1988) are physically more correct and provide more detailed information about the bottom boundary layer, it does not always seem worthwhile to spend the extra calculation effort for these two models. A proper equivalent coefficient in the empirical expression can cover a wide range of practical conditions and should therefore suffice in most circumstances for operational models. It remains essential to use different c values for different wind friction velocities and for different circumstances with different bottom roughness heights, thus an operational model has to be calibrated for the local flow circumstances.

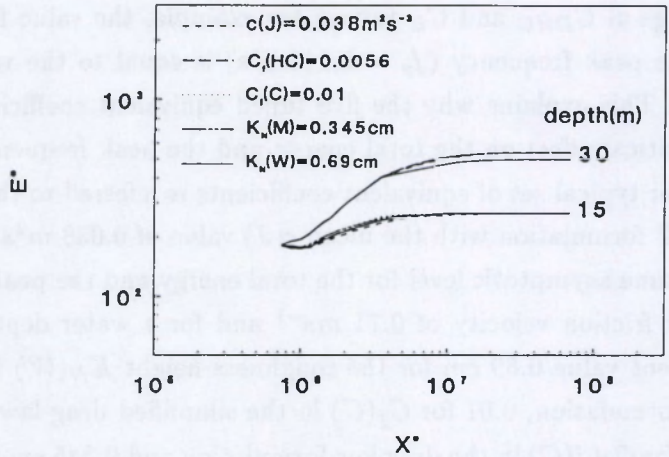

Figure 5.5: Growth curves of nondimensional total energy E^* (equal to Eg^2/u_{a*}^2) as a function of nondimensional fetch X^* (equal to xg/u_{a*}^2) in water of 15 m and 30 m depths for another set of equivalent dissipation coefficients (Here $u_{a*} = 0.71 ms^{-1}$).

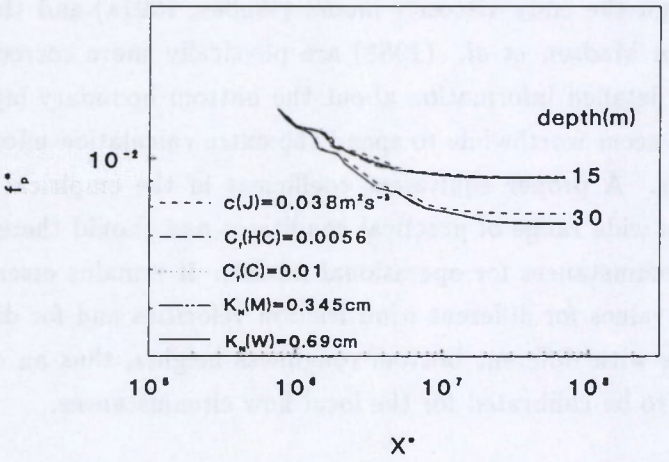

Figure 5.6: Growth curves of nondimensional peak frequency f_p^* (equal to $f_p u_{a*}/g$) as a function of nondimensional fetch X^* (equal to xg/u_{a*}^2) in water of 15 m and 30 m depths for another set of equivalent dissipation coefficients (Here $u_{a*} = 0.71\ ms^{-1}$).

5.3 Implementation of eddy viscosity and drag law models in WAM

5.3.1 Wave models

In chapter 4 we described the wave prediction for the Belgian coastal waters based on the Cycle 4 version of the WAM model. As it was discussed before, the WAM model is a third generation wave model which solves the wave transport equation explicitly without any ad hoc assumption on the shape of the wave spectrum. In this version of the WAM model, the source terms include the wind input, whitecapping, nonlinear interactions and bottom dissipation. For bottom dissipation, the empirical JONSWAP formulation with the mean c value of 0.038 $m^2 s^{-3}$ was applied. This section describes the implementation of the eddy viscosity model and one of the drag law models for the computation of the bottom friction dissipation in the Cycle 4 version of the WAM model.

The basic energy transport equation for a Cartesian coordinates system, in the absence of currents, can be described as

$$\frac{\partial F}{\partial t} + \frac{\partial}{\partial x}(c_g \sin\theta F) + \frac{\partial}{\partial y}(c_g \cos\theta F) + \frac{\partial}{\partial \theta}(c_\theta F) = S_{tot} \qquad (5.2)$$

and

$$c_\theta = \frac{\omega}{\sinh 2kh}(\sin\theta \frac{\partial h}{\partial y} - \cos\theta \frac{\partial h}{\partial x}) \qquad (5.3)$$

The general form of c_θ can be found in section 2.3.1 (equation (2.39)). For source terms, the wind input S_{in} is taken from equation (2.53), the dissipation due to whitecapping is given by equation (2.65) and the nonlinear interactions by equations (2.72) and (2.73). For the bottom friction dissipation in shallow water, the general formulation is equation (3.1). The three different expressions for the bottom friction dissipation retained in this section, are given in Table 5.2, the reader is referred to Luo and Monbaliu (1994) (also see chapter 3) for the detailed description of these coefficients. The hindcast is made on the coarse grid model. The buoy data from stations k13 and ym6 are used. The model domain and the indication of the buoy stations are shown in figure 5.7 (also see section 4.3).

Table 5.2: Three dissipation coefficient formulations.

Formulations	References	Coefficients
$C_J = \frac{2c}{g}$	Hasselmann et al., 1973	$c = 0.038\ m^2 s^{-3}$
$C_{DC} = 2C_f \langle U^2 \rangle^{\frac{1}{2}}$	Collins, 1972	$C_f = 0.015$
$C_E = u^*(T_k(\zeta_0) + T_k^*(\zeta_0))$	Weber, 1991a	$K_N = 4$ cm

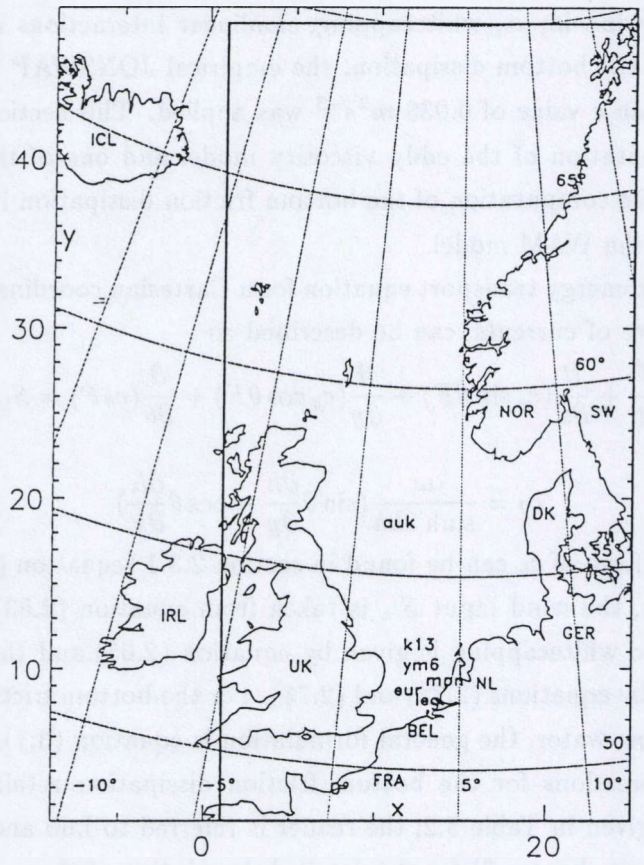

Figure 5.7: The coarse grid domain.

5.3.2 Hindcast results

One month period running from the 1st to the 28th of February 1993 is hindcasted by the WAM model with three original bottom friction formulations, denoted by J1 for the empirical JONSWAP expression ($c = 0.038 m^2 s^{-3}$), DC1 for the Collins' model ($C_f = 0.015$), and E1 for the Weber's eddy viscosity model ($K_N = 4cm$). The wind fields are provided by the United Kingdom Meterological Office (UKMO) in GRIB (GRIdded Binary) and decoded by the Management Unit of the North Sea Mathematical Models (M.U.M.M.). These winds were compared with the satellite data and buoy data. The comparison showed that the wind forcing used to drive the wave model is of good quality (Ovidio *et al.*, 1994a,b).

As an example, figure 5.8 presents a global view of the significant wave height difference between the empirical formulation J1 and the eddy viscosity mode E1 at 6h GMT February 21 1993. The maximum difference for the significant wave height was found in the Dutch coastal zone, in the order of 1.9 m. For the southern North Sea area near the Belgian coast, the difference is in the order of 1 m.

In figures 5.9 and 5.10 the hindcast results for the significant wave height H_s are displayed with the measured data for wave station k13 and ym6, respectively. Table 5.3 shows the statistical analysis for these two buoys and the CPU time used by the whole wave model for a one-day prediction. From Table 5.3 it can be found that at station k13 all three models underestimate the significant wave height as compared to the buoy data. Both the eddy viscosity model and the drag law yield less positive bias (less underestimation) for the significant wave height than the empirical expression used conventionally in the WAM model for the whole period. It means that the application of the eddy viscosity model (E1) or the drag law expression (DC1) for the dissipation coefficient in S_{bf} results in a decreased bottom dissipation for the whole period. However, for storm conditions, the empirical formulation produces much more realistic results as compared to the other two models (see figure 5.9). For example, from

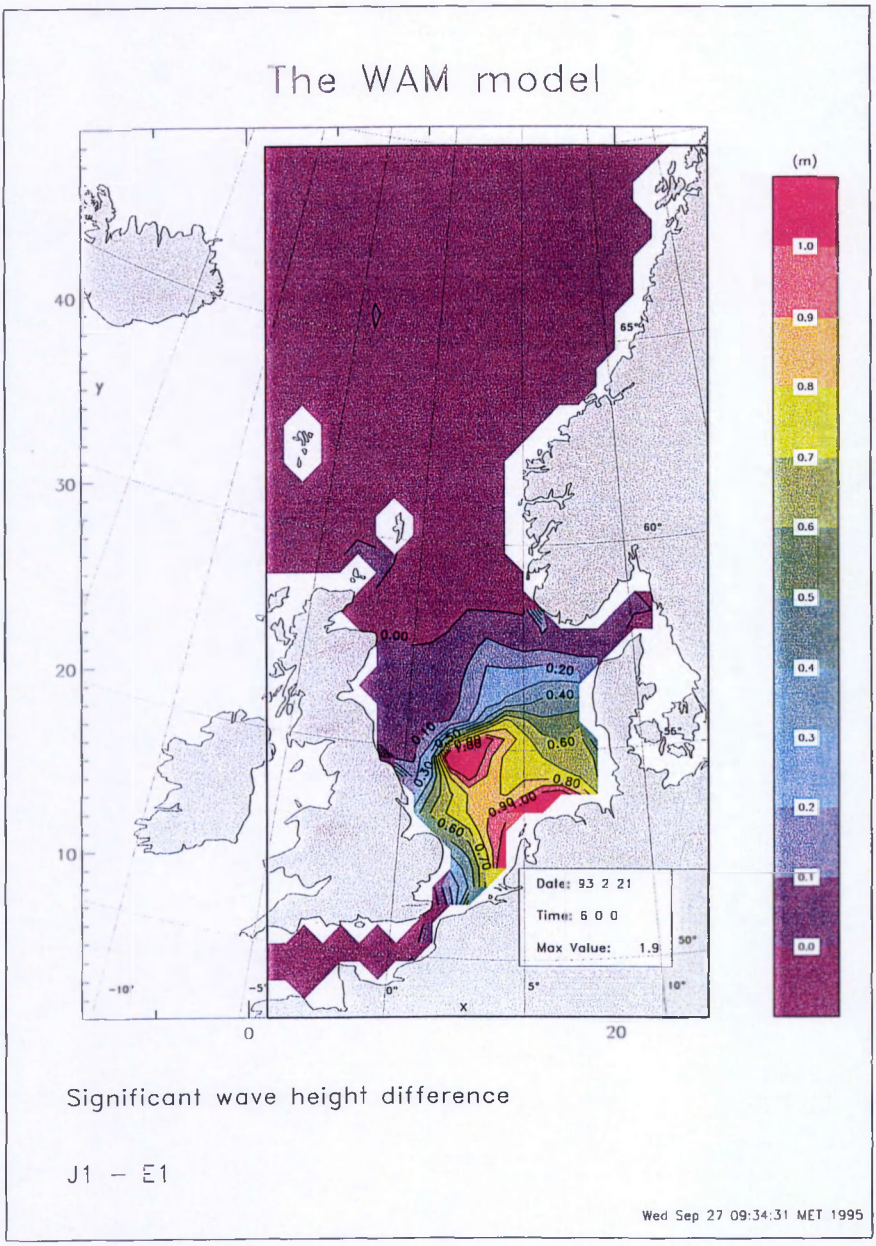

Figure 5.8: Significant wave height difference between J1 and E1 runs at 6h GMT 21st of February 1993

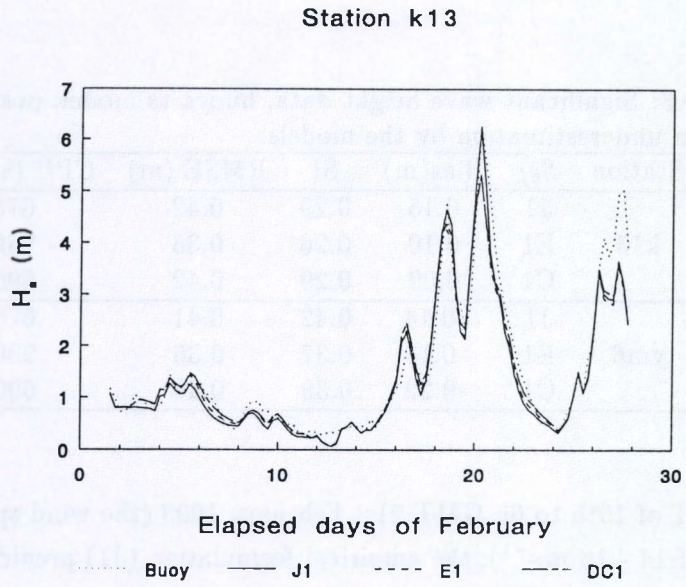

Figure 5.9: Time series of significant wave height from three different bottom friction formulations for February 1993 at station k13.

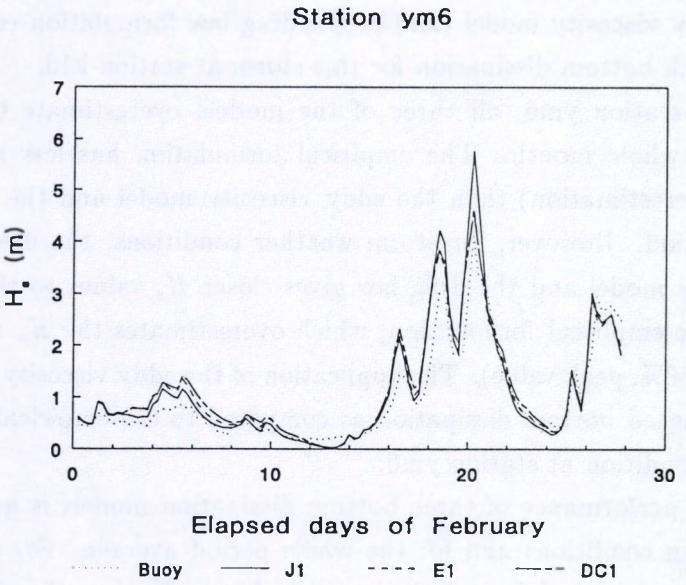

Figure 5.10: Time series of significant wave height from three different bottom friction formulations for February 1993 at station ym6.

Table 5.3: Significant wave height data, buoys *vs* model; positive bias denotes an underestimation by the models.

Station	S_{bf}	Bias(m)	SI	RMSE (m)	CPU (s/day)
k13	J1	0.15	0.29	0.42	675
	E1	0.10	0.26	0.36	930
	C1	0.09	0.29	0.42	690
ym6	J1	-0.14	0.42	0.41	675
	E1	-0.18	0.37	0.36	930
	C1	-0.22	0.39	0.40	690

6h GMT of 19th to 6h GMT 21st February 1993 (the wind speed is in the range of 14 - 18 ms^{-1}), the empirical formulation (J1) predicts significant wave height very close to the buoy data, however, the eddy viscosity model (E1) and the drag law (C1) underestimate the H_s with about 1.1 meter (18%, peak value) as compared to the buoy data. The implementation of the eddy viscosity model (E1) or the drag law formulation (C1) produces too much bottom dissipation for this storm at station k13.

For station ym6, all three of the models overestimate the H_s value for the whole month. The empirical formulation has less negative bias (less overestimation) than the eddy viscosity model and the drag law for this period. However, for storm weather conditions, the use of the eddy viscosity model and the drag law gives closer H_s values to the buoy data than the empirical formulation, which overestimates the H_s with about 2 meter (50%, peak value). The application of the eddy viscosity model yields an enhanced bottom dissipation as compared to the empirical one for this storm condition at station ym6.

The performance of three bottom dissipation models is quite different for storm conditions and for the whole period average. For storm conditions, the empirical formulation predicts larger H_s than the eddy viscosity model and the drag law at both stations. This higher prediction of the H_s resulting from the empirical formulation is more realistic at k13, however,

at ym6 it is much worse, as compared to the buoy data, than the prediction from other two models. For the whole period average, the eddy viscosity model and the drag law produce larger H_s than the empirical one, resulting in closer H_s values to the buoy data at k13 but far away at ym6. The use of a fixed bottom roughness height (in the eddy viscosity model) or a fixed c value (in the empirical formulation) for the whole prediction domain and the whole period is unrealistic. The most serious difference for the wave height prediction is found at storm conditions.

5.4 Test of equivalent coefficients

Different bottom friction dissipation formulations result in quite different growth curves for the total energy and the peak frequency for depth-limited wind generated waves in the fetch-limited case (Luo and Monbaliu, 1994). In section 5.2 equivalent dissipation coefficients were proposed so that different bottom friction dissipation formulations produce the same or nearly the same levels for the total energy and the peak frequency for fetch-limited shallow water condition (also see Luo *et al*, 1994). For example, for a wind velocity of 16.5 ms^{-1}, the eddy viscosity model with bottom roughness height 4 cm, the drag law formulation with C_f of 0.025 and the empirical expression with a c value of 0.0667 m^2s^{-3} are equivalent for the fetch-limited growth curves. Corresponding to the mean value ($c = 0.038m^2s^{-3}$) of the JONSWAP experiments, a bottom roughness height of 0.69 cm in the eddy viscosity model and a C_f value of 0.01 for Collins' model are equivalent. Are these equivalent coefficients still valid for the real circumstances? We tested these equivalent coefficients for the storm conditions. We chose the storm that occurred from 6h GMT 19th to 6h GMT 21st of February 1993, the wind speed in this storm is in the range of 14 - 18 ms^{-1} (close to 15.6 ms^{-1}).

For station k13, the empirical formulation (J1) with dissipation coefficient c of $0.038m^2s^{-3}$ produces the closest results to the buoy measurements among the three formulations. We tested the equivalent coefficients K_N of

Table 5.4: Significant wave height data, buoys *vs* model with equivalent coefficients; positive bias denotes an underestimation by the models.

Station	S_{bf}	Bias(m)	SI	RMSE (m)	CPU (s/day)
	J1	0.15	0.29	0.42	675
k13	E2	0.03	0.24	0.36	954
	C3	0.04	0.25	0.37	739
	J2	-0.03	0.35	0.33	680
ym6	E1	-0.18	0.37	0.36	930
	C2	-0.15	0.35	0.35	737

$0.69cm$ for the eddy viscosity model (denoted by E2), and the equivalent C_f of 0.01 for the Collins' model (denoted by C3) for this station. The resulting time series of the significant wave height is shown in figure 5.11. A global view of the significant wave height difference between J1 and E2 is presented in figure 5.12 at 6h GMT 21st of February 1993. It is found that for this storm the predicted H_s from the three equivalent coefficients are quite close. The statistical analysis (Table 5.4) shows that the equivalent coefficients found from the storm condition also improved the results for the whole period. The H_s bias between the buoy data and the model prediction decreases to $3cm$ for E2 and $4cm$ for C3. The H_s scatter index is also decreased for E2 and C3 as compared to E1 and C1 respectively (Table 5.3).

For station ym6, another set of the equivalent coefficients will be tested. Since the use of the eddy viscosity model (E1) predicted better the significant wave height H_s to the buoy data than the one from the other two formulations, the equivalent coefficients to E1 are: $c = 0.0667m^2s^{-3}$ for the empirical formulation (denoted by J2), and $C_f = 0.025$ for the Collins' model (denoted by C2). The hindcast results for the significant wave height is displayed in figure 5.13, and the statistical data are shown in Table 5.4. One can see that the application of the equivalent coefficients improves the results not only for the storm condition but also for the average prediction

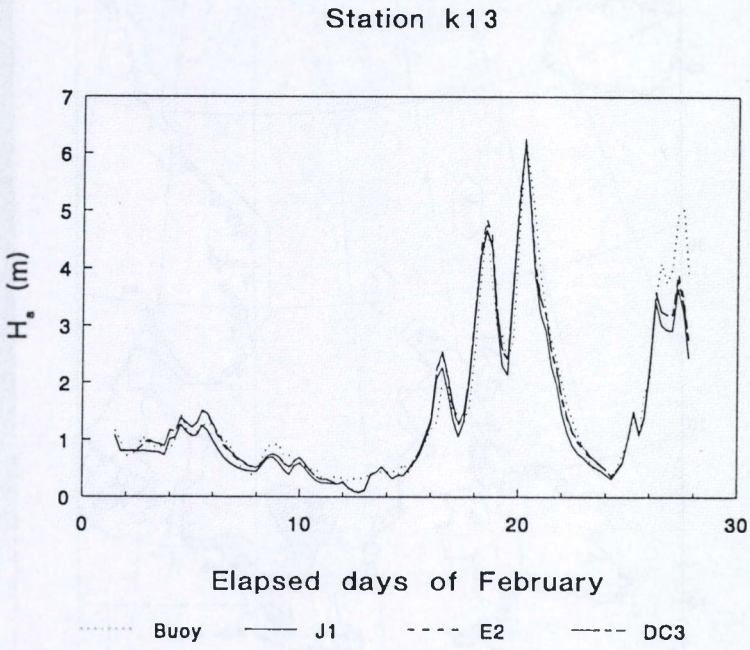

Figure 5.11: Time series of significant wave height of February 1993 at station k13 from one set of equivalent coefficients: $c = 0.038 m^2 s^{-3}$ in J1; $K_N = 0.69 cm$ in E2; $C_f = 0.010$ in DC3.

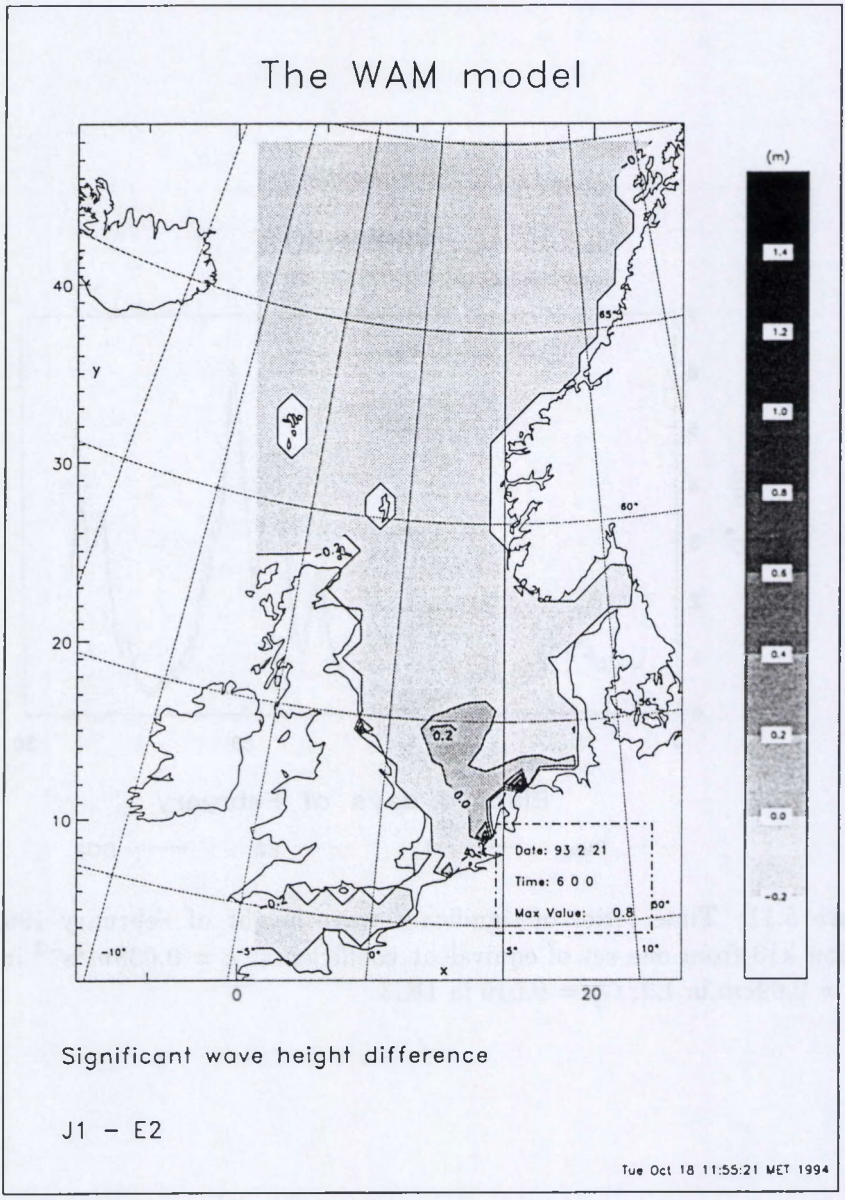

Figure 5.12: Significant wave height difference between J1 and E2 runs at 6h GMT 21st of February 1993

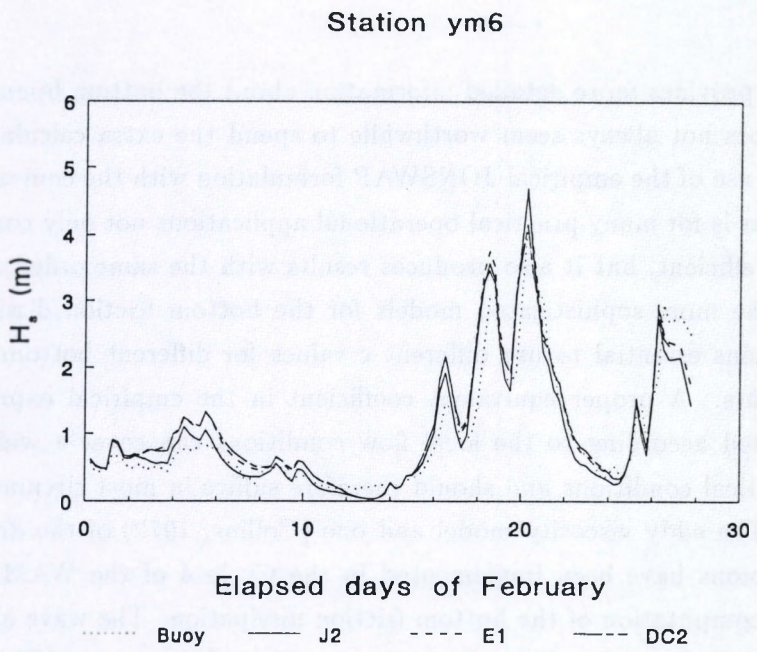

Figure 5.13: Time series of significant wave height of February 1993 at station ym6 from another set of equivalent coefficients: $c = 0.0667 m^2 s^{-3}$ in J2; $K_N = 4.0cm$ in E1; $C_f = 0.025$ in DC2.

in the whole period with respect to the bias, the scatter index and the root mean square error for the significant wave height.

5.5 Conclusions

It is possible to tune the bottom friction dissipation coefficients so that all five formulations give almost the same growth curves for the total energy and the peak frequency. The equivalent coefficients for the empirical formulation and three drag law models were obtained and referred to the bottom roughness height in the eddy viscosity model for three different wind velocities and a nondimensional water depth of 300. The introduced error for other water depths is estimated to be of the order of 5%.

The empirical formulation is the most economical in terms of computational cost. Although the eddy viscosity model is physically more correct

and provides more detailed information about the bottom boundary layer, it does not always seem worthwhile to spend the extra calculation effort. The use of the empirical JONSWAP formulation with the equivalent coefficients is for many practical operational applications not only computationally efficient, but it also produces results with the same order of accuracy as the more sophisticated models for the bottom friction dissipation. It remains essential to use different c values for different bottom roughness heights. A proper equivalent coefficient in the empirical expression calibrated according to the local flow conditions can cover a wide range of practical conditions and should therefore suffice in most circumstances.

The eddy viscosity model and one (Collins, 1972) of the drag law expressions have been implemented in the Cycle 4 of the WAM model for the computation of the bottom friction dissipation. The wave hindcast for the period running from the 1st to the 28th of February 1993 is made by using the WAM Cycle 4 with three different bottom dissipation models in the southern North Sea area. The hindcast results are compared with the buoy data. The comparison shows that the performances of different bottom friction models are quite different for the storm conditions and for the whole period average at two buoy stations. The use of a fixed bottom roughness height (in the eddy viscosity model) or a fixed c value (in the empirical formulation) for the whole prediction domain and the whole period is unrealistic. The application of the equivalent dissipation coefficients tuned in the storm conditions on the basis of the buoy data produces quite closely the significant wave height H_s, and it also improves the results for the whole period with respect to the bias, the scatter index and the root mean square error between the significant wave height prediction and the buoy data.

For different stations, different equivalent dissipation coefficients are suggested. At station k13, the equivalent coefficients c with $0.038 m^2 s^{-3}$ for the empirical formulation, the K_N of $0.69 cm$ for the bottom roughness height in the eddy viscosity model and the C_f of 0.015 for the Collin's expression have improved the significant wave height results for both the

storm condition and the calm condition. For station ym6, one should use another set of the dissipation coefficients: the c of $0.0667 m^2 s^{-3}$ for the empirical formulation, the K_N of $4.0 cm$ for the eddy viscosity model and the C_f of 0.015 for the Collin's expression.

Chapter 6

An Introduction to the Effect of Depth-limited Wave Breaking and Currents

6.1 Introduction

Spectral numerical wave models have been used operationally for many years to forecast sea conditions, either globally or regionally. However, very few models consider the wave breaking due to limited depth and the interactions between waves and tide/surge motion. The bathymetry of the Belgian coastal zone is very complicated. The water depth is quite limited. Water-level changes, currents variation and wave breaking due to limited depth become very important to the wave evolution.

The first goal of this chapter is to get a better understanding of wave breaking process. As a first attempt to this end, the effect of depth-limited wave breaking on the wave evolution in the Belgian shallow zone is investigated numerically . The Cycle 4 version of the WAM model has been extended with a formulation for the depth-limited wave breaking, based on the expression of Battjes and Janssen (1978), which was described in section 2.3.2. Van Vledder (1995) modified this expression for the predic-

tion of the energy loss per spectral component. In the next section, a short description of wave breaking modelling will be given. The wave hindcast along the Belgian coast is made for the period from the 1st to the 31st of October 1992 and for the period from the 1st to the 28th of February 1993. The fine grid, which is described in section 4.4.2, is selected for the model domain. The results can be found in section 6.3.

The interactions between waves and tidal currents have been a very hot topic in recent years. The second goal of this part of the work is to investigate the influence of currents on the wave evolution along the Belgian Coast. Two test runs are made using WAM Cycle 4 with uniform steady currents fields (section 6.4). The nature of coupling the WAM Cycle 4 with a tide surge model will be discussed in section 6.5. Some preliminary results from the coupled wave-tide-surge model (called COWAM4) with an artificial tide and artificial currents are given as well.

6.2 Modelling of depth-induced wave breaking

Two approaches to wave breaking in shallow water have been put forward and modelled recently. One is from the study of Young (1988). He presented a second generation shallow water wave model in which wind input, whitecapping, nonlinear interactions, bottom friction and wave breaking were considered. The wave breaking is imposed through the limiting wave height, which is expressed as

$$\frac{H_s}{L} = 0.12 \tanh(kh) \tag{6.1}$$

where H_s is the significant wave height, L is the wave length, k is the wave number, and h is the water depth.

The above equation is rearranged in terms of the energy spectrum to obtain a limiting value of the total energy E_{max} as

$$E_{max} = \frac{0.0355 c_m^4}{g^2} \tag{6.2}$$

where c_m is the phase speed of the mean frequency of the spectrum.

Equation (6.2) sets a limit on the total energy of the spectrum; however, it gives no information of the limiting spectrum itself. The excess wave energy is removed from the lowest frequencies. Young's model was applied on a nested grid to simulate wave conditions generated during the passage of selected tropical cyclones in the Indian Ocean off the west coast of Australia. This approach is rather coarse since it only removes energy from the lowest frequencies.

Another approach is to distribute the total dissipation rate (of Battjes and Janssen, 1978, described in 2.3.2) in proportion to the local spectral density, on the assumption that the breaking does not alter the spectral shape. Laboratory observations by Beji and Battjes (1993) of wave breaking on and passing over a bar lend support to such an assumption. The work of Vincent *et al.* (1994) also indicated that within the surf zone the distribution of wave dissipation due to breaking is proportional to the energy level and not dependent on frequency. By using this approach, Holthuijsen *et al.* (1993) included the depth-limited breaking term in a recently developed spectral wave model for the coastal zone. Van Vledder (1995) has investigated the performance of a full third generation model in shallow water with formulations for surf breaking and nonlinear triad interactions. He reported that in the coastal zone wave breaking due to limited depth is dominant over the physical effects of the wave growth processes. The energy dissipation by breaking waves over the wave spectrum is formulated as (Van Vledder, 1995)

$$S_{br}(f,\theta) = -\frac{1}{4}\alpha_{br} k_m Q_b H_{max}^2 \frac{F(f,\theta)}{E_{tot}} \tag{6.3}$$

where α_{br} is a constant of order one, Q_b is the local fraction of breaking waves, determined by equation (2.92), k_m is the mean wave number. The criterion for computing the maximum wave height H_{max} is

$$H_{max} = \gamma_d h \tag{6.4}$$

with γ_d a scaling factor.

In the Battjes-Janssen model the maximum wave height (equation (2.94)) is computed according to a combined steepness and depth-limited breaking criterion. Equation (6.4) removes the dependence of wave breaking on wave steepness to avoid the double counting of breaking due to wave steepness in the presence of a whitecapping dissipation source term. It is easily seen that H_{max} becomes negligible in deep water as compared to the water depth.

In this study, the magnitude of wave breaking effect on the wave evolution in the Belgium coastal zone will be examined by the implementation of Van Vledder's model into the Cycle 4 version of the WAM model.

6.3 Hindcast study with inclusion of wave breaking

A two months period from the 1st to the 31st of October 1992 and from the 1st to the 28th of February 1993 is hindcasted by the cycle 4 version of WAM model where the original JONSWAP empirical formulation is taken for the bottom friction dissipation source and the depth-induced wave breaking is included. The runs will be denoted by 'J1BR'. The hindcast study was made on the fine grid model. The fine grid domain was described in section 4.3. Figure 6.1 shows the domain geometry and the indication of the wave stations. For the detailed information about these five stations, one is referred to Table 4.2. The shallowest station is a2b (the water depth is 7.7 m). The hindcast results are compared with the ones from the original WAM Cycle 4 model without inclusion of depth-induced wave breaking, denoted by 'J1'.

6.3.1 October 1992

From the wave hindcast for October, there is no visible difference between model runs with and without wave breaking at the five buoy stations. As an example, the time series for the significant wave height are displayed in figure 6.2 at station a2b. The depth-induced wave breaking does not affect

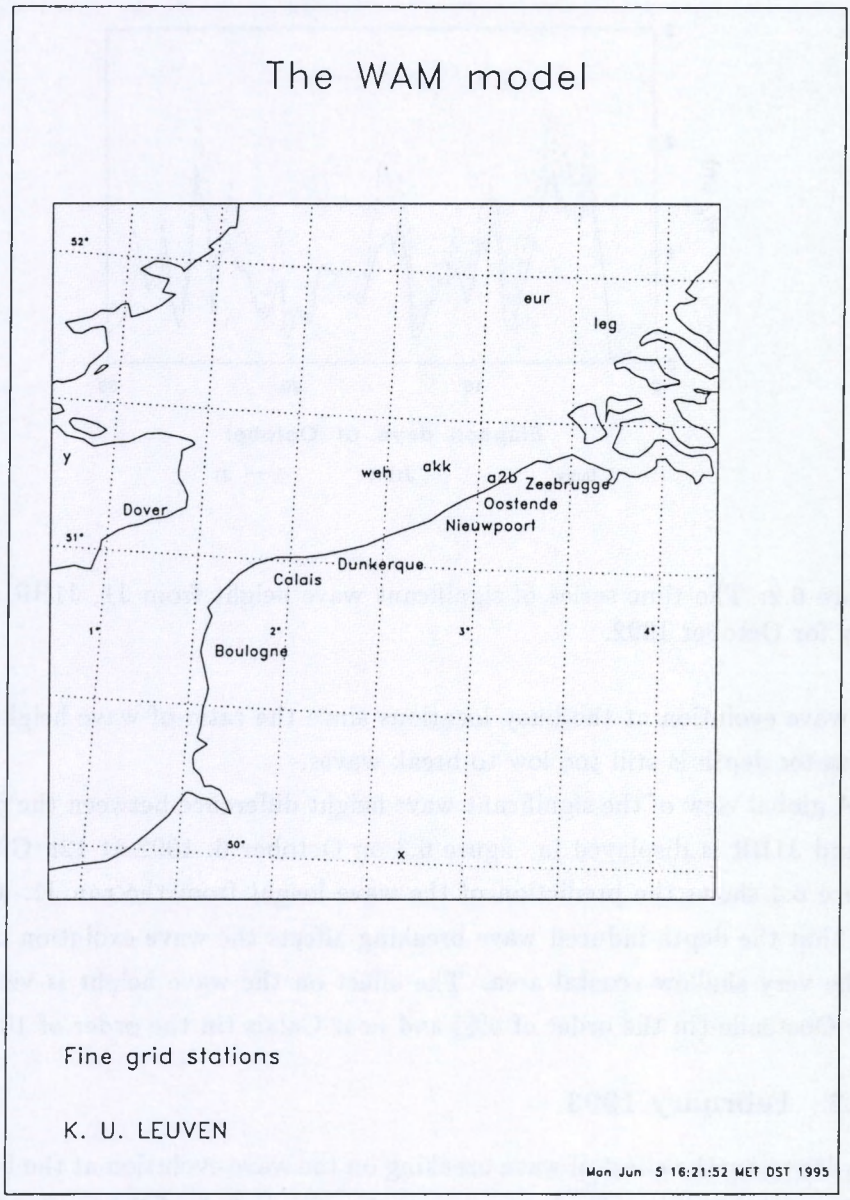

Figure 6.1: The fine grid domain and the buoy locations as indicated by the three letter symbols in Table 4.2.

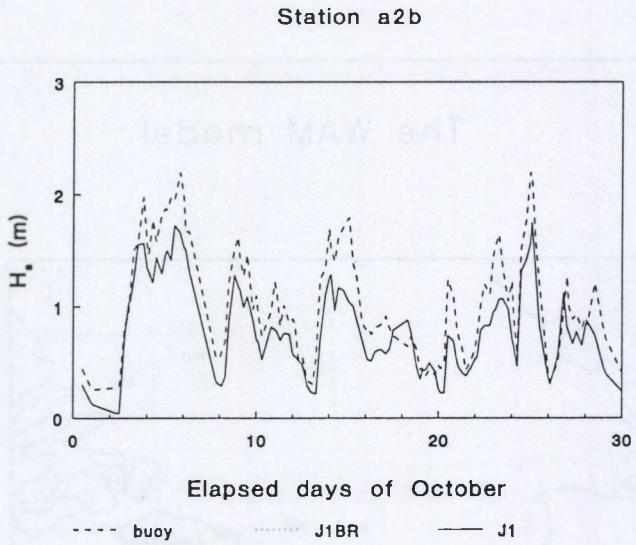

Figure 6.2: The time series of significant wave height from J1, J1BR and buoy for October 1992.

the wave evolution at the buoy locations since the ratio of wave height to the water depth is still too low to break waves.

A global view of the significant wave height difference between the runs J1 and J1BR is displayed in figure 6.3 on October 6, 1992 at 12h GMT. Figure 6.4 shows the prediction of the wave height from the run J1. One sees that the depth-induced wave breaking affects the wave evolution only in the very shallow coastal area. The effect on the wave height is visible near Oostende (in the order of 6%) and near Calais (in the order of 10%).

6.3.2 February 1993

In order to see the effect of wave breaking on the wave evolution at the buoy stations, the hindcast study was made for the period of February 1993, in which much stronger wave activities (than in October) were predicted. Some effects of wave breaking on the significant wave height were predicted at station a2b. No effects were seen at the other stations. Figure 6.5 gives

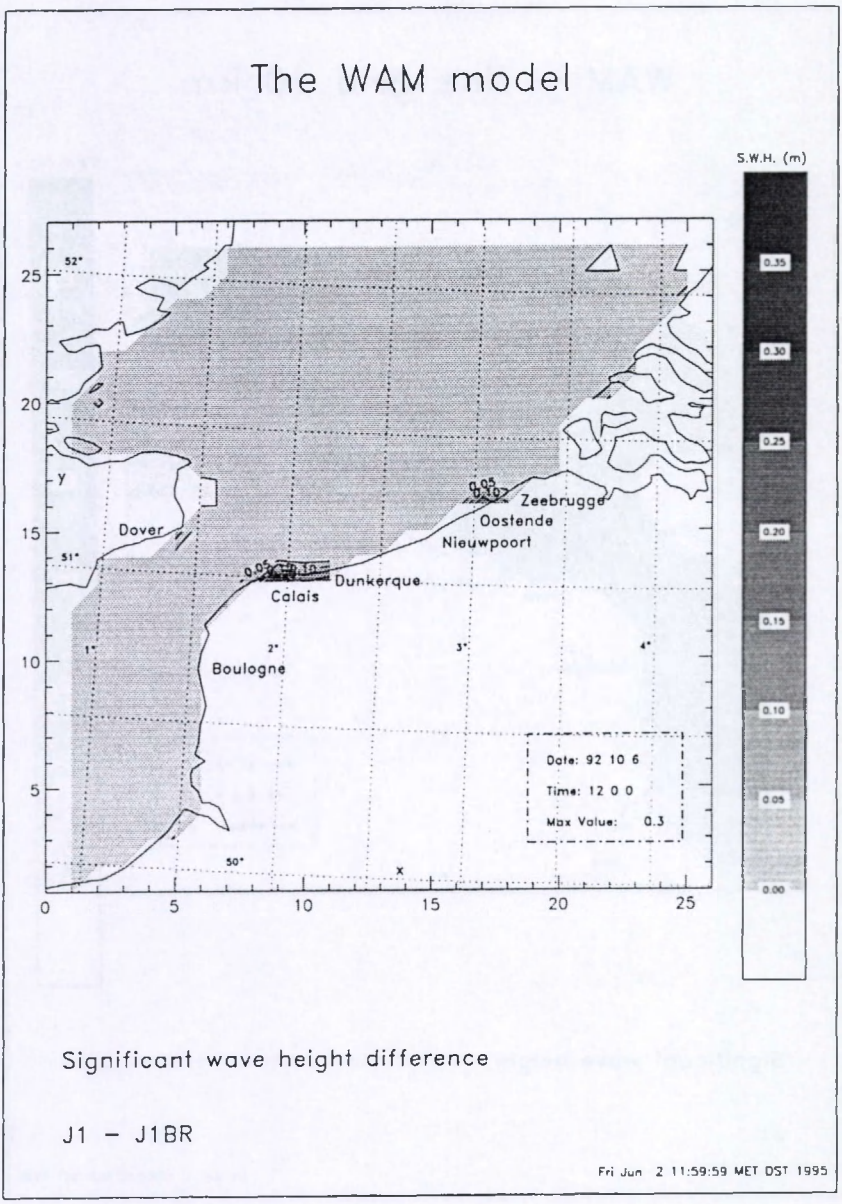

Figure 6.3: The significant wave height difference between the runs J1 and J1BR at 12h GMT 6th of October 1992.

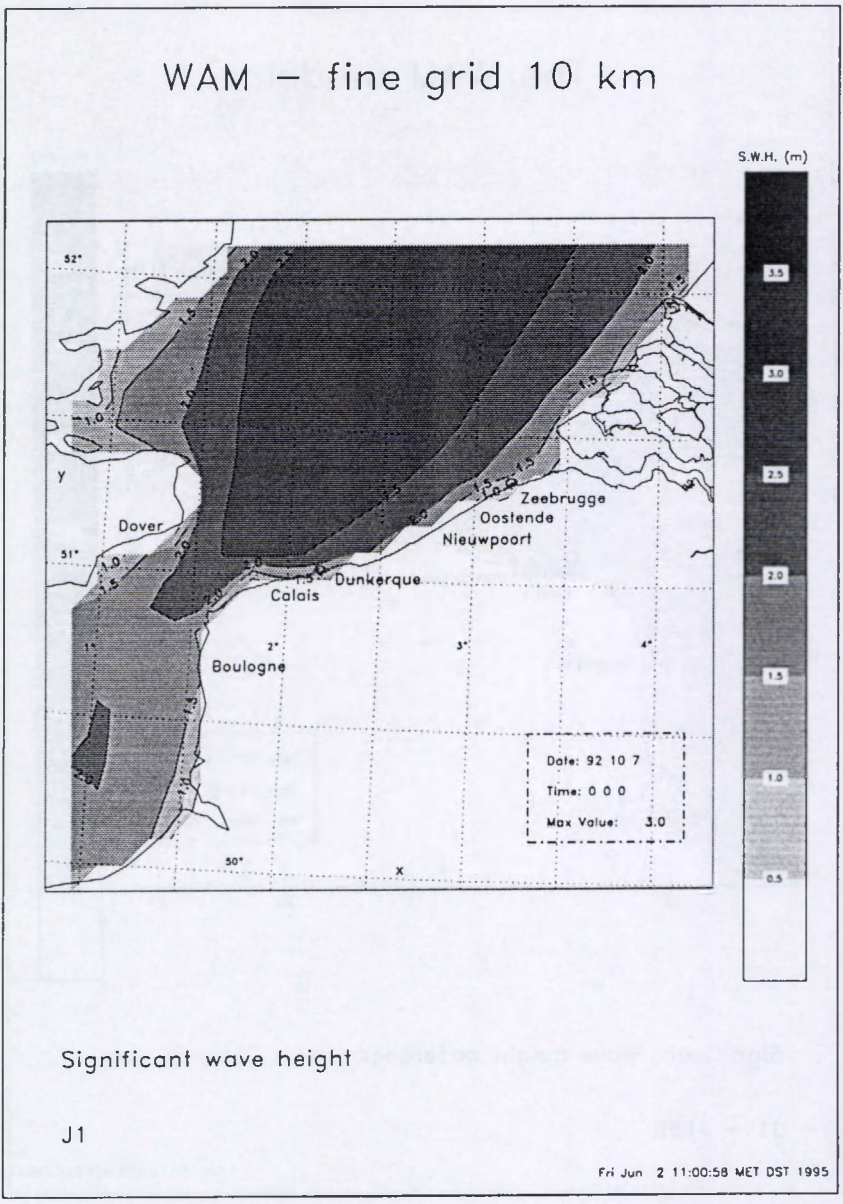

Figure 6.4: The significant wave height predicted by the WAM Cycle 4 (J1) at 12h GMT 6th of October 1992.

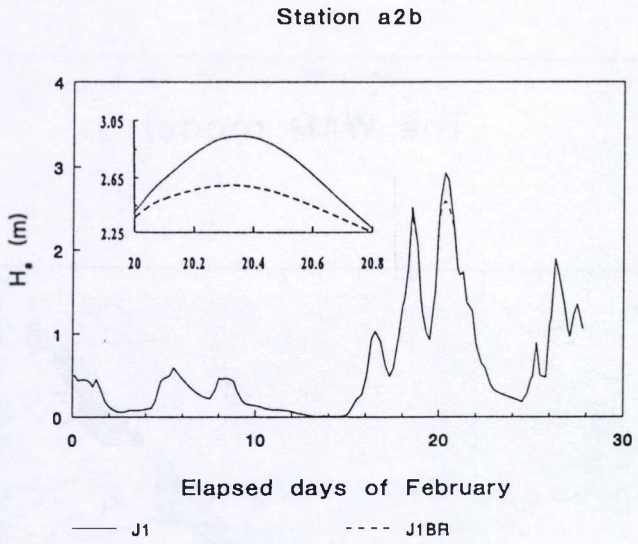

Figure 6.5: The time series of significant wave height from J1, J1BR and buoy for February 1993.

the time series of the predicted significant wave height by the model runs with (J1BR) or without (J1) inclusion of wave breaking. It is found that the maximum effect of the wave breaking on the wave height is in the order of 15% at a2b in storm conditions (21st of February 1993). However, buoy data are needed to verify this effect.

In figure 6.6, the significant wave height difference between model runs (J1 and J1BR) without and with wave breaking is displayed at 7.2h GMT 21st of February 1993 for the global fine grid domain. Figure 6.7 gives the wave height prediction for the fine grid domain at 7.2h GMT 21st of February 1993. In front of the Belgian coast, wave height as large as 3 m is hindcasted by the model. Near the harbour Zeebrugge, the effect of wave breaking on the significant wave height was found in the order of 0.3 m, the wave height is decreased about 12%. The maximum effect of wave breaking on the wave height was found near the Dutch coast, in the order of 1.1 m, which is a reduction of about 40%.

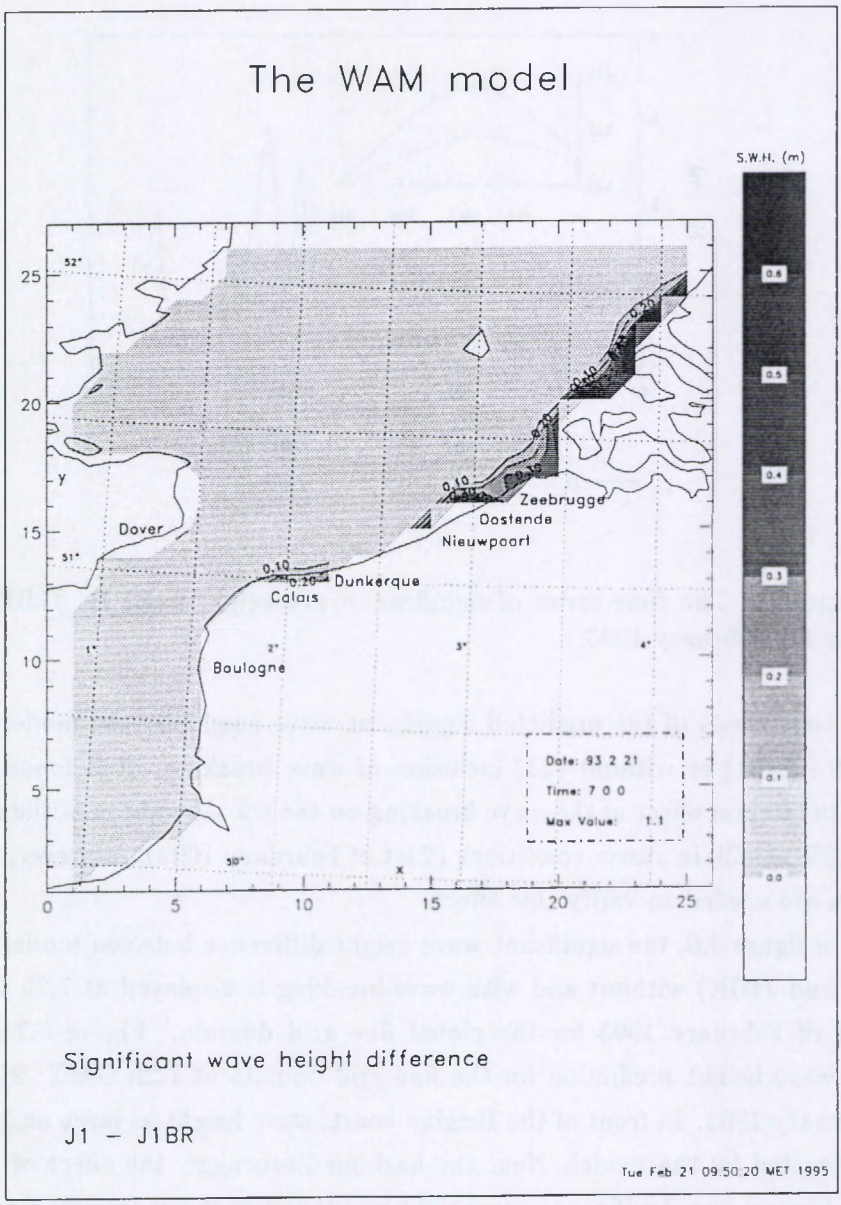

Figure 6.6: The significant wave height difference between J1 and J1BR runs at 7.2h GMT 21st of February 1993.

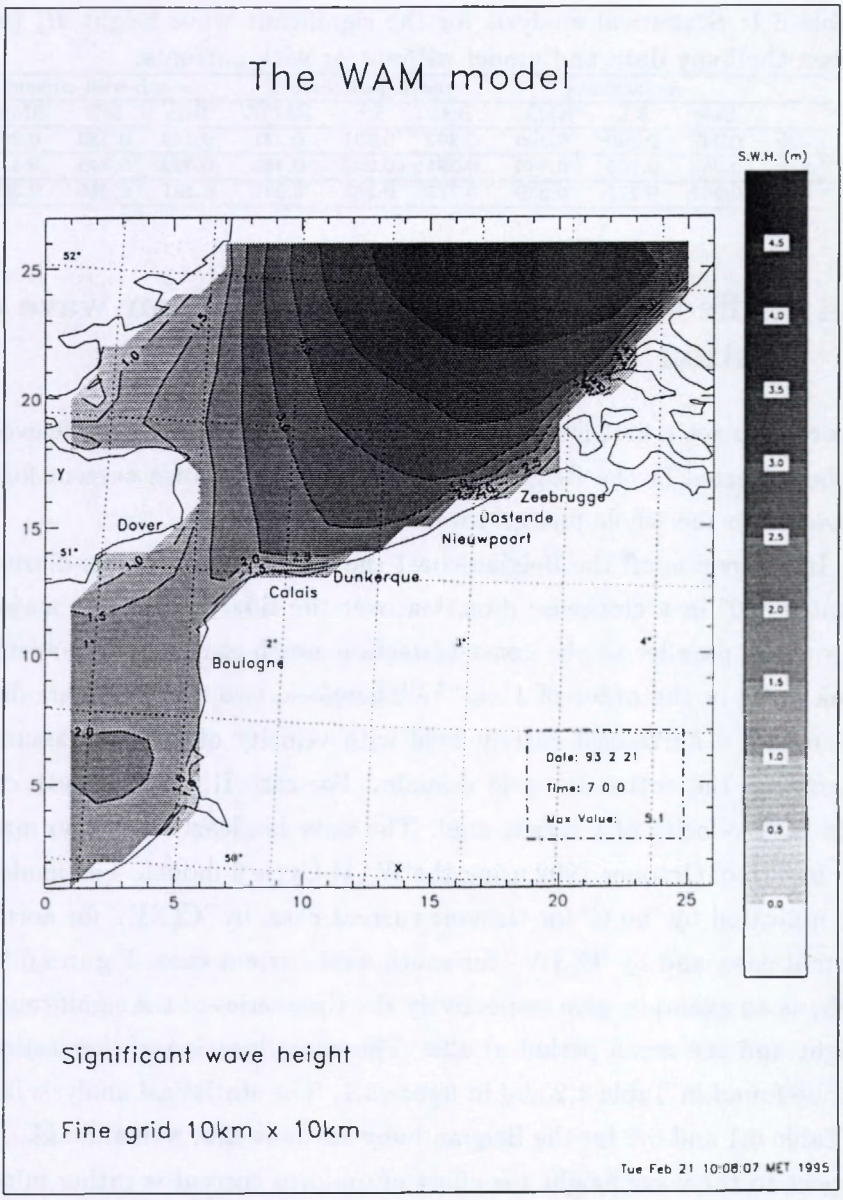

Figure 6.7: The significant wave height predicted by the WAM Cycle 4 (J1) at 7.2h GMT 21st of February 1993.

Table 6.1: Statistical analysis for the significant wave height H_s (m) between the buoy data and model without or with currents.

	no currents			north-east current			south-west current		
	Bias	S.I.	RMSE	Bias	S.I.	RMSE	Bias	S.I.	RMSE
a2b	0.247	0.340	0.306	0.262	0.361	0.321	0.228	0.320	0.291
akk	0.362	0.265	0.440	0.381	0.273	0.450	0.323	0.246	0.414
weh	0.262	0.271	0.330	0.275	0.287	0.347	0.231	0.246	0.304

6.4 Effect of uniform current field on wave evolution

In order to get a first insight in the effect of current on the wave evolution to be expected in the Belgian shallow waters, a uniform current field was imposed on the whole fine grid wave field.

In the region off the Belgian coast the tidal current is semi-diurnal and rotates 360° in a clockwise direction over the tidal cycle. The major axis is roughly parallel to the coast (direction north-east or south-west) with peak flows in the order of 1 ms^{-1}. Therefore, two test cases are defined. For case I, a north-east current field with velocity of 1 m/s is assumed to impose on the entire fine grid domain. For case II, a west-south current field with velocity of 1 m/s is used. The wave hindcast study was made for the month of October 1992 using the WAM Cycle 4 model. The model runs are indicated by 'no C' for without current case, by 'C(NE)' for north-east current case, and by 'C(SW)' for south-west current case. Figures 6.8a and 6.8b, as an example, give respectively the time series of the significant wave height and the mean period at a2b. The exact location of the station a2b can be found in Table 4.2 and in figure 6.1. The statistical analysis is given in Table 6.1 and 6.2 for the Belgian buoy stations a2b, weh and akk. With respect to the wave height the effect of uniform current is rather minor (in the order of $\pm 2\%$ for H_s). The current affects the mean period significantly (in the order of $\pm 15\%$ for T_m).

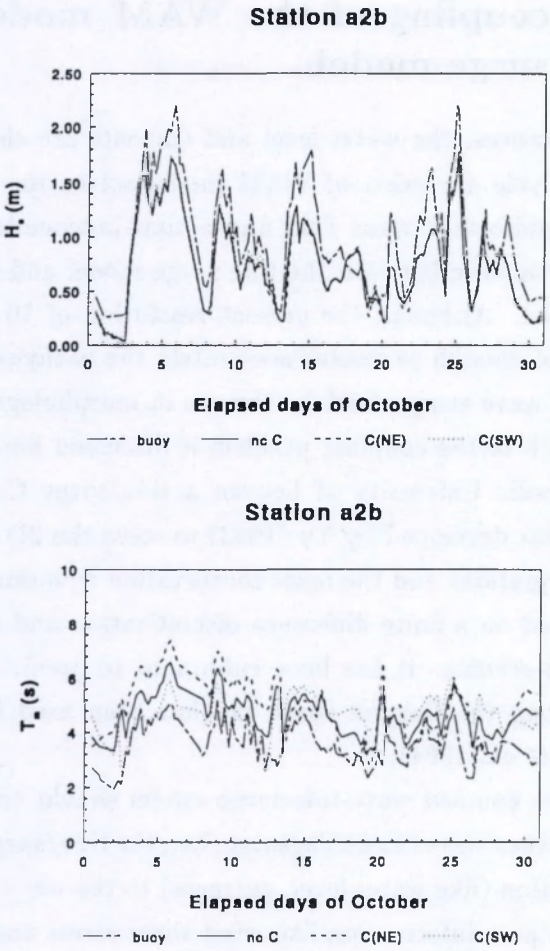

Figure 6.8: Time series of the significant wave height and the mean frequency at station a2b: (a) significant wave height; (b) mean period.

Table 6.2: Statistical analysis for the mean period T_m (s) between the buoy data and model in cases of without or with currents.

	no currents			north-east current			south-west current		
	Bias	S.I.	RMSE	Bias	S.I.	RMSE	Bias	S.I.	RMSE
a2b	-1.113	0.309	1.271	-1.336	0.394	1.660	-1.068	0.311	1.277
akk	-1.025	0.235	1.162	-1.490	0.301	1.555	-0.588	0.206	0.979
wch	-0.528	0.156	0.754	-0.663	0.230	1.123	-0.489	0.161	0.772

6.5 The coupling of the WAM model and the tide/surge model

In real circumstances, the water level and currents are changing in time. However, the Cycle 4 version of WAM model solves the energy balance equation for a uniform current field and a time-independent topography. Therefore, the coupling between the tide surge model and the WAM wave model is essential. Although the present resolution of 10 km x 10 km is still far from fine enough to resolve adequately the bathymetry in order to study details of wave energy field for the use in morphological models, one possible approach to the coupling problem is discussed here.

At the Catholic University of Leuven a tide/surge Continental Shelf Model (CSM) was developed by Yu (1993) to solve the 2D depth averaged shallow water equations and the mass conservation equation. The model is constructed based on a finite difference discretization and a modified ADI time integration scheme. It has been calibrated to predict accurately the tidal motion along the Belgian coast and has been used for storm surge simulation (Yu *et al.*, 1994).

The complete coupled wave-tide-surge model should consider two-way interactions between waves and tide/surge, i.e., the tide/surge model should provide information (like water level, currents) to the wave model, and the wave model can pass information like wind shear stress and bottom stress to the tide model. The first stage of coupling, i.e., one way interaction of the current field passed to the wave model, is discussed here (also see Monbaliu and Luo, 1995). For this kind of coupling, the wave model and the tide/surge model run separately. The current data and the water-level data can be saved every propagation time step in the CSM model. There is a need to update the current field and the water depth in the coupled model. In the WAM4 model, current and water depth information is read in a preprocessing program called PREPROC. In order to update this information in the main program CHIEF, it is necessary to adjust this main program. In the approach taken here the program is adjusted as to make optimal

use of existing routines. In the coupled model, a short subroutine, called COWAM, is written where currents and bathymetry fields are dynamically fetched. A flow chart showing the approach can be found in Monbaliu and Luo (1995). Therefore, the coupled model (COWAM4) will update the bottom dissipation and depth refraction by using the updated water depth, the current refraction by using the updated current information.

The COWAM4 model has been implemented on the fine grid, where the open boundary conditions were determined by the previous coarse results from the WAM4 model. In order to check all the different routines and files structures, an artificial current changing in magnitude but with a constant direction (+ or -) and an artificial water-level change, which are representing the major tidal motion at the Belgian coast, were introduced. Although the approximation is rough, it gives a first indication of what effects are to be expected. Figures 6.9a and 6.9b show the comparison of the significant wave height and the mean period prediction from WAM4 and COWAM4 at station a2b. With respect to the wave height the difference between WAM4 and COWAM4 was in the order of 15% and depth refraction seemed to be dominant. For the mean period the dominant effect is from the current (about 25%), since this influence is felt directly.

6.6 Conclusions

The WAM Cycle 4 model was extended with inclusion of depth-induced wave breaking for the application in the Belgian coastal shallow region. The hindcast study was made on the fine grid domain for the period of October 1992 and of February 1993. It is found that the effect of depth-induced wave breaking is particularly important on the wave evolution in very shallow regions and in very strong storm conditions. More shallow water data is needed to verify the magnitude of this effect. A lot of work still remains to improve our understanding of wave breaking dissipation. It is also instructive to quantitatively investigate the effects of depth-limited wave breaking on the energy balance in fetch-limited near-shore shallow

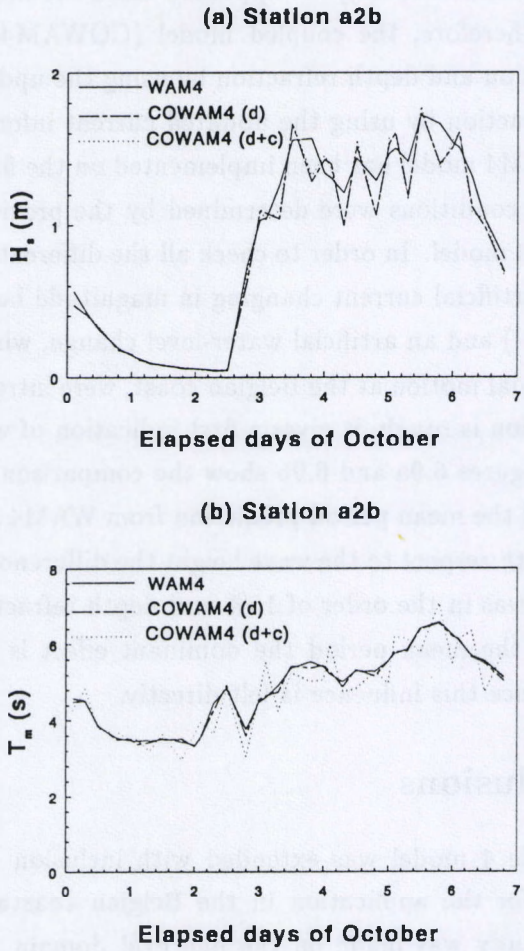

Figure 6.9: Time series of the significant wave height and the mean period from WAM4 and COWAM4: (a) significant wave height; (b) mean period ('d' for 'depth refraction coupled'; 'd+c' for 'depth and current refraction coupled').

water conditions.

To assess the changes in the significant wave height and in the mean frequency from the wave-current interactions, an academic test was made by the use of the WAM Cycle 4 assuming the uniform current field imposed on the fine grid model domain near the Belgian coast. It is concluded that the uniform current has a minor effect on the wave height ($\pm 2\%$) but a significant influence on the mean period ($\pm 15\%$). To improve the wave prediction by using the WAM Cycle 4, it is very essential to couple the wave model and the tidal/surge model so that the model results 'correctly' represent the wave-currents interactions.

A coupled wave-tide-surge model (COWAM4) was developed to account for the effects of non-stationary depth and currents on wave evolution in the Belgian coastal zone. The primary results from COWAM4 with an artificial tide and current indicated that the effect of tide and surge currents and water depth variations on wave evolution is significant (in the order of 15% for H_s and 25% for T_m) in the Belgian coastal waters.

Further work requires the use of the 'real' currents and the 'real' water level predicted by the CSM model in a much finer (than 10 km) nested grid model domain. Validation of the model results against measurements is needed.

Chapter 7

Summary, Conclusions and Recommendations

In this work, attempts have been made to investigate the effects of bottom friction, depth-induced wave breaking, tidal motions and whitecapping dissipation on the wave evolution in shallow water, and to apply the wave model (WAM Cycle 4) to the Belgian coastal waters.

7.1 Effects of different bottom friction formulations on the energy balance

The energy transfer equation has been solved numerically for fetch-limited conditions in waters of limited depth with the five original formulations for the bottom friction dissipation. They are an empirical expression based on the JONSWAP experiment (Hasselmann *et al.*, 1973), three drag law models (Hasselmann and Collins, 1968; Collins, 1972; Madsen *et al.*, 1988) and the eddy viscosity model (Weber, 1991a). The effects of different formulations on the energy balance were inter-compared and evaluated. The results were also compared with the Coastal Engineering Research Centre growth curves. It is found that the formulation of the bottom friction dissipation has quite a significant effect on the energy balance at shallower water depths. It has little effect on the energy balance at larger water depths.

Among the five original formulations for the bottom friction dissipation, a difference as big as 70% for the total energy was reported for a water depth of 15 m and a wind friction velocity of 0.71 ms^{-1}. The empirical JONSWAP formulation with a mean coefficient of 0.038 m^2s^{-3} (Hasselmann *et al.*, 1973) predicts the highest asymptotic energy levels and the lowest asymptotic peak frequency levels; the simplified drag law expression ($C_f = 0.015$, Collins, 1972) yields higher asymptotic energy levels and lower asymptotic frequency levels than the eddy viscosity formulation ($K_N = 4$ cm, Weber, 1991a) and the drag law formulation ($C_f = 0.015$, Hasselmann and Collins, 1968); the Madsen *et al.* drag law model ($K_N = 4$ cm) results in the lowest asymptotic energy levels and the highest asymptotic peak frequency levels. This finding is explained by the fact that the values for the dissipation coefficient C from the five original formulations are quite different and therefore have a different effect when the energy is integrated over the frequency and the angle space.

It is revealed that the whitecapping dissipation is dominant in shallow water. The contribution of bottom friction varies clearly with depth, and also from formulation to formulation. The role of bottom friction dissipation becomes more and more significant when the water becomes more and more shallow, for example, for a water depth of 15 m the total bottom friction dissipation is nearly half of the total whitecapping dissipation. For all five formulations a good balance between the various source terms was found. The bottom friction dissipation is comparable to the whitecapping dissipation on the forward face of the spectrum and around the peak frequency. While on the backward face of the spectrum, the energy is mainly balanced by whitecapping dissipation and nonlinear interactions, and the bottom friction dissipation is rather small. The absolute peak values of the source terms are different for the five bottom friction dissipation models considered.

It has been proven mathematically and numerically that in shallow water cases the scaling ability of energy growth curves with the air friction velocity is model-dependent. The growth curves from the drag law models

with a fixed dissipation coefficient C_f scale with the air friction velocity u_{a*}. The drag law model with a dynamically changing friction factor, the empirical formulation and eddy viscosity model do not scale with the wind friction velocity u_{a*}. It is concluded that the shallow water data which are presented in dimensionless form (scaled with the air friction velocity) cannot be used to evaluate different model results.

7.2 Wave prediction along the Belgian coast

The Cycle 4 version of the WAM model has been implemented on M.U.M.M.'s Convex C230 for wave prediction in the Belgian coastal waters. To verify the implementation of the WAM model on the Convex, a set of benchmark cases supplied with the model was processed. The model transfer from CRAY to CONVEX C230 was successful.

The WAM Cycle 4 model was applied to a coarse grid covering the northwest European continental shelf and to a fine nested grid for the southern North Sea area, where the Belgian coast is located. To evaluate the quality of the WAM model results, validation was made for the period from October 1992 to March 1993 by use of ERS-1 satellite data, buoy data and by the cross comparison between WAM and mu-WAVE.

7.2.1 Validation by use of ERS-1 data

Global grid comparison between the WAM model results and the satellite data showed that the WAM model produces quite good results in the North Sea region and also in the southern North Sea region. However, a large underprediction of the WAM model was found in the whole North Atlantic region. The most severe underestimation of the model lies at the northern and western open sea boundaries. This is due to the fact that the open sea boundaries were treated as fixed walls, where a fetch limited law is applied. The assimilation of the global wave model results forecasted at ECMWF into the coarse grid open boundaries is one measure recommended for future work to improve the model results.

Statistical analysis of the significant wave height between the altimeter data and the WAM model showed that a good agreement between the altimeter and the WAM model is obtained in the North Sea region, with a bias of the order of 0.31 m and a scatter index of the order of 28%. The WAM underestimates the significant wave height for the whole domain, especially in the North Atlantic (open sea) region, with biases of the order of 0.83m.

7.2.2 Validation by use of buoy data

The statistical analysis between the buoy data and the WAM model predictions showed that the WAM model underestimates the significant wave height and overestimates the mean wave period with biases in the order of 0.28 m and 0.56 s, respectively. The significant wave heights predicted by WAM are satisfactory in terms of the bias and the root mean square error as compared to the results found in literature. The scatter index in the order of 36% is too large as compared to that found in literature (in the order of 24%). However, the buoy locations used in this study lie in quite shallow waters, resulting in a higher scatter index than in deep water for similar root mean square errors. The mean period is well simulated by WAM in terms of the bias, the scatter index and the root mean square error as compared to the statistics found in literature.

7.2.3 Comparison between the WAM and the mu-WAVE model

From the global grid comparison between the WAM and the mu-WAVE results it was found that both models perform quite similarly in the North Sea. In the southern North Sea, mu-WAVE predicts a slightly larger significant wave height than WAM. There is a relatively large disparity at the open boundary of the model domain as well as at some physical boundaries. Although both models apply limited fetch laws at these open boundaries, the implementation of these conditions may result in some difference in local behaviour.

The cross comparison between the satellite data, the WAM and the mu-WAVE models results showed that the WAM model produces better results than mu-WAVE for the whole domain, for the North Atlantic region and for the channel region. For the North Sea region, mu-WAVE gives slightly better results than WAM since the mu-WAVE model has been well tuned in the southern North Sea, the main region of interest. Both models underestimate the significant wave height for the whole domain, especially in the North Atlantic (open sea) region.

There exists a good agreement between observation and model hindcast along the satellite subtrack except at the open sea boundary. It was found that the WAM model performs much better for the fast moving storms and responds much faster to wind changes than the mu-WAVE model.

The significant wave height is generally underestimated by both WAM and mu-WAVE when compared to the buoy data. The mu-WAVE model has slightly smaller bias (between the buoy data and the model results) than WAM, with similar scatter indexes and root mean square error. However, WAM in general gives better predictions for storm conditions. The mu-WAVE model underestimates the mean wave period and WAM overestimates it. The reduction of the bias (between the buoy data and model results) achieved by mu-WAVE can be attributed to the fact that mu-WAVE is well tuned in the southern North Sea near the Belgian coast. The better prediction of the wave height by mu-WAVE is at the sacrifice of underestimation of the mean period. The use of tuned source terms in the WAM model should improve the shallow water forecasts.

7.3 Equivalent dissipation coefficients

The equivalent bottom friction dissipation coefficients have been developed so that all five formulations give almost the same growth curves for the total energy and the peak frequency. The equivalent coefficients for the empirical formulation and three drag law models were obtained and referred to the bottom roughness height in the eddy viscosity model for three different

wind velocities and a nondimensional water depth of 300. The introduced error for other water depths is estimated to be of the order of 5%.

The empirical JONSWAP formulation is the most economic model in terms of computation time. The eddy viscosity model is the most expensive one. It needs four times more CPU time than the empirical one. The Madsen *et al.* drag law formulation is the second most expensive model. The simplified drag law expression of Collins is cheaper than the complete drag law formulation of Hasselmann and Collins. For operational wave forecasting models it does not always seem worthwhile to spend the extra calculation effort. The use of the empirical JONSWAP formulation with the equivalent coefficients is for many practical operational applications not only computationally efficient, but it should also produce results with the same order of accuracy as the more sophisticated models for the bottom friction dissipation. It remains essential to use different c values for different circumstances where the bottom roughness height appears different. An equivalent coefficient in the empirical expression calibrated according to the local flow conditions can cover a wide range of practical conditions and should therefore suffice in most circumstances.

The eddy viscosity model and one of the drag law expressions (Collins, 1972) have been implemented in the Cycle 4 of the WAM model for the computation of bottom friction dissipation. The wave hindcast for the period running from the 1st to the 28th February 1993 was made using the Cycle 4 WAM with three different bottom dissipation models in the southern North Sea area. The hindcast results were compared with the buoy data. The comparison shows that the performances of different bottom friction models are quite different for the storm condition and for the whole period average at the two buoy stations. The use of a fixed bottom roughness height (in the eddy viscosity model) or a fixed c value (in the empirical formulation) for the whole prediction domain and the whole period is unrealistic. The equivalent dissipation coefficients tuned for storm conditions predict quite closely H_s, and also improve the results for the whole period average.

For different stations, different equivalent dissipation coefficients are

suggested. At station k13, the equivalent coefficient c with $0.038 m^2 s^{-3}$ for the empirical formulation, the K_N of $0.69 cm$ for the bottom roughness height in the eddy viscosity model and the C_f of 0.015 for the Collin's expression have improved the significant wave height results for both the storm condition and the calm condition. For station ym6, another set of the dissipation coefficients (the c of $0.0667 m^2 s^{-3}$ for the empirical formulation, the K_N of $4.0 cm$ for the eddy viscosity model and the C_f of 0.015 for the Collin's expression) yielded better results.

7.4 Wave breaking and currents effects

The bathymetry of the Belgian coastal zone is very complicated and the water depths are quite limited. The water-level change, currents variation and the wave breaking due to limited depth become clearly very important to the wave evolution.

The WAM Cycle 4 model was extended with inclusion of depth-induced wave breaking for the application to the Belgian coastal shallow region. The hindcast study was made on the fine grid domain for the period of October 1992 and of February 1993. It is found that the effect of depth-induced wave breaking is particularly important on the wave evolution in very shallow regions and in very strong storm conditions. More buoy data are needed to verify this effect.

To assess the changes in the significant wave height and in the mean frequency from the wave-current interactions, an academic test was made by the use of the WAM Cycle 4 assuming a uniform current field imposed on the fine grid model domain near the Belgian coast. It is concluded that the uniform current affects the wave height slightly ($\pm 2\%$) but influences the mean period significantly ($\pm 15\%$).

A coupled wave-tide-surge model (COWAM4) was developed to account for the effects of non-stationary depth and currents on wave evolution in the Belgian coastal zone, in which a one-way interaction was considered. The primary results from COWAM4 with the artificial tide and current

indicated that the effect of tide and surge currents and water depth variations on wave evolution is significant (in the order of 15% for H_s and 25% for f_m) in the Belgian coastal waters.

7.5 Recommendations for future work

The following recommendations are made for the further extension of the present study.

1)For research work regarding the dissipation modelling, especially when connected to morphological processes, a model with a better description of what happens inside the wave boundary layer is preferable. The eddy viscosity model and the drag law model with variable friction factor (with or without movable-bed effects) can provide more detailed information about the bottom boundary layer, and are therefore believed to be physically more correct. However, there is no data evidence to show one preferable to the other. Further study is essential to clarify the true story.

2)In this study, the effect of the tidal current on the bottom friction dissipation has been neglected. In a combined wave-current situation like the Belgian coast this is not necessarily justified when one deals with the wave energy field for the use in morphological models. A two-layer eddy viscosity model as e.g. proposed by Christoffersen and Jonsson (1985) may be a better representation of the combined wave-current flow than a one-layer drag law or a one-layer eddy viscosity model.

3) To improve the wave prediction by the WAM model along the Belgian coastal waters, future efforts are required in the area of data assimilation, with a high resolution in space and direction. More wave physics such as triad nonlinear interactions should be included in the very shallow coastal regions. In the long run the third generation model should replace the current second generation model in use for wave forecasts in the Belgian shallow waters.

4) The coupling of the WAM Cycle 4 model to a tidal/surge (CSM) model has to be investigated further in order to take account for the wave-

currents interactions. Future work should achieve the use of 'real' currents and the 'real' water level predicted from the tidal/surge model (such as CSM model) in a much finer (than 10 km) nested grid for the model domain. Not only do water depth and currents have an effect on the wave evolution (one-way interaction), but the waves have an influence on currents and water levels, i.e., two-way interactions should be considered. Validation of the model results against measurements is needed. Future works (e.g., the coming European Community PROMISE - PReOperational Modelling In the Seas of Europe - project) should improve our understanding of the wave-current interactions.

5) The depth-induced wave breaking was included in this work, which was based on the Battjes and Janssen (1978) expression on the assumption that the breaking does not alter the spectral shape. Although this assumption was supported by the laboratory observations of Beji and Battjes (1993), the limited range of these experimental conditions does not allow wide-ranging conclusions. Further research work is needed in this topic. It is also instructive to quantitatively investigate the effects of depth-limited wave breaking (and triad nonlinear interactions) on the energy balance in fetch-limited shallow water conditions.

Bibliography

1. Abdalla, S. and E. Özhan (1993), "Third-generation wind-wave model for use on personal computers", *J. Waterway, Port, Coastal, and Ocean Eng.*, **119**, 1-14.

2. Abramowitz, M. and I.A. Stegun (1965), "Handbook of mathematical functions", National Bureau of Standards, Washington, D.C.

3. Arthur, R.S.(1949), "Variability in direction of wave travel in ocean surface waves", *Ann. N. Y. Acad. Aci.*, **51**, 511-522.

4. Battjes, J.A. and J.P.F.M. Janssen (1978), "Energy loss and set-up due to breaking of random waves",*Proc. 16th Int. Conf. on Coastal Eng.*, 569-587.

5. Battjes, J.A. and M.J.F. Stive (1985), "Calibration and verification of a dissipation model for random breaking waves", *J. Geophys. Res.*, **90**, (C5), 9159-9167.

6. Beji, S. and J.A. Battjes (1993), "Experimental investigation of wave propagation over a bar", *Coastal Engineering*, **19**, 151-162.

7. Bouws, E. and G.J. Komen (1983), "On the balance between growth and dissipation in an extreme depth-limited wind-sea in the southern North Sea", *J. Phys. Oceanogr.*, **13**, 1653-1658.

8. Brink-Kjaerm, O. (1984), "Depth-current refraction of wave spectra", in Symposium on Description and Modelling of Directional Seas, Paper no. C-7, Technical University Denmark.

9. Cavaleri, L. and P.M. Rizzoli (1981), "Wind wave prediction in shallow water: theory and applications", *J. Geophys. Res.*, **86**, (C11), 10961-10973.

10. Cavaleri, L., L. Bertotti and L. Lionello (1988), "Adriatic implementation of a third generation wave model", *Computer Modelling in Ocean Eng.*, Schrefler and Zienkiewicz (eds) Balkema, Rotterdam.

11. Cavaleri, L., L. Bertotti and P. Lionello (1989), "Shallow water application of the third-generation WAM wave model", *J. Geophys. Res.*, **94**, (C6), 8111-8124.

12. Cavaleri, L., L. Bertotti and P. Lionello (1991), "Wind wave cast in the Mediterranean Sea", *J. Geophys. Res.*, **96**, (C6), 10739-10764.

13. CERC (Coastal Engineering Research Center) (1977), "Shore protection manual", *Fort Belvoir, va.*, **1-3**.

14. Charnock, H. (1955), "Wind stress on a water surface", *Q. J. Royal Meteorol. Soc.*, **81**, 639-640.

15. Christoffersen, J.B. (1982), "Current depth refraction of dissipative water waves", Series paper **30**, Institute of Hydrodynamics and Hydraulic Engineering, Technical University of Denmark.

16. Christoffersen, J.B. and I.G. Jonsson (1985), "Bed friction and dissipation in a combined current and wave motion", *Ocean Eng.*, **12**, 387-423.

17. Collins, J.I.(1972), "Prediction of shallow water spectra", *J. Geophys. Res.*, **93** (C1), 491-508.

18. Dingler, J.R. and D.L. Inman (1976),"Wave-formed ripples in nearshear sands",*Proc. 15th Conf. Coastal Eng.*, Honolulu, 2109-2126.

19. ERS-1 User Handbook (1993), "ERS Publication Division c/o ESTEC", Noordwijk, The Netherlands.

20. Gelci, R., H. Cazalé and J. Vassal (1956), "Utilization des diagrammes de propagation à la Prévision énergétique de la houle", *Bulletin d'information du comité Central d'océanographie et d'études des côtes*, **8**, No. 4, 170-187.

21. Gelci, R., H. Cazalé and J. Vassal (1957), "Prévision de la houle. La méthode des densités spectroangulaires", *Bulletin d'information du comité Central d'océanographie et d'études des côtes*, **9**, 416-435.

22. Grant, W.D. and O.S. Madsen (1982), "Movable bed roughness in unsteady oscillatory flow", *J. Geophys. Res.*, **87**, (C1), 469-481.

23. Günther, H., S. Hasselmann and P.A.E.M. Janssen (1992), "The WAM model cycle 4", Report No. 4, Hamburg.

24. Graber, H.C. and O.S. Madsen (1988), "A finite-depth wind wave model. Part 1: Model description", *J. Phys. Oceanogr.*, **18**, 1465-1483.

25. Hasselmann, K. (1962), "On the non-linear energy transfer in a gravity-wave spectrum, part 1: general theory", *J. Fluid Mech.*, **12**, 481-500.

26. Hasselmann, K. (1963a), "On the non-linear energy transfer in a gravity-wave spectrum, part 2: conservation theorems; wave-particle analogy; irreversibility", *J. Fluid Mech.*, **15**, 273-281.

27. Hasselmann, K. (1963b), "On the non-linear energy transfer in a gravity-wave spectrum, part 3: evaluation of energy flux and swell-sea interaction for a Neumann spectrum", *J. Fluid Mech.*, **15**, 385-398.

28. Hasselmann, K. (1974), "On the spectral dissipation of ocean waves due to whitecapping", *Boundary-Layer Meteorol.*, **6**, 107-127.

29. Hasselmann, K., T.P. Barnett, E. Bouws, H. Carlson, D.E. Cartwright, K. Enke, J.I. Ewing, H. Gienapp, D.E. Hasselmann, P. Kruseman, A. Meerbrug, P. Müller, D.J. Olbers, K. Richter, W. Sell and H. Walden

(1973), "Measurements of wind-wave growth and swell decay during the Joint North Sea Wave Project (JONSWAP)", *Dtsch. Hydrogr. Z.*, **A8(12)**, 95p.

30. Hasselmann, K. and J.I. Collins (1968), "Spectral dissipation of finite-depth gravity waves due to turbulent bottom friction", *J. Mar. Res.*, **26**, 1-12.

31. Hasselmann, S. and K. Hasselmann (1981), "A symmetrical method of computing the nonlinear transfer in a gravity wave spectrum", *Hamb. Geophys. Einzelschr., Ser. A., Wiss. Abh.*, **52**, 163p.

32. Hasselmann, S. and K. Hasselmann (1985a), " The wave model EXACT-NL", In: Ocean wave modeling, the SWAMP group, Plenum Press, New York.

33. Hasselmann, S. and K. Hasselmann (1985b), "Computations and parameterizations of the nonlinear energy transfer in a gravity-wave spectrum, part 1: A new method for efficient computations of the exact nonlinear transfer integral", *J. Phys. Oceanogr.*, **15**, 1369-1377.

34. Hasselmann, S., K. Hasselmann, J.H. Allender and T.P. Barnett (1985), "Computations and parameterizations of the nonlinear energy transfer in a gravity-wave spectrum. Part II: Parameterizations of the non-linear energy transfer for application in wave models", *J. Phys. Oceanogr.*, **15**, 1378-1391.

35. Holthuijsen, L.H., N. Nooij and R.C. Herbers (1993), "A spectral wave model for the coastal zone", *Proc. In. Conf. WAVES '93*, New Orleans, 630-641.

36. Hubbert, K.P. and J. Wolf (1991), "Numerical investigation of depth and current refraction of waves", *J. Geophys. Res.*, **96**, (C2), 2737-2748.

37. Janssen, P.A.E.M. (1989), "Wave-induced stress and the drag of air flow over sea waves", *J. Phys. Oceanogr.*, **19**, 745-754.

38. Janssen, P.A.E.M. (1991), "Quasi-linear theory of wind-wave generation applied to wave forecasting", *J. Phys. Oceanogr.*, **21**, 1631-1642.

39. Jonsson I.G. (1966), "Wave boundary layers and friction factors", *Proc. 10th Int. Conf. Coastal Eng.*, Tokyo, Japan, 127-148.

40. Jonsson I.G. (1980), "A new approach to oscillatory rough turbulent boundary layers", *Ocean Eng.*, **7**, 109-152.

41. Jonssen I.G. and N.A. Carlsen (1976), "Experimental and theoretical investigations in an oscillatory turbulent boundary layer", *J. Hydr. Res.*, **14**, 45-60.

42. Kinsman, B. (1965), "Wind waves: their generation and propagation in the ocean surface", Englewood Cliffs, NJ: Prentice-Hall.

43. Kitaigorodskii, S.A. (1962), "Application of the theory of similarity to the analysis of wind- generated water waves as a stochastic process", *Bull. Acad. Sci. USSR Geophys.*, Ser. no. 1, 73p.

44. Kitaigorodskii, S.A., V.P. Krazitskii and M.M. Zaslavskii (1975), "On Phillips theory of equilibrium range in the spectra of wind generated gravity waves", *J. Phys. Oceanogr.*, **5**, 410-420.

45. Komen, G.J., S. Hasselmann and K. Hasselmann (1984), " On the existence of a fully developed wind-sea spectrum", *J. Phys. Oceanogr.*, **14**, 1271-1285.

46. Komen, G.J., L. Cavaleri, M. Donelan, K. Hasselmann, S. Hasselmann, P.A.E.M. Janssen (1994), " Dynamics and Modelling of Ocean Waves", Cambridge University Press, Cambridge, 532p.

47. Li, C.W. and M. Mao (1992), "Spectral modelling of typhoon-generated waves in shallow waters", *J. Hydr. Res.*, **30**, 611-622.

48. Longuet-Higgins, M.S. (1966), "The refraction of sea waves in shallow water", *J. Fluid Mech.*, **1**, 163-176.

49. Luo, W. (1991), "A third generation wave model: investigation of an implicit scheme to simulate the evolution of fetch limited wind wave", Master thesis, Department of Civil Engineering, K.U.Leuven, Belgium, 1991.

50. Luo, W. (1992), "Derivation of energy dissipation due to bottom friction in finite depth ocean waves", Internal report, Department of Civil Engineering, K.U.Leuven, Belgium.

51. Luo, W. (1995), "Implementation of the cycle 4 version of the WAM model in the Belgian shallow zone", Internal report, Department of Civil Engineering, K.U.Leuven, Belgium.

52. Luo, W. and J. Monbaliu (1994), "Effects of the bottom friction formulation on the energy balance for gravity waves in shallow water", *J. Geophys. Res.*, **99**, (C9), 18,501- 18,511.

53. Luo, W., J. Monbaliu and J. Berlamont (1994), "Equivalent dissipation coefficient for different bottom friction dissipation models in depth-limited wind generated waves", in Proc. Int. Symp.: Waves - Physical and Numerical Modelling, Vancouver, Canada, edited by M.Isaacson and M. Quick, 743-752.

54. Luo, W., J. Monbaliu and J. Berlamont (1995), "Test of equivalent dissipation coefficient for different bottom friction dissipation models in southern North Sea", in Advances in Hydro- Science and Engineering, Vol 2, 1215-1222.

55. Maat, N., C. Kraan and W.A. Oost (1991), "The roughness of wind waves", *Boundary Layer Meteorol.*, **54**, 89-103.

56. Madsen O.S., Y.-K. Poon and H.C. Graber (1988a), "Spectral wave attenuation by bottom friction: theory", *Abstract of Proc. 21st Int.*

Conf. Coastal Eng., Malaga, 492-504.

57. Madsen O.S., Y.-K. Poon and H.C. Graber (1988b), "Spectral wave attenuation by bottom friction: theory", *Proc. 21st Int. Conf. Coastal Eng.*, Malaga, 492-504.

58. Mastenbroek, C., V.K. Makin, A.C. Voorips and G.J. Komen (1994), "Validation of ERS-1 altimater wave heights measurements and assimilation in a North Sea wave model", *Glob. Oc. Atm. Sys.*, **2**, 143-161.

59. Masuda, A. (1980), "Nonlinear energy transfer between wind waves", *J. Phys. Oceanogr.*, **10**, 2082-2093.

60. Miles, J.W. (1957), "On the generation of surface waves by shear flows", *J. Fluid Mech.*, **3**, 185-204.

61. Monbaliu, J. (1992), "Wind and waves: Investigation of an optimization approach to parameter estimation", Ph.D thesis, Department of Civil Engineering, K.U. Leuven, Belgium.

62. Monbaliu, J. (1994), "On the use of the Donelan wave spectral parameter as a measure for the roughness of wind waves", *Boundary Layer Meteorol.*, **67**, 277-291.

63. Monbaliu, J. and W. Luo (1995), "Wave modeling along the Belgian coast using the WAM cycle 4 coupled with a storm surge model", in Computer Modelling of Seas and Coastal Regions II, edited by C.A. Brebbia, L. Traversoni and L.C. Wrobel, Computational Mechanics Publications, 319-326.

64. Nayfeh, A.H. (1973), "Perturbation methods", Wiley Interscienc, New York.

65. Ovidio, F. and D. Van den Eynde (1993), "Validation and improvement of the quality of the operational wave model mu-WAVE by

the use of ERS-1 satellite data", Report MUMM/T3/AR01, 29p, MUMM, Gulledelle 100, B-1200 Brussels, Belgium.

66. Ovidio, F., J.-R. Bidlot and D. Van den Eynde (1994a), "Validation and improvement of the quality of the operational wave model mu-WAVE by the use of ERS-1 satellite data", Report MUMM/T3/AR02, 87p, MUMM, Gulledelle 100, B-1200 Brussels, Belgium.

67. Ovidio, F., J.-R. Bidlot and D. Van den Eynde (1995a), "Validation and improvement of the quality of the operational wave model mu-WAVE by the use of ERS-1 satellite data", Report MUMM/T3/AR03, 37p + A.62p, MUMM, Gulledelle 100, B-1200 Brussels, Belgium.

68. Ovidio, F., J.-R. Bidlot, D. Van den Eynde, W. Luo and J. Monbaliu (1994b), "Validation and improvement of the quality of the operational wave model mu-WAVE by the use of ERS-1, buoy data and the WAM forecast", in the Proceedings of the First ERS-1 Pilot Project Workshop, Toledo, Spain, ESA SP-365, 21-28.

69. Ovidio, F., J.-R. Bidlot, D. Van den Eynde, W. Luo and J. Monbaliu (1995b), "ESR-1 data assimilation in a second generation wave model for the North Sea" in the Proceedings of the Fourth International Workshop on Wave Hindcasting and Forecasting, Banff (in press).

70. Panofsky, H.A. and J.A. Dutton (1985), "Atmospheric turbulence. Models and methods for engineering application", John Wiley & Sons.

71. Phillips, O.M. (1957), "On the generation of waves by turbulent wind", *J. Fluid Mech.*, **2**, 417-445.

72. Phillips, O.M. (1977), "The dynamics of the upper ocean", Cambridge University Press, Cambridge, 336p.

73. Pierson, W.J., G. Neumann and R.W. James (1955), "Practical methods for observing and forecasting ocean waves by means of wave spectra and statistics", H.O. Pub. 603, US Navy Hydrographic Office.

74. Riepma, H.W. and E. Bouws (1989), "Preliminary results of the NODWAM wave model", SIWWHF, P.248-256.

75. Romeiser, R. (1993), "Global validation of the wave model WAM over a one-year period using geosat wave height data", *J. Geophys. Res.*, **98**, (C3), 4713-4726.

76. Sell, W. and K. Hasselmann (1972), "Computations of nonlinear energy transfer for JONSWAP and empirical wind-wave spectra", *Rep. Inst. Geophys.*, Univ. Hamburg.

77. Shemdin, O., K. Hasselmann, S.V. Hsiao and K. Herterich (1978), "Nonlinear and linear bottom interaction effects in shallow water", in *Turbulent Fluxes Through the Sea Surface, Wave Dynamics and Prediction*, NATO *Conf. Ser. V*, **1**, 647-665, Plenum, New York.

78. Smith, S.D., R.J. Anderson, W.A. Oost, C. Kraan, N. Maat, J. DeCosmo, K.B. Katsaros, K.L. Davidson, K. Bumke, L. Hasse and H.M. Chadwick (1992), "Sea surface wind stress and drag coefficients: the HEXOS results", *Boundary Layer Meteorol.* **30**, 109-142.

79. Snyder, R.L., F.W. Dobson, J.A. Elliott and R.B. Long (1981), "Array measurements of atmospheric pressure fluctuations above surface gravity waves", *J. Fluid Mech.*, **102**, 1-59.

80. Sverdrup, H.U. and W.H. Munk (1947), "Wind sea and swell: Theory of relations for forecasting", H.O. Pub. 601, US Navy Hydrographic Office, Washington, DC, 44p.

81. SWAMP group (1985), "Sea wave modeling project (SWAMP). An intercomparison study of wind wave predictions models, part 1: Principal results and conclusions", In: Ocean wave modeling, Plenum Press, New York, 256p.

82. SWIM group (1985), "Shallow water intercomparison of wave prediction models (SWIM)", *Q. J. Royal Meteorol. Soc.*, **111**, 1087-1113.

83. Tolman, H.L. (1990), "Wind wave propagation in tidal seas", *Communications on hydraulic and geotechnical engineering*, Delft University of Technology, **Rep. no. 90- 1**, 135pp.

84. Tolman, H.L. (1991a), "Effects of tides and storm surges on North Sea wind waves", *J. Phys. Oceanogr.*, **21**, 766-781

85. Tolman, H.L. (1991b), "A third-generation model for wind waves on slowly varying unsteady, and inhomogeneous depths and current", *J. Phys. Oceanogr.*,**21**, 782-797.

86. Tolman, H.L. (1994), "Wind-waves and moveable-bed bottom-friction", *J. Phys. Oceanogr.*, **24**, 994-1009.

87. Trowbridge, J. and O.S. Madsen (1984), "Turbulent wave boundary layers, 1: model formulation and first order solution", *J. Geophys. Res.*, **89**, (C5), 7989-7999.

88. Van den Eynde, D., Validation of the swell prediction model muWAVE: simulation of the six month period October 1987 to March 1988, Report MUMM for project Deiningsprediktiemodel, Gulledelle 100, B-1200 Brussels, Belgium, 1991.

89. Van Rijn, L.C. (1991), "Principles of fluid flow and surface waves in rivers, estuaries, seas, and oceans", AQUA Publications.

90. Verhagen, L.A. and I.R. Young (1995), "The growth of wind waves in shallow water", *Proc. 24th Int. Conf. on Coastal Eng.*, Kobe, Japan (in press).

91. Vledder, G.Ph. van, J.G. de Ronde and M.J.F. Stive (1995), "Verification of a full spectral wind wave model in extremely shallow water", *Proc. 24th Int. Conf. on Coastal Eng.*, Kobe, Japan (in press).

92. WAMDI Group (1988), "The WAM model - a third generation ocean wave prediction model", *J. Phys. Oceanogr.*, **18**, 1775-1810.

93. Webb, D.J. (1978), "Non-linear transfers between sea waves", *Deep-sea Res.*, **25**, 279-298.

94. Weber, S.L.(1988), "The energy balance of finite depth gravity waves", *J. Geophys. Res.*, **93** (C4), 3601-3607.

95. Weber, S.L.(1989), "Surface gravity waves and turbulent bottom friction", *PhD thesis*, University of Utrecht, The Nederlands.

96. Weber, S.L.(1991a), "Eddy-viscosity and drag-law models for random ocean wave dissipation", *J. Fluid Mech.*, **232**, 73-98.

97. Weber, S.L.(1991b), "Bottom friction for wind sea and swell in extreme depth-limited situations", *J. Phys. Oceanogr.*, **21**, 149-172.

98. Wu, J. (1982), "Wind-stress coefficients over sea surface from breeze to hurricane", *J. Geophy. Res.*, **87**, (C12), 9704-9706.

99. Young, I.R. (1988), "A shallow water spectral model", *J. Geophys. Res.*, **93**, (C5), 5113-5129.

100. Young, I.R. and L.A. Verhagen (1994), "The evolution of wind-waves in finite depth water", in The Air Sea Interface, edited by M.A. Donelan, W.H. Hui, and W.J. Plant, The University of Toronto Press, Toronto.

101. Yu, C.S. (1993), "Modelling shelf sea dynamics", Ph.D thesis, Department of Civil Engineering, K.U.Leuven, Belgium.

102. Yu, C.S., Marcus, M. and Monbaliu, J. (1994), "Numerical modelling of storm surges along the Belgian coast", in *Proc. of Int. Conf. on Computation Methods in Water Resources X*, UK, 1331-1340.

103. Zambresky, L.F. (1986a), "The WAMS project, study II: second test of a shallow water, third generation model against data", unpublished report, KNMI, De Bilt, The Netherlands.

104. Zambresky, L.F. (1986b), "The WAMS project, study III: a study of surface winds", unpublished report, KNMI, De Bilt, The Netherlands.

105. Zambresky, L.F. (1989), "A verification study of the global WAM model: December 1987 - November 1988", ECMWF Techn. report 63, ECMWF, Reading.

Appendix A

Rate of Change of Frequency

In Chapter 2, the rate of change of (apparent) frequency is given by equations (2.37) and (2.39). How are these two formulations derived from the definition equation?

$$c_\Omega = \frac{d\Omega}{dt} \tag{A.1}$$

Remind the following relations:

$$\begin{aligned}
\omega^2 &= gk \tanh kh \\
(c_g)_i &= \frac{\partial \omega}{\partial k_i} = \frac{\partial \omega}{\partial k}\frac{k_i}{k} = c_g(\sin\theta, \cos\theta) \\
\Omega &= \omega + \mathrm{k}\cdot\mathrm{U} \\
(c_{ga})_i &= \frac{\partial \Omega}{\partial k_i} = \frac{\partial \omega}{\partial k_i} + u_i \\
\frac{d}{dt} &= \frac{\partial}{\partial t} + (c_{ga})_j \frac{\partial}{\partial x_j} \\
(c_{ga})_1 &= c_x = c_g \sin\theta + u \\
(c_{ga})_2 &= c_y = c_g \cos\theta + v
\end{aligned}$$

$$\frac{\partial k_i}{\partial t} + \frac{\partial \Omega}{\partial x_i} = 0$$

where i equals to 1 and 2.

Since $\Omega = \Omega(\mathbf{k}, \mathbf{U}, h)$, one can easily find that

$$\begin{aligned}
\frac{d\Omega}{dt} &= \frac{\partial \Omega}{\partial t} + (c_{ga})_j \frac{\partial \Omega}{\partial x_j} \\
&= \frac{\partial \Omega}{\partial k_j}\frac{\partial k_j}{\partial t} + \frac{\partial \omega}{\partial h}\frac{\partial h}{\partial t} + \frac{\partial \Omega}{\partial u_j}\frac{\partial u_j}{\partial t} + (c_{ga})_j \frac{\partial \Omega}{\partial x_j} \\
&= (c_{ga})_j(-\frac{\partial \Omega}{\partial x_j}) + \frac{\partial \omega}{\partial h}\frac{\partial h}{\partial t} + k_j \frac{\partial u_j}{\partial t} + (c_{ga})_j \frac{\partial \Omega}{\partial x_j} \\
&= \frac{\partial \omega}{\partial h}\frac{\partial h}{\partial t} + k_j \frac{\partial u_j}{\partial t} \\
&= \frac{\partial \omega}{\partial h}\frac{\partial h}{\partial t} + k \sin\theta \frac{\partial u}{\partial t} + k \cos\theta \frac{\partial v}{\partial t} \qquad \text{(A.2)}
\end{aligned}$$

The formulation of $\frac{d\omega}{dt}$ is derived as follows:

$$\begin{aligned}
\frac{d\omega}{dt} &= \frac{\partial \omega}{\partial h}\frac{dh}{dt} + \frac{\partial \omega}{\partial k_i}\frac{dk_i}{dt} \\
&= \frac{\partial \omega}{\partial h}(\frac{\partial h}{\partial t} + (c_{ga})_i \frac{\partial h}{\partial x_i}) + \frac{\partial \omega}{\partial k_i}(\frac{\partial k_i}{\partial t} + (c_{ga})_j \frac{\partial k_i}{\partial x_j}) \qquad \text{(A.3)}
\end{aligned}$$

and

$$\begin{aligned}
\frac{\partial k_i}{\partial t} &= -\frac{\partial \Omega}{\partial x_i} \\
&= -\frac{\partial \Omega}{\partial k_j}\frac{\partial k_j}{\partial x_i} - \frac{\partial \Omega}{\partial h}\frac{\partial h}{\partial x_i} - \frac{\partial \Omega}{\partial u_j}\frac{\partial u_j}{\partial x_i} \\
&= -(c_{ga})_j \frac{\partial k_i}{\partial x_j} - \frac{\partial \omega}{\partial h}\frac{\partial h}{\partial x_i} - k_j \frac{\partial u_j}{\partial x_i} \qquad \text{(A.4)}
\end{aligned}$$

substitute equation(A.4) into equation(A.3)

$$\begin{aligned}
\frac{d\omega}{dt} &= \frac{\partial \omega}{\partial h}(\frac{\partial h}{\partial t} + ((c_g)_i + u_i)\frac{\partial h}{\partial x_i}) + \frac{\partial \omega}{\partial k_i}(-\frac{\partial \omega}{\partial h}\frac{\partial h}{\partial x_i} - k_j \frac{\partial u_j}{\partial x_i}) \\
&= \frac{\partial \omega}{\partial h}(\frac{\partial h}{\partial t} + u_i \frac{\partial h}{\partial x_i}) - c_g \frac{k_i k_j}{k}\frac{\partial u_j}{\partial x_i} \qquad \text{(A.5)}
\end{aligned}$$

i.e.,

$$\begin{aligned}
\frac{d\omega}{dt} &= \frac{\omega k}{\sinh 2kh}(\frac{\partial h}{\partial t} + u\frac{\partial h}{\partial x} + v\frac{\partial h}{\partial y}) \\
&\quad -c_g k \sin\theta(\sin\theta \frac{\partial u}{\partial x} + \cos\theta \frac{\partial u}{\partial y}) \\
&\quad -c_g k \cos\theta(\sin\theta \frac{\partial v}{\partial x} + \cos\theta \frac{\partial v}{\partial y}) \qquad \text{(A.6)}
\end{aligned}$$

Appendix B

The Stereographic Projection

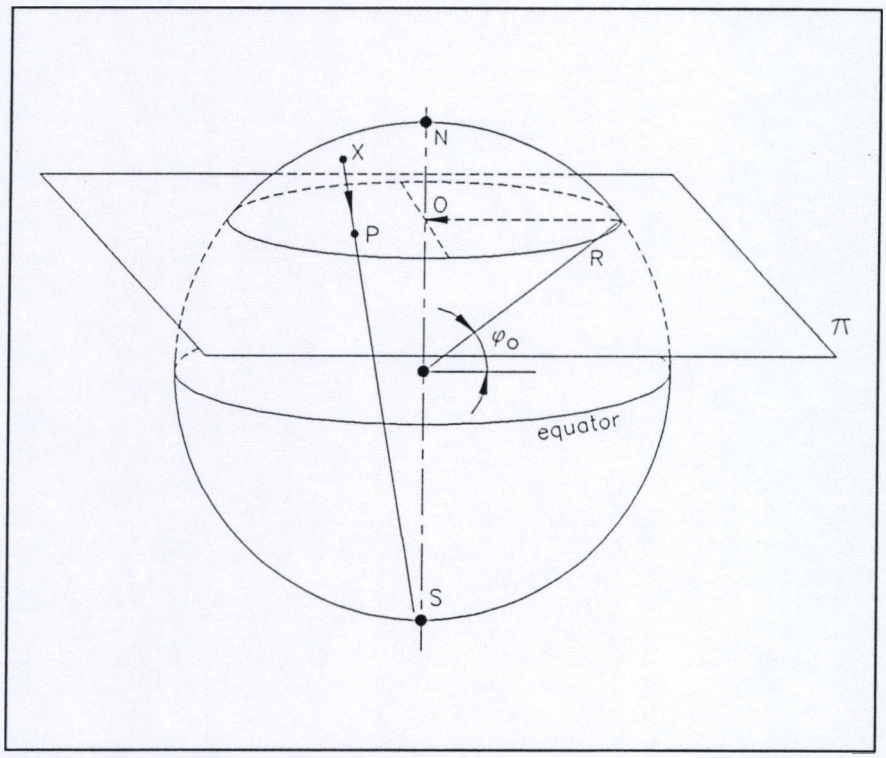

Related Activities

1. Luo, W. (1992), "Derivation of energy dissipation due to bottom friction in finite depth ocean waves", Internal report, Department of Civil Engineering, K. U. Leuven, Belgium.

2. Luo, W. (1995), "Implementation of the cycle 4 version of the WAM model in the Belgian shallow water zone", Internal report, Department of Civil Engineering, K. U. Leuven, Belgium.

3. Luo, W. and J. Monbaliu (1993): "Effects of bottom friction formulation on fetch- limited growth curves in shallow water", Workshop on shallow water wave modelling, Thessaloniki, Greece, October, 1993.

4. Luo, W. and J. Monbaliu (1994), "Effects of the bottom friction formulation on the energy balance for gravity waves in shallow water", *J. Geophys. Res.*, **99**, (C9), 18,501-18,511.

5. Luo, W. and J. Monbaliu (1995), "On the use of equivalent dissipation coefficients for wave energy dissipation due to bottom friction in the third generation wave model", has been submitted for publication in *Coastal Engineering*

6. Luo, W., J. Monbaliu and J. Berlamont (1994), "Equivalent dissipation coefficient for different bottom friction dissipation models in depth-limited wind generated waves", in Proc. Int. Symp.: Waves - Physical and Numerical Modelling, Vancouver, Canada, edited by M. Isaacson and M. Quick, 743-752.

7. Luo, W., J. Monbaliu and J. Berlamont (1995), "Test of equivalent dissipation coefficient for different bottom friction dissipation models in the southern North Sea", in Advances in Hydro- Science and Engineering, Vol 2, 1215-1222.

8. Luo, W., J. Monbaliu and J. Berlamont (1996), "Bottom friction dissipation in the Belgian coastal region", has been submitted for publication in Twenty-fifth International Conference on Coastal Engineering, to be held in Orlando, Florida, U.S.A., September, 1996.

9. Monbaliu, J. and W. Luo (1994): "Wave prediction along the Belgian coast by using the WAM model", 10 years BELGICA.

10. Monbaliu, J. and W. Luo (1995), "Wave modelling along the Belgian coast using the WAM cycle 4 coupled with a storm surge model", in Computer Modelling of Seas and Coastal Regions II, edited by C.A. Brebbia, L. Traversoni and L.C. Wrobel, Computational Mechanics Publications, 319-326.

11. Ovidio, F., J.-R. Bidlot, D. Van den Eynde, W. Luo and J. Monbaliu (1994), "Validation and improvement of the quality of the operational wave model mu-WAVE by the use of ERS-1, buoy data and the WAM forecast", in the Proceedings of the First ERS-1 Pilot Project Workshop, Toledo, Spain, ESA SP-365, 21-28.

12. Ovidio, F., J.-R. Bidlot, D. Van den Eynde, W. Luo and J. Monbaliu (1995), "ESR-1 data assimilation in a second generation wave model for the North Sea" in the Proceedings of the Fourth International Workshop on Wave Hindcasting and Forecasting, Banff (in press).

13. Ovidio, F., J.-R. Bidlot, D. Van den Eynde, W. Luo and J. Monbaliu (1994), "Validation and improvement of the quality of the operational wave model mu-WAVE by the use of ERS-1, buoy data and the WAM forecast", submitted for publication in *J. Marine Systems.*

Biographical Sketch

Weimin LUO was born on the 4th of September 1965, in Hunan, China. In 1985, she graduated from Wuhan University of Hydraulic and Electric Engineering, China, with a Bachelor of Engineering. In 1988, she completed her Master degree, specialized in Fluid Machinery and Fluid Dynamic Engineering, from Wuhan University of Hydraulic and Electric Engineering, China. The subject of her research is 'Numerical Simulation and Experiment Verification of Flow Field in Jet Pump'. This work investigated the microstructure of the velocity flow field in a jet pump.

In June 1988, she was employed as an engineer in Department of Hydraulic Machinery, Institute of Water Conservancy and Hydroelectric Power Research of Chinese Academy of Sciences, Beijing, China. She was involved with a project on 'turbine-model test' for Tianjin Power Equipment Factory. In 1989, she became a free researcher in Laboratory of Thermodynamics, Department of Mechanical Engineering, Catholic University of Leuven, Belgium. She was involved with some fundamental research work in the field of jet pump.

In 1990, she came to the Hydraulic Laboratory of K. U. Leuven. There she became involved with Oceanography. In 1991, she completed her pre-doctoral study, a pre-requisite for the Ph.D, with a great distinction (83%). The subject of her pre-doctoral thesis is 'Investigation of an Implicit Scheme to Simulate the Evolution of Fetch-limited Ocean Wind Wave. Since October 1991, she has started work on this thesis under the supervision of Prof. dr. ir. J. Berlamont.